

Magnetic helicity inverse transfer in isothermal supersonic magnetohydrodynamic turbulence

vorgelegt von
M. Sc.
Jean-Mathieu Teissier

an der Fakultät II – Mathematik und Naturwissenschaften
der Technischen Universität Berlin
zur Erlangung des akademischen Grades

Doktor der Naturwissenschaften
- Dr. rer. nat. -

genehmigte Dissertation

Promotionsausschuss:

Vorsitzender: Prof. Dr. Holger Stark
Gutachter: Prof. Dr. Wolf-Christian Müller
Gutachter: Dr. Roland Grappin

Tag der wissenschaftlichen Aussprache: 11.12.2019

Berlin 2020

*To God Elohim,
I give all glory, thanks and praise*

Acknowledgements

First of all, my deepest thanks go to my parents, who did and are doing a great job, by constantly giving love and encouraging me from the beginning to always ask questions. I would have never guessed that Dad teaching me to program in Qbasic ages ago and Mom bringing my brother Adrien and me to the Cité des Sciences et de l'Industrie to observe ants, build houses and play water games would lead me to numerical astrophysics someday. Special thanks to Adrien for having the talent of making even trifle things look joyful. I am also incredibly thankful to my wife Dina for her amazing support, even helping me calculate square roots in my head.

My first contact with the research world has been with PD Dr. Stefanie Russ. At that time, even though I enjoyed studying natural sciences, I did not feel a particular attraction towards scientific research. This was changed through a relatively short internship, and I am very thankful to her for this.

Regarding the present work, my profound gratitude goes to my supervisor Prof. Dr. Wolf-Christian Müller, for his inspiring role, wonderful and positive energy and constant availability and efforts during the whole project, including at the end the proofreading and the numerous precious comments, suggestions and corrections on the present thesis. I am also very grateful for the financial support by the Berlin International Graduate School in Model and Simulation based Research (BIMoS). High-performance computing resources for this research project have been provided by the North-German Supercomputing Alliance (HLRN) and the Max Planck Computing and Data Facility (MPCDF), without which no result of the present work could have been obtained.

My gratitude also goes to Prof. Dr. Dieter Breitschwerdt, director of the Zentrum für Astronomie und Astrophysik, where all groups can do research together in a pleasant and constructive atmosphere. I would also like to thank my BIMoS mentor Prof. Dr. Jörn Sesterhenn for his valuable guidelines regarding some numerical aspects in fluid dynamics.

My sincere appreciation goes as well to all the current members of the research group Müller as well as to its past members I could interact with, including the bachelor and master students with whom it's always a pleasure to do research with. More particularly, I would like to express my deep gratitude to Benjamin and Jiahan for their proofreading of this dissertation, Raquel for the help regarding the German abstract, Philipp for his introducing me to gnuplot and Oliver for the long-term IT-support and the pleasant teamwork on building the numerical solver used for the direct numerical simulations. The numerical scheme would not have been implemented so quickly without the hard preliminary work done by Dr. Prabal Singh Verma, whom I also mention gratefully. Finally, I would also like to give thanks to Patrycja and Silke for the valuable administrative support.

Abstract

This work deals with magnetic spectral transport and structure formation processes in statistically homogeneous plasma turbulence described in the ideal single fluid magneto-hydrodynamic (MHD) approximation. Of particular interest is the influence of compressibility on these nonlinear dynamics, that is usually neglected in this context but of potential relevance for many astrophysical systems exhibiting large Mach number turbulence.

The fundamental process under investigation in this respect is the inverse spectral transfer of magnetic helicity, $\mathcal{H}^M = \int \mathbf{a} \cdot \mathbf{b} dV$ (with $\mathbf{b} = \nabla \times \mathbf{a}$ the magnetic field), to ever larger scales. Its transport is studied through direct numerical simulations of large-scale-driven compressible isothermal plasma turbulence. To this end, the time evolution of steady-state turbulence of varying levels of compressibility is analysed in Fourier and configuration space under continuous injection of random small scale helical magnetic fluctuations.

Several quantities present self-similar spectral scaling laws, which are consistent with a tendency towards equipartition in terms of magnetic and kinetic energies and helicities. When the large-scale mechanical driving is solenoidal, the scaling exponents are relatively close to those observed in previous research in incompressible MHD, even at Mach numbers $\mathcal{M} = v_{rms}/c_s \sim 10$ (with v_{rms} the standard deviation of turbulent velocity fluctuations and c_s the constant sound speed). For a purely compressive large-scale driving however, significant deviations are already observed at relatively low Mach numbers (of the order of 3). This suggests that compressible effects in astrophysical flows may already considerably affect magnetic structure formation at relatively small Mach numbers, in situations where the turbulence drivers are rather compressive. These deviations can however be alleviated by appropriate changes of variable, hinting at some universality in the inverse transfer behaviour over a wide range of compressibility.

A Fourier-space analysis of the spectral transfers reveals furthermore the presence of three phenomena in the global picture of the magnetic helicity inverse transport: a local inverse transfer, a non-local inverse transfer and a direct local transfer (where “local” refers to the distance of the involved Fourier wavevectors). A projection on the curl operator’s eigenvectors (helical decomposition) of the magnetic and velocity fields allows to assess the relative importance of the different helical contributions, including the role of the compressive part of the velocity field on these three phenomena. The latter contributes to the inverse transfer essentially through non-local transfers and takes the leading role in the direct local transfer in highly compressible flows.

In addition to the physical aspects, this work presents some contributions to the development of robust higher-order numerics, beneficial to attain low numerical dissipation at acceptable computational expense.

Kurzzusammenfassung

Diese Arbeit beschäftigt sich mit magnetischen spektralen Transport- und Strukturbildungsprozesse in statistisch-homogener Plasmaturbulenz im Rahmen der idealen magneto-hydrodynamischen (MHD) Einflüssigkeitsnäherung. Im Fokus liegt der Einfluss der Kompressibilität auf die nichtlineare Dynamik, der in vielen astrophysikalischen Systemen mit hohen Machzahlen von potenzieller Relevanz ist, jedoch in diesem Kontext üblicherweise vernachlässigt wird. Der betrachtete grundlegende Prozess in dieser Hinsicht ist der inverse Spektraltransfer der magnetischen Helizität, $\mathcal{H}^M = \int \mathbf{a} \cdot \mathbf{b} dV$ (mit dem Magnetfeld $\mathbf{b} = \nabla \times \mathbf{a}$), zu immer größeren Skalen. Dieser Transport wird durch direkte numerische Simulationen von großskalig-getriebener kompressibler isothermer Plasmaturbulenz untersucht. Zu diesem Zweck wird die Zeitentwicklung stationärer Turbulenzsysteme mit unterschiedlichen Kompressibilitätsgraden, die einer kontinuierlichen Injektion von zufälligen kleinskaligen helikalen magnetischen Fluktuationen unterliegen, in Fourier- und Konfigurationsraum analysiert.

Mehrere Variablen zeigen selbstähnliche spektrale Skalierungsgesetze, die mit einer Tendenz zur Gleichverteilung zwischen magnetischen und kinetischen Energien und Helizitäten im Einklang stehen. Mit einem solenoidalen großskaligen mechanischem Antrieb werden Exponenten beobachtet, die ähnlich zu denjenigen sind, die in der bisherigen Forschung in der inkompressiblen MHD gefunden wurden. Dieses gilt selbst bei Machzahlen $\mathcal{M} = v_{rms}/c_s \sim 10$ (definiert mit der Standardabweichung der turbulenten Geschwindigkeitsfluktuationen, v_{rms} , und dem konstanten Schallgeschwindigkeit c_s). Mit einem rein kompressiven großskaligen Antrieb sind jedoch signifikante Abweichungen schon bei relativ geringen Machzahlen (der Größenordnung 3) zu sehen. Das deutet darauf hin, dass kompressible Effekte schon bei relativ geringen Machzahlen die Bildung von magnetischen Strukturen in astrophysikalischen Strömungen erheblich beeinflussen können, wenn die Turbulenzanreger eher kompressiv sind. Diese Abweichungen können jedoch durch entsprechende Variablenänderungen abgeschwächt werden, was eine gewisse Universalität des inversen Transfers über einen breiten Bereich der Kompressibilität andeutet.

Eine Fourier-Analyse des Spektraltransfers zeigt ferner das Vorhandensein dreier Phänomene im Gesamtbild des inversen Transfers magnetischer Helizität: lokalen inversen Transfer, nicht lokalen inversen Transfer und lokalen direkten Transfer (wobei "lokal" sich auf den Abstand der beteiligten Fourierwellenvektoren bezieht). Eine Projektion auf die Eigenvektoren des Rotationsoperators (helikale Zerlegung) der Magnet- und Geschwindigkeitsfelder ermöglicht es, die Bedeutung der verschiedenen helikalen Beiträge sowie den Einfluss des kompressiven Teils des Geschwindigkeitsfeldes auf diese drei Phänomene zu beurteilen und zu vergleichen. Der kompressive Geschwindigkeitsanteil trägt zum inversen Transport im Wesentlichen durch nicht-lokalen Transfer bei und übernimmt in hochkompressiblen Strömungen die Hauptrolle des lokalen direkten Transfers.

Neben den physikalischen Aspekten präsentiert diese Arbeit einige Beiträge zur Entwicklung von robusten numerischen Verfahren höherer Ordnung, die vorteilhaft sind, um die numerische Dissipation mit akzeptablem Rechenaufwand zu reduzieren.

Contents

1	Introduction	19
1.1	General framework	19
1.2	Novelty of this work and methodology	20
1.3	Organisation of the dissertation	21
2	Physical model and analysis tools	23
2.1	General description	23
2.1.1	Governing equations	24
2.1.2	Distribution among and transfers across scales	25
2.2	Direct and inverse transfers	29
2.2.1	Direct hydrodynamic cascade	29
2.2.2	Quadratic ideal invariants	31
2.2.3	Magnetic helicity and inverse transfer	32
2.2.4	Alfvén and helicity effects	36
2.3	Helical decomposition	38
2.3.1	Helical triadic interactions	39
2.3.2	Derivations of the geometric factor	40
2.4	Shell-to-shell transfers	42
2.4.1	Magnetic helicity transfers	43
2.4.2	Energy exchanges	44
2.4.3	Other transfer functions and notations	47
2.4.4	Shell-to-shell helical transfers	48
2.5	Summary	49
3	Numerical method	53
3.1	General framework	53
3.2	Fallback strategy	55
3.2.1	Reconstruction methods used	56
3.2.2	ROM computation	57
3.2.3	Application of the ROM	58
3.3	Driving of the system	59
3.3.1	Hydrodynamic forcing	59
3.3.2	Electromotive forcing	61
3.4	Fourier spectra and shell-to-shell transfer functions	62
3.5	Summary: performed runs	63
3.5.1	Main runs	63
3.5.2	Other runs	65

4	Inverse transfer: general aspects	67
4.1	Initial hydrodynamic steady-state	67
4.1.1	Mach number time evolution	68
4.1.2	Kinetic energy spectra	69
4.1.3	Mass density statistics	73
4.1.4	Conclusion	79
4.2	Magnetic helicity injection	79
4.2.1	Emergence of magnetic structure	80
4.2.2	Effects on the hydrodynamic variables	86
4.3	Importance of the large scale velocity field	91
4.4	Summary	92
5	Power-law scaling and Alfvénic balance	93
5.1	Power-law scaling	94
5.1.1	Magnetic energy and helicity	95
5.1.2	Alfvén velocity and helicity	96
5.1.3	Kinetic energy and helicity	99
5.1.4	Summary of the scaling behaviours	102
5.2	Alfvénic balance	104
5.2.1	Considered ratios	104
5.2.2	Subsonic and transonic runs	105
5.2.3	Highly compressive runs	106
5.2.4	Supersonic solenoidally-driven runs	107
5.3	Conclusion	110
6	Spectral transfer analysis	111
6.1	Fourier transfer spectra	112
6.2	Transfer functions: 2D plots	115
6.2.1	Helical decomposition	116
6.2.2	Role of the mediator	119
6.2.3	Energy exchanges	121
6.3	Geometric triadic factors	128
6.4	Additional measurements	135
6.4.1	Comparison with other runs	135
6.4.2	Comparison with previous research	138
6.5	Summary	141
7	Discussion and conclusion	143
7.1	Electromotive forcing variations	143
7.2	Scheme’s order and resolution	147
7.2.1	Level of details	150
7.2.2	Magnetic helicity conservation	150
7.2.3	Power-law scaling and Alfvénic balance	153
7.3	Conclusion	154
A	Technical details	157
A.1	Generation of the initial hydrodynamic frames	157
A.2	Runs’ parameters	159
A.3	Fallback statistics	159
A.4	Additional shell-to-shell analysis tools	162

<i>CONTENTS</i>	13
A.4.1 Relative importance of energy exchanges in the “wings”	162
A.4.2 Normalised geometric factor shape	162
B Discretisation order and dissipation	165
C Supplementary material	171
C.1 Power-law scaling and Alfvénic balance	171
C.2 Heterochiral terms	175

Nomenclature

The vectors are in bold font. When the vector's coordinates can be complex, such as in Fourier space, a hat $\hat{\cdot}$ is also present. The conjugate of a complex number is signified with a * star and the matrix transposition with the superscript T . The entries are ordered alphabetically, first the entries using the Roman alphabet, then the ones using the Greek alphabet.

- a** Magnetic vector potential, so that $\mathbf{b} = \nabla \times \mathbf{a}$ (section 2.2.3).
- b** Magnetic field – implicitly normalised by $\sqrt{\mu_0}$ (with μ_0 the vacuum permeability) so that $\frac{1}{2}\mathbf{b}^2$ is the magnetic energy density (section 2.1.1).
- \mathbf{b}_Y^X Shell-filtered (when Y is present – section 3, if not, then it contains all Fourier shells), helically-decomposed (when X is present, if not, it is the sum of all helical parts) magnetic field, in configuration space. When present, the superscript $X \in \{P, N\}$ stands for the positive helical and negative helical part of the magnetic field, respectively (section 2.4.4).
- C_{CFL} Courant number (section 3.1).
- c_s Sound speed, taken constant to 0.1 in the isothermal case (sections 2.1.1, 3.5.1).
- dV Infinitesimal volume element.
- e Total adiabatic energy density (section 2.1.1).
- $E^A = \mathcal{P}(\mathbf{v}_A)$ Alfvén velocity power spectrum (section 5.1.2).
- $E^K = \mathcal{P}(\mathbf{w})$ Kinetic energy power spectrum (section 2.1.2).
- $E^M = \mathcal{P}(\mathbf{b})$ Magnetic energy power spectrum (section 2.1.2).
- $E^U = \mathcal{P}(\mathbf{u})$ Power spectrum of the $\rho^{1/3}$ -weighted velocity (section 4.1.2).
- $E^V = \mathcal{P}(\mathbf{v})$ Specific kinetic energy power spectrum (section 2.1.2).
- $\mathcal{E}^K = \frac{1}{2}\rho|\mathbf{v}|^2$ Kinetic energy density, in configuration space (section 2.4.2).
- $\mathcal{E}^M = \frac{1}{2}|\mathbf{b}|^2$ Magnetic energy density, in configuration space (section 2.4.2).
- $\mathcal{E}^\rho = \rho c_s^2 \ln(\rho/\rho_0)$ Isothermal compressive potential energy density (section 2.2.2).
- $g_{k,p,q}^{s_k, s_p, s_q} = (\hat{\mathbf{h}}_p^{s_p*} \times \hat{\mathbf{h}}_q^{s_q*}) \cdot \hat{\mathbf{h}}_k^{s_k*}$ Helical triadic geometric factor (section 2.3.1).
- $G = |g|$ Helical triadic geometric factor's magnitude (section 6.3).
- $H^A = \mathcal{Q}(\mathbf{v}_A, \nabla \times \mathbf{v}_A)$ Alfvénic helicity spectrum (section 5.1.2).

- $H^J = \mathcal{Q}(\mathbf{j}, \mathbf{b})$ Current helicity spectrum (section 2.2.4).
- $H^M = \mathcal{Q}(\mathbf{a}, \mathbf{b})$ Magnetic helicity spectrum (section 2.1.2).
- $H_{f,\mathbf{k}}$ Magnetic helicity fraction at wavenumber \mathbf{k} (section 2.2.3).
- h_f Helical fraction of the electromotive forcing (section 3.5.1).
- $H^V = \mathcal{Q}(\mathbf{v}, \nabla \times \mathbf{v})$ Kinetic helicity spectrum (section 2.1.2).
- $\mathcal{H}^A = \int \mathbf{v}_A \cdot (\nabla \times \mathbf{v}_A) dV$ Alfvénic helicity (section 5.1.2).
- $\mathcal{H}^C = \int \mathbf{v} \cdot \mathbf{b} dV$ Cross-helicity (section 2.2.2).
- $\mathcal{H}^J = \int \mathbf{j} \cdot \mathbf{b} dV$ Current helicity (section 2.2.3).
- $\mathcal{H}^M = \int \mathbf{a} \cdot \mathbf{b} dV$ Magnetic helicity (section 2.2.3).
- $\hat{\mathbf{h}}_{\mathbf{k}}^{s_k}$ Helical eigenvector such that $i\mathbf{k} \times \hat{\mathbf{h}}_{\mathbf{k}}^{s_k} = s_k \hat{\mathbf{h}}_{\mathbf{k}}^{s_k}$ with $s_k \in \{+, 0, -\}$ (section 2.3.1).
- $\mathcal{I}_{\mathcal{H}^M}$ Magnetic helicity integral scale (relation (4.4)).
- $\mathbf{j} = \nabla \times \mathbf{b}$ Electric current (section 2.1.1).
- $\mathbf{k}, k = |\mathbf{k}|$ Wavevector \mathbf{k} , and corresponding wavenumber $|\mathbf{k}|$ (section 2.1.2).
- K Integer index for the wavenumber shell containing the modes so that $K \leq |\mathbf{k}|/\kappa < K + 1$ (section 2.1.2). In magnetic helicity shell-to-shell transfers, used for the receiving magnetic field shell (section 2.4.3).
- $K_{max} = N/2$ Largest numerically resolved wavenumber shell (section 2.2.1).
- $K_{inj}^{\mathcal{H}^M} = 50$ Shell around which magnetic helicity is injected in this work (section 4.2.1).
- $K_{inj}^{\mathcal{H}^M*} = 8$ Shell around which magnetic helicity is injected in reference [3] (section 6.4.2).
- K_s Sonic wavenumber shell (section 2.2.1).
- $L = 1$ Simulation box size (section 3.1).
- \mathcal{M} Time-averaged RMS steady-state Mach number (section 2.2.1). In the context of shell-to-shell transfers, this letter is used for terms expliciting the mediating role of a certain field (section 2.4.3).
- N Linear resolution of the computational domain (section 3.1).
- p Thermal pressure (section 2.1.1).
- $\mathcal{P}(\mathbf{f}) = \frac{1}{2} \mathcal{Q}(\mathbf{f}, \mathbf{f})$ Power spectrum of field \mathbf{f} (section 2.1.2).
- $\mathcal{P}^{comp.}(\mathbf{f})$ Power spectrum of the compressive part of field \mathbf{f} (section 2.1.2).
- $\mathcal{P}^{sol.}(\mathbf{f}) = \mathcal{P}(\mathbf{f}) - \mathcal{P}^{comp.}(\mathbf{f})$ Power spectrum of the solenoidal part of field \mathbf{f} (section 2.1.2).
- $\mathcal{Q}(\mathbf{f}, \mathbf{g})$ Shell-integrated dot-product of the Fourier transforms of \mathbf{f} and \mathbf{g} (section 2.1.2).
- $R_{inj} = \frac{\epsilon_{inj}^M}{\epsilon_{inj}^K}$ Magnetic-to-kinetic energy injection ratio (section 3.5.1).

- $ROM_{i,j,k}^n$ Reconstruction order in the n -direction at cell (i, j, k) (section 3.2).
- t Time variable, expressed in code units.
- t_{auto} Autocorrelation time of the Ornstein-Uhlenbeck forcing (section 3.3.1).
- $\mathcal{T}_{xy}^{\mathcal{E}^j}(S, T)$ Energy transfer rates from shell S of field x to shell T of field y , where $x, y \in \{v, b\}$ can be the velocity or the magnetic field (section 2.4.2).
- $\mathcal{T}^{\mathcal{H}^M}$ Magnetic helicity transfer rate. When written $\mathcal{T}^{\mathcal{H}^M}(Q, P, K)$, it is from shell Q to shell K , mediated by the velocity field at shell P . The sum $\mathcal{T}^{\mathcal{H}^M}(Q, K) = \sum_P \mathcal{T}^{\mathcal{H}^M}(Q, P, K)$ is the total transfer rate from shell Q to shell K (sections 2.4.1) and $\mathcal{T}^{\mathcal{H}^M}(K) = \sum_Q \mathcal{T}^{\mathcal{H}^M}(Q, K)$ is the magnetic helicity transfer spectrum (section 2.1.2). When a subscript is present, it corresponds to helically-decomposed contributions (section 2.4.4).
- $t_{\mathcal{T}} = \frac{L}{2c_s \mathcal{M}}$ Turbulent turnover-time (section 4.1.1).
- $t_{\mathcal{T}}^*$ An *a priori* estimate of the turbulent turnover-time (section A.1).
- $\mathbf{u} = \rho^{1/3} \mathbf{v}$ Density-weighted velocity field, with $\rho^{1/3}$ (section 2.2.1).
- \mathcal{U} Letter used in the context of shell-to-shell transfers for terms that can neither be interpreted as shell-to-shell transfers on their own, nor as terms expliciting the mediating role of a certain field (section 2.4.3).
- \mathbf{v} Velocity field (section 2.1.1).
- \mathbf{v}_Y^X Shell-filtered, helically-decomposed velocity field, in configuration space (see \mathbf{b}_Y^X). The X superscript can take the values $\{P, C, N\}$ for the positive helical, compressive and negative helical parts of the velocity field, respectively (section 2.4.4).
- $\mathbf{v}_A = \frac{\mathbf{b}}{\sqrt{\rho}}$ Alfvén velocity field (section 5.1.2).
- $v_{rms} = \sqrt{\langle |\mathbf{v}|^2 \rangle}$ Root mean square velocity (relation (2.29)).
- $\mathbf{w} = \sqrt{\rho} \mathbf{v}$ Density-weighted velocity field, with $\sqrt{\rho}$ (section 2.1.2).
- $\mathbf{x} = (x, y, z)$ 3D position vector (in some context, when there is no ambiguity, it designates only the \mathbf{x} -direction).
- $\Pi^{\mathcal{H}^M}(K) = \sum_{K_0=1}^K \mathcal{T}^{\mathcal{H}^M}(K_0)$ Magnetic helicity spectral flux (section 2.1.2).
- γ_{adia} Ratio of specific heats (section 2.1.1).
- Δt Time-step used for the numerical integration (section 3.1).
- $\Delta x = \Delta y = \Delta z = L/N$ Fixed grid-size of the computational domain (section 3.1).
- $\epsilon_{in,j}^{\mathcal{H}^M}$ Estimate of the magnetic helicity injection rate (relation (4.5)).
- $\epsilon_{in,j}^K$ Kinetic energy injection rate (section 3.3.1).
- $\epsilon_{in,j}^M$ Magnetic energy injection rate (section 3.3.2).
- ζ Spectral weight of the Ornstein-Uhlenbeck forcing (section 3.3.1).

$\kappa = \frac{2\pi}{L}$ Smallest wavenumber in the system (section 2.1.2).

ρ Mass density (section 2.1.1).

$\rho_0 = 1$ Mean mass density in the system (section 3.5.1).

$\tau_{(p,\Delta t),(4,3,2,1)}^\pm$ Thresholds used for the fallback approach (section 3.2.2).

$\Psi^A = \frac{\mathcal{P}^{comp.}(\mathbf{v}_A)}{\mathcal{P}(\mathbf{v}_A)}$ Alfvén velocity compressive ratio spectrum (section 5.1.2).

$\Psi^V = \frac{\mathcal{P}^{comp.}(\mathbf{v})}{\mathcal{P}(\mathbf{v})}$ Velocity compressive ratio spectrum (section 4.1.2).

Abbreviations

CFL Courant Friedrichs Lewy (stability criterion – section 3.1)

CWENO Central Weighted Essentially Non Oscillatory (section 3.1)

DLT Direct Local Transfer (section 6.2)

EOC Experimental Order of Convergence (appendix B)

LIT Local Inverse Transfer (section 6.2)

LSF Least Squares Fit (section 4.2.1)

MHD Magnetohydrodynamics (section 1.1)

NLIT Non-Local Inverse Transfer (section 6.2)

PDF Probability Distribution Function (section 4.1.3)

RMS Root Mean Square (section 2.2.1)

ROM Reconstruction Order Map (section 3.2)

SSPRK Strong Stability-Preserving Runge-Kutta (section 3.1)

Chapter 1

Introduction

1.1 General framework

Contrary to what people experience in their everyday life, where most of the matter is in a solid, liquid or gaseous state, by far most of the visible matter in the Universe is in the plasma state. A plasma is a quasi-neutral ionised gas, which means that in a given volume element, there are roughly equal amounts of positive and negative charges, whose collective behaviour prevents macroscopic charge density fluctuations. As such, its dynamics is interlinked with the electric and magnetic fields: a given point charge generates an electric field, while a moving charge generates a magnetic field, both of which affect the other charges, leading to momentum and energy exchanges over long ranges and a subsequent complex collective behaviour [13].

While a complete description of a plasma would require the knowledge of the electric and magnetic fields as well as all free carriers' positions and velocities, such an approach cannot be used in practice to simulate a plasma's behaviour on computers, due to their huge amount. Moreover, when studying the macroscopic plasma behaviour, what a single plasma particle does at a specific time is of no concern: for the collective plasma dynamics only statistical averages matter. For these reasons, one resorts in computational plasma physics to some physical approximation. The simplest description of a plasma is to consider it as a single electrically conducting fluid, in the framework of (single fluid) magnetohydrodynamics (or MHD). Approximating the plasma as a fluid assumes large enough space and time scales so that local thermodynamic quantities are well defined (length scales considerably larger than the Debye length, and the electron and ion gyroradii) and their temporal variations are slow compared to the occurring microscopic processes (time scales considerably larger than the inverse plasma frequency and the periods of electron and ion cyclotron motions) [60].

In space, non-ideal effects due to molecular viscosity and resistivity are generally rather weak, so that the framework of ideal MHD, where both viscosity and resistivity are neglected, is often used in the astrophysical community.

As a consequence of the very weak non-ideality and enormous characteristic spatial scales, flows in space are commonly turbulent. Turbulence is a phenomenon encountered relatively often in everyday life as well, which manifests itself for example in rivers, or waterfalls, or smoke from chimneys ([85], section 1.1), where the motion of a single fluid element is unpredictable. Turbulence is a very complex nonlinear phenomenon still lacking comprehensive theoretical understanding, where a wide spectrum of structures of very different sizes interact with one another. In 3D turbulence, the kinetic and magnetic energies cascade from the largest scales to the smallest scales where dissipative effects

are predominant, through the breaking-up of similar-sized eddies ([85], chapter 6). Such a transfer from large to small scales is referred to as “direct” since the energy is transferred in Fourier space from small wavenumbers (large scales) to greater ones (small scales). Apart from the total energy, another ideal invariant of the MHD equations is the magnetic helicity [38, 104]. Magnetic helicity quantifies topological aspects of the magnetic field, such as its linkage, twist, writhe and knottedness [80]. As an ideal invariant, it has very important consequences in many astrophysical situations, since its quasi-conservation constrains the magnetic field’s time evolution. Magnetic helicity dynamics play for example an important role in solar flares and coronal mass ejections [72]. Contrary to the kinetic and magnetic energies however, the magnetic helicity is subject to an inverse transfer [48], which makes it a potentially important ingredient in the generation and sustainment of large-scale magnetic fields in the Universe.

1.2 Novelty of this work and methodology

Up to the present day, the inverse transfer of magnetic helicity has been mostly studied assuming incompressibility of the plasma [3, 74, 82]. Some investigations have been performed in the compressible case, but only in the subsonic and transonic regimes [8, 34, 25]. The incompressible approximation in astrophysical MHD turbulence is mostly considered for two reasons: (*i*) for the sake of simplicity, since this assumption renders the thermodynamic pressure a passive quantity and the velocity field is strictly solenoidal in this context and (*ii*) the enhanced complexity of numerical techniques allowing the simulation of compressible flows with an improved accuracy, which have been designed only relatively recently, with the advent of computationally efficient conservative methods of high discretisation order (where “high order” means here an order greater than or equal to four), robust enough to handle strong discontinuities [58, 59, 94, 75, 11, 28].

However, the incompressible approximation is far from being realistic in many astrophysical settings. Indeed, relatively low temperatures are commonly observed, so that the fluid velocity often greatly exceeds the sound speed of the medium. In the some regions of the interstellar medium, root mean square (RMS) Mach numbers (the ratio of the fluid velocity to the sound speed) of the order of 10 are thus commonly encountered ([37], section 4.2). At such supersonic speeds, shocks and discontinuities are frequent, which are incompatible with an incompressible description of the plasma.

The present work makes one step towards a more realistic description by considering effects of compressibility on the nonlinear dynamics of magnetic helicity. To this aim, direct numerical simulations are performed in the framework of isothermal ideal single fluid MHD on triply periodic domains. The governing equations are solved by a fourth-order finite-volume dimension-by-dimension solver, which delivers numerical solutions of convincing accuracy already at the 512^3 and 1024^3 considered resolutions. Hydrodynamic turbulent steady-states with varying RMS Mach numbers and compressibility are generated by a large-scale mechanical driving, injecting energy in the two smallest wavenumber shells. The steady-state RMS Mach numbers considered range from 0.1 to about 11, which is the typical order of magnitude observed in the interstellar medium. The magnetic helicity inverse transfer is investigated by injecting small-scale fully helical magnetic fluctuations around the wavenumber shell 50 through an electromotive forcing.

Previous research performed in the incompressible case has shown that during the magnetic helicity inverse transfer, several quantities exhibit a power-law scaling in Fourier space [74, 82]. A tendency towards equipartition between magnetic and kinetic energies and helicities has also been observed and justified through phenomenological approaches

[74, 82, 53]. The shell-to-shell transfer formalism also revealed the presence of both local and non-local processes during the inverse transfer [3]. More recently, the use of the so-called “helical decomposition” (a projection on the eigenvectors of the curl operator in Fourier space) allowed to make some predictions regarding the strength and locality of different helical contributions in the transfer dynamics, confirmed through direct numerical simulations [69].

The above-mentioned aspects are reviewed and extended to highly compressible turbulent flows. Hence, the results are gained by Fourier analysis of several relevant quantities and the extension of the shell-to-shell and helical decomposition formalisms to compressible MHD.

1.3 Organisation of the dissertation

The physical model used, compressible ideal isothermal MHD, is presented in chapter 2, alongside with the required analysis tools (Fourier, shell-to-shell and helical decomposition analysis). Relations to previous relevant research in compressible hydrodynamics and in the magnetic helicity inverse transfer are also explicit. A more exhaustive presentation of the thesis’ organisation is available at the end of that chapter, after the theoretical notions and analysis tools have been described in more detail.

The high-order numerical method used is described in chapter 3, which details as well the protocol of the numerical experiments.

Chapters 4 to 6 present the obtained main results. Chapter 4 presents general aspects of the magnetic helicity inverse transfer, with an emphasis on magnetic structure growth. Chapter 5 reviews some spectral scalings observed in the incompressible case and proposes an extension of the dynamical balance leading to quasi-equipartition in terms of magnetic and kinetic energies and helicities, valid in the highly compressible case. Chapter 6 makes joint use of the shell-to-shell and helical decomposition analysis in order to assess the roles of the different helical components in the spectral dynamics.

Lastly, chapter 7 summarises the obtained results, discusses their robustness through several parameter studies and gives some concluding remarks.

Chapter 2

Physical model and analysis tools

Most of the visible matter in the Universe is in the plasma state, an ionised gas presenting collective behaviour whose dynamics interact with the magnetic field [13]. The simplest description of an astrophysical plasma is to consider it as a single conducting fluid in the framework of ideal magnetohydrodynamics (MHD). In space, the molecular viscosity and resistivity are indeed generally low, so that non-ideal effects can often be neglected. Furthermore, due to the very low viscosity, the flows are commonly turbulent. Since the sound speed scales as the square root of the temperature, which is rather low in astrophysical systems of interest (even though different conditions can apply in some regions of space), it is common to observe turbulent highly supersonic flows, as in the interstellar medium ([37] section 4.2, [19] section 12.2.1). In turbulence, a wide spectrum of structures of very different sizes interact with one another, so that Fourier analysis represents a very valuable tool.

Section 2.1 offers thus a general description of the physical model used, introducing both the compressible ideal MHD equations and the Fourier analysis. In MHD turbulence, several physical phenomena interact. The predominant ones in the numerical experiments considered in the present work are the direct cascades of magnetic and kinetic energies, where energy injected at large scales is transferred to ever smaller scales, where dissipation dominates and the inverse transfer of magnetic helicity, where large scale structures are formed from small scale magnetic noise. Section 2.2 describes these aspects, starting with the direct cascade of energy in the incompressible case and then reviewing recent results from hydrodynamic compressible turbulence. It also gives the definition of magnetic helicity and reviews its basic properties, with an emphasis on the inverse transfer.

Sections 2.3 and 2.4 introduce the helical decomposition and the shell-to-shell transfer analysis, which are apart from the simple Fourier analysis described in section 2.1.2 the main tools used in the present work.

Lastly, a summary of this chapter is given in section 2.5, where special emphasis is put on relating the present dissertation with previous research, while introducing the next chapters' contents.

2.1 General description

This section aims at introducing the general mathematical framework: the compressible ideal MHD equations (section 2.1.1) and the Fourier space spectral analysis (section 2.1.2).

2.1.1 Governing equations

The MHD equations are a combination of the Navier-Stokes' and Maxwell's equations and can be written, in the absence of viscosity and resistivity (ideal MHD) and neglecting gravity and relativistic effects ([19], section 2.1):

$$\partial_t \rho = -\nabla \cdot (\rho \mathbf{v}), \quad (2.1)$$

$$\partial_t (\rho \mathbf{v}) = -\nabla \cdot \left(\rho \mathbf{v} \mathbf{v}^T + \left(p + \frac{1}{2} |\mathbf{b}|^2 \right) I - \mathbf{b} \mathbf{b}^T \right), \quad (2.2)$$

$$\partial_t \mathbf{b} = \nabla \times (\mathbf{v} \times \mathbf{b}), \quad (2.3)$$

with the constraint (absence of magnetic monopoles):

$$\nabla \cdot \mathbf{b} = 0. \quad (2.4)$$

Here I is the 3×3 identity matrix, ρ the mass density, \mathbf{v} the velocity, \mathbf{b} the magnetic field and p the (thermal) gas pressure. The magnetic field is implicitly normalised by $\sqrt{\mu_0}$ with μ_0 the vacuum permeability so that $\frac{1}{2} |\mathbf{b}|^2$ is the magnetic energy density and the Lorentz force is $\mathbf{j} \times \mathbf{b}$ with $\mathbf{j} = \nabla \times \mathbf{b}$ the electric current (see below).

This particular form of the ideal MHD equations is called “conservative” ([98], section 3.1.1) and is well suited when using a finite-volume numerical scheme to solve them, as in the present work (see chapter 3). The name “conservative” comes from the fact that equations of the form $\partial_t \mathbf{f} = \nabla \cdot \mathbf{g}$ correspond to conservation laws for closed systems, according to the divergence theorem. For example, the mass continuity equation (2.1) implies conservation of mass. The momentum balance (2.2) can be derived when considering a fluid element of volume δV subject to the pressure force $-\delta V \nabla p$ and the Lorentz force $\delta q \mathbf{E} + \delta \mathbf{j} \times \mathbf{b}$ with $\delta q \approx 0$ the charge of the quasineutral fluid element and $\delta \mathbf{j} = \mathbf{j} \delta V$ the electric current it carries ([19], section 2.1). All other volume forces, including the gravity, are neglected. The electric current \mathbf{j} can be deduced through Ampère's law $\mathbf{j} = \nabla \times \mathbf{b}$, when neglecting the displacement current, an approximation valid in the non-relativistic case $|\mathbf{v}| \ll c$ with c the speed of light in vacuum. The magnetic field time evolution comes from Faraday's law. In the restframe of the fluid element, the electric field is according to the generalised Ohm's law $\mathbf{E}' = \eta \mathbf{j}$. Since the resistivity $\eta = 0$ in the ideal MHD framework, this gives $\mathbf{E} = -\mathbf{v} \times \mathbf{b}$ in the laboratory frame through a Galilean transformation, which leads to equation (2.3) since $\partial_t \mathbf{b} = -\nabla \times \mathbf{E}$ (Maxwell-Faraday equation).

Even though no explicit dissipative terms linked with viscosity or resistivity are considered in ideal MHD, numerical dissipation still occurs, predominantly at small scales. No explicit dissipative terms are considered because of two reasons: (i) ideal MHD corresponds to the minimal level of dissipation achievable numerically, so that magnetic helicity is best conserved in this case, (ii) implementing such terms is linked with additional numerical complexity and costs, since they may require a significantly smaller timestep or the use of an implicit time integrator due to their elliptical nature. The ideal MHD approach presents nonetheless a major drawback, namely the lack of control over the dissipation terms, since the numerical non-idealities are not known *a priori* and complex to measure (they are furthermore expected to depend nonlinearly on the solution).

In order to close the system of equations, a gas equation of state has to be added to this physical description. Most commonly in the astrophysical community, either the adiabatic or the isothermal equation of state is used. For the adiabatic equation of state,

the pressure can be written:

$$p = (\gamma_{adia} - 1) \left(e - \frac{1}{2} \rho |\mathbf{v}|^2 - \frac{1}{2} |\mathbf{b}|^2 \right), \quad (2.5)$$

with γ_{adia} the ratio of specific heats and e the total energy density, comprising the kinetic energy $\frac{1}{2} \rho |\mathbf{v}|^2$, the magnetic energy $\frac{1}{2} |\mathbf{b}|^2$ and the internal energy $\frac{p}{\gamma_{adia} - 1}$. In this case, the sound speed c_s and the pressure are related through $c_s = \sqrt{\gamma_{adia} p / \rho}$. The total energy density e is governed by:

$$\partial_t e = -\nabla \cdot \left((e + p + \frac{1}{2} |\mathbf{b}|^2) \mathbf{v} - (\mathbf{v} \cdot \mathbf{b}) \mathbf{b} \right). \quad (2.6)$$

Contrary to the adiabatic case, the isothermal equation of state assumes a constant temperature in the whole domain, which implies a constant sound speed c_s . The pressure is then related with the density through:

$$p = \rho c_s^2, \quad (2.7)$$

Both the adiabatic and the isothermal equations of state correspond to asymptotic limits, which are good approximations in different astrophysical systems. In the isothermal case, the temperature is kept constant throughout the whole considered domain. This is the case for example when the system is in contact with a reservoir at constant temperature or when certain cooling mechanisms take place. In the adiabatic case, all changes in internal energy occur through work: no heat conduction (either molecular or radiative) takes place.

In the interstellar medium, the isothermal equation of state describes well regions of low enough density, so that they are optically thin, allowing radiative cooling. This situation happens notably in the early phase of a molecular gas cloud collapse: the gravitational potential energy lost by compression is released via radiation, so that the temperature of the plasma stays nearly constant. At a later stage however, the plasma becomes optically thick due to the rising mass density, so that radiation can not escape the plasma. In this case, the temperature rises in a nearly adiabatic way ([31], section 12.2).

In the present work, the adiabatic equation of state is used in order to test the numerical method, since a lot of standard tests for MHD solvers make use of it. However, the numerical experiments are run using an isothermal equation of state. This choice is made for the sake of simplicity, since the main aim of the present work is to assess the influence of compressibility on the magnetic helicity inverse transfer dynamics. The simplest model compatible with this aim, both from the physical and the numerical perspectives, is isothermal MHD. An adiabatic equation of state is indeed associated with additional numerical and physical complexity (see section 3.1). Assessing the influence of other effects, such as a non-constant temperature (using diverse equations of state, like the adiabatic one), the presence of gravity or relativistic effects, are possibilities for future work.

2.1.2 Distribution among and transfers across scales

In turbulence, structures with sizes varying on a very wide range of scales interact with each other. For this reason, Fourier analysis has revealed itself a very valuable tool for their study. The Fourier transform of a field allows indeed to investigate the distribution of its energy and helicity among scales. In the same way, the study in Fourier space of a field's governing equations allows to deduce information about energy and helicity

transfers across scales. For a field \mathbf{f} in a 3D periodic cubic domain of length L , the Fourier transform $\hat{\mathbf{f}}$ is defined by:

$$\hat{\mathbf{f}}_{\mathbf{k}} = \frac{1}{L^3} \int e^{-i\mathbf{k}\cdot\mathbf{x}} \mathbf{f}(\mathbf{x}) dV. \quad (2.8)$$

In the discrete formalism required by the use of numerical methods, this translates into ([22], chapter 11):

$$\hat{\mathbf{f}}_{\mathbf{k}} = \frac{1}{N_x N_y N_z} \sum_{\mathbf{x}} e^{-i\mathbf{k}\cdot\mathbf{x}} \mathbf{f}(\mathbf{x}), \quad (2.9)$$

with \mathbf{x} discrete coordinates on the Cartesian grid used, with resolutions N_x, N_y and N_z in the three spatial directions and \mathbf{k} the wavevector, which takes values of the form $\mathbf{k} = (\frac{2\pi}{L}g_x, \frac{2\pi}{L}g_y, \frac{2\pi}{L}g_z)$ with g_m integers in the range $[-N_m/2, N_m/2 - 1]$. The field in configuration space is then:

$$\mathbf{f}(\mathbf{x}) = \sum_{\mathbf{k}} e^{i\mathbf{k}\cdot\mathbf{x}} \hat{\mathbf{f}}_{\mathbf{k}}. \quad (2.10)$$

The vector \mathbf{k} is called the “wavevector” and its module $k = |\mathbf{k}|$ is called the “wavenumber”.

The total energy $\mathcal{E}_T^{\mathbf{f}}$ and helicity $\mathcal{H}^{\mathbf{f}}$ of field \mathbf{f} are then defined by:

$$\mathcal{E}_T^{\mathbf{f}} = \int \mathcal{E}^{\mathbf{f}} dV = \int \frac{1}{2} \mathbf{f}(\mathbf{x}) \cdot \mathbf{f}(\mathbf{x}) dV, \quad (2.11)$$

$$\mathcal{H}^{\mathbf{f}} = \int \mathbf{f}(\mathbf{x}) \cdot (\nabla \times \mathbf{f}(\mathbf{x})) dV, \quad (2.12)$$

with $\mathcal{E}^{\mathbf{f}}$ the energy density of field \mathbf{f} . Please note that the helicity is sometimes defined by $\frac{1}{2} \mathbf{f} \cdot (\nabla \times \mathbf{f})$ in the literature. In the present work, the convention without this $\frac{1}{2}$ factor is used. With these definitions, the contributions of a certain mode with wavevector \mathbf{k} to the field’s energy per unit mass and helicity are respectively, due to Parseval’s theorem:

$$E_{\mathbf{k}}^{\mathbf{f}} = \frac{1}{2} \hat{\mathbf{f}}_{\mathbf{k}}^* \cdot \hat{\mathbf{f}}_{\mathbf{k}}, \quad (2.13)$$

$$H_{\mathbf{k}}^{\mathbf{f}} = \hat{\mathbf{f}}_{\mathbf{k}}^* \cdot (i\mathbf{k} \times \hat{\mathbf{f}}_{\mathbf{k}}). \quad (2.14)$$

Summing these contributions for all Fourier modes in a shell of a given radius gives the shell-integrated Fourier power and helicity spectra:

$$E_K^{\mathbf{f}} = \sum_{K \leq |\mathbf{k}|/\kappa < K+1} E_{\mathbf{k}}^{\mathbf{f}}, \quad (2.15)$$

$$H_K^{\mathbf{f}} = \sum_{K \leq |\mathbf{k}|/\kappa < K+1} H_{\mathbf{k}}^{\mathbf{f}}, \quad (2.16)$$

where $\kappa = \frac{2\pi}{L}$ is the smallest wavenumber in the system and the wavevectors such that $K \leq |\mathbf{k}|/\kappa < K + 1$ build the so-called “ K -shell”. Such shell-integrated Fourier spectra are only meaningful for statistically isotropic systems, which is the case in the present work. They express the energy and helicity distribution in wavenumber space, which can be interpreted as the distribution among the scales: the “ \mathbf{f} -eddies” of size $\frac{L}{2K}$ carry $E_K^{\mathbf{f}}$ units of “ \mathbf{f} -energy” and contribute to $H_K^{\mathbf{f}}$ units of “ \mathbf{f} -helicity” in total.

Two subtleties are worth to be mentioned at this stage:

1. As will be shown in section 2.2.3, magnetic helicity is not defined as the helicity of the magnetic field but as the helicity of its vector potential. Hence the terminology described in this section cannot be directly applied to the magnetic field, even though the ideas behind are of course still applicable: the magnetic energy spectrum E^M is the one built with the magnetic field \mathbf{b} whereas the magnetic helicity spectrum H^M is built with the help of its vector potential \mathbf{a} . Both have the same superscript M even though they are built from two different fields.
2. While in the incompressible case, the kinetic energy is simply $\mathcal{E}^K = \frac{1}{2}|\mathbf{v}|^2$ (multiplied by a constant density $\rho_0 = 1$), it is $\mathcal{E}^K = \frac{1}{2}\rho|\mathbf{v}|^2$ in the compressible case, with a non-constant ρ . The energy spectrum E^V built with the velocity field \mathbf{v} according to equations (2.13) and (2.15) is called “specific kinetic energy spectrum” (one can also find “volume-weighted kinetic energy spectrum” in the literature or “velocity power spectrum”) and does not correspond directly to the kinetic energy. In order to relate the energy spectrum to the kinetic energy, one needs to apply the relations written above to the velocity field weighted with $\sqrt{\rho}$: $\mathbf{w} = \sqrt{\rho}\mathbf{v}$. This spectrum is noted E^K . However, the kinetic helicity spectrum H^V is built with \mathbf{v} directly, not with \mathbf{w} .

In the present work, the expression “ \mathbf{f} power spectrum” is also used as a synonym to “energy spectrum based on field \mathbf{f} ” and is noted $\mathcal{P}(\mathbf{f})$. For example, “the velocity power spectrum”, or the “ \mathbf{v} power spectrum” are other expressions for the specific kinetic energy spectrum. Please note that this implies a factor $\frac{1}{2}$, as introduced in equation (2.13). In the literature, the “power spectrum” of a field \mathbf{f} refers sometimes to the spectrum built on $\hat{\mathbf{f}}_{\mathbf{k}}^* \cdot \hat{\mathbf{f}}_{\mathbf{k}}$ without the $\frac{1}{2}$ factor.

In order to simplify the notations, the following operator is used:

$$\mathcal{Q}(\mathbf{f}, \mathbf{g})_K = \sum_{K \leq |\mathbf{k}|/\kappa < K+1} \hat{\mathbf{f}}_{\mathbf{k}}^* \cdot \hat{\mathbf{g}}_{\mathbf{k}}. \quad (2.17)$$

With this definition, $\mathcal{P}(\mathbf{f}) = \frac{1}{2}\mathcal{Q}(\mathbf{f}, \mathbf{f})$ and the magnetic helicity spectrum $H^M = \mathcal{Q}(\mathbf{a}, \mathbf{b})$.

In the case of compressible turbulence, considering the compressive part of the velocity power spectrum for example also gives useful insights. For an arbitrary field \mathbf{f} , the compressive part of the power spectrum is derived by considering the Fourier components parallel to the wavevector, that is:

$$E_K^{\mathbf{f}, \text{comp.}} = \sum_{K \leq |\mathbf{k}|/\kappa < K+1} \frac{1}{2} |\hat{\mathbf{f}}_{\mathbf{k}} \cdot \mathbf{k}|^2 / |\mathbf{k}|^2. \quad (2.18)$$

Another notation for the compressive part of the \mathbf{f} power spectrum is $\mathcal{P}^{\text{comp.}}(\mathbf{f})$. The solenoidal part of the power spectrum is then the difference $E_K^{\mathbf{f}, \text{sol.}} = \mathcal{P}^{\text{sol.}}(\mathbf{f}) = \mathcal{P}(\mathbf{f}) - \mathcal{P}^{\text{comp.}}(\mathbf{f})$.

This decomposition in solenoidal and compressive part is in essence a Helmholtz decomposition of the field $\mathbf{f} = \nabla \times \mathbf{g} + \nabla(\Phi)$ in a divergence-free (solenoidal) part $\nabla \times \mathbf{g}$ which corresponds to vectors orthogonal to \mathbf{k} in Fourier space and in a curl-free (compressive, or “dilatational”) component $\nabla(\Phi)$ which is parallel to \mathbf{k} in Fourier space. The solenoidal part of the velocity field is responsible for vortex structures whereas the compressive part leads to shock and rarefactions ([37], section 4.4).

In order to study the system’s dynamics, it is also very instructive to consider transfer across scales. The time evolution of a field \mathbf{f} energy and helicity is given by:

$$\partial_t \mathcal{E}^{\mathbf{f}} = \int \mathbf{f} \cdot \partial_t \mathbf{f} dV, \quad (2.19)$$

$$\partial_t \mathcal{H}^{\mathbf{f}} = \int [(\partial_t \mathbf{f}) \cdot (\nabla \times \mathbf{f}) + \mathbf{f} \cdot \partial_t (\nabla \times \mathbf{f})] dV, \quad (2.20)$$

$$= 2 \int (\partial_t \mathbf{f}) \cdot (\nabla \times \mathbf{f}) dV. \quad (2.21)$$

$$= 2 \int \mathbf{f} \cdot \partial_t (\nabla \times \mathbf{f}) dV. \quad (2.22)$$

Relations (2.21) and (2.22) can be obtained by using the identity $\nabla \cdot (\mathbf{f} \times \mathbf{g}) = \mathbf{f} \cdot (\nabla \times \mathbf{g}) - \mathbf{g} \cdot (\nabla \times \mathbf{f})$ and the divergence theorem for a periodic domain. These relations are valid even when \mathbf{f} is not purely solenoidal. In particular they still apply for the velocity field in the compressible case.

The relations (2.19) and (2.21) allow to define the transfer rate Fourier spectra:

$$\mathcal{T}^{\mathcal{E}^{\mathbf{f}}} = \mathcal{Q}(\mathbf{f}, \partial_t \mathbf{f}), \quad (2.23)$$

$$\mathcal{T}^{\mathcal{H}^{\mathbf{f}}} = 2\mathcal{Q}(\partial_t \mathbf{f}, \nabla \times \mathbf{f}), \quad (2.24)$$

with \mathcal{Q} the operator defined in relation (2.17). These transfer spectra allow to see the variations of energy and helicity contained at certain scales and infer from them the direction and strength of transfers, whether they are direct (from large scales to small scales, that is, from small K to large K), or inverse (from small scales to large scales, or equivalently from large K to small K). For conserved quantities such as the magnetic helicity or for energy transfers between energy reservoirs (such as the kinetic \leftrightarrow magnetic energy transfers) or within the same reservoir (such as transfers of magnetic or kinetic energy between scales), it is even possible to determine exactly the direction and strength of transfers of these quantities from any particular shell to any other particular shell. An approach for this purpose is explained in section 2.4. Integrating the helicity $\mathcal{H}^{\mathbf{f}}$ or energy $\mathcal{E}^{\mathbf{f}}$ transfer spectra from shell 1 to shell K gives the so-called ‘‘spectral flux’’:

$$\Pi^j = \sum_{K_0=1}^K \mathcal{T}_{K_0}^j, \quad (2.25)$$

with $j \in \{\mathcal{H}^{\mathbf{f}}, \mathcal{E}^{\mathbf{f}}\}$. These spectral fluxes express the transfer rate of the considered quantity coming into the ball of radius K from all shells $K_0 > K$ outside the ball. Considering spectral fluxes allow for example to assess the presence of an ‘‘inertial range’’ (see section 2.2.1) where some dynamics of the system are neither influenced by energy injection nor by its dissipation. A roughly constant spectral flux in a certain domain is a good indicator for such an inertial range.

Fourier spectra are analysed through chapters 4 to 6. While chapter 4 gives rather general aspects of the hydrodynamic turbulent steady state and the magnetic helicity inverse transfer, including Fourier spectra related to the velocity field and magnetic helicity, chapter 5 looks for scaling laws (power exponents) in Fourier spectra of several other relevant quantities, aiming at the extension of a relation established in the incompressible case (see section 2.2.4). Finally, chapter 6 considers spectral transfer rates and fluxes, using as well the helical decomposition (section 2.3) and shell-to-shell transfers (section 2.4) and allows to disentangle some aspects of the magnetic helicity inverse transfer in supersonic compressible turbulence.

2.2 Direct and inverse transfers

In 3D MHD turbulence, several competing processes take place, leading to complex non-linear dynamics. As in the hydrodynamic case, the kinetic and magnetic energies exhibit direct cascades, being transferred from the largest to ever smaller scales, until dissipative effects dominate. On the contrary, magnetic helicity is transferred from small scales to larger scales, leading to the formation and sustainment of large scale structures. While the direct cascade of kinetic energy in the framework of incompressible hydrodynamic turbulence has been well established since the middle of the previous century, a rigorous approach in the framework of compressible turbulence is still relatively new since major advances, including the demonstration of the presence of an inertial range (see below), have been done only in the present decade. Thus, this section reviews first the incompressible hydrodynamic direct cascade picture, with an emphasis on spectral scaling laws, and presents relatively new results in the compressible case, showing how the scaling exponents are expected to change with increasing compressibility.

Then, the MHD ideal quadratic invariants are introduced, since they present important constraints on the system's dynamics. The magnetic helicity, one of them, is then presented in greater detail, with a focus on its inverse transfer key property. Links are established with previous research, which explain the magnetic helicity inverse transfer as a competition between two effects, namely the ‘‘Alfvén effect’’ and the ‘‘helicity effect’’, and showed the presence of a certain ‘‘Alfvénic balance’’ and several scaling laws in the Fourier spectra.

2.2.1 Direct hydrodynamic cascade

The idea of the kinetic energy cascade in hydrodynamic turbulence dates back to the 1920s ([85], chapter 6). L. F. Richardson proposed that the kinetic energy, which is injected in the turbulent system at the largest scales through a mechanical driving, is transferred successively to ever smaller scales through the inviscid breaking-up of large unstable eddies in smaller ones, these smaller eddies experiencing the same process, until the dissipation of this energy at the smallest scales through viscous processes [89]. This picture implies the existence of a so-called ‘‘inertial range’’ between the energy input at the largest scales and the small scale dissipation where the energy flux is constant, independent of the scale, since the energy cascades to smaller and smaller scales without being lost. A. N. Kolmogorov developed these ideas further, leading to the eponym 1941 theory. With the help of three hypotheses, he could derive exact relations, leading to quantitative predictions¹. One of these is the ‘‘four-fifths’’ law [61], which leads to the following prediction for the kinetic energy spectrum in the inertial range of incompressible hydrodynamic turbulence [47, 85]:

$$E_K^V \sim \epsilon^{2/3} K^{-5/3}, \quad (2.26)$$

with ϵ the energy dissipation rate. This prediction has been supported through numerous experimental data ([47, 85] and references therein) and can be recovered through a phenomenological approach based on a dimensional analysis. Assuming an eddy of size l with a typical velocity v_l , the typical time for this eddy to experience a significant deformation (and a consecutive break-up in smaller eddies) is the eddy turnover time $t_l \sim l/v_l$.

¹The hypotheses Kolmogorov used as well as the complete derivations are not repeated here. Only some background concepts relevant for the understanding of simulation results in the framework of compressible MHD turbulence are briefly outlined here. The interested reader is kindly referred to the cited literature.

Hence, the energy flux Π from scales close to l to smaller scales can be estimated as ([47], chapter 7):

$$\Pi \sim v_l^2/t_l \sim v_l^3/l. \quad (2.27)$$

Since in the inertial range the energy flux is independent of the scale, it has to be equal to the energy dissipation rate ϵ . This leads to:

$$v_l^2 \sim \epsilon^{2/3} l^{2/3}, \quad (2.28)$$

from which relation (2.26) follows since a Fourier energy spectrum is dimensionally an energy density.

How supersonic a flow is can be measured by the root mean square (RMS) Mach number, defined by:

$$\mathcal{M} = \sqrt{\left\langle \frac{|\mathbf{v}|^2}{c_s} \right\rangle} = v_{rms}/c_s, \quad (2.29)$$

with $\langle f \rangle = \frac{1}{L^3} \int f dV$ the volume average of the quantity f . In the present work, runs with either a purely solenoidal or compressive driving (see sections 2.1.2 and 3.3.1), with RMS Mach numbers ranging from about 0.1 to about 11 are considered. These values correspond to typical values seen in the interstellar medium ([37], section 4.2).

Most of the turbulent flow's steady state physical properties are determined by both the RMS Mach number and the forcing's degree of compressivity [45]. When for low \mathcal{M} , the Kolmogorov $K^{-5/3}$ scaling is expected for the velocity power spectrum $E^V = \mathcal{P}(\mathbf{v})$, the scaling changes at high \mathcal{M} and/or with the forcing's degree of compressivity.

Indeed, for highly supersonic turbulence, the velocity spectrum is expected to display a Burgers scaling [29] $E_K^V \sim K^{-2}$. This is due to the fact that a discontinuity (step function) exhibits a K^{-2} power spectrum ([22], chapter 22) and in supersonic shock-dominated turbulence, the velocity field is expected to be essentially a superposition of such discontinuities.

However, the Kolmogorov scaling can be recovered with an appropriate change of variable. Based on the phenomenological compressible model of C. W. von Weizsäcker [101] and the assumption of a constant kinetic energy density transfer rate $\sim \frac{\rho v^2}{t_l} \sim \frac{\rho v^3}{l} \sim \frac{(\rho^{1/3} v)^3}{l}$ [67], one obtains through the same analysis as done in relations (2.27) and (2.28) but replacing v by $\rho^{1/3} v$ that the power-spectrum of the velocity field weighted with $\rho^{1/3}$: $\mathbf{u} = \rho^{1/3} \mathbf{v}$ should follow the $K^{-5/3}$ Kolmogorov scaling [46].

This has indeed been verified numerically for highly supersonic isothermal solenoidally-driven turbulence, up to a RMS Mach number of approximately 17 [62, 45, 43]. However, for compressively-driven turbulence, deviations from this $\mathcal{P}(\mathbf{u}) \sim K^{-5/3}$ scaling have been observed [43]. These deviations are compatible with the theoretical predictions of reference [49], which takes into account, in addition to the kinetic energy, the potential energy stored in density fluctuations (see section 2.2.2). This reference predicts $\mathcal{P}(\mathbf{u}) \sim K^{-19/9}$ for isothermal flows with a strong compressive $\nabla \cdot \mathbf{v}$ component (as is the case for compressively-driven turbulence) and proposes a transition to the $\mathcal{P}(\mathbf{u}) \sim K^{-5/3}$ spectrum around the so-called ‘‘sonic wavenumber’’ (see below).

Please note that in order to apply the above arguments to compressible turbulence, both the locality of transfers (since the energy should flow from a larger eddy to similar-sized smaller ones) and the existence of an inertial range in compressible turbulence have to be established. These two aspects have been proven rigorously at a later time as compared to the theoretical predictions of references [46, 49], in references [4] and [5] respectively.

The transition from the compressible to the Kolmogorov scaling ($K^{-2} \rightarrow K^{-5/3}$ for the velocity power spectra and $K^{-19/9} \rightarrow K^{-5/3}$ for $\mathcal{P}(\mathbf{u})$ in compressively-driven turbulence) is expected to happen around the so-called ‘‘sonic wavenumber’’ K_s [91, 45, 43, 49], defined by:

$$\int_{K_s}^{K_{max}} E_K^V dK \approx \frac{1}{2} c_s^2, \quad (2.30)$$

with K_{max} the largest numerically resolved wavenumber. It corresponds to the wavenumber at which the mean square turbulent velocity fluctuations are comparable to those of a fluid at RMS Mach number 1. With other words, the scales where $K \gtrsim K_s$ are in the supersonic regime and those where $K_s \gtrsim K$ in the subsonic one.

Power spectra of \mathbf{v} and \mathbf{u} in the hydrodynamic case are presented in section 4.1.2 with data from the main runs and confronted to the results mentioned in the present section. Since the inertial range corresponds to a range of scales neither influenced by the driving nor by the dissipative effects, a good enough scale separation is required in order to see the expected inertial range scaling. This scale separation has furthermore to be big enough in order to counteract the so-called ‘‘bottleneck effect’’ close to the viscous scales, which contaminates the inertial range (see section 4.1.2). As a consequence, the expected theoretical scaling can only be observed in a very limited spectral domain, unless one resorts to very high resolutions, which are difficult to achieve with present day computing resources. One can mention with this respect the project presented in reference [44], which aims at observing the transition region from supersonic to subsonic turbulence around the sonic wavenumber from a run at resolution 10048³.

2.2.2 Quadratic ideal invariants

The MHD equations present three quadratic ideal invariants ([104, 103] and [19], section 2.3), both in the incompressible and the polytropic cases $p \sim \rho^m$ (which includes the isothermal case with $m = 1$ and the adiabatic case $m = \gamma_{adia}$):

1. The total energy. In the incompressible case, it is the sum of the kinetic and the magnetic energy. In the compressible case, energy can also be stored in a third form: for an adiabatic equation of state, it can be stored as internal energy $\frac{p}{\gamma_{adia}-1}$, which is linked with the temperature, whereas in the isothermal case, even though the temperature is constant in the system, energy can still be stored in a potential form as density fluctuations [63]:

$$\mathcal{E}^\rho = \rho c_s^2 \ln(\rho/\rho_0), \quad (2.31)$$

with ρ_0 the mean mass density in the system. In 3D MHD turbulence, both the kinetic and the magnetic energies exhibit a direct cascade from large to small scales ([19], section 5.2.2).

2. The cross-helicity, $\mathcal{H}^C = \int \mathbf{v} \cdot \mathbf{b} dV$ which is a measure of the magnetic and velocity fields alignment. It also exhibits a direct cascade ([19], section 5.2.2).
3. The magnetic helicity, described in greater detail in section 2.2.3, which is, contrary to the total energy and the cross-helicity, a purely magnetic quantity. As explained in that section, it expresses topological aspects of the magnetic field and exhibits an inverse transfer.

These ideal invariants are important constraints for the system's time evolution. Even when non-ideal effects are present, they decay at different rates, a phenomenon called “selective decay”. Magnetic helicity and cross-helicity are in general better conserved than the energy ([96, 16] and [19], section 4.2.1). This is why a helical magnetic field without cross-helicity is expected to relax to a state of minimum energy compatible with a quasi-conservation of the initial magnetic helicity, that is, a force-free field $\nabla \times \mathbf{b} = \lambda \mathbf{b}$ with λ a constant [104]. This was conjectured for the first time in the 70s by J. B. Taylor [95] and received experimental support ([14] and references therein). Another consequence of the selective decay is the so-called “dynamic alignment” of the velocity and magnetic fields: when cross-helicity is present, since it decays slower than the energy, the relaxed state is expected to be the one with minimum energy for a given cross-helicity value, namely $\mathbf{v} = \pm \mathbf{b}$, at each point in space, which is a pure Alfvénic state ([19], section 4.2.1).

In forced turbulence, dynamical alignment is thus expected to occur, which has the effect of quenching the nonlinear dynamics since an alignment between \mathbf{v} and \mathbf{b} means a smaller $\mathbf{v} \times \mathbf{b}$ term appearing in the magnetic field evolution equation. In the present work, this effect is unwanted, since the object of study is the inverse transfer of another invariant, namely the magnetic helicity. It is hence important to check whether the cross-helicity in the system is low in the considered runs. A measure for the magnetic field-velocity field correlations is $\rho_C = \frac{\mathcal{H}^C}{2\sqrt{\mathcal{E}^M \mathcal{E}^V}}$ with $\mathcal{E}^V = \frac{1}{2} \int |\mathbf{v}|^2 dV$ the specific kinetic energy in the system and $\mathcal{E}^M = \frac{1}{2} \int |\mathbf{b}|^2 dV$ the total magnetic energy. In the runs presented in this work, even though $|\rho_C|$ indeed tends to grow with time, it remains very low, under 0.035 for all the runs, so that only the direct cascade of energy and the inverse transfer of magnetic helicity are expected to play an important role in the nonlinear dynamics.

2.2.3 Magnetic helicity and inverse transfer

Contrary to what its name suggests, the magnetic helicity \mathcal{H}^M is not the helicity of the magnetic field \mathbf{b} . Instead, the magnetic helicity \mathcal{H}^M is defined as the helicity of the magnetic vector potential \mathbf{a} (with $\mathbf{b} = \nabla \times \mathbf{a}$):

$$\mathcal{H}^M = \int \mathbf{a} \cdot \mathbf{b} dV. \quad (2.32)$$

The name “helicity” comes from the fact that streamlines of a flow such that $\mathbf{v} \cdot (\nabla \times \mathbf{v})$ is big have a helical shape (figure 2.1.(b)). Magnetic helicity is thus a measure of topological aspects of the magnetic field, expressing how magnetic flux tubes are twisted, writhed, knotted and linked [80, 17, 21]. The linkage refers to how multiple magnetic flux tubes are interlinked with one another (figure 2.1.(a)). Using Gauss’ theorem, one can show that the magnetic helicity of two linked flux tubes with constant magnetic field magnitudes B_1 and B_2 and magnetic flux Φ_1 and Φ_2 is $\pm 2\Phi_1\Phi_2$ [17, 21]. “Twist”, “writhe” and “knottedness” refer to topological aspects of single flux tubes: the twist refers to how the magnetic field lines in a specific flux tube rotate around its axis, in the same way that the “ladder-shaped” DNA in living cells winds around its axis, whereas the writhe refers to the helical structure of the axis itself, in the same way that DNA is wrapped around proteins called histones. Topologically, units of writhe and twist can be interchanged (figure 2.1.(c)). Units of twist (or writhe) are related with linkage inside a flux tube, as can be shown experimentally using strips of paper, tape and scissors [21]. As for knots, they can be viewed as an assemblage of links and writhes (figure 2.1.(d), remade from reference [80]).

The helicity of the magnetic field $\mathcal{H}^J = \int \mathbf{b} \cdot (\nabla \times \mathbf{b}) dV = \int \mathbf{b} \cdot \mathbf{j} dV$ is also a very relevant quantity called “current helicity”. Indeed, magnetic helicity cannot be measured directly

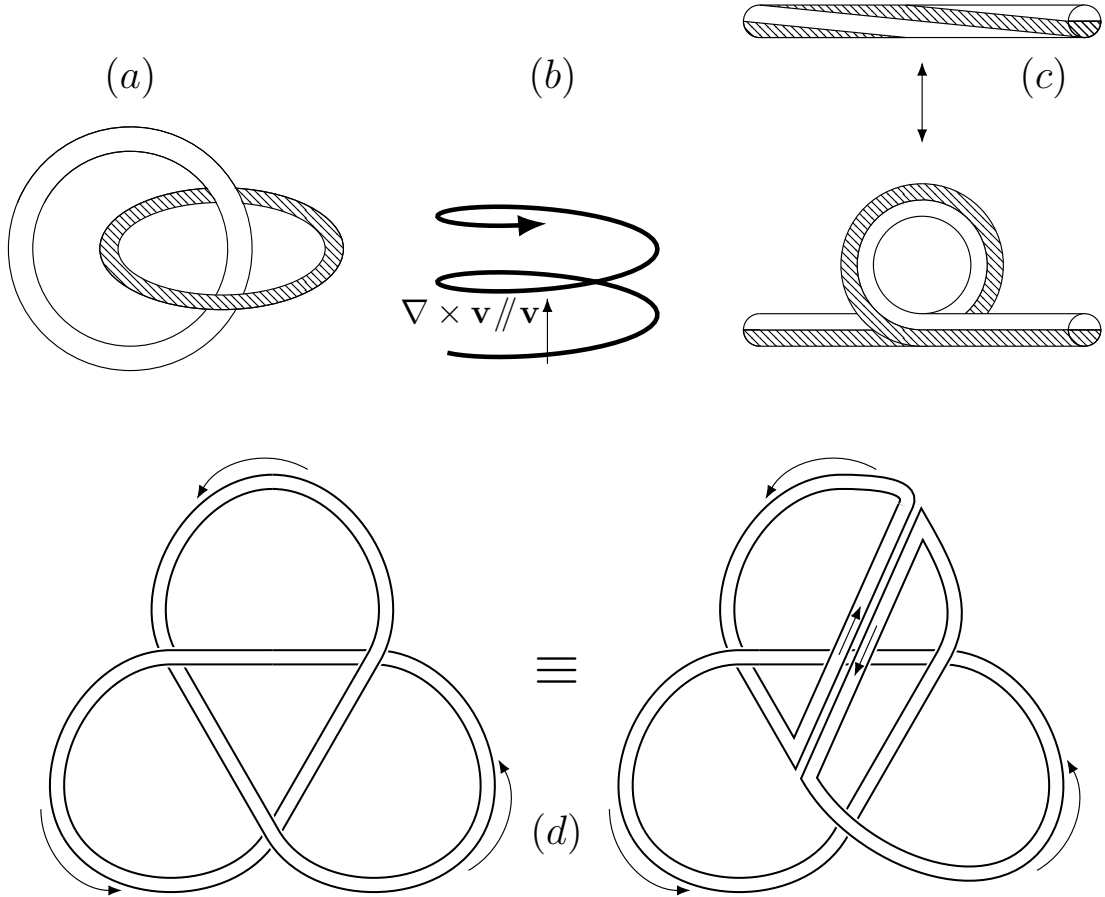


Figure 2.1: Diverse expressions of helicity. (a) Helicity as a measure of linkage. (b) Streamline in a (positive) helical flow. (c) Top: twist, bottom: writhe of a flux tube. (d) Knotted flux tube, equivalent to a writhed tube and a link between two tubes, visible when inserting two flux tubes of opposite helicity. Subfigure remade from reference [80].

but has to be deduced, under certain assumptions, from current helicity measurements [27]. For example, vector magnetograms of the sun’s active regions allowed to find negative current helicity in the northern hemisphere and positive current helicity in the southern one, from which a like-signed repartition of magnetic helicity in each hemisphere was concluded ([27] section 2.1.2 and references therein). The current helicity is however, contrary to the magnetic helicity, not an ideal invariant.

The magnetic helicity invariance is a direct consequence of relation (2.21) applied to the magnetic vector potential (that is $\mathbf{f} = \mathbf{a}$), and was first proven in the late 50s by W. M. Elsässer and L. Woltjer independently [38, 104]. Indeed, the ideal evolution equation for \mathbf{a} can be deduced by “uncurling” equation (2.3):

$$\partial_t \mathbf{a} = \mathbf{v} \times \mathbf{b} + \nabla(\Phi), \quad (2.33)$$

with $\nabla(\Phi)$ determined by the gauge condition. Choosing the gauge so that the scalar potential vanishes, as in reference [104], one obtains that $\mathbf{b} \cdot \partial_t \mathbf{a} = 0$, which, plugged in relation (2.21) gives $\partial_t \mathcal{H}^M = 0$. Please note that no assumption was made regarding the velocity field. In fact, one could even replace in this proof the velocity field by any well-behaved vector field, which would not even need to be a solution of the MHD equations. This means in particular that the magnetic helicity is an ideal invariant for compressible

turbulence as well. This also means that, in a system with truly zero resistivity, one cannot inject or remove magnetic helicity by acting on the velocity field only²: action on the magnetic field directly is needed. This is in contrast with the magnetic energy since it can be changed through kinetic \leftrightarrow magnetic energy transfers, or with the cross-helicity which can be changed by applying for example a mechanical forcing parallel to the magnetic field.

Since in a periodic domain with no mean magnetic field the magnetic helicity is gauge invariant [15, 27], another gauge choice would not affect the magnetic helicity invariance. Indeed, changing \mathbf{a} to $\mathbf{a} + \nabla(\Phi)$ with Φ an arbitrary scalar field gives:

$$\mathcal{H}^M = \int (\mathbf{a} + \nabla(\Phi)) \cdot \mathbf{b} dV = \int \mathbf{a} \cdot \mathbf{b} dV + \int \nabla \cdot (\Phi \mathbf{b}) dV - \int \Phi (\nabla \cdot \mathbf{b}) dV. \quad (2.34)$$

The second term on the right-hand side is zero using the divergence theorem on a closed (or periodic) domain, whereas the third term is zero because of the magnetic field solenoidality. In open volumes, or when field lines leave the considered closed volume (when, for example, a mean-magnetic field is present so that $\mathbf{b} \cdot \mathbf{n} \neq 0$ on the boundaries with \mathbf{n} a vector normal to the boundary's surface), magnetic helicity is not gauge invariant anymore. One can however extend the magnetic helicity definition to a gauge-invariant one in these cases, namely the “relative magnetic helicity”, where “relative” means in relation to a potential curl-free magnetic field \mathbf{b}^{ref} which verifies the boundary condition $\mathbf{b}^{ref} \cdot \mathbf{n} = \mathbf{b} \cdot \mathbf{n}$ [17, 27]. Since many astrophysical systems are in fact open, the study of relative magnetic helicity is also a very relevant topic. In the present work however, only periodic domains are considered, so that the reader interested in other boundary conditions is kindly referred to the cited literature.

In the present work, the Coulomb gauge $\nabla \cdot \mathbf{a} = 0$ is used. This gauge is very practical when using periodic boundary conditions since it allows to determine the magnetic vector potential in a straightforward way through a passage in Fourier space. Indeed, for any solenoidal field $\mathbf{f} = \nabla \times \mathbf{g}$ (for the magnetic field, $\mathbf{b} = \nabla \times \mathbf{a}$), its Fourier coefficients $\hat{\mathbf{f}}_{\mathbf{k}}$ verify $i\mathbf{k} \times \hat{\mathbf{f}}_{\mathbf{k}} = k^2 \hat{\mathbf{g}}_{\mathbf{k}}$. One can hence define a “rot⁻¹” operator such that $\mathbf{g} = \mathbf{rot}^{-1}(\mathbf{f})$ is the field with Fourier coefficients $\hat{\mathbf{g}}_{\mathbf{k}} = \frac{i\mathbf{k} \times \hat{\mathbf{f}}_{\mathbf{k}}}{k^2}$.

As an ideal invariant, magnetic helicity is an important constraint for the temporal evolution of magnetic fields, which has important consequences in many physical situations. Because of the very low resistivity in space, the magnetic field is very efficiently “frozen into the plasma” ([60], section 2.5), so that rotational motions naturally generate helical fields. As mentioned above, the sun presents helical fields and it has been shown that magnetic helicity dynamics play an important role in solar flares and coronal mass ejections [72]. Thus, the sun emits magnetic helicity in the interplanetary medium through these eruptive events [64], but as well through the solar wind [18]. At the largest scales, this is manifested through the Parker spiral. In laboratory plasmas, magnetic helicity is an important quantity related to the magnetic confinement of reversed-field-pinch fusion devices [39].

²Please note however that, when a non-zero resistivity is present, should it be because of purely numerical dissipative effects, one can still obtain finite magnetic helicity in a system even when starting with non-helical initial conditions. In kinematic dynamo numerical experiments for example, such as the one in reference [25], helical velocity fluctuations are injected at small scales. These induce magnetic helical fluctuations of different signs so that they cancel out in total. However, the helical contributions of one sign experience mostly a direct transfer, whereas those of the opposite sign experience mostly an inverse transfer. Since at small scales, the dissipative effects are more important, the system accumulates magnetic helicity of one sign in the end.

Contrary to the kinetic and magnetic energies, which present a direct transfer in wavenumber space, that is from large to ever smaller scales, where dissipation dominates, magnetic helicity is transferred from small scales towards larger scales. This is one of the most important properties of magnetic helicity, which could explain the presence of large scale magnetic fields throughout the Universe. The possibility of an inverse transfer of magnetic helicity was first proposed in the 70s by U. Frisch et al. [48] and rapidly confirmed through numerical experiments [86, 87, 76, 8, 34, 25, 3, 74, 82]. Two arguments justifying the existence of an inverse transfer are given in reference [48]: one which will not be repeated in more detail, based on absolute equilibrium distributions (see as well reference [19], section 5.2) and the other argument based on the so-called “realisability condition”, which is in essence the Cauchy-Schwarz inequality applied to the magnetic helicity in Fourier space:

$$|H_{\mathbf{k}}^M| = |(\hat{\mathbf{a}}_{\mathbf{k}}^{sol})^* \cdot \hat{\mathbf{b}}_{\mathbf{k}}| \leq |\hat{\mathbf{a}}_{\mathbf{k}}^{sol}| |\hat{\mathbf{b}}_{\mathbf{k}}| = \frac{1}{|\mathbf{k}|} |\hat{\mathbf{b}}_{\mathbf{k}}|^2 = \frac{2E_{\mathbf{k}}^M}{|\mathbf{k}|}, \quad (2.35)$$

where $\hat{\mathbf{a}}_{\mathbf{k}}^{sol}$ is the solenoidal part of the magnetic vector potential (using the Coulomb gauge is equivalent to require $\hat{\mathbf{a}}_{\mathbf{k}}^{sol} = \hat{\mathbf{a}}_{\mathbf{k}}$), so that $|\hat{\mathbf{b}}_{\mathbf{k}}| = |\mathbf{k}| |\hat{\mathbf{a}}_{\mathbf{k}}^{sol}|$ due to the orthogonality of \mathbf{k} and $\hat{\mathbf{a}}_{\mathbf{k}}^{sol}$. From this realisability condition follows the definition of the “magnetic helicity fraction”:

$$H_{f,\mathbf{k}} = \frac{|\mathbf{k}| H_{\mathbf{k}}^M}{2E_{\mathbf{k}}^M}, \quad (2.36)$$

which is the ratio of the contribution to magnetic helicity of mode \mathbf{k} as compared to its maximum possible contribution compatible with the realisability condition and is hence a number between -1 and +1. A fraction of +1 or -1 means that the realisability condition (2.35) is saturated and the field is then said to be “fully (positive/negative) helical” or “with maximal (positive/negative) helicity” (at this wavevector). Following the argument in reference [48], let an initial state be a purely magnetic state confined in two wavevectors \mathbf{p} and \mathbf{q} with maximal positive helicity, that is: a total energy $E_{\mathbf{p}}^T + E_{\mathbf{q}}^T = E_{\mathbf{p}}^M + E_{\mathbf{q}}^M$ with magnetic helicity $H_{\mathbf{p}}^M + H_{\mathbf{q}}^M = \frac{2E_{\mathbf{p}}^T}{|\mathbf{p}|} + \frac{2E_{\mathbf{q}}^T}{|\mathbf{q}|}$. Then, assuming all the magnetic helicity and energy is transferred to another wavevector \mathbf{k} , the conservation of total energy and magnetic helicity imposes:

$$E_{\mathbf{k}}^T = E_{\mathbf{p}}^T + E_{\mathbf{q}}^T, \quad (2.37)$$

$$H_{\mathbf{k}}^M = \frac{2E_{\mathbf{p}}^T}{|\mathbf{p}|} + \frac{2E_{\mathbf{q}}^T}{|\mathbf{q}|}. \quad (2.38)$$

This requires $|\mathbf{k}| \leq \max(|\mathbf{p}|, |\mathbf{q}|)$. Indeed, if $|\mathbf{k}| > \max(|\mathbf{p}|, |\mathbf{q}|)$, then

$$\frac{2E_{\mathbf{k}}^T}{|\mathbf{k}|} = \frac{2(E_{\mathbf{p}}^T + E_{\mathbf{q}}^T)}{|\mathbf{k}|} < \frac{2E_{\mathbf{p}}^T}{|\mathbf{p}|} + \frac{2E_{\mathbf{q}}^T}{|\mathbf{q}|} = H_{\mathbf{k}}^M, \quad (2.39)$$

and the realisability condition would be broken at wavevector \mathbf{k} since $E_{\mathbf{k}}^M \leq E_{\mathbf{k}}^T$. As a consequence, when choosing $|\mathbf{p}| = |\mathbf{q}|$, then $|\mathbf{k}| \leq |\mathbf{p}|$, which means that the magnetic helicity tends to be transferred to lower wavenumbers, that is, to larger scales.

Using similar dimensional arguments as the ones in the phenomenological direct cascade model (see relations (2.27)-(2.28)), a prediction for the scaling law of the magnetic

helicity spectrum in the incompressible case can be derived [86]. Namely, assuming a constant magnetic helicity flux in the inverse transfer range yields:

$$\Pi^{\mathcal{H}^M} \sim \frac{a_l b_l}{t_l} \sim \frac{a_l b_l v_l}{l} \sim \left(\frac{a_l b_l}{l} \right)^{3/2}, \quad (2.40)$$

where the dimensional relation $v_l \sim b_l \sim (a_l b_l / l)^{1/2}$ was used (in the incompressible case, $v_l \sim b_l$, since the density is constant). A constant flux implies then:

$$a_l b_l \sim l, \quad (2.41)$$

which means that a K^{-2} spectrum is predicted in the inverse transfer inertial range. Although this prediction was indeed confirmed by numerical integration of the eddy-damped quasi-normal Markovian (EDQNM – see below) closure model [86], incompressible MHD direct numerical simulations showed significantly steeper spectra. In decaying turbulent fields with magnetic helicity localised at large scales, both exponents close to -3.7 [53] and -3.3 [79] were observed. In a numerical experiment investigating the magnetic helicity inverse transfer in a decaying field, where the initial magnetic helicity is localised at small scales, an exponent close to -3.6 has been measured [74, 82]. For an numerical setup closer to the one of the present work, where magnetic helicity is injected through an electromotive forcing at small scales, an exponent close to -3.3 has been observed [74, 82]. A physical understanding explaining the observed numerical value of this inverse transfer exponent is still missing up to the present day.

Regarding the terminology, the magnetic helicity inverse transfer is sometimes labelled as a “cascade” in the literature. However, the concept of “cascade” is usually associated with local interactions, as in the direct (local) cascade of energy in the hydrodynamic case. Since the magnetic helicity inverse transfer is in fact associated with non-local effects as well, the expression “magnetic helicity inverse cascade” is not used in the present work. When the word “cascade” is used, for example in chapter 6, it implies the locality of transfers.

2.2.4 Alfvén and helicity effects

The EDQNM closure model (in incompressible turbulence) is based on the assumptions that the turbulent velocity field probability distribution function is “quasi-normal” in the sense that the fourth-order moments can be expressed as the sum of second-order moments, while all odd-order moments, except the first and the third ones, are assumed to be negligible. The effect of all neglected high-order statistical moments is modelled by a phenomenological eddy damping rate [84], which acts as additional attenuation on the third-order moments (such as the energy flux). The very short exponentially decaying auto-correlation time of turbulent fluctuations is exploited by eliminating “memory integrals” from the EDQNM description – a procedure referred to as “Markovianization”. It has been extended to MHD turbulence in reference [86]. In this framework, it has been shown that the inverse transfer of magnetic helicity can be viewed as a competition between the dynamo mechanism (or helicity effects) and the Alfvén effect, both defined below. Indeed, one can write to lowest order the non-local (labelled “NL”) contributions to the time evolution of the magnetic and kinetic energies and helicities in shell K as [86]:

$$(\partial_t E_K^V)_{NL} \approx -K\Gamma_K(E_K^V - E_K^M), \quad (2.42)$$

$$(\partial_t E_K^M)_{NL} \approx K\Gamma_K(E_K^V - E_K^M) + \alpha_K^R K^2 H_K^M, \quad (2.43)$$

$$(\partial_t H_K^V)_{NL} \approx -K\Gamma_K(H_K^V - K^2 H_K^M), \quad (2.44)$$

$$(\partial_t H_K^M)_{NL} \approx (\Gamma_K/K)(H_K^V - K^2 H_K^M) + \alpha_K^R E_K^M, \quad (2.45)$$

with E^M and E^V the magnetic energy and specific kinetic energy spectra and H^M and H^V the magnetic and kinetic helicity spectra. Multiplying H^M by K^2 gives then the current helicity spectrum. The influence of the large scale (as compared to K) magnetic energy is contained in the Γ_K term and α_K^R contains the influence of the small scale residual helicity (defined in shell K as $H_K^R = H_K^V - K^2 H_K^M$ so that $\alpha_K^R = (-4/3) \int \theta H_K^R$ with $\theta > 0$ a triad-relaxation time factor depending on the geometry of the interactions, the integration taking place over small scales). The exact expressions of Γ_K and α_K^R can be found in reference [86] and are not repeated here since they are not necessary for the qualitative picture. Through these equations, one can see that:

1. The large scale magnetic field (present in the Γ_K factor) tends to lead to equipartition between magnetic and kinetic energies on the one hand and between current and kinetic helicities on the other hand: in a timescale of the order of the Alfvén time associated with the large-scale magnetic field, the magnetic and kinetic field would relax to equipartition, that is $E_K^V \approx E_K^M$ and $H_K^V \approx K^2 H_K^M$. This effect is called the “Alfvén effect” since a state with such an equipartition could be the state where the velocity and magnetic field fluctuations $\tilde{\mathbf{v}}$ and $\tilde{\mathbf{b}}$ verify $\tilde{\mathbf{v}} = \pm \tilde{\mathbf{b}}$ in configuration space, which corresponds to Alfvén waves.
2. The small scale residual helicity destabilises the magnetic energy and helicity at larger scales, leading to their exponential growth (when $\alpha_K^R > 0$, which means an excess of small-scale current helicity as compared to small-scale kinetic helicity) or decay (when $\alpha_K^R < 0$) with a rate proportional to $K|\alpha_K^R|$. This effect is called in reference [86] the “kinetic and magnetic helicity effects”, which is linked with the α dynamo theory when considering not only the kinetic helicity but the destabilising role of the magnetic helicity as well: the difference between current and kinetic helicities is here the “motor” of the instability.

These two effects explain the inverse transfer of magnetic helicity through the following picture ([86] and [19], section 6.2): the injection of magnetic helical fluctuations at a certain shell K_0 , such that the small-scale residual helicity becomes negative, leads to a destabilisation of the magnetic energy and helicity spectra at larger scales (for example $\frac{1}{2}K_0$) through the helicity (or “dynamo”) effect. As a consequence, magnetic energy and helicity is transferred to larger scales, enhancing the large scale magnetic field. This large scale magnetic field encourages in turn equipartition at lower scales through the Alfvén effect, which implies a relaxation of the small-scale residual helicity to zero, that is a quenching of the helicity effect. The inverse transfer continues however, since the destabilised magnetic and helicity spectra at shell $\frac{1}{2}K_0$ with a finite residual helicity induces a destabilisation at even larger scales $\frac{1}{4}K_0$.

Even though this picture allows a qualitative understanding of some aspects of the inverse transfer dynamics, it is however incomplete, since only the dominant non-local interactions are considered. Indeed, local interactions also play an important role in the magnetic helicity inverse transfer dynamics (section 6.2).

In practice, one does not observe exact equipartition $E_K^V = E_K^M$ and $K^2 H_K^M = H_K^V$ in direct numerical simulations with finite magnetic helicity. However, a tendency towards equipartition has indeed been observed in the incompressible case through the following balance [79, 53, 74, 82]:

$$\frac{E^V}{E^M} \propto \frac{H^V}{H^J}, \quad (2.46)$$

with $H^J = K^2 H^M$ the current helicity spectrum. This balance has been justified through three different ways:

1. Reference [53] invokes partial Alfvénisation of the flow (through the Alfvén effect), so that $E^V \sim E^M$ and $H^V \sim K^2 H^M$ on the Alfvén timescale associated with the large scale magnetic field.
2. Another phenomenological argument in the framework of mean-field dynamo theory is given in reference [53], which links the magnetic helicity transfers between small and large scales with the kinetic helicity.
3. References [74, 82] propose a dynamical equilibrium between the shearing (which destroys structures through advection) and twisting (which lead to greater helical fields) effects of turbulent fluctuations in the EDQNM model, which gives relation (2.46) after dimensional analysis.

Relation (2.46) is approximately observed in the decaying MHD turbulence direct numerical simulations of references [79, 53], that is, in the direct cascade region. However, in the numerical experiments of references [74, 82], where magnetic helical fluctuations are injected at small scales, even though this relation is well observed for the scales smaller than the one at which the electromotive forcing takes place, reference [82] argued that another balance is more consistent with the data in the inverse transfer region, namely:

$$\left(\frac{E^V}{E^M}\right)^\gamma \propto \frac{H^V}{H^J}, \quad (2.47)$$

with an exponent $\gamma = 2$. This balance with an exponent of 2 is as well better suited for the decaying inverse transfer numerical experiment [82].

The balance (2.46), with an exponent $\gamma = 1$, is however not inconsistent with the numerical data, neither. Reference [74] established that during the inverse transfer of magnetic helicity, a lot of fields exhibit scaling law behaviours in Fourier space. The scaling exponents found for E^V , E^M , H^M and H^V in that work (summarised in table 4.4 of reference [74]) are rather compatible with an exponent $\gamma = 1$, as compared to $\gamma = 2$, both in the forced and the decaying case studied there. The exponent $\gamma = 2$ seems to give better results because the spectra involved in the balance exhibit scaling laws on slightly different domains.

In the present work, scaling laws are also sought for several fields and compared to the results of reference [74] in chapter 5. In that chapter, relation (2.47) (with both exponents $\gamma = 1$ and $\gamma = 2$) is also tested both for subsonic and supersonic runs and an extension of the same is proposed for the compressible case.

2.3 Helical decomposition

The helical decomposition makes use of the fact that the curl operator is diagonalisable in Fourier space. As a consequence, solenoidal fields can be decomposed in so-called ‘‘helical

modes”, which correspond in configuration space to flow lines forming either a left- or right-handed helix (see figure 2.1.(b)). Single triadic interactions between helical modes in 3D incompressible hydrodynamic turbulence were studied in reference [102], leading to the conclusion that not only direct energy transfers towards smaller scales are possible, but as well inverse transfers, in particular when all three interacting modes have the same helicity sign. Since in turbulent systems a large number of triads interact with each other, considering single triad interactions is – even though insightful – however not enough to draw definitive conclusions on the dynamics of the whole system [81]. Direct numerical simulations of 3D hydrodynamic steady-state incompressible turbulent flows using the helical decomposition allowed indeed at a later point the confirmation of the existence of a sub-dominant inverse energy cascade in the globally direct cascade of energy, which is associated with like-signed helical interactions [1].

The single triad approach of reference [102] was relatively recently extended to the incompressible MHD case, where it was used as a basis to develop a helical MHD shell model [65]. This extension was used in order to study helical single triad interactions [68, 69], which lead to some predictions regarding which helical combinations are susceptible to exhibit inverse transfers, as well as about the locality and strength of triadic interactions, as a function of the triad shapes and helical combinations.

The formalism used in the incompressible case [102, 65, 69] is reviewed here and extended to compressible MHD in order to include the compressive part of the velocity field, associated with the eigenvalue 0 of the curl operator. Analysis based on the helical decomposition is carried out in chapter 6, where the role and relative importance of the different helical components of the magnetic and velocity fields are measured, including the role of the velocity field’s compressive part.

2.3.1 Helical triadic interactions

The curl operator in Fourier space, $\hat{\mathbf{f}} \rightarrow i\mathbf{k} \times \hat{\mathbf{f}}$, possesses three eigenvalues: $0, +k, -k$ (with $k = |\mathbf{k}|$), associated with the unitary eigenvectors $\hat{\mathbf{h}}_{\mathbf{k}}^0, \hat{\mathbf{h}}_{\mathbf{k}}^+$ and $\hat{\mathbf{h}}_{\mathbf{k}}^-$, defined by [27]:

$$\hat{\mathbf{h}}_{\mathbf{k}}^0 = \mathbf{k}/|\mathbf{k}|, \quad (2.48)$$

$$\hat{\mathbf{h}}_{\mathbf{k}}^{\pm} = \frac{1}{\sqrt{2}} \frac{\mathbf{k} \times (\mathbf{k} \times \hat{\mathbf{e}}) \mp ik(\mathbf{k} \times \hat{\mathbf{e}})}{k^2 \sqrt{1 - (\mathbf{k} \cdot \hat{\mathbf{e}}/k)^2}}, \quad (2.49)$$

where $\hat{\mathbf{e}}$ is an arbitrary unitary vector non-parallel to \mathbf{k} . The helical eigenvectors $\hat{\mathbf{h}}_{\mathbf{k}}^{\pm}$ are sometimes called “Chandrasekhar-Kendall functions” [32]. Together with $\hat{\mathbf{h}}_{\mathbf{k}}^0$, they define an orthonormal basis in Fourier space, which can be seen as an extension of the Helmholtz decomposition: for a field decomposed in this base, the component along $\hat{\mathbf{h}}_{\mathbf{k}}^0$ corresponds to the dilatational (curl-free) component, since the divergence operator is $\hat{\mathbf{f}} \rightarrow i\mathbf{k} \cdot \hat{\mathbf{f}}$ in Fourier space, whereas the $\hat{\mathbf{h}}_{\mathbf{k}}^+$ and $\hat{\mathbf{h}}_{\mathbf{k}}^-$ vectors are a base of the plane containing the purely solenoidal contributions, the $\hat{\mathbf{h}}_{\mathbf{k}}^+$ - and $\hat{\mathbf{h}}_{\mathbf{k}}^-$ -components corresponding to circularly polarised Fourier modes with opposite polarity [102].

For the magnetic and the velocity fields, the Fourier decomposition (relation (2.10)) can thus be extended to the helical decomposition:

$$\mathbf{b} = \sum_{\mathbf{k}} \sum_{s_k} b_{\mathbf{k}}^{s_k} \hat{\mathbf{h}}_{\mathbf{k}}^{s_k} e^{i\mathbf{k} \cdot \mathbf{x}}, \quad (2.50)$$

$$\mathbf{v} = \sum_{\mathbf{p}} \sum_{s_p} v_{\mathbf{p}}^{s_p} \hat{\mathbf{h}}_{\mathbf{p}}^{s_p} e^{i\mathbf{p} \cdot \mathbf{x}}, \quad (2.51)$$

with $s_k \in \{+, -\}$ for both circular polarisation of the magnetic field and $s_p \in \{+, 0, -\}$, since it includes the compressive part $s_p = 0$ along \mathbf{p} for the velocity field.

This basis is very convenient for the study of helical transfers. Indeed, decomposing for example the magnetic vector potential in this basis gives:

$$\hat{\mathbf{a}}_{\mathbf{k}} = a_{\mathbf{k}}^0 \hat{\mathbf{h}}_{\mathbf{k}}^0 + a_{\mathbf{k}}^+ \hat{\mathbf{h}}_{\mathbf{k}}^+ + a_{\mathbf{k}}^- \hat{\mathbf{h}}_{\mathbf{k}}^-. \quad (2.52)$$

The Coulomb gauge condition corresponds then to the choice $a^0 = 0$. Formulated in this way, it is clear that this gauge condition is the one that minimises the $L2$ -norm of the magnetic vector potential. Then, the magnetic field can be deduced by:

$$\hat{\mathbf{b}}_{\mathbf{k}} = k(a_{\mathbf{k}}^+ \hat{\mathbf{h}}_{\mathbf{k}}^+ - a_{\mathbf{k}}^- \hat{\mathbf{h}}_{\mathbf{k}}^-). \quad (2.53)$$

This means that the contribution of mode \mathbf{k} to the field's helicity and energy are respectively:

$$H_{\mathbf{k}}^M = k(|a_{\mathbf{k}}^+|^2 - |a_{\mathbf{k}}^-|^2), \quad (2.54)$$

$$E_{\mathbf{k}}^M = \frac{1}{2}k^2(|a_{\mathbf{k}}^+|^2 + |a_{\mathbf{k}}^-|^2). \quad (2.55)$$

Plugging the helical decompositions (2.50) and (2.51) in the magnetic field time evolution equation (2.3) yields, after projection on the helical vector $\hat{\mathbf{h}}_{\mathbf{k}}^{s_k}$ [65]:

$$\partial_t b_{\mathbf{k}}^{s_k} = s_k k \sum_{\mathbf{k}+\mathbf{p}+\mathbf{q}=0} \sum_{s_p, s_q} v_{\mathbf{p}}^{s_p*} b_{\mathbf{q}}^{s_q*} g_{k,p,q}^{s_k, s_p, s_q}, \quad (2.56)$$

where the unicity of the Fourier decomposition and the Hermitian symmetry ($\hat{\mathbf{f}}_{\mathbf{k}} = \hat{\mathbf{f}}_{-\mathbf{k}}^*$, where the star $*$ denotes the complex conjugate) were used. The factor $g_{k,p,q}^{s_k, s_p, s_q} = (\hat{\mathbf{h}}_{\mathbf{p}}^{s_p*} \times \hat{\mathbf{h}}_{\mathbf{q}}^{s_q*}) \cdot \hat{\mathbf{h}}_{\mathbf{k}}^{s_k}$ is a geometric factor that depends on the helical components (s_k, s_p, s_q) and the considered triad. This geometric factor has been derived in reference [102] in the incompressible case ($s_p \in \{+, -\}$). The next subsection reviews these derivations and extends them to the compressible $s_p = 0$ case. Indeed, the derivations leading to equation (2.56) do not require the velocity field to be solenoidal, so that this relation is still valid in the compressible case.

Noticing that the expression (2.56) is unchanged when interchanging \mathbf{p} and \mathbf{q} , one can arrive at symmetric expressions in terms of \mathbf{p} and \mathbf{q} , as the ones in references [102, 65, 69]. In the framework of the present dissertation, such a symmetric formulation does not bring additional insights.

2.3.2 Derivations of the geometric factor

Starting with the incompressible case and following the notations of reference [102], the helical vectors $\hat{\mathbf{h}}_{\mathbf{k}}^{s_k}$, $\hat{\mathbf{h}}_{\mathbf{p}}^{s_p}$ and $\hat{\mathbf{h}}_{\mathbf{q}}^{s_q}$ are first expressed in a well-chosen base, local for each triad. Namely, the unitary vectors $\boldsymbol{\lambda}$ and $\boldsymbol{\mu}_{\mathbf{m}}$ for $\mathbf{m} \in \{\mathbf{k}, \mathbf{p}, \mathbf{q}\}$ are defined by:

$$\boldsymbol{\lambda} = \frac{\mathbf{k} \times \mathbf{p}}{|\mathbf{k} \times \mathbf{p}|} = \frac{\mathbf{p} \times \mathbf{q}}{|\mathbf{p} \times \mathbf{q}|} = \frac{\mathbf{q} \times \mathbf{k}}{|\mathbf{q} \times \mathbf{k}|}, \quad (2.57)$$

$$\boldsymbol{\mu}_{\mathbf{m}} = \frac{\mathbf{m} \times \boldsymbol{\lambda}}{|\mathbf{m}|} \quad (2.58)$$

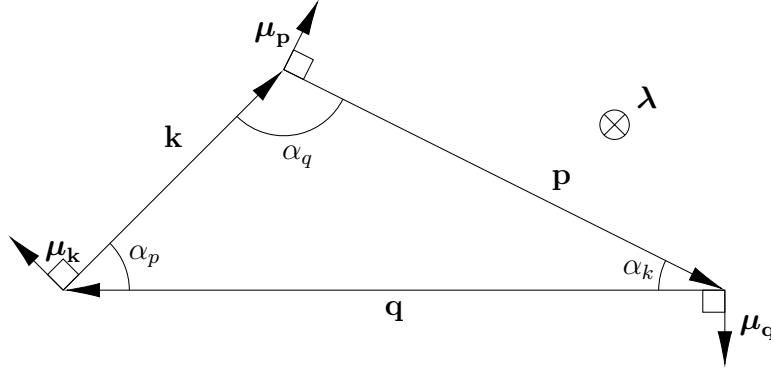


Figure 2.2: Illustration of the triad and definition of the vectors and angles used for the helical geometric factor derivation. Remade from reference [102].

In this basis, shown in figure 2.2, the helical vectors $\hat{\mathbf{h}}_{\mathbf{m}}^{s_m}$ (relation (2.48)) can be written:

$$\hat{\mathbf{h}}_{\mathbf{m}}^{s_m} = e^{i s_m \phi_m} (\boldsymbol{\lambda} + i s_m \boldsymbol{\mu}_{\mathbf{m}}), \quad (2.59)$$

with ϕ_m a certain angle. After some algebra, one finds then, in the incompressible case [102]:

$$\begin{aligned} g_{k,p,q}^{s_k,s_p,s_q} &= (\hat{\mathbf{h}}_{\mathbf{p}}^{s_p*} \times \hat{\mathbf{h}}_{\mathbf{q}}^{s_q*}) \cdot \hat{\mathbf{h}}_{\mathbf{k}}^{s_k*}, \\ &= -e^{-i(s_k \phi_k + s_p \phi_p + s_q \phi_q)} s_k s_p s_q (s_k \sin(\alpha_k) + s_p \sin(\alpha_p) + s_q \sin(\alpha_q)), \end{aligned} \quad (2.60)$$

where the angles α_m are defined in figure 2.2. The law of sines $\frac{\sin(\alpha_k)}{k} = \frac{\sin(\alpha_p)}{p} = \frac{\sin(\alpha_q)}{q} = \frac{2\mathcal{A}}{kpq}$ with \mathcal{A} the area of the triangle leads to:

$$g_{k,p,q}^{s_k,s_p,s_q} = -e^{-i(s_k \phi_k + s_p \phi_p + s_q \phi_q)} s_k s_p s_q \frac{2\mathcal{A}}{kpq} (s_k k + s_p p + s_q q), \quad (2.61)$$

Heron's formula allows to write $\mathcal{A} = \sqrt{h(h-k)(h-p)(h-q)}$ with $h = \frac{k+p+q}{2}$. The final expression is then, after some algebra [102]:

$$g_{k,p,q}^{s_k,s_p,s_q} = -e^{-i\phi_s} s_k s_p s_q (s_k k + s_p p + s_q q) \frac{\sqrt{2k^2 p^2 + 2p^2 q^2 + 2q^2 k^2 - k^4 - p^4 - q^4}}{2kpq}, \quad (2.62)$$

with $\phi_s = (s_k \phi_k + s_p \phi_p + s_q \phi_q)$. This relation expresses the geometric factor for interactions either in the incompressible case, or in the compressible case when only the solenoidal part of the velocity field is involved, that is, when $s_p \in \{+, -\}$. For $s_p = 0$, which stands for interactions involving the compressive part of the velocity field, $\hat{\mathbf{h}}_{\mathbf{p}}^{s_p} = \mathbf{p}/p$ so that it cannot be expressed in the form of relation (2.59). In that case:

$$(g_{k,p,q}^{s_k,s_p,s_q})_{s_p=0} = \left(\frac{\mathbf{p}}{p} \times \hat{\mathbf{h}}_{\mathbf{q}}^{s_q*} \right) \cdot \hat{\mathbf{h}}_{\mathbf{k}}^{s_k*}, \quad (2.63)$$

$$= e^{-i(s_k \phi_k + s_q \phi_q)} (\boldsymbol{\mu}_{\mathbf{p}} - i s_q \cos(\alpha_k) \boldsymbol{\lambda}) \cdot (\boldsymbol{\lambda} - i s_k \boldsymbol{\mu}_{\mathbf{k}}), \quad (2.64)$$

$$= i e^{-i(s_k \phi_k + s_q \phi_q)} (s_k \cos(\alpha_q) - s_q \cos(\alpha_k)). \quad (2.65)$$

$$(2.66)$$

The cosine rule gives $\cos(\alpha_k) = \frac{kp^2+kq^2-k^3}{2kpq}$ (and similarly for $\cos(\alpha_q)$). Introducing $S = s_k$ so that $s_q = \pm S$, one obtains after simplifications:

$$(g_{k,p,q}^{s_k,s_p,s_q})_{s_k=S,s_p=0,s_q=\pm S} = \frac{\mp iS}{2kpq} e^{-iS(\phi_k \pm \phi_q)} (k \mp q)(p^2 - k^2 - q^2 \mp 2qk). \quad (2.67)$$

The magnitude of the geometric factors derived in this subsection are plotted in the (p, q) plane in section 6.3. They allow to explain some aspects regarding the locality and relative strength of different helical contributions (section 6.3).

2.4 Shell-to-shell transfers

Shell-to-shell transfer analysis has revealed itself to be a valuable tool in order to investigate the spectral energy and helicity transfers between fields and scales, allowing among others to measure the locality of the interactions as well as the direction of the transfers, whether they are direct or inverse. This approach has been used in hydrodynamic incompressible turbulence in reference [78]. In incompressible MHD, shell-to-shell magnetic helicity transfer rates have been investigated in reference [3], whereas shell-to-shell energy transfer rates among and between the magnetic and kinetic energy reservoirs have been investigated in reference [2]. This approach has recently been extended to the isothermal compressible MHD case [55]. In the isothermal compressible MHD case, one may also cite reference [25], even though the considered transfer matrix for the magnetic field is not decomposed in magnetic \leftrightarrow magnetic and magnetic \leftrightarrow kinetic exchanges there.

The shell-to-shell transfer analysis consists of making a partition in n shells S_1, \dots, S_n of the $[1, K_{max}]$ interval, so that $S_1 \cup \dots \cup S_n = [1, K_{max}]$, and decompose all relevant fields through the filter:

$$\mathbf{f}(\mathbf{x}) = \sum_j \mathbf{f}_j(\mathbf{x}) \text{ with } \mathbf{f}_j(x) = \sum_{|\mathbf{k}|/\kappa \in S_j} \hat{\mathbf{f}}_{\mathbf{k}} e^{i\mathbf{k} \cdot \mathbf{x}}, \quad (2.68)$$

where \mathbf{f} can be the velocity field, the magnetic field, the magnetic vector potential, etc. The filtered field \mathbf{f}_j corresponds to the part of the field with modes only in the shell S_j .

In the present work, the particular choice $S_j = [j, j + 1[$, as in references [2, 3] is chosen. This means that the field \mathbf{f}_K is the filtered \mathbf{f} field with only the wavenumbers such that $K \leq |\mathbf{k}|/\kappa = |\mathbf{k}|L/(2\pi) < K + 1$. It is hence directly related to the shell-integrated Fourier transfer spectra of section 2.1.2. When using this decomposition however, also called ‘‘linear binning’’, one has to be careful when interpreting the locality of transfers, since it may lead to an overestimation of non-local transfers [6, 55]. In order to relate the results more naturally to phenomenological arguments and spectra exhibiting power-laws, a so-called ‘‘logarithmic binning’’ should be used, where the shell boundaries are equidistant on a logarithmic scale, for example with the shell boundaries given by 2^m with $m \geq 0$ for the so-called ‘‘octave binning’’. The linear binning is preferred here since the electromotive forcing injecting magnetic helical fluctuations at small scales (see sections 3.3.2 and 3.5.1) is still done at relatively large scales ($K \approx 50$), which means that an octave binning for example would leave a too little amount of shells and make the analysis of the shell-to-shell transfer features more difficult to distinguish from one another (see chapter 6).

In the following, the approach used in references [2, 3], where incompressible MHD is considered, is reviewed and extended to the compressible case for the magnetic helicity and magnetic energy transfers, including the exchanges with the kinetic energy reservoir.

2.4.1 Magnetic helicity transfers

The time evolution of $\mathcal{H}_K^M = \int \mathbf{a}_K \cdot \mathbf{b}_K dV$, the magnetic helicity present in shell K , is governed in ideal MHD and with the absence of forcing by [3]:

$$\begin{aligned} \partial_t \mathcal{H}_K^M &= 2 \int \partial_t \mathbf{a}_K \cdot \mathbf{b}_K dV, \\ &= 2 \int \partial_t \mathbf{a} \cdot \mathbf{b}_K dV, \\ &= 2 \int \mathbf{b}_K \cdot (\mathbf{v} \times \mathbf{b}) dV. \end{aligned} \quad (2.69)$$

The first equality comes from relation (2.21) applied to $\mathbf{f} = \mathbf{a}_K$, the second one from the property that for any two fields \mathbf{f} and \mathbf{g} and two shells K, Q with $K \neq Q$, $\int \mathbf{f}_K \cdot \mathbf{g}_Q dV = 0$ since they do not have any Fourier mode in common and the third by using the evolution equation of the magnetic vector potential (2.33).

Introducing a second shell-filtered decomposition, this evolution equation can be reformulated as:

$$\partial_t \mathcal{H}_K^M = \sum_Q \mathcal{T}^{\mathcal{H}^M}(Q, K), \quad (2.70)$$

with $\mathcal{T}^{\mathcal{H}^M}(Q, K)$ the transfer rate of magnetic helicity from shell Q to shell K , defined by³:

$$\mathcal{T}^{\mathcal{H}^M}(Q, K) = 2 \int \mathbf{b}_K \cdot (\mathbf{v} \times \mathbf{b}_Q) dV. \quad (2.71)$$

This term can indeed be interpreted as a transfer rate from shell Q to shell K through the antisymmetric property $\mathcal{T}^{\mathcal{H}^M}(Q, K) = -\mathcal{T}^{\mathcal{H}^M}(K, Q)$: the magnetic helicity exiting shell Q in favour of shell K can be viewed as the opposite of the magnetic helicity exiting shell K in favour of shell Q . The velocity field, which acts as a mediator here, can also be decomposed in shells [78], giving the transfer rates:

$$\mathcal{T}^{\mathcal{H}^M}(Q, P, K) = 2 \int \mathbf{b}_K \cdot (\mathbf{v}_P \times \mathbf{b}_Q) dV. \quad (2.72)$$

This third decomposition allows to differentiate the mediating role of the velocity field depending on its scale, as done in section 6.2.2. Please note that for the magnetic helicity transfers, no formal change appear for the transfer function when considering compressible flows.

³Please note that in reference [3] the notations are slightly different, with the K and Q shells exchanged: $T_h(K, Q)$ in that paper represents the magnetic helicity received by shell K from shell Q . In that paper as well, a factor 2 is missing since the convention $\mathcal{H}^M = \frac{1}{2} \int \mathbf{a} \cdot \mathbf{b} dV$ is used.

2.4.2 Energy exchanges

In this subsection, the shell-to-shell energy transfers among and between the magnetic and kinetic energy reservoirs are reviewed in the incompressible case, before extending the method to the compressible case. In the incompressible case, the ideal MHD equations can be formulated as [2]:

$$\partial_t \mathbf{v} = -(\mathbf{v} \cdot \nabla) \mathbf{v} - \nabla(p + \frac{1}{2}|\mathbf{b}|^2) + (\mathbf{b} \cdot \nabla) \mathbf{b}, \quad (2.73)$$

$$\partial_t \mathbf{b} = -(\mathbf{v} \cdot \nabla) \mathbf{b} + (\mathbf{b} \cdot \nabla) \mathbf{v}, \quad (2.74)$$

$$\nabla \cdot \mathbf{v} = \nabla \cdot \mathbf{b} = 0, \quad (2.75)$$

when assuming a constant density $\rho = 1$. In this case, the energy can be stored in two forms: as kinetic $\mathcal{E}^K = \frac{1}{2} \mathbf{v}^2$ and as magnetic $\mathcal{E}^M = \frac{1}{2} \mathbf{b}^2$ energy. Their time evolution is governed by:

$$\partial_t \mathcal{E}^K = \underbrace{-\mathbf{v} \cdot ((\mathbf{v} \cdot \nabla) \mathbf{v})}_{Ia} + \underbrace{\mathbf{v} \cdot ((\mathbf{b} \cdot \nabla) \mathbf{b})}_{Ib} - \mathbf{v} \cdot \nabla(p + \frac{1}{2}|\mathbf{b}|^2), \quad (2.76)$$

$$\partial_t \mathcal{E}^M = \underbrace{-\mathbf{b} \cdot ((\mathbf{v} \cdot \nabla) \mathbf{b})}_{IIa} + \underbrace{\mathbf{b} \cdot ((\mathbf{b} \cdot \nabla) \mathbf{v})}_{IIb}. \quad (2.77)$$

In order to see which terms correspond to energy exchanges, it is useful to reformulate the Ia, Ib, IIa and IIb terms in relations (2.76)-(2.77). The term Ib becomes, using the index notation:

$$\begin{aligned} \mathbf{v} \cdot ((\mathbf{b} \cdot \nabla) \mathbf{b}) &= v_j b_i \partial_i b_j, \\ &= v_j \partial_i (b_i b_j) - v_j b_j \partial_i b_i, \\ &= \partial_i (v_j b_i b_j) - (b_i b_j) \partial_i v_j, \\ &= \nabla \cdot ((\mathbf{v} \cdot \mathbf{b}) \mathbf{b}) - \mathbf{b} \cdot ((\mathbf{b} \cdot \nabla) \mathbf{v}), \end{aligned} \quad (2.78)$$

where the solenoidality of the magnetic field $\partial_i b_i = 0$ was used. One can recognise in this last expression the opposite of term IIb . Using the same technique and the solenoidality of the velocity field, one can reformulate the terms Ia and IIa :

$$-\mathbf{v} \cdot ((\mathbf{v} \cdot \nabla) \mathbf{v}) = -\frac{1}{2} \nabla \cdot (|\mathbf{v}|^2 \mathbf{v}), \quad (2.79)$$

$$-\mathbf{b} \cdot ((\mathbf{v} \cdot \nabla) \mathbf{b}) = -\frac{1}{2} \nabla \cdot (|\mathbf{b}|^2 \mathbf{v}). \quad (2.80)$$

These derivations allow to interpret these two terms as a redistribution of kinetic (respectively magnetic) energy among scales, since they can be rewritten in a conservative form $\nabla \cdot (\dots)$ and their integral over the whole periodic domain vanishes owing to Gauss' theorem. On the other hand, the integral of terms Ib and IIb are exactly opposite (see relation (2.78)). They hence correspond to an energy exchange between the kinetic and magnetic fields.

Regarding the pressure term $\mathbf{v} \cdot \nabla(p + \frac{1}{2}|\mathbf{b}|^2)$ of equation (2.76), since a gradient has only dilatational components (along \mathbf{k} in Fourier space), it plays in the incompressible case the role of keeping the velocity field solenoidal by removing the curl-free contributions from the $(\mathbf{v} \cdot \nabla) \mathbf{v}$ and $(\mathbf{b} \cdot \nabla) \mathbf{b}$ terms ([85], section 6.4.2) and can be rewritten in the conservative form $\nabla \cdot ((p + \frac{1}{2}|\mathbf{b}|^2) \mathbf{v})$.

Introducing shell decompositions, the kinetic energy \mathcal{E}_P^K stored in shell P and the magnetic energy \mathcal{E}_K^M stored in shell K are governed by (in the ideal incompressible case, in the absence of forcing) [2]:

$$\partial_t \mathcal{E}_P^K = \sum_R \mathcal{T}_{vv}^{\mathcal{E}^K, inc.}(R, P) + \sum_K \mathcal{T}_{bv}^{\mathcal{E}^K, inc.}(K, P), \quad (2.81)$$

$$\partial_t \mathcal{E}_K^M = \sum_P \mathcal{T}_{vb}^{\mathcal{E}^M, inc.}(P, K) + \sum_Q \mathcal{T}_{bb}^{\mathcal{E}^M, inc.}(Q, K), \quad (2.82)$$

with the energy transfer functions defined by:

$$\mathcal{T}_{vv}^{\mathcal{E}^K, inc.}(R, P) = - \int \mathbf{v}_P (\mathbf{v} \cdot \nabla) \mathbf{v}_R dV, \quad (2.83)$$

$$\mathcal{T}_{bv}^{\mathcal{E}^K, inc.}(K, P) = \int \mathbf{v}_P (\mathbf{b} \cdot \nabla) \mathbf{b}_K dV, \quad (2.84)$$

$$\mathcal{T}_{bb}^{\mathcal{E}^M, inc.}(Q, K) = - \int \mathbf{b}_K (\mathbf{v} \cdot \nabla) \mathbf{b}_Q dV, \quad (2.85)$$

$$\mathcal{T}_{vb}^{\mathcal{E}^M, inc.}(P, K) = \int \mathbf{b}_K (\mathbf{b} \cdot \nabla) \mathbf{v}_P dV. \quad (2.86)$$

The transfer term $\mathcal{T}_{xy}^{\mathcal{E}^j, inc.}(S, T)$ represents the energy transfer rate in the incompressible case from shell S of field $x \in \{v, b\}$ (kinetic or magnetic) to shell T of field $y \in \{v, b\}$. The superscript $\mathcal{E}^j \in \{\mathcal{E}^K, \mathcal{E}^M\}$ stands hence for the receiving field and is redundant, but kept for clarity reasons. The terms written in relations (2.83)-(2.86) correspond in this order to the shell-to-shell expressions of the terms Ia , Ib , IIa and IIb in relations (2.76) and (2.77). It can be shown through similar derivations than the ones in relation (2.78) that they verify the antisymmetric property: $\mathcal{T}_{xy}(S, T) = -\mathcal{T}_{yx}(T, S)$, validating the interpretation in terms of energy transfers between fields and shells (or across scales in a certain field for $x = y$).

In the compressible case, several changes occur. The velocity field is not solenoidal anymore and the magnetic field evolution is now governed by [27]:

$$\partial_t \mathbf{b} = -(\mathbf{v} \cdot \nabla) \mathbf{b} + (\mathbf{b} \cdot \nabla) \mathbf{v} - \mathbf{b}(\nabla \cdot \mathbf{v}), \quad (2.87)$$

while the momentum equation reads:

$$\partial_t(\rho \mathbf{v}) = -\nabla \cdot (\rho \mathbf{v} \mathbf{v}^T) - \nabla(p + \frac{1}{2}|\mathbf{b}|^2) + (\mathbf{b} \cdot \nabla) \mathbf{b}, \quad (2.88)$$

or, using the conservation of mass [54]:

$$\partial_t \mathbf{v} = -(\mathbf{v} \cdot \nabla) \mathbf{v} - \frac{1}{\rho} \nabla(p + \frac{1}{2}|\mathbf{b}|^2) + \frac{1}{\rho} (\mathbf{b} \cdot \nabla) \mathbf{b}. \quad (2.89)$$

One can notice that the velocity equation is exactly the same as the one in the incompressible case if one sets $\rho = 1$. In the compressible case, there is a third energy reservoir apart from the magnetic and kinetic ones. In the adiabatic case, this is the internal energy $\frac{p}{\gamma_{adia}-1}$ (linked with the temperature), whereas in the isothermal case, even though the temperature is constant in the system, energy can still be stored in a potential form as density variations [63] $\mathcal{E}^\rho = \rho c_s^2 \ln(\rho/\rho_0)$ with ρ_0 the mean mass density in the

system. The time evolution of these three energy reservoirs in the isothermal case follows the equations:

$$\begin{aligned}\partial_t \mathcal{E}^K &= \frac{1}{2}(\partial_t(\rho \mathbf{v}) \cdot \mathbf{v} + \partial_t \mathbf{v} \cdot (\rho \mathbf{v})), \\ &= \underbrace{-\nabla \cdot \left(\frac{1}{2}\rho|\mathbf{v}|^2\mathbf{v}\right)}_{Ia} + \underbrace{\mathbf{v} \cdot ((\mathbf{b} \cdot \nabla)\mathbf{b}) - \mathbf{v} \cdot \nabla\left(\frac{1}{2}|\mathbf{b}|^2\right)}_{Ib} \underbrace{-\mathbf{v} \cdot \nabla(p)}_{Ic},\end{aligned}\quad (2.90)$$

$$\partial_t \mathcal{E}^M = \underbrace{-\mathbf{b} \cdot ((\mathbf{v} \cdot \nabla)\mathbf{b}) - \frac{1}{2}|\mathbf{b}|^2\nabla \cdot \mathbf{v}}_{IIa} + \underbrace{\mathbf{b} \cdot ((\mathbf{b} \cdot \nabla)\mathbf{v}) - \frac{1}{2}|\mathbf{b}|^2\nabla \cdot \mathbf{v}}_{IIb},\quad (2.91)$$

$$\partial_t \mathcal{E}^p = -\nabla \cdot (p\mathbf{v} + p\mathbf{v} \ln(\rho)) + \underbrace{\mathbf{v} \cdot \nabla(p)}_{IIIc}.\quad (2.92)$$

The term Ia in equation (2.90) corresponds to Ia in the incompressible equation (2.76) and is here already written in conservative form. It corresponds to a redistribution of the kinetic energy across scales. The Ic term corresponds to exchanges with the isothermal compressive potential energy reservoir, since it is the opposite of the $IIIc$ term. Please note that the new term containing the velocity field divergence, $-|\mathbf{b}|^2\nabla \cdot \mathbf{v}$ in equation (2.91) has been split in two halves. This is because, as shown in the following, the IIa term written in this form is a conservative term, whereas the IIb term corresponds to energy exchanges between the magnetic and kinetic fields and is the counterpart of term Ib in the kinetic energy equation.

Indeed, contrary to the incompressible case where kinetic \leftrightarrow magnetic energy exchanges were only possible through magnetic stretching, the term associated with the magnetic pressure $-\nabla\left(\frac{1}{2}|\mathbf{b}|^2\right)$ is not conservative in the compressible case anymore, since the velocity field presents dilatational components. The term Ib includes thus now the magnetic pressure and can be rewritten:

$$\mathbf{v} \cdot ((\mathbf{b} \cdot \nabla)\mathbf{b}) - \mathbf{v} \cdot \nabla\left(\frac{1}{2}|\mathbf{b}|^2\right) = \nabla \cdot ((\mathbf{v} \cdot \mathbf{b})\mathbf{b}) - \frac{1}{2}|\mathbf{b}|^2\nabla \cdot \mathbf{v} - \mathbf{b} \cdot ((\mathbf{b} \cdot \nabla)\mathbf{v}) + \frac{1}{2}|\mathbf{b}|^2\nabla \cdot \mathbf{v}\quad (2.93)$$

This shows that the non-conservative contribution $-\mathbf{b} \cdot ((\mathbf{b} \cdot \nabla)\mathbf{v}) + \frac{1}{2}|\mathbf{b}|^2\nabla \cdot \mathbf{v}$ in the kinetic energy equation (2.90) corresponds exactly to the opposite of the IIb term in the magnetic energy evolution and is hence associated to energy exchanges between the kinetic and magnetic fields.

Regarding the IIa term in relation (2.91), it is indeed conservative. Using the same technique that lead to equation (2.80) in the incompressible case without assuming velocity field solenoidality yields:

$$-\mathbf{b} \cdot (\mathbf{v} \cdot \nabla)\mathbf{b} = -\frac{1}{2}\nabla \cdot (|\mathbf{b}|^2\mathbf{v}) + \frac{1}{2}|\mathbf{b}|^2\nabla \cdot \mathbf{v}.\quad (2.94)$$

In conclusion, the shell-to-shell energy transfer functions involving the magnetic field in the compressible case can be deduced by adding to relations (2.84)-(2.86) a term corresponding to the magnetic pressure:

$$\mathcal{T}_{bv}^{\mathcal{E}^K}(K, P) = \int (\mathbf{v}_P(\mathbf{b} \cdot \nabla)\mathbf{b}_K - \frac{1}{2}(\mathbf{v}_P \cdot \nabla)(\mathbf{b} \cdot \mathbf{b}_K))dV, \quad (2.95)$$

$$\mathcal{T}_{bb}^{\mathcal{E}^M}(Q, K) = \int (-\mathbf{b}_K(\mathbf{v} \cdot \nabla)\mathbf{b}_Q - \frac{1}{2}(\mathbf{b}_K \cdot \mathbf{b}_Q)\nabla \cdot \mathbf{v})dV, \quad (2.96)$$

$$\mathcal{T}_{vb}^{\mathcal{E}^M}(P, K) = \int (\mathbf{b}_K(\mathbf{b} \cdot \nabla)\mathbf{v}_P - \frac{1}{2}(\mathbf{b}_K \cdot \mathbf{b})\nabla \cdot \mathbf{v}_P)dV. \quad (2.97)$$

These terms correspond, in this order, to the terms *Ib*, *IIa* and *IIb* of equations (2.90)-(2.91). Again, the antisymmetric properties $\mathcal{T}_{bb}^{\mathcal{E}^M}(Q, K) = -\mathcal{T}_{bb}^{\mathcal{E}^M}(K, Q)$ and $\mathcal{T}_{vb}^{\mathcal{E}^M}(P, K) = -\mathcal{T}_{bv}^{\mathcal{E}^K}(K, P)$ can be proven.

Please note that the shell-to-shell kinetic energy transfers cannot be expressed as simply by only considering the filtered velocity field \mathbf{v}_P , since the corresponding *Ia* term in relation (2.90) contains the density. A possible approach is to consider a shell-decomposition of the variable $\mathbf{w} = \sqrt{\rho}\mathbf{v}$. This approach has been carried out in reference [55], where transfers in compressible MHD among and between the kinetic and magnetic energy reservoirs are considered. As a consequence of filtering \mathbf{w} instead of \mathbf{v} , the transfer functions differ in that work, as compared to those derived here. Nevertheless, the present choice of filtering the velocity field \mathbf{v} and not \mathbf{w} is based on the fact that in the equations governing the magnetic field time evolution, the velocity field appears, not \mathbf{w} . Moreover, since the kinetic helicity is defined as the helicity of the velocity field and helically-decomposed transfers are studied here (see section 2.4.4), it is more natural to work with \mathbf{v} . In addition, in this dissertation, the shell-to-shell kinetic energy transfers are not considered. However, this means that special care has to be taken when interpreting the plots of $\mathcal{T}_{vb}^{\mathcal{E}^M}$: even though $\mathcal{T}_{vb}^{\mathcal{E}^M}(P, K)$ represents indeed transfers of kinetic energy to magnetic energy, one cannot say that “kinetic energy at shell *P* is transformed in magnetic energy at shell *K*”, since only the velocity field, not \mathbf{w} is considered. One can merely state that “ $\mathcal{T}_{vb}^{\mathcal{E}^M}(P, K)$ units of kinetic energy associated with the velocity field shell *P* are transformed to magnetic energy at shell *K*”.

Shell-to-shell energy exchanges are considered in section 6.2.3.

2.4.3 Other transfer functions and notations

In the framework of the present dissertation, for shell-to-shell transfer functions, the shell index *K* and *Q* are always associated with the magnetic field, whereas the shell index *P* is always associated with the velocity field. Furthermore, aside from the above-defined functions, other functions are also considered:

$$\mathcal{T}_{vbT}^{\mathcal{E}^M}(P, K) = \int \mathbf{b}_K(\mathbf{b} \cdot \nabla)\mathbf{v}_P dV, \quad (2.98)$$

$$\mathcal{T}_{vbP}^{\mathcal{E}^M}(P, K) = \int -\frac{1}{2}(\mathbf{b}_K \cdot \mathbf{b})\nabla \cdot \mathbf{v}_P dV, \quad (2.99)$$

$$\mathcal{M}_{vb}^{\mathcal{E}^M}(Q, K) = \int (\mathbf{b}_K \cdot (\mathbf{b}_Q \cdot \nabla)\mathbf{v} - \frac{1}{2}(\mathbf{b}_K \cdot \mathbf{b}_Q)\nabla \cdot \mathbf{v})dV, \quad (2.100)$$

$$\mathcal{U}^{\mathcal{E}^M}(Q, K) = \int \mathbf{b}_K \cdot \nabla \times (\mathbf{v} \times \mathbf{b}_Q)dV. \quad (2.101)$$

Relations (2.98) and (2.99) correspond to the individual contributions to kinetic-to-magnetic energy transfer rates due to the magnetic stretching term and the magnetic

pressure term respectively, so that $\mathcal{T}_{vb}^{\mathcal{E}^M} = \mathcal{T}_{vb\Gamma}^{\mathcal{E}^M} + \mathcal{T}_{vbP}^{\mathcal{E}^M}$. Relation (2.100) is similar to relation (2.97), but where the magnetic field acting as a mediator of the kinetic \leftrightarrow magnetic energy transfers is filtered in shells. It does *not* represent transfers from magnetic shell Q to magnetic shell K , but changes of magnetic energy in shell K coming from/flowing to the kinetic field, under the mediation of the magnetic field at shell Q . This is why, in order to prevent confusion, the letter \mathcal{M} is used, for “mediation” instead of the letter \mathcal{T} (“transfer”). Similarly, $\mathcal{U}^{\mathcal{E}^M}(Q, K) = \mathcal{M}_{vb}^{\mathcal{E}^M}(Q, K) + \mathcal{T}_{bb}^{\mathcal{E}^M}(Q, K)$ (relation (2.101)) is a hybrid term which represents the total change of magnetic energy in shell K due to both transfers to/from the magnetic field at shell Q mediated by the whole velocity field and transfers to/from the kinetic field mediated by the magnetic field at shell Q . It allows to see the general importance of the Q shell of the magnetic field for the transfers to/from the K shell. In order to prevent confusion, neither the \mathcal{M} nor the \mathcal{T} letters are used, but the \mathcal{U} letter is used instead for this hybrid function.

In order to underline some other specific aspects of the magnetic helicity inverse transfer, other functions similar to the above-defined ones are also considered. These are defined in the section where they appear and the nomenclature used is based on the here presented notations.

2.4.4 Shell-to-shell helical transfers

The helical decomposition introduced in section 2.3 is combined here with the shell-to-shell transfers. This is done in order to assess the influence of the compressive part of the velocity field on the magnetic helicity inverse transfer and compare it to the contributions coming from the positive and negative helical parts of the magnetic and velocity fields. The magnetic and velocity fields expressed in Fourier space can indeed be projected on a helical basis and then transformed to configuration space. The resulting fields are noted \mathbf{b}^P and \mathbf{b}^N for the positive helical part of the magnetic field and its negative helical part respectively. As for the positive and negative helical parts of the velocity field, they are noted analogously \mathbf{v}^P and \mathbf{v}^N , and the compressive part is noted \mathbf{v}^C . As a consequence, the magnetic helicity transfer function $\mathcal{T}^{\mathcal{H}^M}$ expressed in equation (2.72) can be split into twelve contributions: two for the magnetic field at shell K , three for the velocity field at shell P and two for the magnetic field at shell Q , expressed below in the sum:

$$\mathcal{T}^{\mathcal{H}^M}(Q, P, K) = \sum_{s_K \in \{P, N\}} \sum_{s_P \in \{P, C, N\}} \sum_{s_Q \in \{P, N\}} \mathcal{T}_{s_K s_P s_Q}^{\mathcal{H}^M}, \quad (2.102)$$

with

$$\mathcal{T}_{s_K s_P s_Q}^{\mathcal{H}^M}(Q, P, K) = 2 \int \mathbf{b}_K^{s_K} \cdot (\mathbf{v}_P^{s_P} \times \mathbf{b}_Q^{s_Q}) dV. \quad (2.103)$$

Among these twelve $\mathcal{T}_{s_K s_P s_Q}^{\mathcal{H}^M}$ terms, those where $s_K = s_Q$ are conservative and can directly be interpreted as magnetic helicity transfers from shell Q to shell K mediated by the shell P of the \mathbf{v}^{s_P} field, since they are antisymmetric⁴: $\mathcal{T}_{s_K s_P s_K}^{\mathcal{H}^M}(Q, P, K) = -\mathcal{T}_{s_K s_P s_K}^{\mathcal{H}^M}(K, P, Q)$. These are the $\mathcal{T}_{s_K s_P s_Q}^{\mathcal{H}^M}$ terms with $(s_K, s_P, s_Q) \in \{(P, P, P), (P, C, P), (P, N, P), (N, P, N), (N, C, N), (N, N, N)\}$, which are shortly denoted by “*PPP*”, “*PNP*”, “*PCP*”, “*NPN*”, “*NCN*” and “*NNN*” terms in the following.

On the contrary, those where $s_K \neq s_Q$ are not conservative, since in this case $\mathcal{T}_{s_K s_P s_Q}^{\mathcal{H}^M}(Q, P, K) \neq -\mathcal{T}_{s_K s_P s_Q}^{\mathcal{H}^M}(K, P, Q)$. Nevertheless, when considering them in pairs,

⁴This is due to the fact that $\mathbf{f} \cdot (\mathbf{g} \times \mathbf{h}) = \mathbf{h} \cdot (\mathbf{f} \times \mathbf{g}) = -\mathbf{h} \cdot (\mathbf{g} \times \mathbf{f})$ for any vectors \mathbf{f} , \mathbf{g} and \mathbf{h} .

one can build three more conservative terms [1]. Indeed, for any $s_P \in \{P, C, N\}$, $\mathcal{T}_{P s_P N}^{\mathcal{H}^M}(Q, P, K) = -\mathcal{T}_{N s_P P}^{\mathcal{H}^M}(K, P, Q)$, which means that the sum of these two terms, $\mathcal{T}_{S s_P S}^{\mathcal{H}^M} = \mathcal{T}_{P s_P N}^{\mathcal{H}^M} + \mathcal{T}_{N s_P N}^{\mathcal{H}^M}$ is antisymmetric. The “S” letter in the subscript stands here for “symmetrised”. The three SPS , SCS and SNS terms will be referred to as “heterochiral” since they represent magnetic helicity exchanges through interactions involving different helical signs for the *magnetic* field. In the present work, the word “heterochiral” is *not* used for the PNP and NPN terms which have different helical signs for the magnetic and velocity fields but the *same* helical sign for the magnetic field shells.

These shell-to-shell helically decomposed transfer rates are used as an analysis tool in chapter 6.

Furthermore, expressing the velocity and magnetic fields with the help of their Fourier coefficients (relation (2.10)) gives:

$$\mathcal{T}^{\mathcal{H}^M}(Q, P, K) = 2 \sum_{\substack{K \leq |\mathbf{k}|/\kappa < K+1 \\ P \leq |\mathbf{p}|/\kappa < P+1 \\ Q \leq |\mathbf{q}|/\kappa < Q+1}} \int e^{i(\mathbf{k}+\mathbf{p}+\mathbf{q}) \cdot \mathbf{x}} \hat{\mathbf{b}}_{\mathbf{k}} \cdot (\hat{\mathbf{v}}_{\mathbf{p}} \times \hat{\mathbf{b}}_{\mathbf{q}}) dV. \quad (2.104)$$

The integral vanishes for $\mathbf{k} + \mathbf{p} + \mathbf{q} \neq 0$. Using a helical decomposition (relations (2.50) and (2.51)), one obtains hence:

$$\mathcal{T}^{\mathcal{H}^M}(Q, P, K) \sim \sum_{\substack{K \leq |\mathbf{k}|/\kappa < K+1 \\ P \leq |\mathbf{p}|/\kappa < P+1 \\ Q \leq |\mathbf{q}|/\kappa < Q+1 \\ \mathbf{k}+\mathbf{p}+\mathbf{q}=0}} \sum_{\substack{s_k \in \{+, -\} \\ s_p \in \{+, 0, -\} \\ s_q \in \{+, -\}}} \int b_{\mathbf{k}}^{s_k} v_{\mathbf{p}}^{s_p} b_{\mathbf{q}}^{s_q} g_{\mathbf{k}, \mathbf{p}, \mathbf{q}}^{s_k, s_p, s_q} dV, \quad (2.105)$$

with $g_{\mathbf{k}, \mathbf{p}, \mathbf{q}}^{s_k, s_p, s_q}$ the triadic helical geometric factor (see section 2.3). Relation (2.105), shows that this geometric factor, which is strictly speaking valid only for triadic interactions, is nonetheless a good approximation for the shell-to-shell transfers, especially at high wavenumbers. For each shell-to-shell transfer term, the wavevectors \mathbf{k} , \mathbf{p} , \mathbf{q} are indeed constrained, with $|\mathbf{k}| \in [\kappa K, \kappa(K+1)[$ (and $\kappa = \frac{2\pi}{L}$), and similarly for \mathbf{p} and \mathbf{q} , so that $g_{\mathbf{k}, \mathbf{p}, \mathbf{q}}^{s_k, s_p, s_q}$ does not change much for the wavevectors varying inside a shell at high enough wavenumbers. Section 6.3 uses this idea and shows that both the relative strength and locality of the helically-decomposed terms can be explained through this geometric factor.

2.5 Summary: previous research and aim of the present dissertation

Turbulence is a very complex phenomenon, which has been and still is often studied in the incompressible case for the sake of simplicity. This is mostly due to both facts that finding exact results regarding turbulent systems is a very difficult task and that numerical techniques allowing simulation of compressible flows with high accuracy have been designed only relatively recently. For instance, a rigorous proof of the existence of an inertial range in compressible turbulence has only been provided in the past decade [5]. For the numerical aspects: the first Essentially Non-Oscillatory (ENO) schemes, high-order accurate methods able to adapt to discontinuities, were designed in the late 80s and extended to the more stable Weighted ENO (WENO) schemes during the 90s [56, 70, 58, 94]. However, robust higher-order finite-volume schemes require additional numerical techniques, some of which were developed in the last decade. These include appropriate higher-order time integration techniques [59], as well as an appropriate treatment of very strong discontinuities

[11, 12]. Recent developments lead furthermore to significant sparing regarding computing costs by allowing numerically efficient dimension-by-dimension approaches [75, 28]. Viable finite-volume numerical schemes with high accuracy are thus relatively recent.

With this perspective, the present work makes a step further regarding realism, by including effects of compressibility in flows with RMS Mach numbers up to about 11, close to what is observed in the interstellar medium.

In the framework of compressible MHD turbulence with low cross-helicity, the nonlinear dynamics are expected to be dominated by the direct cascade of energy and the inverse transfer of magnetic helicity. The inverse transfer of magnetic helicity is hence studied through direct numerical simulations by injecting small scale helical magnetic fluctuations in a hydrodynamic steady-state. Using the numerical method described in chapter 3 and the analysis tools described in the present chapter, several aspects are considered, which are split in three result chapters.

Chapter 4 is concerned with the initial compressible hydrodynamic steady-state to which magnetic helical fluctuations are injected, as well as more general aspects regarding the magnetic helicity inverse transfer. Chapter 5 is devoted to the finding of scaling laws in the Fourier spectra, as well as the extension of the Alfvénic balance (relation (2.47)) in the compressible case. Using jointly the helical decomposition and shell-to-shell transfer analysis, chapter 6 disentangles some aspects of the nonlinear dynamics, considering the relative strength and locality of the different helical contributions, assessing among others the role of the compressive part of the velocity field.

Finally, chapter 7 discusses the robustness of the gained results by changing the parameters of the electromotive forcing and considering different resolutions and numerical schemes of varying order. It also provides a summary of the main results and mentions some limitations regarding their applicability to real systems.

Below follows a more thorough description of the main aspects studied in this dissertation, as well as their relations with previous research:

1. Regarding the initial hydrodynamic steady state, power spectra of the velocity field \mathbf{v} as well as of $\mathbf{u} = \rho^{1/3}\mathbf{v}$ for several RMS Mach number flows with either a purely solenoidal or purely compressive large scale mechanical forcing are compared. Indeed, as explained in section 2.2.1, while an incompressible Kolmogorov $K^{-5/3}$ scaling is expected for $\mathcal{P}(\mathbf{v})$ for flows with low compressibility, a Burgers K^{-2} scaling is expected for supersonic shock-dominated turbulence. The Kolmogorov scaling is expected to be recovered for $\mathcal{P}(\mathbf{u})$ when using a purely solenoidal mechanical forcing, whereas a $K^{-19/9}$ scaling is expected when using a purely compressive driving [46, 49]. These aspects have been verified in previous compressible isothermal direct numerical simulations [62, 45, 43] and are reviewed in section 4.1.
2. The small scale magnetic helicity fluctuations are expected to be transferred to ever larger scales [48], as described in section 2.2.3. This has been confirmed through numerical integration of the EDQNM model [86] as well as through direct numerical simulations, both in the incompressible [87, 76, 3, 74, 82] and in the compressible case [8, 34, 25]. In the compressible case however, only low Mach number flows have been considered so far: isothermal compressible subsonic turbulence with a maximum RMS Mach number of about 0.2 – 0.3 [34, 25], or mildly supersonic adiabatic compressible turbulence with a maximum RMS Mach number oscillating around unity [8]. As explained in section 3.5.1, the present work considers highly compressible isothermal turbulence with RMS Mach numbers ranging up to about 11

for solenoidally-driven runs and up to about 8 for compressively-driven runs, which are relatively close to the values observed for the interstellar medium ([37], section 4.2). Section 4.2 attests the presence of this magnetic helicity inverse transfer in high Mach number turbulence and explores some aspects regarding its effect both on the velocity field, and indirectly on the density statistics.

3. A dimensional analysis similar to the phenomenological one leading to the $K^{-5/3}$ Kolmogorov energy spectrum in incompressible hydrodynamic turbulence predicts a K^{-2} scaling law for the magnetic helicity spectrum (section 2.2.3). However, even though this spectrum was indeed observed in numerical integration of the EDQNM closure model [86], simulations done in incompressible MHD turbulence give significantly steeper exponents [79, 53, 74, 82]. For the numerical setup closest to the one used here, with magnetic helicity injection at small scales [74, 82], the exponent in the inverse transfer range was found to be close to -3.3 . Section 4.2 shows that the incompressible -3.3 exponent is also found for the subsonic and mildly supersonic cases, but that this exponent becomes flatter with higher compressibility.
4. In the incompressible case, several other scaling laws in the inverse transfer region have been found [74], as well as an Alfvénic balance written in relation (2.47), which has also been observed in other numerical experiments [79, 53]. Scaling laws are also sought for in section 5.1 and compared to those obtained in the incompressible case. Section 5.2 proposes an extension of relation (2.47) valid in the highly compressible case.
5. The helical decomposition formalism used for the study of single triad helical mode interactions in incompressible hydrodynamic turbulence [102] has been extended to the MHD incompressible case [65, 69]. Through geometric factors analysis, it has been deduced that for magnetic modes of positive helicity, the transfers are expected to be stronger and more non-local when mediated by a velocity mode of positive helicity, as compared to a mediation by a velocity mode of negative helicity [69]. This approach is extended here to compressible MHD. The geometric factor for compressive velocity modes mediations derived in section 2.3.2 are displayed together with the incompressible helical geometric factors in section 6.3. These geometric factors are put in correspondence with the locality and strength of the different helical contributions to the magnetic helicity transfer rates observed in chapter 6.
6. Using magnetic helicity shell-to-shell transfers, it has been shown in incompressible MHD that its inverse transfer exhibits non-local features, especially at later times, when magnetic energy reaches larger scales, and that a subdominant direct cascade of magnetic helicity can also be found [3]. Hints for such a direct cascade at later times in subsonic isothermal MHD have also been described in reference [25]. In the present work, the shell-to-shell transfers formulation is combined with the helical decomposition approach as described in section 2.4.4 and used extensively in chapter 6. Some comparisons with the incompressible case are made in section 6.4.2 .
7. Shell-to-shell energy exchanges both among and between the magnetic and kinetic energy reservoirs are considered in section 6.2.3, allowing to disentangle some aspects of the nonlinear inverse transfer. For this purpose, the incompressible MHD approach of reference [2] is extended as described in section 2.4.2.

Chapter 3

Numerical method

Higher-order numerical methods offer significant advantages as compared to lower-order schemes (in the present context, methods of order strictly lower than four). Because of their higher accuracy, they allow to reach a certain results' quality at significantly lower resolutions. Hence, even though they are computationally more expensive at a given resolution, they allow to spare computing resources in the end since a lower-order scheme would need way finer grids to achieve a given quality. This fact is illustrated with the standard 3D MHD vortex problem in appendix B. For turbulent systems, the influence of the scheme's order and the numerical resolution are discussed in section 7.2.

The numerical method used to solve the MHD equations (2.1)-(2.3) is a fourth-order semi-discrete dimension-by-dimension finite-volume scheme, with a constrained-transport method in order to ensure the solenoidality of the magnetic field. The implementation details are described in references [100, 97] and only a short summary is presented here, together with some refinements specific to the present work which are needed in order to handle high Mach number flows (sections 3.1 and 3.2). The reader interested in the technical details which are not specific to this dissertation is kindly referred to these publications.

In addition, section 3.3 details how the mechanical large scale driving and the electro-motive small scale forcing are done. Section 3.4 presents how the Fourier transformation and the shell-to-shell helically-decomposed transfer functions are computed. Finally, section 3.5 concludes by detailing the protocol of the numerical experiments and the runs performed.

3.1 General framework

The numerical domain $[0, L] \times [0, L] \times [0, L]$ with $L = 1$ is discretised using a Cartesian coordinate system with fixed grid-sizes $\Delta x = \Delta y = \Delta z = L/N$ with N the linear resolution. The boundary conditions are periodic in the three directions. As implied by the use of a finite-volume method ([98], section 3.2), the density and momentum fields $(\rho, \rho\mathbf{v})$ (as well as the total energy density e when using an adiabatic equation of state) are discretised as volume averages whereas the magnetic field components are defined as staggered area averages on faces normal to the direction of each component, as needed for the constrained-transport approach [41]. More precisely, a cell indexed by the integers $(i, j, k) \in [1, N]^3$ contains the information about the volume averages in the domain $[x_i - \Delta x/2, x_i + \Delta x/2] \times [y_j - \Delta y/2, y_j + \Delta y/2] \times [z_k - \Delta z/2, z_k + \Delta z/2]$ with $x_i = (i - 1/2)\Delta x$, $y_j = (j - 1/2)\Delta y$ and $z_k = (k - 1/2)\Delta z$ the cell centres and the magnetic field components (b_x, b_y, b_z) defined as area averages $(x, y, z) \in \{x_i - \Delta x/2\} \times [y_j - \Delta y/2, y_j + \Delta y/2] \times [z_k - \Delta z/2, z_k + \Delta z/2]$,

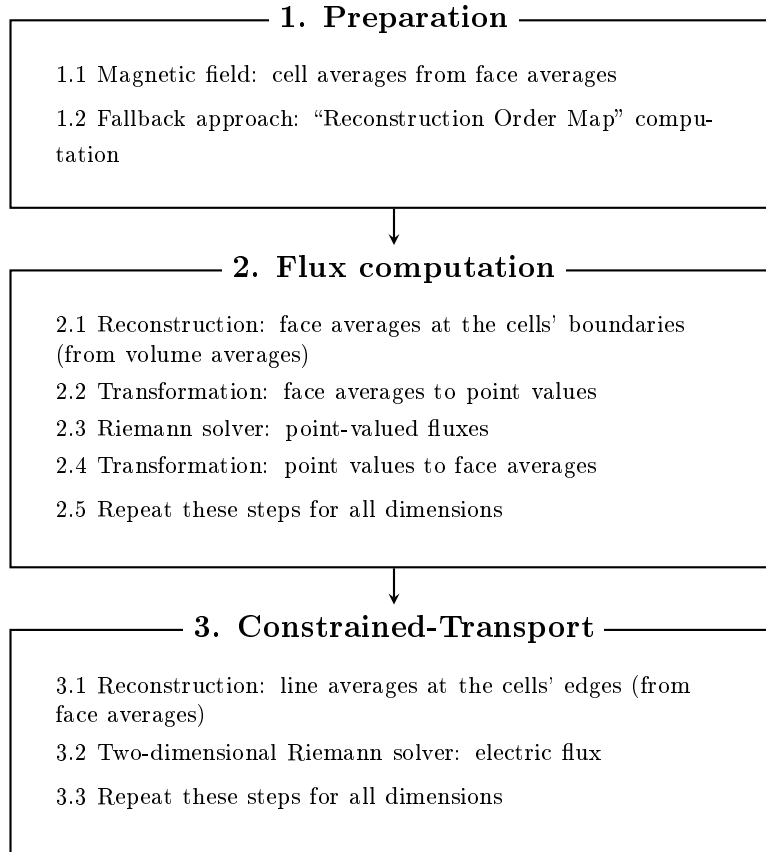


Figure 3.1: Workflow of the right-hand-side computation.

$(x, y, z) \in [x_i - \Delta x/2, x_i + \Delta x/2] \times \{y_j - \Delta y/2\} \times [z_k - \Delta z/2, z_k + \Delta z/2]$ and $(x, y, z) \in [x_i - \Delta x/2, x_i + \Delta x/2] \times [y_j - \Delta y/2, y_j + \Delta y/2] \times \{z_k - \Delta z/2\}$ respectively. The finite-volume method ensures that the volume-averaged quantities are intrinsically conserved, since what exits one cell enters a neighbouring cell and vice-versa. As a consequence, when using an adiabatic equation of state (see section 2.1.1), all kinetic energy and magnetic energy lost by numerical non-ideal effects is transformed in internal energy (heat). This leads to an increase in temperature of the system over time when considering forced turbulence, since the fate of all the injected energy is to be transformed in heat through the non-ideal numerical effects. As a consequence, a steady-state cannot be obtained without an internal energy sink, which is linked with additional numerical complexity. For this reason, the isothermal equation of state is preferred in this work. For the runs presented here, the sound speed is fixed to $c_s = 0.1$.

In numerical MHD simulations, it is very important to implement a strategy to keep the solenoidality of the magnetic field ($\nabla \cdot \mathbf{b} = 0$), since $|\nabla \cdot \mathbf{b}|$ would typically grow in time because of numerical approximations otherwise, causing unphysical effects [23, 24]. The constrained-transport approach [41] ensures that the second-order approximation of $\nabla \cdot \mathbf{b}$ is inherently preserved up to machine precision, in a very similar way that the volume-averaged quantities are conserved in the finite-volume framework.

The workflow of the right-hand-side computation is shown in figure 3.1. The numerical scheme used is almost identical to the one of references [100, 97]. The magnetic field cell averages are computed from the area averages through a fourth-order polynomial interpolation, owing to the property that the magnetic field components are continuous along

their respective directions [71]. The Rusanov flux [90] and a multidimensional version of the same [10] are used for the computation of the interfacial fluxes and of the electric field line averages to be plugged in the constrained-transport algorithm respectively. The numerical method solves three times a one-dimensional problem instead of solving directly a three-dimensional problem (dimension-by-dimension approach), which significantly increases numerical run-time efficiency, since only neighbouring cells in one spatial dimension need to be considered for the reconstruction polynomials, and not a whole neighbouring three-dimensional region.

Some differences with references [100, 97] appear in the treatment of strong discontinuities, which influence the reconstruction steps and the passage through point values (steps 2.1, 2.2, 2.4 and 3.1 in figure 3.1). Strong shocks in high Mach number flows cause indeed serious difficulties regarding the robustness of the numerical method. This is because the reconstruction procedure can generate unphysical values such as a negative density (or pressure in the adiabatic case) in their neighbourhood. This issue is particularly pronounced for schemes of higher order of accuracy, as the fourth-order one used here. Lower-order methods are indeed more diffusive: they smooth out the small scale structures but have the positive side effect of smoothing out unphysical reconstruction variations as well, whereas higher-order methods might fail to preserve a non-oscillatory behaviour around strong shocks, causing oscillations that are less smoothed out with time. A way to handle this issue is to use a so-called “fallback approach”, or “flattening” [35, 11, 83], which adapts the reconstruction order locally. The aim is to use the high-order methods (fourth-order Central Weighted Non Oscillatory (CWENO) reconstruction [66] and passage through point values [75, 28]) in smooth regions but resort to lower-order methods near strong gradients. This is done according to a “reconstruction order map” (step 1.2 in figure 3.1). The fallback strategies presented in references [100, 97] have revealed themselves to be insufficient for the purpose of the present work due to the very high density gradients achieved by the high Mach number flows and thus some refinements are used here. These modifications, presented in section 3.2, are only empirically based: in the runs presented here, they allowed to reach higher compressibility levels while limiting the amount of lower-order reconstructions. However, as written in appendix A.3, even though most of the cells are reconstructed at high-order for low Mach number flows, the amount of lower-order reconstructions is far from negligible at high Mach numbers. A more rigorous approach which should lead to less lower-order reconstructions would be very beneficial, but is not in the scope of the present work.

Lastly, the same time integration method as in references [100, 97] is used, namely a ten-stage fourth-order SSPRK (strong stability-preserving Runge-Kutta) method, described in the pseudocode 3 of reference [59]. Using a SSPRK method presents two advantages. First, it avoids the generation of additional oscillations through the time integration step [51, 52]. Second, it allows larger timesteps as compared to standard Runge-Kutta schemes, since its linear stability region is typically greater, resulting in a gain in efficiency. The timestep Δt is adapted at each iteration: at the first stage of the Runge-Kutta algorithm, the maximum timestep compatible with the Courant-Friedrichs-Lewy (CFL) criterion is taken and then kept for the remaining nine stages [100, 97]. The Courant number is set to $C_{CFL} = 1.5$ for all the runs considered here.

3.2 Fallback strategy

The fallback strategy [35, 11, 83], consists of two steps: (i) marking the cells which should be reconstructed at lower order (the computation of a “Reconstruction Order Map” or

“ROM” in the following), (ii) applying this ROM to the reconstruction steps and the passage through point values. These two aspects are described in this section after giving an overview of the different reconstruction methods used.

3.2.1 Reconstruction methods used

As described in the next subsection, the ROM contains decimal values between one and four, which correspond to the reconstruction order to be done locally. Here, only a very brief summary of each of the used methods of order one to four is outlined. The reader interested in the technical details is kindly referred to the cited literature. For a one-dimensional problem, the reconstruction procedure in a finite-volume scheme consists in determining the boundary values $u_{i\pm 1/2} = u(x_i \pm \Delta x/2)$ of a variable u in cell i when knowing the cell average $\bar{u}_i = \frac{1}{\Delta x} \int_{x_i - \Delta x/2}^{x_i + \Delta x/2} u(x) dx$ in cell i and a certain amount of neighbouring cells, depending on the order of the method. This method is then generalised to 2D (from area to line) and 3D (from volume to area) reconstructions in the dimension-by-dimension framework.

1. The highest-order method is the fourth-order CWENO reconstruction method [66]. The main idea of this method is, as for all WENO schemes [70, 93, 94], to divide the reconstruction stencil into sub-stencils which are weighted according to the smoothness of the quantity to be reconstructed. The weights are chosen so that if the solution is smooth in the reconstruction stencil, the method gives a fourth-order reconstruction, but if a discontinuity is present, the sub-stencil(s) associated with it correspond(s) to a vanishing weight. Formally, it looks like the following:

$$u(x_i \pm \frac{\Delta x}{2}) = w_L P_L(x \pm \frac{\Delta x}{2}) + w_C P_C(x \pm \frac{\Delta x}{2}) + w_R P_R(x \pm \frac{\Delta x}{2}), \quad (3.1)$$

with P_L , P_C and P_R the reconstruction polynomials associated with the (L)eft, (C)entral and (R)ight sub-stencils respectively (which are functions of the $(\bar{u})_i$) and w_L , w_C , w_R their respective positive weights, which sum up to unity. The implementation is exactly the same as in references [100, 97], including the value of the few free parameters and the use of a global smoothness indicator common for all the reconstructed variables.

2. The third-order method used is the limO3 method [30, 77]:

$$u(x_i + \frac{\Delta x}{2}) = \bar{u}_i + \frac{\bar{u}_{i+1} - \bar{u}_i}{2} \Phi(\theta_i), \quad (3.2)$$

$$u(x_i - \frac{\Delta x}{2}) = \bar{u}_i - \frac{\bar{u}_i - \bar{u}_{i-1}}{2} \Phi(\theta_i^{-1}), \quad (3.3)$$

with $\Phi(\theta) = (1-\chi)P_3(\theta) + \chi\hat{\Phi}(\theta)$ a function of the slope ratio $\theta_i = (\bar{u}_i - \bar{u}_{i-1})/(\bar{u}_{i+1} - \bar{u}_i)$. The polynomial $P_3(\theta)$ gives quadratic reconstruction, whereas the $\hat{\Phi}$ function is the third-order limiter. A smooth transition between limited and unlimited reconstructions happens through the χ term. The detailed expressions can be found in references [30, 77] and are not repeated here. The free parameters r and ϵ , defined in reference [77], are taken equal to the values in that work: $r = 1$ and $\epsilon = 10^{-12}$.

3. For the second-order method, the Total Variation Diminishing limiter of Van-Leer is used [99, 106]:

$$u(x_i \pm \frac{\Delta x}{2}) = \bar{u}_i \pm \frac{\max[(\bar{u}_{i+1} - \bar{u}_i)(\bar{u}_i - \bar{u}_{i-1}), 0]}{\bar{u}_{i+1} - \bar{u}_{i-1}} \quad (3.4)$$

4. Lastly, in extreme cases, the numerical scheme can resort to first-order reconstruction by considering the reconstructed variable as constant in the whole cell, as in Godunov's scheme [50]:

$$u(x_i \pm \frac{\Delta x}{2}) = \bar{u}_i. \quad (3.5)$$

These four reconstruction methods are compared with respect to numerical dissipation effects in appendix B, where they are used to advect the standard 3D MHD vortex problem.

3.2.2 ROM computation

A combination of two shock indicators is used in order to compute the ROM. They are here expressed for reconstructions along the \mathbf{x} -direction (for reconstructions in the \mathbf{y} - and \mathbf{z} -directions, the expressions are analogous):

1. The first shock indicator is based on the spatial gradients of the pressure (which is the same as the one for the density when using an isothermal equation of state):

$$s_{p,i,j,k}^x = \frac{|p_{i+1,j,k} - p_{i-1,j,k}|}{p_{i,j,k}}. \quad (3.6)$$

This indicator is also used in references [100, 97].

2. The other shock indicator is based on the temporal variations of the density. Since $\partial_t \rho = -\nabla \cdot (\rho \mathbf{v})$, one can estimate the variation of the density in cell (i, j, k) during a timestep Δt due to the x -momentum through:

$$\Delta \rho_{i,j,k} \approx -\Delta t \frac{(\rho v_x)_{i+1,j,k} - (\rho v_x)_{i-1,j,k}}{2\Delta x}. \quad (3.7)$$

Based on this estimate, the following shock indicator can be built, which is in substance the ratio of the density variations by the density in a cell (aside from multiplicative constants):

$$s_{\Delta t,i,j,k}^x = \frac{\widetilde{\Delta t} (\rho v_x)_{i+1,j,k} - (\rho v_x)_{i-1,j,k}}{\rho_{i,j,k} \Delta x}, \quad (3.8)$$

with $\widetilde{\Delta t}$ an estimate of the timestep. An estimate is needed here, since the largest timestep compatible with the CFL criterion used in the Runge-Kutta time integration scheme can only be derived after the maximum propagation speed of information, which corresponds to fast magnetosonic waves, has been computed on the interfaces between cells [100]. However, in order to know these maximum propagation speeds, reconstructions have to be performed, which are done according to the ROM, based on the shock indicators, including $s_{\Delta t}^x$. Since the computation of the $s_{\Delta t}^x$ occurs first in the algorithm, a rough estimate for the timestep is taken, obtained by plugging the cell averaged values in the fast magnetosonic speed expressions, which are then used in the CFL criterion.

This shock indicator is positive when $\Delta\rho_{i,j,k}$ is negative, which means when there is a risk to obtain negative densities during the considered iteration. It presents furthermore the same monotonicity as the shock indicator based on the spatial gradients: for greater gradients, it is greater.

For each of these shock indicators, six thresholds, $\tau_{4,m}^+ \leq \tau_{3,m}^- \leq \tau_{3,m}^+ \leq \tau_{2,m}^- \leq \tau_{2,m}^+ \leq \tau_{1,m}^-$ are defined which lead to two reconstruction order maps, ROM_m^x with $m \in \{p, \Delta t\}$ based on s_p^x and $s_{\Delta t}^x$ respectively:

$$ROM_{m,i,j,k}^x = \begin{cases} 4, & \text{if } s_{m,i,j,k}^x < \tau_{4,m}^+, \\ 4 - \frac{s_{m,i,j,k}^x - \tau_{4,m}^+}{\tau_{3,m}^- - \tau_{4,m}^+}, & \text{if } \tau_{4,m}^+ \leq s_{m,i,j,k}^x \leq \tau_{3,m}^-, \\ 3, & \text{if } \tau_{3,m}^- < s_{m,i,j,k}^x < \tau_{3,m}^+, \\ 3 - \frac{s_{m,i,j,k}^x - \tau_{3,m}^-}{\tau_{2,m}^- - \tau_{3,m}^-}, & \text{if } \tau_{3,m}^+ \leq s_{m,i,j,k}^x \leq \tau_{2,m}^-, \\ \dots, & \end{cases} \quad (3.9)$$

until $ROM_m^x = 1$ for $s_{m,i,j,k}^x > \tau_{1,m}^-$, so that ROM_m^x is a continuous piecewise affine function of s_m^x . The values of the thresholds ($\tau_{i,m}^\pm$) for each run are given in appendix A.2. The two reconstruction order maps obtained, one for each shock indicator, are merged into a final ROM^x used for the reconstructions by taking their minimum:

$$ROM_{i,j,k}^x = \min(ROM_{p,i,j,k}^x, ROM_{\Delta t,i,j,k}^x). \quad (3.10)$$

For highly supersonic problems, an additional refinement is used. The numerical stability can be improved if regions that are about to be affected by a shock are also associated with a lower-order reconstruction [11]. This is done by considering the pressure variations (or equivalently the density variations in the isothermal case):

$$\begin{aligned} ROM_{i,j,k}^x &= \min(\widetilde{ROM}_{i,j,k}^x, \widetilde{ROM}_{i+1,j,k}^x) \text{ if } p_{i+1,j,k} > p_{i,j,k}, \\ ROM_{i,j,k}^x &= \min(\widetilde{ROM}_{i,j,k}^x, \widetilde{ROM}_{i-1,j,k}^x) \text{ if } p_{i-1,j,k} > p_{i,j,k}, \end{aligned} \quad (3.11)$$

with \widetilde{ROM} indicating here the ROM obtained through the merging of the ROM_p and $ROM_{\Delta t}$ reconstruction order maps (see equation (3.10)).

3.2.3 Application of the ROM

The ROM influences the reconstruction steps in the following way: when $ROM_{i,j,k}^x$ is an integer, the reconstruction method of order $ROM_{i,j,k}^x$ mentioned in section 3.2.1 is used. When it is between two integers, a weight $w_{i,j,k}^{f,x}$ is defined by taking its decimal part and the reconstructed values at the boundaries are given by:

$$u_{i\pm 1/2,j,k} = w_{i,j,k}^{f,x} R_{i\pm 1/2,j,k}^{[ROM_{i,j,k}^x]} + (1 - w_{i,j,k}^{f,x}) R_{i\pm 1/2,j,k}^{[ROM_{i,j,k}^x]}, \quad (3.12)$$

with $[ROM_{i,j,k}^x]$ (resp. $\lceil ROM_{i,j,k}^x \rceil$) the largest (resp. smallest) integer such that $[ROM_{i,j,k}^x] \leq ROM_{i,j,k}^x$ (resp. $ROM_{i,j,k}^x \leq \lceil ROM_{i,j,k}^x \rceil$) and $R_{i\pm 1/2,j,k}^m$ is the reconstructed value obtained thanks to the reconstruction method of order m . With these notations, the weight is defined by $w_{i,j,k}^{f,x} = ROM_{i,j,k}^x - [ROM_{i,j,k}^x]$. This allows a smooth transition between higher-order and lower-order reconstruction in the vicinity of strong discontinuities and shocks. The ROM defined above is used for volume-to-face average

reconstructions. For the face-average-to-edge reconstructions needed in the framework of the constrained-transport procedure, the minimum of the two ROM values surrounding the face is taken. As an example, for a reconstruction along the \mathbf{y} -direction of a face normal to the \mathbf{z} -direction $(i, j, k - 1/2)$, this gives:

$$ROM_{i,j,k-1/2}^y = \min(ROM_{i,j,k-1}^y, ROM_{i,j,k}^y). \quad (3.13)$$

Lastly, the passage through point values is also influenced by the ROM. A transformation is required, but only for schemes of order higher than two [100]. Hence, when $2 < ROM < 3$ at a certain face, a flattening also occurs for these steps:

$$\begin{aligned} u_{i+1/2,j,k}^p &= u_{i+1/2,j,k} - \frac{w_{i+1/2,j,k}^{f,y}}{24} (u_{i+1/2,j-1,k} - 2u_{i+1/2,j,k} + u_{i+1/2,j+1,k}) \\ &\quad - \frac{w_{i+1/2,j,k}^{f,z}}{24} (u_{i+1/2,j,k-1} - 2u_{i+1/2,j,k} + u_{i+1/2,j,k+1}), \end{aligned} \quad (3.14)$$

$$\begin{aligned} u_{i+1/2,j,k} &= u_{i+1/2,j,k}^p + \frac{w_{i+1/2,j,k}^{f,y}}{24} (u_{i+1/2,j-1,k}^p - 2u_{i+1/2,j,k}^p + u_{i+1/2,j+1,k}^p) \\ &\quad + \frac{w_{i+1/2,j,k}^{f,z}}{24} (u_{i+1/2,j,k-1}^p - 2u_{i+1/2,j,k}^p + u_{i+1/2,j,k+1}^p), \end{aligned} \quad (3.15)$$

where $u_{i+1/2,j,k}^p = u(x_i + \Delta x/2, y_j, z_k)$ is the point value in the middle of the considered face. The origin of this relation can be found in reference [100] around equation 59 and in section 3.3 (of that reference) and is not repeated here.

3.3 Driving of the system

The driving is done both through a hydrodynamic (or “mechanical”) and an electromotive (or “magnetic”) forcing. The mechanical forcing generates the initial hydrodynamic turbulent steady-state at a desired RMS Mach number and with a desired compressibility, and maintains this turbulent steady-state by constantly injecting energy at large scales since energy is lost by numerical diffusion due to the finite resolution of the system, predominantly at small scales. The electromotive forcing injects magnetic fluctuations with a defined amount of magnetic helicity, which inverse transfer is investigated.

3.3.1 Hydrodynamic forcing

In order to stir the fluid at large scales, a stochastic process with a finite autocorrelation timescale is chosen, namely the Ornstein-Uhlenbeck process [40, 92], which can be described by the following stochastic differential equation in Fourier space:

$$d\mathbf{F}_{\mathbf{k}}^{\text{OU}}(t) = -\mathbf{F}_{\mathbf{k}}^{\text{OU}}(t) \frac{dt}{t_{\text{auto}}} + F_0 \left(\frac{2\sigma(\mathbf{k})^2}{t_{\text{auto}}} \right)^{1/2} \underline{\mathcal{P}}^\zeta \cdot d\mathbf{W}(t). \quad (3.16)$$

The first term on the right hand side corresponds to an exponential decay with a time constant t_{auto} called the autocorrelation time: this is the characteristic duration the forcing needs in order to “forget” its current state. The second term is a diffusion term modelled by a Wiener process so that $d\mathbf{W}(t) = dt\mathbf{N}(0, dt)$ with \mathbf{N} a 3D Gaussian distribution with

zero mean and standard deviation dt . This process can be mathematically interpreted as a continuous random walk. It is furthermore adjusted by a spectral profile $\sigma(\mathbf{k})$ which will be defined shortly below and a constant amplitude F_0 which value is not relevant since the applied forcing in real space is renormalised so that a constant energy injection rate takes place. The projection tensor \mathcal{P}^ζ in Fourier space, written in index notation, is:

$$\begin{aligned}\mathcal{P}_{ij}^\zeta(\mathbf{k}) &= \zeta \mathcal{P}_{ij}^{\zeta \perp} + (1 - \zeta) \mathcal{P}_{ij}^{\zeta \parallel}, \\ &= \zeta \delta_{ij} + (1 - 2\zeta) \frac{k_i k_j}{|k|^2},\end{aligned}\tag{3.17}$$

where $\mathcal{P}_{ij}^{\zeta \parallel} = k_i k_j / |k|^2$ and $\mathcal{P}_{ij}^{\zeta \perp} = \delta_{ij} - \mathcal{P}_{ij}^{\zeta \parallel}$ are the projection operators along \mathbf{k} and on the plane orthogonal to \mathbf{k} respectively and the parameter ζ is called the ‘‘spectral weight’’. Hence, the extreme case $\zeta = 1$ corresponds to a fully solenoidal forcing whereas $\zeta = 0$ corresponds to a fully compressive forcing. The mechanical forcing is applied only at the largest scales, at the modes in the $K = 1$ and $K = 2$ shells, which leads to the spectral profile $\sigma(\mathbf{k}) = 1$ for $1 \leq |\mathbf{k}|/\kappa < 3$ and $\sigma(\mathbf{k}) = 0$ otherwise.

The forcing field is not updated at each of the ten stages of the fourth-order SSPRK time integration scheme, but only after a complete passage through these ten stages. This approach is done for the sake of simplicity. The aim of the mechanical driving is to generate and sustain a steady turbulent state by compensating the loss of energy through numerical dissipation. Hence, being closer to an ideal Ornstein-Uhlenbeck process is not of relevance here. The field \mathbf{F}^{OU} is thus updated in Fourier space through:

$$\mathbf{F}^{\text{OU}} \leftarrow \mathbf{F}^{\text{OU}} + \Delta \mathbf{F}_{\mathbf{k}}^{\text{OU}}(t),\tag{3.18}$$

where $\Delta \mathbf{F}_{\mathbf{k}}^{\text{OU}}(t)$ corresponds to relation (3.16) with $dt = \Delta t$. Then, the \mathbf{F}^{OU} Fourier coefficients are transformed to configuration space, giving \mathbf{f}^{OU} , where it leads to an update of the momentum variables through:

$$(\rho \mathbf{v}) \leftarrow (\rho \mathbf{v}) + \rho \Delta t A \mathbf{f}^{\text{OU}}.\tag{3.19}$$

The resulting forcing field is multiplied by a factor A at each iteration so that a constant energy injection rate is achieved. Indeed, with $A \mathbf{f}^{\text{OU}}$ the applied acceleration field, the gain in kinetic energy after its application can be estimated as:

$$\Delta \mathcal{E}^K = \frac{1}{2} A^2 \Delta t^2 \sum_{i,j,k} \rho_{i,j,k} (\mathbf{f}^{\text{OU}}_{i,j,k})^2 + A \Delta t \sum_{i,j,k} \rho_{i,j,k} \mathbf{v}_{i,j,k} \cdot \mathbf{f}^{\text{OU}}_{i,j,k}.\tag{3.20}$$

In order to achieve a constant energy injection rate ϵ_{inj}^K such that $\Delta \mathcal{E}^K = \epsilon_{inj}^K \Delta t$, a second-order polynomial equation in A needs to be solved, similarly to what is done in reference [73]. As in that paper, the largest root of the equation is taken for A . Furthermore, the above-defined driving leads to a weak mean velocity field in the system, whose magnitude does not grow in time. Since the magnetic field is however not Galilean invariant, this weak mean velocity field is removed at each iteration.

Please note that in equation (3.19), an external acceleration field is used to update the momentum, not an external force field. An external force field would be directly applied to the momentum without multiplication by the density and would hence have the form $(\rho \mathbf{v}) \leftarrow (\rho \mathbf{v}) + A \Delta t \mathbf{f}^{\text{OU}}$. The forcing through an acceleration is preferred since it allows a greater inertial range, as compared to an external force field driving [63, 5].

3.3.2 Electromotive forcing

In order to study the inverse transfer of magnetic helicity, an electromotive forcing takes place, which injects helical magnetic fluctuations at small scales. This electromotive forcing is a δ -correlated process (white noise) with a defined helicity fraction (see section 2.2.3), injecting a determined quantity of magnetic energy ϵ_{inj}^M per time unit.

The magnetic helicity fraction can be set by appropriate choosing of the forcing amplitudes along the $\hat{\mathbf{h}}_{\mathbf{k}}^+$ and $\hat{\mathbf{h}}_{\mathbf{k}}^-$ curl eigenvectors such that $i\mathbf{k} \times \hat{\mathbf{h}}_{\mathbf{k}}^\pm = \pm k \hat{\mathbf{h}}_{\mathbf{k}}^\pm$ (see section 2.3). Writing the electromotive forcing field applied to the magnetic field in this basis gives indeed:

$$\mathbf{F}_{\mathbf{k}}^M = B_{\mathbf{k}}^+ e^{i\theta_{\mathbf{k}}^+} \hat{\mathbf{h}}_{\mathbf{k}}^+ + B_{\mathbf{k}}^- e^{i\theta_{\mathbf{k}}^-} \hat{\mathbf{h}}_{\mathbf{k}}^-, \quad (3.21)$$

with $B_{\mathbf{k}}^+$ and $B_{\mathbf{k}}^-$ positive real amplitudes and $\theta_{\mathbf{k}}^+, \theta_{\mathbf{k}}^-$ real numbers containing the phase information. In order to achieve a given helical fraction of $h_f \in [-1, +1]$, the most straightforward is to set each mode's $B_{\mathbf{k}}^\pm$ amplitudes such that:

$$\frac{kH_{\mathbf{k}}^M}{2E_{\mathbf{k}}^M} = \frac{(B_{\mathbf{k}}^+)^2 - (B_{\mathbf{k}}^-)^2}{(B_{\mathbf{k}}^+)^2 + (B_{\mathbf{k}}^-)^2} = h_f, \quad (3.22)$$

where use of relations (2.54), (2.55) and (2.53) has been made. This gives a condition on the squared amplitude ratio between both helical components:

$$\frac{(B_{\mathbf{k}}^+)^2}{(B_{\mathbf{k}}^-)^2} = \frac{1 + h_f}{1 - h_f}. \quad (3.23)$$

With a condition on the contribution of mode \mathbf{k} to the magnetic energy injection of the form $\frac{1}{2}((B_{\mathbf{k}}^+)^2 + (B_{\mathbf{k}}^-)^2) = \sigma^M(\mathbf{k})$ with $\sigma^M(\mathbf{k})$ a certain function of \mathbf{k} , this allows to determine uniquely the amplitudes $B_{\mathbf{k}}^+$ and $B_{\mathbf{k}}^-$.

The shells $K_{min}^F \leq K \leq K_{max}^F$ are forced, with $K_{min}^F = 48$ and $K_{max}^F = 52$. The energy distribution function among the modes peaks at $(K_{min}^F - K_{max}^F)/2 = 50$ and is inspired by reference [20]:

$$\sigma^M(\mathbf{k}) = \begin{cases} 0 & \text{for } |\mathbf{k}|/\kappa < K_{min}^F \text{ or } |\mathbf{k}|/\kappa \geq K_{max}^F + 1, \\ \exp \left[\frac{1}{2} \left(\frac{|\mathbf{k}|/\kappa - (K_{min}^F + K_{max}^F)/2}{K_0} \right)^2 \right]^2 & \text{for } K_{min}^F \leq |\mathbf{k}|/\kappa < K_{max}^F + 1, \end{cases} \quad (3.24)$$

with $K_0 = 4$ and the phases $\theta_{\mathbf{k}}^\pm$ are chosen randomly, uniformly in the interval $[0, 2\pi]$.

At each timestep, after the ten stages of the SSPRK time integrator are performed, the forcing field \mathbf{F}^M is thus generated randomly in Fourier space and then transformed in configuration space, giving \mathbf{f}^M which is used to update the magnetic field components through:

$$\mathbf{b} \leftarrow \mathbf{b} + \Delta t A \mathbf{f}^M. \quad (3.25)$$

This choice of injecting magnetic helical fluctuations after the time integrator's ten stages, and not at each stage, is done both for the sake of simplicity and in order to treat both the mechanical and the electromotive driving in a similar way. Similarly to the update of the momentum, a factor A is applied in order to achieve a constant magnetic energy injection rate. This factor is determined by taking the largest root of the second-order polynomial equation in A :

$$\Delta \mathcal{E}^M = \frac{1}{2} A^2 \Delta t^2 \sum_{i,j,k} (\mathbf{f}_{i,j,k}^M)^2 + A \Delta t \sum_{i,j,k} \mathbf{b}_{i,j,k} \cdot \mathbf{f}_{i,j,k}^M. \quad (3.26)$$

Since the constrained-transport approach is used in this numerical solver, the magnetic field is defined as area averages, so that $(\mathbf{b}_{i,j,k})_x$ represents here the area-averaged magnetic field on the face centred at $(x_i - \Delta x/2, y_j, z_k)$ and normal to the \mathbf{x} -direction and similarly for the other components. Because of this, some subtleties arise regarding the transformation of the electromotive forcing field \mathbf{F}^M to configuration space. As defined through relation (3.21), the Fourier coefficients correspond indeed to the Fourier transform of the electromotive forcing field defined as *point values*, all three components being defined *at the same point*. Hence, one has to apply some multiplications on the Fourier components which correspond to an offset and an integration in configuration space, in order to change these Fourier coefficients to those corresponding to the staggered area-integrated magnetic field components. For example, for the \mathbf{x} -component of the forcing Fourier coefficients:

$$F_x^M(\mathbf{k}) \leftarrow F_x^M(\mathbf{k}) \times e^{ik_x \Delta x/2} \times \frac{e^{ik_y \Delta y/2} - e^{-ik_y \Delta y/2}}{ik_y} \times \frac{e^{ik_z \Delta z/2} - e^{-ik_z \Delta z/2}}{ik_z} \times \frac{1}{\Delta y \Delta z}. \quad (3.27)$$

The first factor corresponds in configuration space to an offset from cell centres (x_i, y_j, z_k) to face centres $(x_i - \Delta x/2, y_j, z_k)$ since $\hat{f}_k = \hat{f}_k e^{ika}$ for $f(x) = g(x + a)$. The second and third factors correspond to an integration on the domain $(y, z) \in [y_j - \Delta y/2, y_j + \Delta y/2] \times [z_k - \Delta z/2, z_k + \Delta z/2]$ since $\hat{f}_k = \hat{g}_k (e^{ikb} - e^{-ika}) / (ik)$ for $f(x) = \int_a^b g(t) dt$, and the last factor is a normalisation since area *averages* are considered.

An analogous procedure is applied to the other two components of the forcing Fourier coefficients. These transformed coefficients are the ones used in order to update the staggered area-averaged magnetic field in configuration space through relation (3.25). Without this transformation step, the applied forcing field on the area averages would not be divergence-free and the dilatational components introduced by the electromotive forcing would be preserved by the constrained-transport algorithm up to machine precision, leading to unphysical effects.

3.4 Fourier spectra and shell-to-shell transfer functions

The Fourier spectra are computed in the present work by identifying the point values in the middle of the cells with the cells' volume averages, and transforming these point values through the FFTW library. This approach, although second-order accurate, is done because of two reasons: (i) the spectra differ only minimally, as compared to those obtained when performing a volume average-to-point value transformation similar to the one in relation (3.14) which would lead to fourth-order accurate point-values, (ii) for highly shocked problems, high-order accuracy cannot be maintained in the vicinity of strong shocks anyways.

In practice, the differences between the spectra computed from point values or from volume averages present noticeable differences only at relatively high wavenumbers. At the electromotively forced scales ($K \approx 50$), the differences are smaller than 5%, both in the low Mach number cases and in the highly compressible runs.

Furthermore, when Fourier spectra are shown in this dissertation, an implicit normalisation is assumed, so as to refer more easily to physical quantities. Unless specified

otherwise, the velocity power spectra $E^V = \mathcal{P}(\mathbf{v})$ are always normalised by the squared isothermal sound speed c_s^2 so that, in fact, $E_K^V = \sum_{K \leq |\mathbf{k}|/\kappa < K+1} \frac{1}{2} \left(\frac{|\hat{\mathbf{v}}_{\mathbf{k}}|}{c_s} \right)^2$. However, this expression is noted $\mathcal{P}(\mathbf{v})$ and not $\mathcal{P}(\mathbf{v}/c_s)$ for the sake of simplicity. Similarly, power spectra of quantities involving the density, such as $\mathbf{u} = \rho^{1/3}\mathbf{v}$ or $\mathbf{w} = \rho^{1/2}\mathbf{v}$ are normalised in addition to c_s^2 by the mean density ρ_0 with an appropriate exponent ($\rho_0^{2/3}$ and ρ_0 respectively, even though this makes no difference for the mean density $\rho_0 = 1$ considered in this work). The same happens for the magnetic energy spectra: \mathbf{b} has the same dimension as \mathbf{w} , so that a normalisation by $\rho_0 c_s^2$ takes place both for $E^M = \mathcal{P}(\mathbf{b})$ and for the magnetic helicity spectra. The other Fourier spectra are normalised through the same logic.

As for the shell-to-shell helically-decomposed magnetic helicity transfer functions (see section 2.4.4), they are computed through the following algorithm:

1. Project the Fourier transformed magnetic and velocity fields on the helical eigenvectors (see section 2.3), obtaining hence (in Fourier space) $(\hat{\mathbf{b}}^P, \hat{\mathbf{b}}^N)$ the positive and negative helical parts of the magnetic field and $(\hat{\mathbf{v}}^P, \hat{\mathbf{v}}^N, \hat{\mathbf{v}}^C)$, for both helical parts and the compressive part of the velocity field.
2. For each considered (P_0, Q_0) shells:
 - (a) Transform each helical part (including the compressive part) of the velocity field, filtered by keeping only the P_0 shell and each helical part of the magnetic field, filtered at shell Q_0 , to configuration space. Thus, the fields $\mathbf{v}_{P_0}^{sP}$ and $\mathbf{b}_{Q_0}^{sQ}$ with $s_P \in \{P, C, N\}$ and $s_Q \in \{P, N\}$ are obtained.
 - (b) Compute the six cross products $\mathbf{v}_{P_0}^{sP} \times \mathbf{b}_{Q_0}^{sQ}$ and transform them to Fourier space.
 - (c) Project these Fourier-transformed cross products on $\hat{\mathbf{b}}^P$ and $\hat{\mathbf{b}}^N$. This gives the values of the twelve helical contributions of $\mathcal{T}^{\mathcal{H}^M}$ for $1 \leq K \leq K_{max}$, $P = P_0$ and $Q = Q_0$ with $K_{max} = N/2$ the largest resolved wavenumber shell.

The other transfer functions (for example, those involving magnetic \leftrightarrow kinetic energy exchanges) are computed analogously. Since these computations involve many Fourier transformations, associated with non-negligible computing resources, they are limited to the $(P, Q) \in [1, 64]^2$ shells, which require $64 \times 64 \times 5$ Fourier-to-configuration space transformations and $64 \times 64 \times 6$ configuration-to-Fourier space transformations. This is why the 2D plots of chapter 6 are displayed in the $[1, 64] \times [1, 64]$ domain. They include however the effects of the smallest scales as well (for example, $\mathcal{T}^{\mathcal{H}^M}(Q, K)$ assumes a sum over all P , including $P > 64$). This information is obtained by performing $2 \times 64 \times (5+6) + 1 \times (5+6)$ additional transformations: (i) $64 \times (5+6)$ when filtering over all the shells $P \in [65, K_{max}]$ at once, iterating over $Q \in [1, 64]$, (ii) $64 \times (5+6)$ transformations when filtering over all the shells $Q \in [65, K_{max}]$ at once, iterating over $P \in [1, 64]$ and (iii) lastly, $5+6$ transformations when filtering over all shells $(P, Q) \in [65, K_{max}]^2$ at once.

3.5 Summary: performed runs

3.5.1 Main runs

The inverse transfer of magnetic helicity is mainly studied by injecting magnetic helical fluctuations at small scales, starting with a hydrodynamic turbulent steady-state at resolution 512^3 with varying compressibility. The computational domain is a cube

$[0, L] \times [0, L] \times [0, L]$ with $L = 1$, with triply periodic boundary conditions and the isothermal sound speed is fixed to $c_s = 0.1$. The mean density in the system is $\rho_0 = 1$.

The use of higher-order numerics allows to achieve good quality results already at the 512^3 resolution, as compared to the quality obtained with lower-order schemes (appendix B). The main results obtained in this work are furthermore confirmed through selected higher 1024^3 runs (section 7.2), hinting at a good convergence of the observed spectral scalings with respect to the numerical resolution.

As described in section 3.3.1, the hydrodynamic driving field inserts a defined amount of kinetic energy per unit time ϵ_{inj}^K in the system at large scales ($1 \leq K \leq 2$). In fully developed turbulence, this energy cascades down to the smallest scales where numerical viscosity dominates, leading to a statistical steady-state with a constant time-averaged root mean square (RMS) Mach number \mathcal{M} . Not only the RMS Mach number but also the spectral weight ζ of the mechanical forcing is of importance for the compressible turbulent statistics [45]. Runs with RMS Mach numbers varying between about 0.1 and 11 are investigated. Regarding the spectral weight, only both extremes $\zeta = 1$ and $\zeta = 0$ corresponding respectively to purely solenoidally-driven and purely compressively-driven turbulence are considered. The results of reference [45], which compares isothermal hydrodynamic numerical simulations using either a purely solenoidal or a purely compressive forcing with observational data from the interstellar medium, indicate that these two extreme cases are improbable in nature. These extreme cases are nevertheless considered here so as to assess in the first place the presence of compressibility effects on the nonlinear inverse transfer dynamics. More realistic settings, including mixtures of compressible modes or other forcing mechanisms, are possibilities for future work.

The technical details about the generation of the initial 512^3 hydrodynamic steady-state frames from a fluid with mean density $\rho_0 = 1$, initially at rest, including how a desired \mathcal{M} is obtained and how this steady-state RMS Mach number is measured are explained in appendix A.1.

Assuming a power-law velocity scaling, an estimate for the sonic wavenumber K_s (see relation (2.30)) as a function of \mathcal{M} can be derived, which gives when assuming a Burgers $E^V \sim K^{-2}$ scaling [43]:

$$K_s \approx K_{inj} \mathcal{M}^2, \quad (3.28)$$

with K_{inj} the scale at which kinetic energy is injected. For the main runs, the magnetic helicity injection takes place around $K \approx 50$. This is why runs at $\mathcal{M} \approx 5$ and $\mathcal{M} \approx 7$ are considered. Indeed, the estimate in relation (3.28) leads to a sonic wavenumber between 25 and 50 for $\mathcal{M} \approx 5$ and above 49 for $\mathcal{M} \approx 7$. At $\mathcal{M} \approx 7$, one would hence expect that all scales in the inverse transfer region are in the supersonic regime and at $\mathcal{M} \approx 5$ that a transition from subsonic to supersonic could be visible. These are the (s)olenoidally-driven runs labelled M5s and M7s which present a steady-state RMS Mach number of 5.06 and 7.03 respectively. Using the same parameters for the kinetic energy injection rate but a purely (c)ompressive forcing gives the runs labelled M5c and M8c with $\mathcal{M} \approx 5.05$ and $\mathcal{M} \approx 7.87$ respectively.

In order to allow some comparison points with the incompressible case, a subsonic and a transonic solenoidally-driven run M01s and M1s are considered, with $\mathcal{M} \approx 0.116$ and $\mathcal{M} \approx 1.09$ respectively. A purely compressively-driven run M1c with the same kinetic energy injection rate as the M1s run, which presents $\mathcal{M} \approx 0.797$ is also considered as a comparison point for turbulence with high $\nabla \cdot \mathbf{v}$ components with relatively low velocities.

As shown in section 4.2.1 however, the power-law scaling found for the magnetic helicity spectra present relatively little change for the solenoidally-driven M5s and M7s runs as

compared to the incompressible case. Therefore, an additional solenoidally-driven run, M11s with $\mathcal{M} \approx 11.1$ is considered. On the contrary, the M5c run already exhibits clear departures from the incompressible exponent. This is the reason why an additional compressively-driven M3c run with $\mathcal{M} \approx 2.80$ is considered as well.

The parameters for the main solenoidally-driven runs M01s, M1s, M5s, M7s and M11s, as well as the main compressively-driven runs M1c, M3c, M5c, M8c are summarised in the appendix, table A.1.

Starting with the hydrodynamic steady-state, magnetic energy is injected at a constant rate ϵ_{inj}^M through an electromotive forcing at the scales $48 \leq K \leq 52$. Two relevant quantities here are the ratio of energy injections $R_{inj} = \epsilon_{inj}^M / \epsilon_{inj}^K$ as well as the helicity fraction h_f of the injected fluctuations. In the main runs, the fluctuations are fully positive helical ($h_f = +1$). This choice, not physically motivated, is made for the sake of simplicity, so that magnetic helicity of one sign dominates the system at all scales. As for the energy injection ratio, it is $R_{inj} = 1$ for all the runs but M1s and M01s. For M1s, $R_{inj} = 2$ and $R_{inj} = 4$ for M01s. These choices of h_f and R_{inj} are made so that clear scaling exponents are observed fast enough in the Fourier spectra: section 7.1 addresses the influence of R_{inj} and h_f in more detail.

Furthermore, for simplicity reasons, even though the RMS Mach number experiences big changes for some of the runs when the electromotive forcing is set on, as shown in section 4.2.2, the runs maintain their label from the hydrodynamic steady-state, apart for M1s and M01s which are renamed M1s2 and M01s4 as a reminder of the fact that $R_{inj} \neq 1$.

3.5.2 Other runs

In addition to the 512^3 main runs described in the previous subsection, some other runs are performed in order to assess the effects of various parameters. These include:

- Runs at higher (1024^3) and lower (256^3) resolutions, in order to check for numerical convergence of the results. This is particularly relevant since, as shown in chapter 4, the numerical resolution is too low in order to capture the discontinuities well enough. Comparisons between 512^3 and 1024^3 hydrodynamic spectra take place in section 4.1.2, whereas discussions about the robustness of some results with respect to numerical resolution are done in section 7.2.
- Some runs are also performed using a lower-order second-order scheme (section 7.2). This is done in order to check the robustness of the results with respect to the reconstruction method used, since for the highly compressible runs, a relatively high amount of cells is indeed reconstructed at lower-order through the fallback approach (appendix A.3). Even though its applicability to turbulent systems is limited, an analysis of the effects of resolution and used reconstruction method for the classical MHD vortex problem is shown in appendix B.
- Since an energy injection ratio of $R_{inj} > 1$ is used for the M1s2 and M01s4 runs, a parameter study varying R_{inj} and h_f starting with the M1s hydrodynamic steady-state is performed in section 7.1.
- Previous numerical experiments studied the inverse transfer of magnetic helicity by injecting solely magnetic helical fluctuations at small scales [3, 74]. In order to relate to them, a run labelled *Mf* (for “(only) (m)agnetically (f)orced”) is performed, where the mechanical forcing is deactivated and ϵ_{inj}^M is equal to ϵ_{inj}^K of the M1s run.

Chapter 4

Inverse transfer: general aspects

The inverse transfer of magnetic helicity is studied by injecting small scale magnetic helical fluctuations in steady-state hydrodynamic turbulent flows. The protocol of the numerical experiments is described in section 3.5.1.

These steady-state flows are generated through a large scale mechanical driving, which is either purely solenoidal or purely compressive. Section 4.1 presents statistical aspects of the hydrodynamic steady-states, with an emphasis on velocity power spectra and probability distribution functions (PDF) of the logarithm mass density. In that section, comparisons with previous research in compressible isothermal hydrodynamic turbulence are made and some numerical limits are pointed out.

The Fourier spectra shown are normalised as described in section 3.4.

For each turbulent hydrodynamic steady-state, a certain frame is chosen where the electromotive forcing injecting magnetic helical fluctuations is switched on. Section 4.2 presents general aspects of the magnetic helicity inverse transfer. The growth of magnetic structures in highly supersonic turbulence as well as magnetic helicity spectral scaling laws are shown and compared to the incompressible case. Magnetic helicity injection has also important consequences on the velocity field and the density statistics, which are outlined there as well.

In order to relate to previous research, the Mf run, which is only magnetically-driven (see section 3.5.2), is briefly discussed in section 4.3, where the importance and role of the large scale velocity field is assessed.

Finally, section 4.4 gives a summary of this chapter's results.

In the present chapter, only general aspects of the inverse transfer are presented. More results are shown in chapters 5 and 6. Chapter 5 considers scaling laws of several other quantities and proposes an extension of the Alfvénic balance (relation (2.47)) to highly compressible flows. Chapter 6 disentangles the contributions from the different helical components of the velocity field (including its compressive part) to the general inverse transfer picture by using the helical decomposition in the framework of shell-to-shell transfers.

4.1 Initial hydrodynamic steady-state

As described in section 3.3.1, the hydrodynamic driving field inserts a defined amount of kinetic energy per unit time ϵ_{inj}^K in the system at large scales. In fully developed turbulence, this energy cascades down to the smallest scales where numerical viscosity dominates (see section 2.2.1), leading to a statistical steady-state with a constant time-averaged root mean square (RMS) Mach number \mathcal{M} . The computational domain is a cube

$[0, L] \times [0, L] \times [0, L]$ with $L = 1$ and triply periodic boundary conditions. The isothermal sound speed is fixed to $c_s = 0.1$ and the mean mass density is $\rho_0 = 1$.

The parameters for the solenoidally-driven runs up to $\mathcal{M} \approx 11$ and the compressively-driven runs up to $\mathcal{M} \approx 8$ are summarised in the appendix, table A.1. The runs M01s, M1s, M5s, M7s and M11s, labelled with an “s” are (s)olenoidally-driven and present a steady-state RMS Mach number $\mathcal{M} \approx 0.116, 1.09, 5.06, 7.03$ and 11.1 respectively, whereas the M1c, M3c, M5c and M8c runs, (c)ompressively-driven, present a steady-state RMS Mach number $\mathcal{M} \approx 0.797, 2.80, 5.05$ and 7.87 respectively. The technical details about the generation of these frames, including how a desired \mathcal{M} is obtained and how this steady-state RMS Mach number is measured are explained in appendix A.1.

Both extreme types of driving (either purely solenoidal or purely compressive) lead to very different steady-states, both with respect to the velocity spectra and the mass density statistics. Power spectra linked with the velocity field are considered, namely the specific kinetic energy spectrum $\mathcal{P}(\mathbf{v})$ and power spectrum of $\mathbf{u} = \rho^{1/3}\mathbf{v}$, a quantity which is expected to recover the $K^{-5/3}$ Kolmogorov energy spectrum for low $\nabla \cdot \mathbf{v}$ compressible flows (see section 2.2.1). Even though general agreement with the theoretical predictions is found, deviations from the expected theoretical scaling laws are observed which can be attributed to numerical issues. Furthermore, mass density statistics show that compressively-driven turbulence present significantly more very low density regions as compared to solenoidally-driven turbulence at a given RMS Mach number.

4.1.1 Mach number time evolution

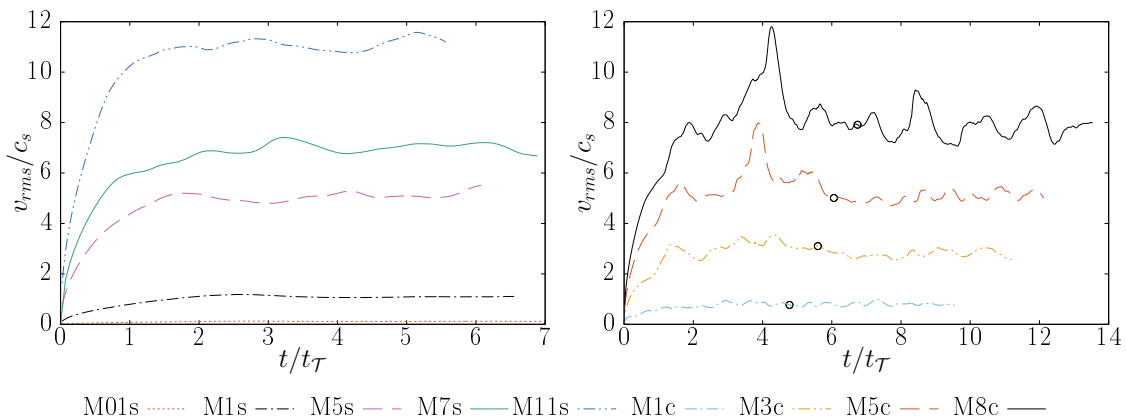


Figure 4.1: Time evolution of the main runs’ RMS Mach number, resolution 256^3 . The black circles for the compressively-driven runs correspond to the instant $6t_{\mathcal{T}}^*$ where the upscaling to resolution 512^3 takes place (see appendix A.1), whereas for the solenoidally-driven runs, the curves end at $6t_{\mathcal{T}}^*$.

Figure 4.1 shows the time evolution of the RMS Mach number v_{rms}/c_s for the main runs at resolution 256^3 , starting from the initial instant when the fluid is at rest. For the solenoidally-driven as well as for the M1c and M3c runs, the convergence to a steady-state is observed after a duration of the order of $2t_{\mathcal{T}}$ with $t_{\mathcal{T}} = L/(2c_s\mathcal{M})$ the turbulent turnover time, consistently with previous research [43]. For the M5c and M8c runs however, the presence of a peak close to $4t_{\mathcal{T}}$ can be noted. This peak is also present in reference [43] even though at a later time and with a smaller amplitude. For this reason, the steady-state RMS Mach number is computed for the solenoidally-driven runs by averaging over a time window starting at $t = 2.5t_{\mathcal{T}}^*$ whereas for the compressively-driven runs the time window starts later, at $t = 6t_{\mathcal{T}}^*$, with $t_{\mathcal{T}}^*$ an estimate of the turbulent turnover time, as described

in appendix A.1. For all the runs, the steady-state is already reached after $6t_{\mathcal{T}}^*$ (marked by circles for the compressively-driven runs in figure 4.1) which is the instant when the 256^3 simulations are upscaled to resolution 512^3 (see appendix A.1). Magnetic helicity fluctuations are injected after letting the system adapt to its new resolution.

4.1.2 Kinetic energy spectra

In this subsection, several Fourier spectra linked with the velocity field are presented and related to previous research mentioned in section 2.2.1. Unless specified otherwise, the Fourier spectra have been obtained by averaging over about 40 spectra done at resolution 512^3 after adaptation to the new resolution. These spectra are equally spaced in time in a range of about $4t_{\mathcal{T}}$ for each run. The hydrodynamic runs have also been upscaled to resolution 1024^3 for comparison purposes. Due to the increased numerical cost of higher-resolution runs, these Fourier spectra are snapshots, done after the steady-state has been reached.

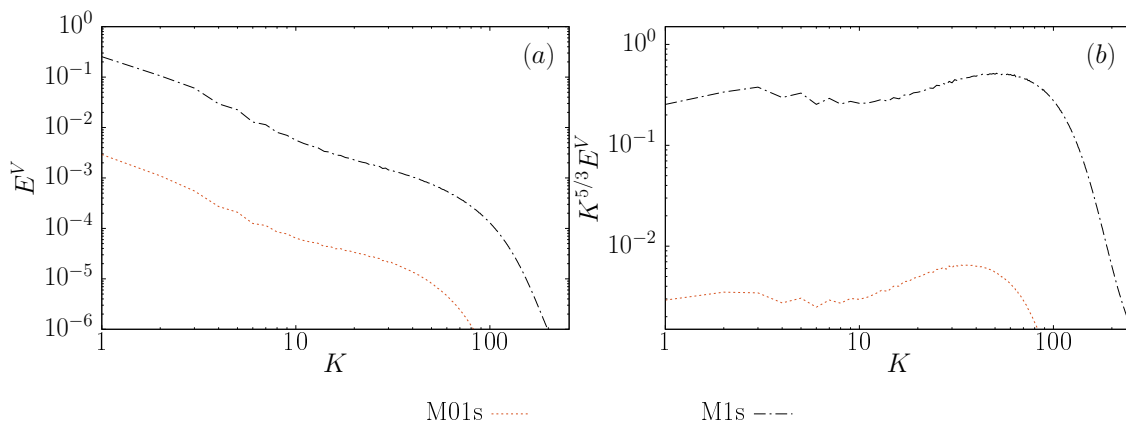


Figure 4.2: Time-averaged steady-state spectra for the M01s and M1s runs at resolution 512^3 . (a) Specific kinetic energy, (b) compensated by $K^{5/3}$.

The steady-state specific kinetic energy spectra $E^V = \mathcal{P}(\mathbf{v})$ for the subsonic and transonic solenoidally-driven runs M01s and M1s, which are expected to follow a $K^{-5/3}$ Kolmogorov scaling are shown in figure 4.2. This scaling is indeed visible in a very limited wavenumber range $4 \lesssim K \lesssim 10$. At large scales, the spectra are influenced by the forcing, whereas at small scales, the well documented “bottleneck effect” [42, 36, 57, 62, 74, 26, 1] comes into play and causes a deviation from this scaling. The bottleneck effect has been widely observed in numerical simulations [36, 62, 74, 1]. Even though not fully understood yet, its origin is considered to rest upon the quenching of nonlinear triadic interactions close to the viscous cut-off, leading to a pile-up of energy before the viscous interval of scales which contaminates the inertial range [42]. The bottleneck phenomenon is more pronounced if the viscous falloff becomes steeper. It is thus often prominent in numerical systems with high-order reconstruction which translates to pronounced hyper-viscous terms of high-order in K . This bottleneck due to the quenching of nonlinear interactions coexists with a numerically generated hump caused by erroneous small-scale fluctuations, which are not smoothed out by the high-order numerics. Thus, the bottleneck effect is often considered as an “unwanted guest” in numerical simulations which hinders the observation of the inertial range, but with whom one has to live.

At higher \mathcal{M} , the specific kinetic energy spectra are expected to display a Burgers scaling: $E_K^V \sim K^{-2}$ (see section 2.2.1). However, figures 4.3.(a-b), which show E^V for the

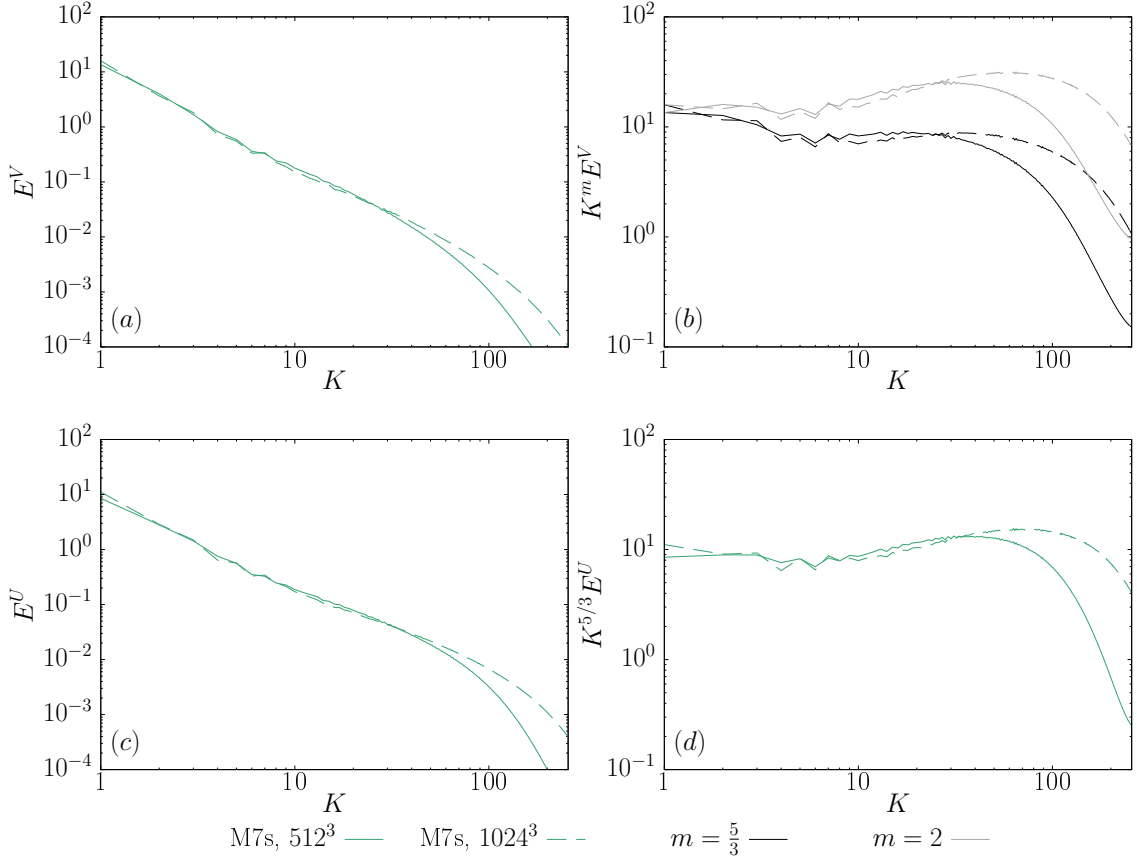


Figure 4.3: Time-averaged steady-state spectra for the M7s run, resolution 512^3 . The 1024^3 spectra are snapshots. (a) Specific kinetic energy. (b) Same spectra as subfigure (a) but compensated by K^m with $m \in \{\frac{5}{3}, 2\}$. (c) Power spectra of $\mathbf{u} = \rho^{1/3}\mathbf{v}$. (d) Same spectra as subfigure (c) but compensated by $K^{5/3}$.

M7s run, seem to indicate that a $K^{-5/3}$ slope would be more appropriate. This can also be attributed to the bottleneck effect. Indeed, reference [62], figure 6, shows E^V spectra for a similar setup (there, $\mathcal{M} \approx 6$ is obtained through a different forcing mechanism albeit at the same large scales), where no clear range with the Burgers scaling is visible at resolution 512^3 . A tiny range of about a decade with a K^{-2} scaling starts to be visible at resolution 1024^3 in that figure. Figure 7 in that paper shows furthermore that in the region contaminated by the bottleneck effect, the E^V spectrum goes as $K^{-1.72}$, which is very close to $K^{-5/3}$. As a matter of fact, the bottleneck effect happened to “trick” researchers when supersonic turbulence seemed to give the same $K^{-5/3}$ scaling as in incompressible turbulence [26]. Figure 4.3.(a-b) (in the present work), shows a similar behaviour: at resolution 1024^3 for the M7s run, the appearance of a range with a K^{-2} scaling for $K \lesssim 10$ is vaguely visible. This suggests that for higher \mathcal{M} , almost all the inertial range is contaminated by the bottleneck effect at resolution 512^3 , or even 1024^3 , and a higher numerical resolution is required in order to observe clearly the proper inertial range scaling.

In the work presented here, obtaining the exact hydrodynamic inertial range scaling is not of capital importance, since the dynamics in the spectral range where the magnetic helicity inverse transfer takes place are expected to be dominated by the aforementioned inverse transfer. However, this issue illustrates very well the need for a validation of the results at higher resolution, as discussed in section 7.2. Furthermore, the exponents found have to be taken with appropriate caution, since the small structures and shocks are clearly

underresolved for high \mathcal{M} .

For the compressively-driven M8c run, the bottleneck effect leads to slightly flatter E^V spectra as compared to the Burgers K^{-2} scaling, even though the hump is less pronounced as compared to the M7s solenoidally-driven run, see figure 4.4.

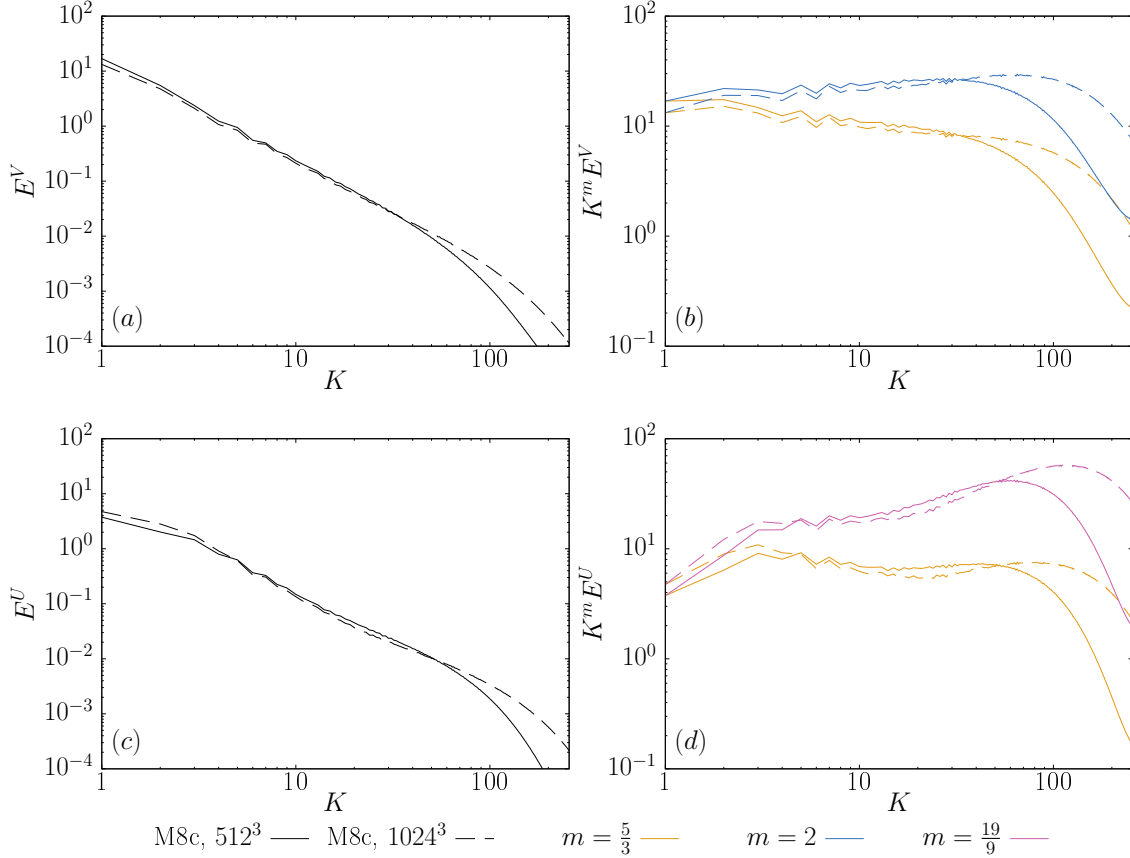


Figure 4.4: Time-averaged steady-state spectra for the M8c run, resolution 512³, the 1024³ spectra are snapshots. (a) Specific kinetic energy. (b) Same spectra as subfigure (a) but compensated by K^m with $m \in \{\frac{5}{3}, 2\}$. (c) Power spectra of $\mathbf{u} = \rho^{1/3}\mathbf{v}$. (d) Same spectra as subfigure (c) but compensated by K^m with $m \in \{\frac{5}{3}, \frac{19}{9}\}$.

Figures 4.3.(c-d) and 4.4.(c-d) display $E^U = \mathcal{P}(\mathbf{u})$, the power spectrum of $\mathbf{u} = \rho^{1/3}\mathbf{v}$, for the M7s and M8c runs. As mentioned in section 2.2.1, $\mathcal{P}(\mathbf{u})$ is expected to recover a $K^{-5/3}$ scaling for highly compressible turbulence with a moderate $\nabla \cdot \mathbf{v}$ component, whereas for a strong $\nabla \cdot \mathbf{v}$ component, some theoretical predictions suggest a $K^{-19/9}$ scaling [62, 45, 43, 49]. Consistently with these theoretical predictions, the 1024³ spectra present a small range with a scaling close to $K^{-5/3}$ for $K \lesssim 10$ for the M7s run and a steeper slope consistent with $K^{-19/9}$ for the M8c one.

Regarding the spectra of the other main runs, which are not shown here: the M5s and M11s spectra look qualitatively similar to the M7s ones. In the same way, the M5c spectra look similar to the M8c ones, whereas the M1c ones are closer to a Kolmogorov $K^{-5/3}$ scaling and the M3c spectra exhibit a scaling intermediate between the M1c and the M5c one.

Furthermore, the power spectra of $\mathbf{w} = \sqrt{\rho}\mathbf{v}$, which are directly related to the kinetic energy in the compressible case, exhibit flatter spectra as compared to $\mathcal{P}(\mathbf{u})$ and $\mathcal{P}(\mathbf{v})$ for the supersonic runs (figures not shown), consistently with previous research [62].

A quantity relevant in order to evaluate the strength of the flow's $\nabla \cdot \mathbf{v}$ component,

is the compressive ratio $\Psi^V = \mathcal{P}^{comp.}(\mathbf{v})/\mathcal{P}(\mathbf{v})$ (see section 2.1.2) which is a measure of the fraction of compressible velocity fluctuations as a function of scale. When for the M1s run, less than about 10% of the energy is in the compressible part of the spectrum at all well-resolved scales, this ratio is roughly 1/3 for the M5s, M7s and M11s runs in a significant region (see figure 4.5.(a)), as observed in previous research [45, 43]. It might be surprising to see that the compressive ratio is lower for the M11s and M7s runs as compared to the M5s run, even though they have a higher RMS Mach number. This is probably due to the lack of numerical resolution, as can be inferred from figure 8 in reference [43] where the compressive ratio is plotted for several resolutions: the compressive ratio tends indeed to grow with the resolution. For the compressively-driven runs (figure 4.5.(b)), the compressive ratio is close to 1 at the forcing scales (but not equal to 1 since solenoidal modes are indirectly produced through shock collisions [43]) and about 1/2 in a reasonable range of wavenumbers for the M5c and M8c runs, as observed in reference [45]. The higher compressive ratio, as compared to the solenoidally-driven runs, implies a more important $\nabla \cdot \mathbf{v}$ component, which have significant influence on the mass density statistics (section 4.1.3).

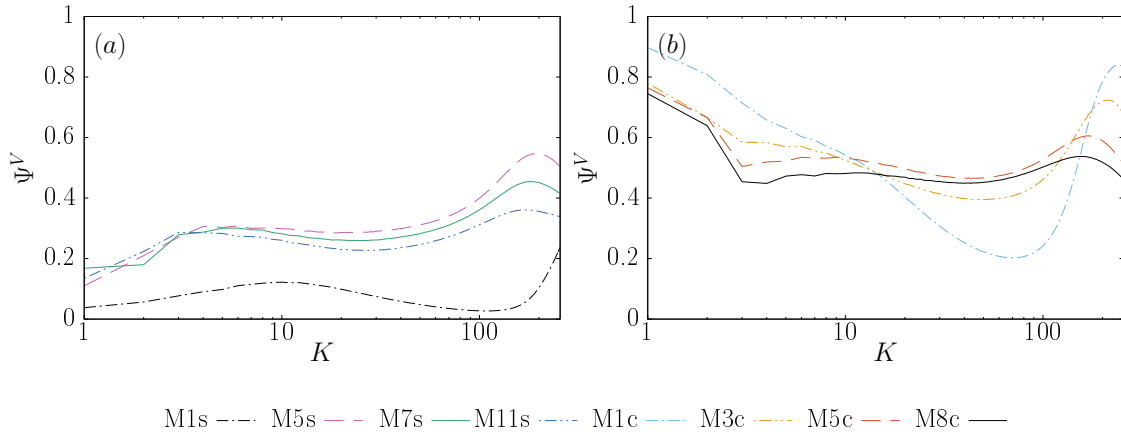


Figure 4.5: Time-averaged steady-state velocity compressive ratio spectra at resolution 512^3 . The M01s run exhibits a ratio very close to zero at all scales (except at the very smallest) and is not shown here.

Lastly, the validity of relation (3.28), which predicts a sonic wavenumber-RMS Mach number dependence $K_s \sim \mathcal{M}^2$ (see section 2.2.1) is checked through figure 4.6. This relation is not well verified when $\mathcal{M} \gtrsim 5$ for the 512^3 runs. At resolution 1024^3 on the other hand, it is quite well followed up to $\mathcal{M} \approx 7$, but not for $\mathcal{M} \gtrsim 8$. This is because, when the resolution is too low, the velocity power spectra drop too rapidly at large wavenumbers, leading to an underestimation of K_s . This is another indication of the fact that the small scale structures are underresolved for most highly supersonic runs at resolution 512^3 .

When injecting magnetic helicity however, magnetic energy is transformed in kinetic energy around the $K = 50$ shell, leading to a way higher sonic wavenumber, as shown in section 4.2.2.

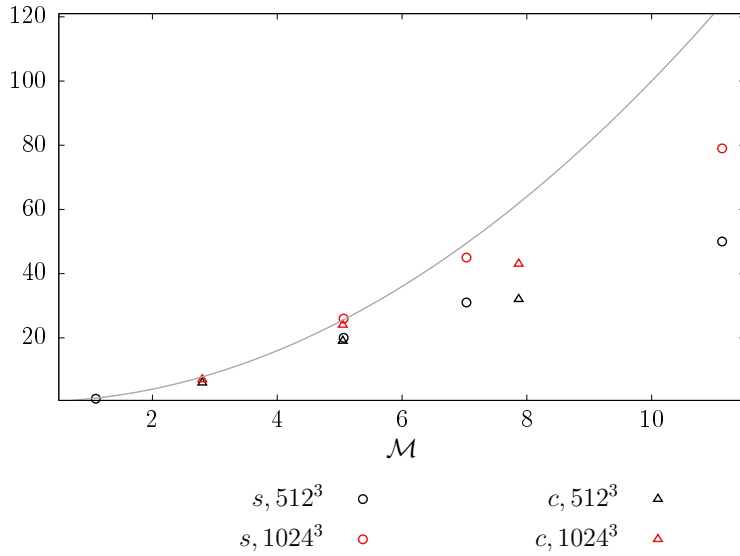


Figure 4.6: Sonic wavenumber shell for the main supersonic solenoidally-driven (s) and compressively-driven (c) runs of this work, hydrodynamic steady-state, at resolution 512^3 (time-averaged) and 1024^3 (snapshots). The gray line is the function $x \rightarrow x^2$.

4.1.3 Mass density statistics

As the mass density is governed by $\partial_t \rho = -\nabla \cdot (\rho \mathbf{v})$, it is particularly sensitive to the compressive part of the velocity field. A purely compressive forcing implies hence a direct effect on the mass density, whereas a purely solenoidal forcing can only induce density variations indirectly. At a given RMS Mach number, the density contrast is hence expected to be greater for compressively-driven runs than for solenoidally-driven ones.

This is shown in figures 4.7 and 4.8 for the transonic and supersonic runs. The compressively-driven runs exhibit more shocks (even at lower \mathcal{M}) and very low density regions as compared to the solenoidally-driven ones (the colour bar spans over six orders of magnitude for the high Mach number compressively-driven runs, but only over three orders of magnitude for the solenoidally-driven ones). For the supersonic runs, regions of high density tend to form filamentary structures, possibly caused by planar intersecting shock waves [88].

In order to quantify the differences in the density ranges, probability distribution functions (PDF) of $s = \log_{10}(\rho/\rho_0)$ are shown at the bottom of figures 4.7 and 4.8 for the solenoidally-and compressively-driven runs respectively. The PDFs are normalised so that the area under the curves is equal to one, which means that when picking any cell in the computational domain, $\int_{s_1}^{s_2} P(s) ds$ is the probability to have s in the interval $[s_1, s_2]$ in that cell. The distributions are wider with increasing \mathcal{M} and the most probable density goes to lower values since the conservation of mass implies that the appearance of high density peaks needs to be compensated by low density regions elsewhere.

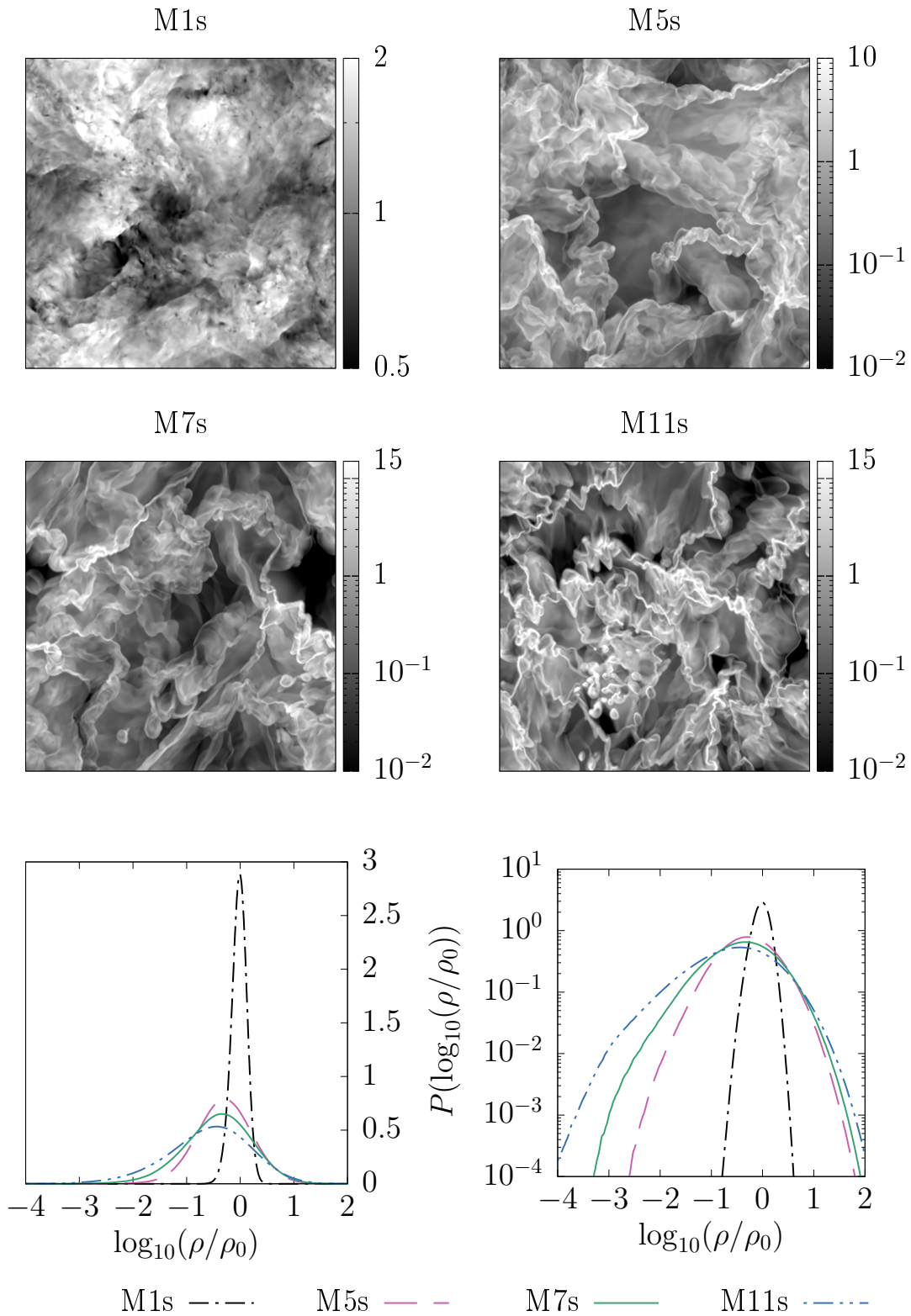


Figure 4.7: Top and middle: slices of the mass density for the M1s, M5s, M7s and M11s runs at steady-state, resolution 512^3 , logarithmic scale. Bottom: time-averaged PDF of $\log_{10}(\rho/\rho_0)$ for the same runs, both in linear (left) and logarithmic scale (right).

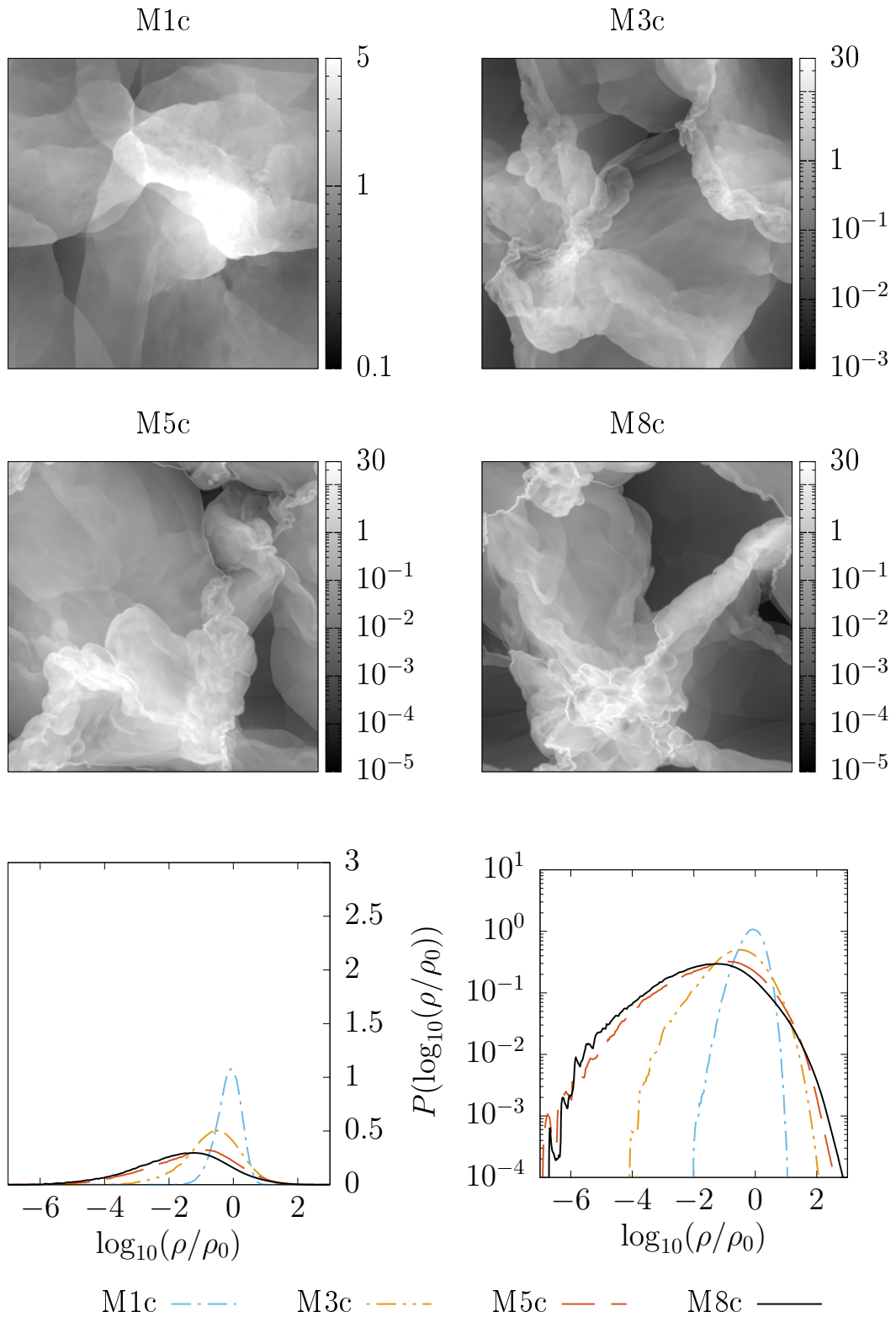


Figure 4.8: Top and middle: slices of the mass density for the M1c, M3c, M5c and M8c runs at steady-state, resolution 512^3 , logarithmic scale. Bottom: time-averaged PDF of $\log_{10}(\rho/\rho_0)$ for the same runs, both in linear (left) and logarithmic scale (right).

A measure of the density spread is given by the standard deviation of s , defined by:

$$\sigma_s = \sqrt{\langle (s - \langle s \rangle)^2 \rangle}, \quad (4.1)$$

with $\langle s \rangle = \frac{1}{N^3} \sum_{i,j,k} \log_{10}(\rho_{i,j,k}/\rho_0)$ its mean. The standard deviations computed for the transonic and supersonic main runs are listed in table 4.1. Another measure of the density spread is the most compact range of logarithmic densities which includes 95 percent and 99 percent of the cells, that is, the $[\rho_{min}, \rho_{max}]$ interval with smallest $s_{max} - s_{min} = \log_{10}(\rho_{max}/\rho_0) - \log_{10}(\rho_{min}/\rho_0)$ such that:

$$\int_{s_{min}}^{s_{max}} P(s) ds = \chi, \quad (4.2)$$

with $\chi \in \{0.95, 0.99\}$. The computed values are also displayed in table 4.1.

Table 4.1: Density spread for the main transonic and supersonic runs, measured by time averaging of at least 40 frames equally-spaced in time over an interval of roughly $4t_\tau$. The error estimates for the $\log_{10}(\rho/\rho_0)$ standard deviation correspond to the $1 - \sigma$ error of the snapshot-to-snapshot variations, which means that the expressed range contains the standard deviation of at least 68% of the considered frames.

Run	$\log_{10}(\rho/\rho_0)$ standard deviation	$[\rho_{min}, \rho_{max}], \chi = 0.95$	$[\rho_{min}, \rho_{max}], \chi = 0.99$
M1s	0.144 \pm 0.005	[0.489, 1.77]	[0.385, 2.19]
M5s	0.515 \pm 0.022	$[5.03 \times 10^{-2}, 5.21]$	$[2.11 \times 10^{-2}, 10.7]$
M7s	0.634 \pm 0.043	$[2.11 \times 10^{-2}, 6.42]$	$[6.38 \times 10^{-3}, 14.0]$
M11s	0.782 \pm 0.042	$[6.77 \times 10^{-3}, 7.92]$	$[1.56 \times 10^{-3}, 17.8]$
M1c	0.382 \pm 0.039	[0.123, 3.64]	$[6.02 \times 10^{-2}, 5.21]$
M3c	0.836 \pm 0.14	$[4.19 \times 10^{-3}, 8.66]$	$[9.11 \times 10^{-4}, 18.3]$
M5c	1.33 \pm 0.27	$[9.10 \times 10^{-5}, 11.3]$	$[9.07 \times 10^{-6}, 37.5]$
M8c	1.38 \pm 0.19	$[3.40 \times 10^{-5}, 9.19]$	$[4.04 \times 10^{-6}, 36.4]$

The standard deviations obtained for the M5s and M5c runs are comparable to those of reference [45], table 2. In that work, the natural logarithm is considered, so that a standard deviation of 1.35 and 3.15 for $\ln(\rho/\rho_0)$ for the solenoidally-driven run and compressively-driven one respectively, at resolution 512^3 with $\mathcal{M} \approx 5.5$ in reference [45] corresponds to standard deviations of 0.586 and 1.37 for $\log_{10}(\rho/\rho_0)$ respectively, which are quite close to those given in table 4.1, even though slightly higher, since their RMS Mach number is slightly higher as well.

The logarithm density PDF's snapshot-to-snapshot variations are very important when using a compressive driving, as compared to the solenoidally-driven turbulent systems. This is shown through the so-called " $1 - \sigma$ " temporal fluctuations of the $\log_{10}(\rho/\rho_0)$ standard deviation (error indicators in table 4.1), which corresponds to the range containing the standard deviation of at least 68% of the considered logarithm mass density snapshots. The $1 - \sigma$ temporal fluctuations observed for the M5s run are comparable to the ones observed in the solenoidal run of reference [45] with a similar Mach number. For the M5c run however, they are significantly higher (even greater than for the M8c run), probably because of an extreme large-scale event in the flow dynamics. Its impact on the power-law scalings does not seem to be problematic however, as shown through the spectra in this chapter and in chapter 5.

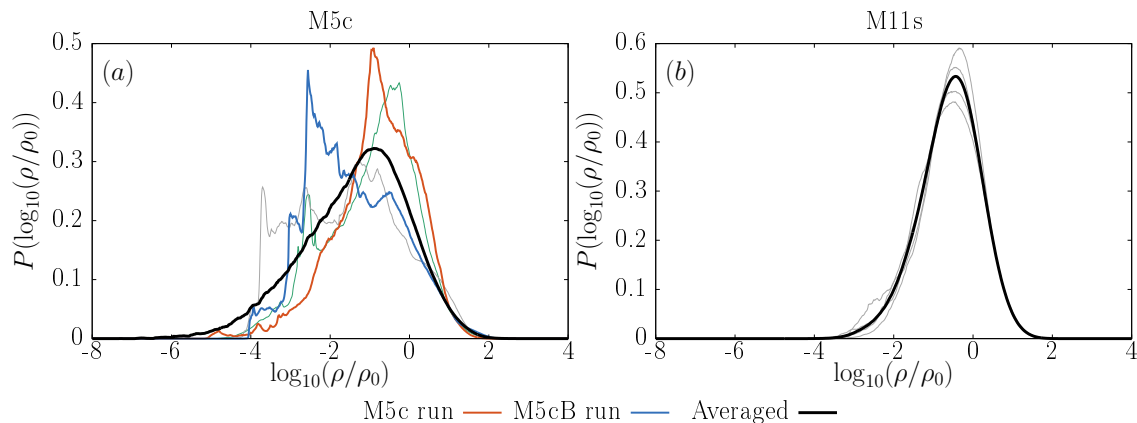


Figure 4.9: Density PDFs for (a) the M5c and (b) the M11s runs. The thickest black lines are the time-averaged PDFs which can also be seen on figures 4.7 and 4.8. The other curves correspond to snapshots. Among these snapshots, the thicker red and blue PDFs for the M5c run correspond to frames which are taken as initial conditions for the magnetic helicity injection (the MHD M5c run starting with the hydrodynamic frame corresponding to the red PDF is labelled “M5c”, whereas the one corresponding to the blue PDF is labelled “M5cB”).

The strong variability of the logarithm density PDF is illustrated through figure 4.9, which shows different snapshots for the M5c and M11s runs. The logarithm density PDF is more irregular and changes considerably between snapshots for the M5c run, whereas the shape remains relatively close to the averaged one for the M11s one, even though it has a two times higher RMS Mach number. As a consequence of this variability for the compressively-driven runs, the particular choice of the initial hydrodynamic frame to which magnetic helicity is injected leads to significant differences in some aspects of its inverse transfer, see section 4.2.1.

Striking differences between the compressively- and solenoidally-driven runs are also visible when considering the averaged column density:

$$\rho_{j,k}^{LS} = \frac{1}{N_x} \sum_i \rho_{i,j,k}, \quad (4.3)$$

with (i, j, k) the index of the cells and N_x the linear resolution in the \mathbf{x} -direction (512 in this case). This quantity corresponds to an integration along a line of sight and is as such closer to what an observer could see in nature. The fact that compressively-driven turbulence exhibits higher density contrasts and more low density regions, as compared to the solenoidally-driven runs is illustrated in figure 4.10 (see as well the projections in references [45, 43]).

When helical magnetic fluctuations are injected in these hydrodynamic turbulent frames, the mass density statistics are significantly affected. This is shown in section 4.2.2.

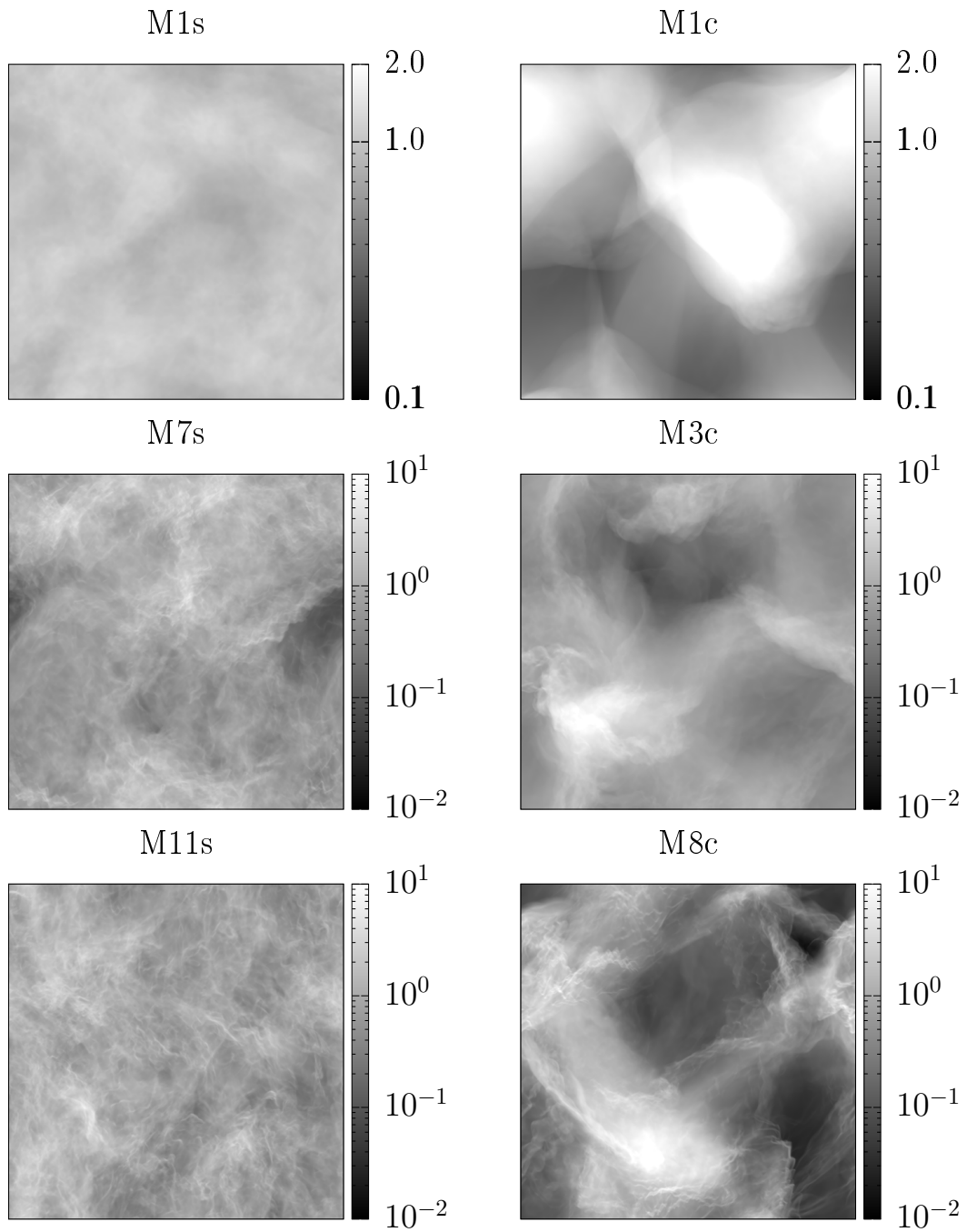


Figure 4.10: Averaged column density for several solenoidally- and compressively-driven runs. The scales are the same between the left and right subfigures for easier comparison.

4.1.4 Conclusion

Consistently with previous research [45, 43], for all the main runs, a steady-state is reached after a duration of several $t_{\mathcal{T}}$. The specific kinetic energy spectrum and the power spectrum of $\mathbf{u} = \rho^{1/3}\mathbf{v}$ are consistent with previous research as well, even though they hint at underresolved numerical simulations and present significant bottleneck contamination. Although the dynamics in the magnetic helicity inverse transfer range are expected to be dominated by the aforementioned inverse transfer, these issues mean that the measured exponents are to be taken with appropriate caution. Section 7.2 discusses this issue in more detail.

The forcing type (purely solenoidal or purely compressive) has a very important impact on both the velocity spectra compressive ratio and the mass density statistics. A purely compressive driving leads to more shocks, greater density contrasts and a more important steady-state snapshot-to-snapshot variation in the logarithmic density PDFs as compared to purely solenoidal driving.

Comparisons between compressible isothermal simulations and observations of the interstellar medium (in the Perseus molecular cloud) indicate that in nature, the extreme cases of a purely solenoidal or a purely compressive driving are both very unlikely [45]. In the interstellar medium, turbulence is thought to be driven by rotating motions on the largest scales, self-gravity at intermediate scales and stellar feedback at intermediate to small scales ([37], section 5.5). As examples of driving mechanisms in nature, one can cite, among many others, shear and the magneto-rotational instability, which are mostly solenoidal drivers and gravity and supernovae which result mostly in a compressive driving. Stellar winds are also drivers which entail both compressive and solenoidal aspects.

4.2 Magnetic helicity injection

This section aims at giving a general description of the occurring inverse transfer of magnetic helicity, when magnetic helical fluctuations are injected into the hydrodynamic steady-state, as described in section 3.5.1. As such, only few Fourier spectra are shown. A more detailed analysis of the observed scaling law behaviours is done in chapter 5.

Magnetic helicity is injected by switching on the electromotive forcing at a particular instant in time during the hydrodynamic steady-state. The fully helical fluctuations are injected around the shell $K \approx 50$ and are normalised in order to provide a constant magnetic energy injection rate ϵ_{inj}^M . For all the runs considered above but the M01s and M1s ones, the magnetic-to-kinetic energy injection ratio $R_{inj} = \epsilon_{inj}^M / \epsilon_{inj}^K$ is set to unity. However, for the M01s and the M1s runs, $R_{inj} = 4$ and $R_{inj} = 2$ respectively, so that convergence to a power-law behaviour is observed faster (see section 3.5.1). As a consequence, all the runs keep their hydrodynamic label, apart the M1s and M01s runs which are relabelled “M1s2” and “M01s4” as a reminder of the use of $R_{inj} \neq 1$.

Furthermore, since snapshot-to-snapshot logarithmic density PDF variations are very important for compressively-driven runs, two different starting frames are considered for the M5c run. The run labelled in the following “M5c” corresponds to the frame with the PDF given by the red curve of figure 4.9, whereas the run labelled “M5cB” corresponds to the blue curve, which peaks at lower mass densities.

In the following, the growth of magnetic structures is assessed, as well as the influence of the inverse transfer on the velocity field and the density statistics.

As shown in section 4.2.2, the RMS Mach number experiences big changes as compared to the hydrodynamic case for highly compressible flows. Nevertheless, the turbulent

turnover time t_τ still refers to the one obtained in the *hydrodynamic steady state*, even after magnetic helicity injection is switched on. The time origin $t = 0$ is reset and corresponds to the instant when the electromotive forcing starts.

4.2.1 Emergence of magnetic structure

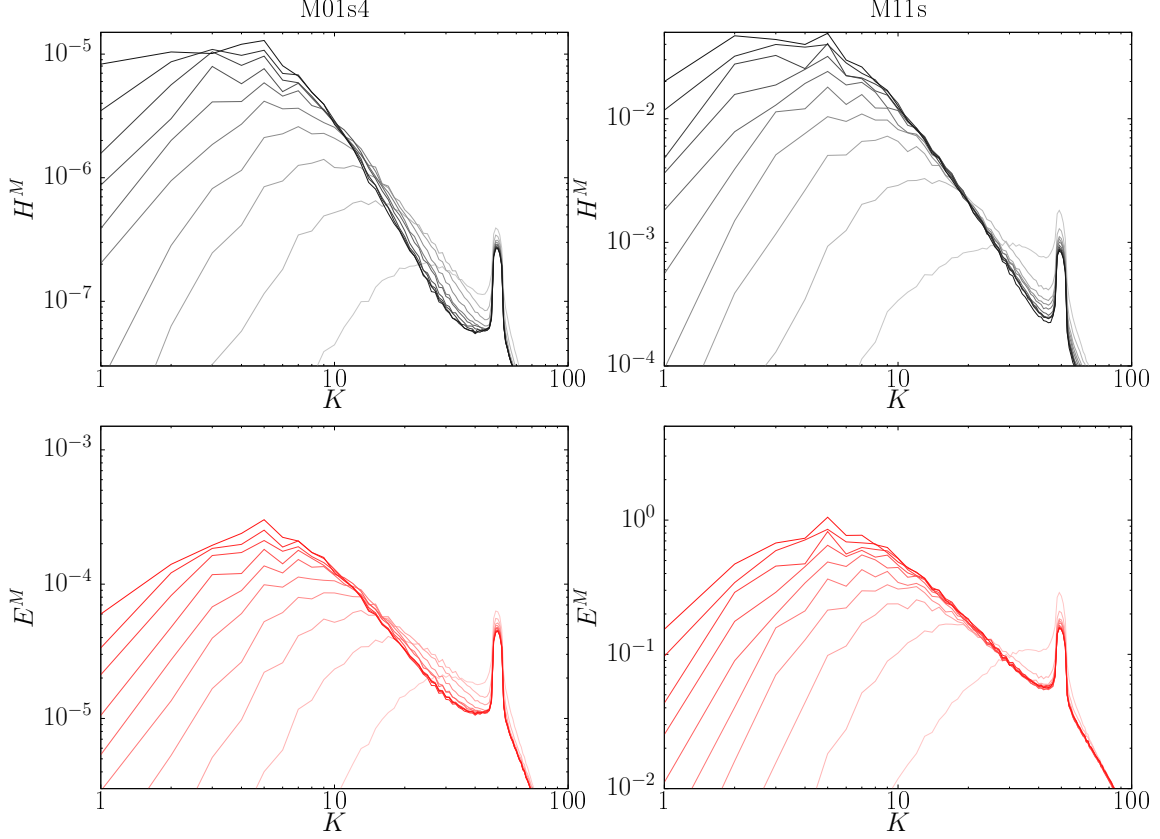


Figure 4.11: Inverse transfer of magnetic helicity for the M01s4 and M11s runs, resolution 512^3 : 10 magnetic helicity (black) and magnetic energy (red) spectra equally spaced in time are shown, from $t = t_f/10$ until $t_f = 3.5t_\tau$ and $t_f = 2.2t_\tau$ for the M01s and M11s runs respectively. The darker the curve, the further in time it is.

According to expectation (see section 2.2.3), the injected magnetic helicity exhibits an inverse transfer towards larger scales. This is shown in figure 4.11 for the M01s4 and M11s runs, which are the two extreme solenoidally-driven cases. This inverse transfer of magnetic helicity also implies an inverse transfer of magnetic energy according to the realisability condition, also visible on that figure.

The inverse transfer occurs faster with increasing \mathcal{M} . Indeed, for lower densities, the Lorentz force $(\nabla \times \mathbf{b}) \times \mathbf{b} = -\nabla(\frac{1}{2}|\mathbf{b}|^2) + \nabla \cdot (\mathbf{b}\mathbf{b}^T)$ has a greater impact on the velocity field, since $\partial_t \mathbf{v} = \dots + \frac{1}{\rho}(\nabla \times \mathbf{b}) \times \mathbf{b}$, which backreacts on the magnetic field evolution. This is shown through figure 4.12.(a), which displays the magnetic helicity integral scale $\mathcal{I}_{\mathcal{H}^M}$ as a function of time for the five M01s4, M1s2, M5s, M7s and M11s runs. The integral scale corresponds to the scale around which most of the magnetic helicity is present and is defined by:

$$\mathcal{I}_{\mathcal{H}^M} = L \frac{\int_K K^{-1} H^M dK}{\int_K H^M dK}. \quad (4.4)$$

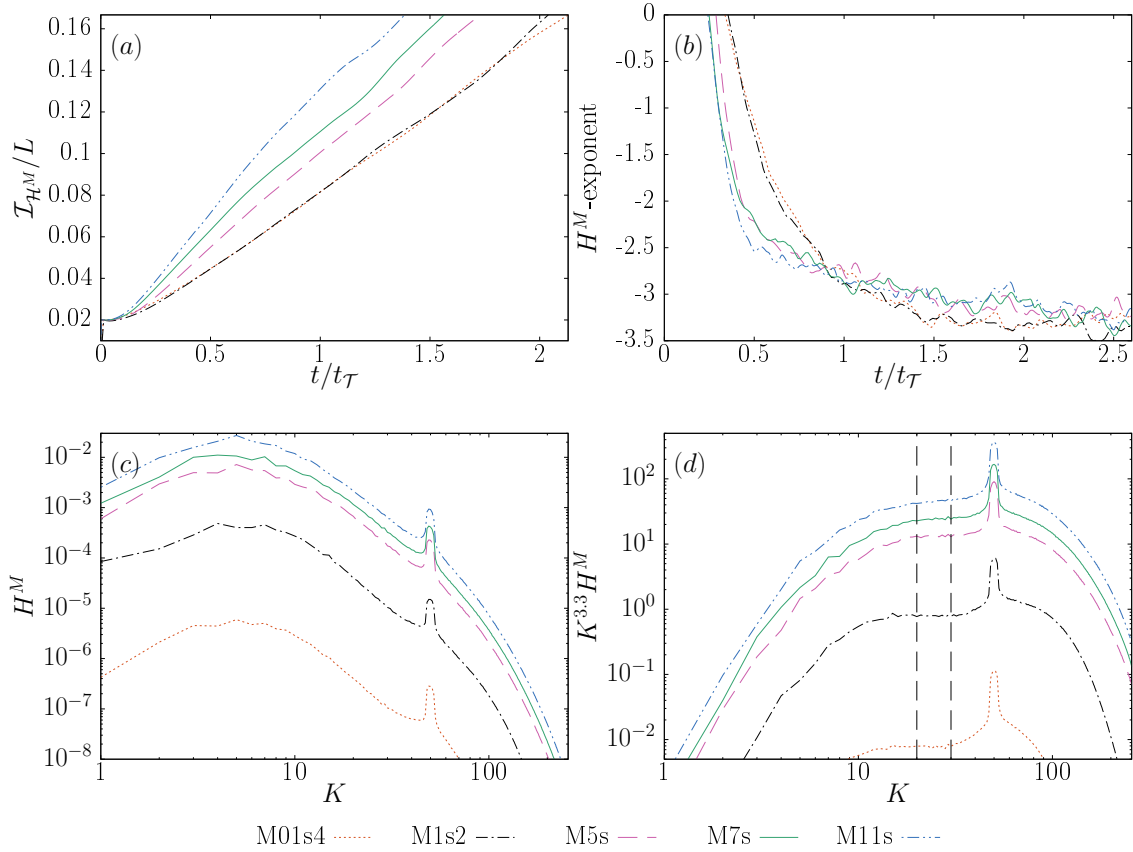


Figure 4.12: Data from magnetic helicity spectra for the main solenoidally-driven runs, at resolution 512^3 . (a) Magnetic helicity integral as a function of time. (b) Magnetic helicity exponent in the region $20 \leq K \leq 30$ computed through a LSF. (c) Magnetic helicity spectra at the instants t such that the integral scale $\mathcal{I}_{HM} = \frac{1}{6}L$. These instants are 2.13, 2.04, 1.73, 1.56 and 1.38 (in units of their respective t_τ) for the M01s4, M1s2, M5s, M7s and M11s runs respectively. (d) Same spectra as (c), compensated by $K^{3.3}$. The two vertical lines delimit the region where the LSF takes place.

In order to compare the spectra of the different runs with each other, a different instant is chosen for each run, namely the respective one when $\mathcal{I}_{HM} = \frac{1}{6}L$. This choice is motivated by the required spectral distance both from the forcing and the largest scales, so as to limit pollution of the scaling range from the electromotive driving and boundary effects. Since the box size is limited, large-scale condensation is indeed expected to occur at later times. A large-scale damping is not implemented in the present work, contrary to reference [74], both because of numerical simplicity and in order to avoid large-scale pollution of the scaling range, the inverse transfer range in the present work being already relatively small.

The magnetic helicity spectra for the solenoidally-driven runs look all very similar, exhibiting a power-law behaviour $H_K^M \sim K^m$ with $m \approx -3.32, -3.32, -3.23, -3.11$ and -3.03 obtained from a least squares fit (LSF) in the region $20 \leq K \leq 30$ for the M01s4, M1s2, M5s, M7s and M11s runs respectively (figure 4.12.(c)). This exponent, close to -3.3 for the M01s4 and M1s2 runs, has also been found in a similar numerical setup in the incompressible case [74, 82] (see section 2.2.3). Even though the spectra are flatter for the hypersonic runs, the deviations from the incompressible spectral index are not that important, considering the fact that the mass density spreads over three to four orders of magnitude in the M7s and M11s runs (see table 4.1).

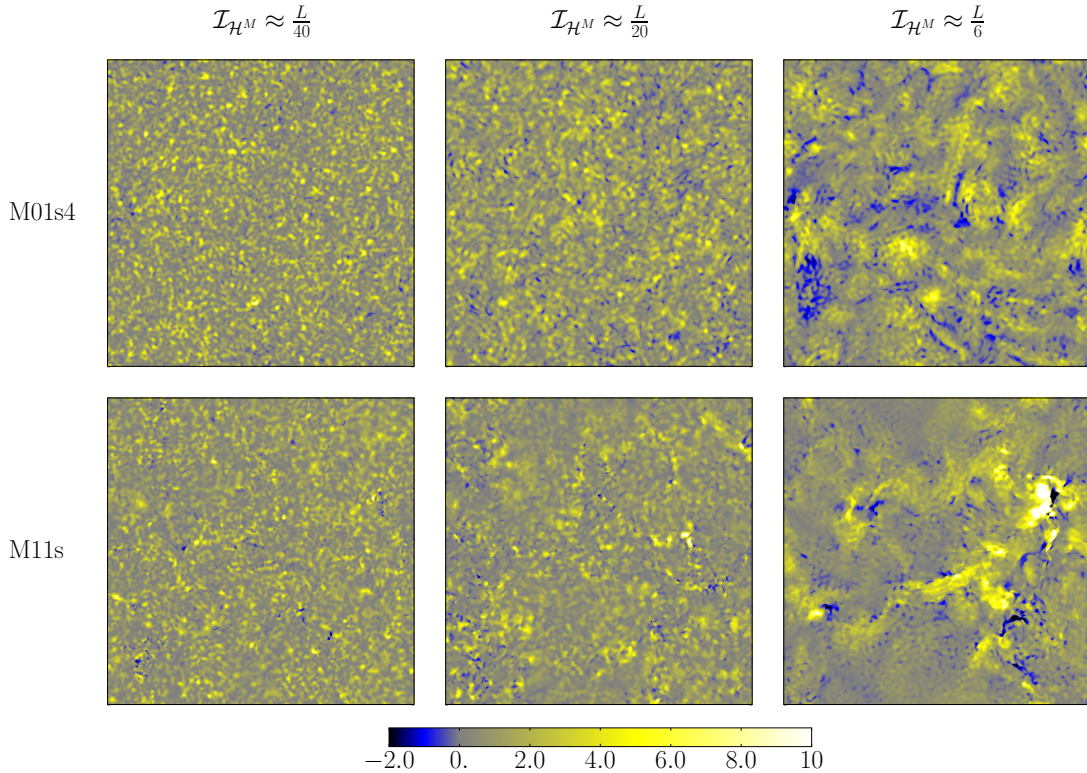


Figure 4.13: Time evolution of magnetic helicity density slices for the M01s4 and M11s runs, normalised by the mean magnetic helicity density in the system. The instants are chosen so that $\mathcal{I}_{\mathcal{H}^M} \approx \frac{L}{40}$, $\mathcal{I}_{\mathcal{H}^M} \approx \frac{L}{20}$ and $\mathcal{I}_{\mathcal{H}^M} \approx \frac{L}{6}$ (from left to right).

Nevertheless, despite the similar slopes in Fourier space for the solenoidally-driven runs, compression effects on the magnetic structures are clearly visible in configuration space (figure 4.13). This figure shows the magnetic structures' growth through the time evolution of magnetic helicity density slices, where the magnetic helicity density $\mathbf{a} \cdot \mathbf{b}$ (the Coulomb gauge $\nabla \cdot \mathbf{a}$ is used) is normalised by its mean in the whole system. Magnetic vortex-like structures are evenly distributed for the M01s4 run, whereas for the M11s run, the structures are distributed inhomogeneously, due to the presence of shock waves. The fact that there are regions with negative magnetic helicity is normal: even though the contribution of each shell in Fourier space to the magnetic helicity in the system is positive, it does not mean that it has to be positive everywhere in configuration space.

Regarding the compressively-driven runs, the time evolution of the magnetic energy and helicity spectra are shown in figure 4.14 for the two extreme M1c and M8c runs. The spectra are way flatter for the most compressive M8c run as compared to the M1c and the solenoidally-driven runs, especially at early times. It is only after the magnetic helicity has been transferred in a short time of about $0.3t\tau$ to scales about 10 times larger than the forcing scale that the slope increases significantly, while remaining considerably flatter than for the least compressible runs. For the supersonic M3c, M5c and M8c runs, the magnetic helicity spectra scale as $H^M \sim K^m$ with $m \approx -3.17, -2.64, -2.16, -2.33$ for the M1c, M3c, M5c and M8c runs respectively, this exponent being measured through a LSF in the region $15 \leq K \leq 25$ at an instant when $\mathcal{I}_{\mathcal{H}^M} \approx \frac{1}{6}L$. This is considerably flatter, as compared to the exponents found for the solenoidally-driven runs. These exponents remain flatter at later times as well.

The precise numerical values of these exponents, measured from a single realisation,

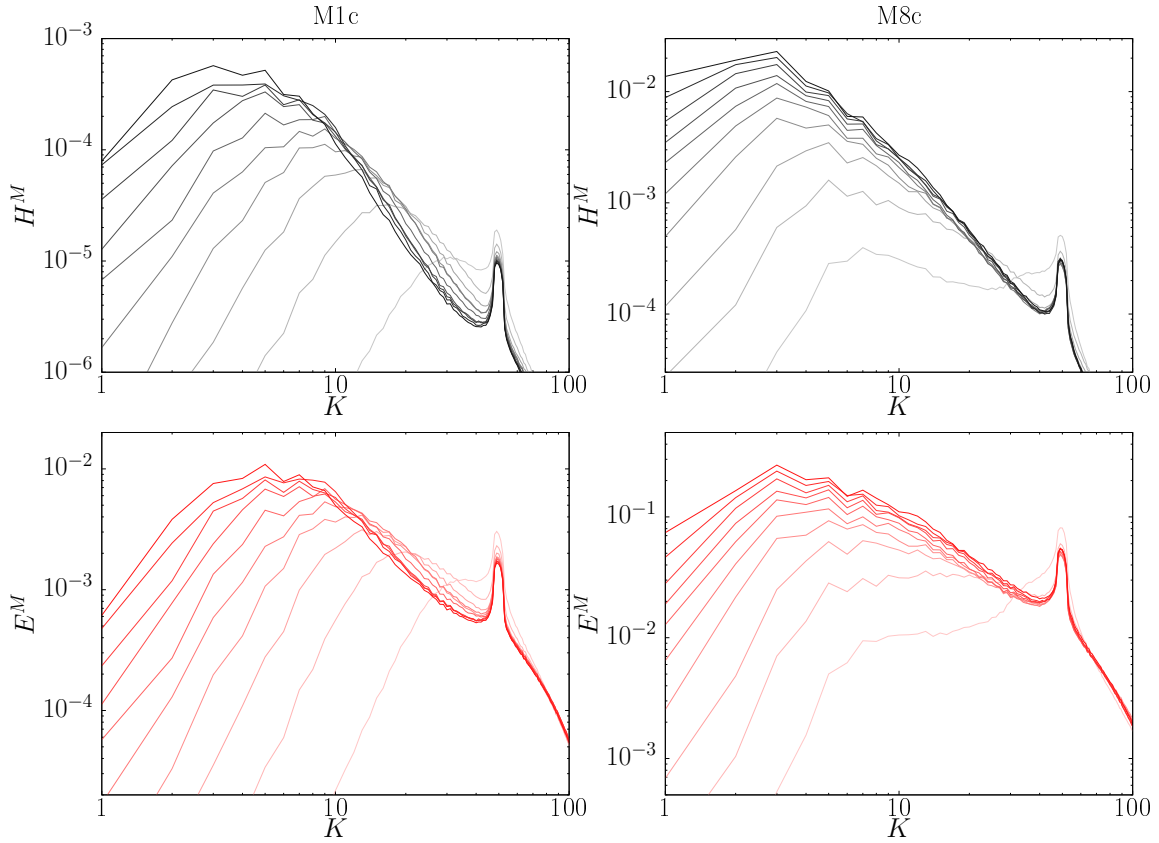


Figure 4.14: Inverse transfer of magnetic helicity for the M1c and M8c runs, resolution 512^3 : 10 magnetic helicity (black) and magnetic energy (red) spectra equally spaced in time are shown, from $t = t_f/10$ until $t_f = 2.4t_\tau$ and $t_f = 1.6t_\tau$ for the M1c and M8c runs respectively. The darker the curve, the further in time it is.

is however not very significant for highly supersonic compressively-driven flows. For the M5cB run, where the initial conditions present more regions of very low density (blue curve in figure 4.9), the spectral index measured in the same region is considerably flatter than for the M5c (and even for the M8c) run, namely $m \approx -1.49$.

A comparison of figures 4.12.(a) and 4.15.(a) shows that magnetic structures are formed faster for the compressively-driven runs: when more than $1.2 t_\tau$ is needed to reach $\mathcal{I}_{\mathcal{H}^M} \approx \frac{1}{6}L$ for the solenoidally-driven runs up to $\mathcal{M} \approx 11$, this integral scale is already reached before one turbulent turnover time for $\mathcal{M} \gtrsim 3$ for the compressively-driven runs.

In the analysis described above, a faster growth of the magnetic helicity integral scale $\mathcal{I}_{\mathcal{H}^M}$ has been interpreted as a faster magnetic helicity inverse transfer. However, a faster growth of the integral scale could also be linked with a higher magnetic helicity dissipation in the inverse transfer range, either through non-ideal numerical effects or through some physical mechanism which would “push” the magnetic helicity to small scales, leading to a predominant peak at lower wavenumbers. In order to rule out this possibility, figure 4.17 displays the total magnetic helicity in the system $\mathcal{H}^M = \int \mathbf{a} \cdot \mathbf{b} dV$, normalised by an estimate of its injection rate:

$$\epsilon_{inj}^{\mathcal{H}^M} = \frac{2\epsilon_{inj}^M h_f}{2\pi K_{inj}^{\mathcal{H}^M} L}, \quad (4.5)$$

with $K_{inj}^{\mathcal{H}^M} = 50$ the wavenumber shell around which the electromotive forcing takes

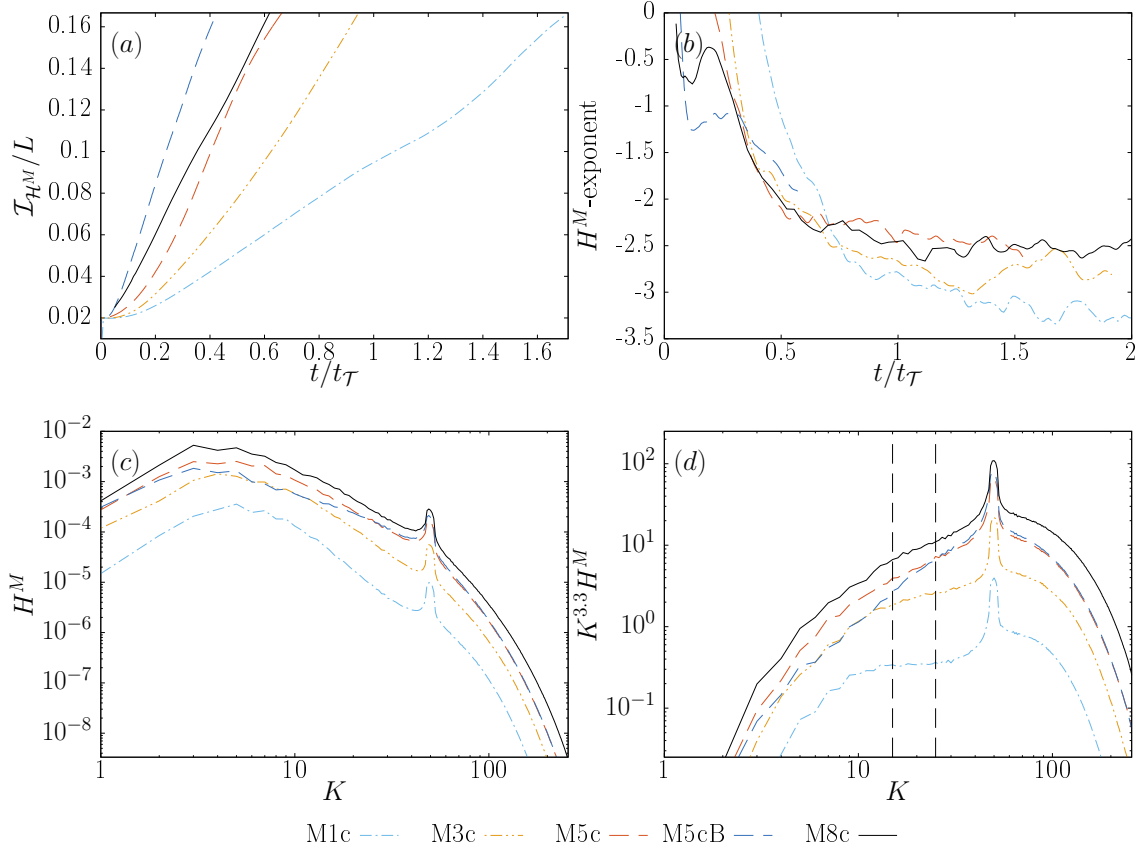


Figure 4.15: Data from magnetic helicity spectra for the main compressively-driven runs, at resolution 512^3 . (a) Magnetic helicity integral scale as a function of time. (b) Magnetic helicity exponent in the region $15 \leq K \leq 25$ computed through a LSF. (c) Double-logarithmic plot of the magnetic helicity spectra at the instants t such that the integral scale $\mathcal{I}_{\mathcal{H}^M} = \frac{1}{6}L$. These instants are 1.71, 0.945, 0.664, 0.426 and 0.619 (in units of their respective $t_{\mathcal{T}}$) for the M1c, M3c, M5c, M5cB and M8c runs respectively. (d) Same spectra as (c), compensated by $K^{3.3}$. The two vertical lines delimit the region where the LSF takes place.

place and h_f the helical fraction of the injected fluctuations (which is +1 for the runs presented here). At very early times, the slope is close to one, indicating mainly conservative nonlinear transfers. Rapidly however, the slope decreases. As will be shown in chapter 6, a sub-dominant direct cascade of magnetic helicity, associated with the direct cascade of magnetic energy, is indeed occurring. Since small scales are associated with greater non-idealities, the dissipation of magnetic helicity increases. Looking at figure 4.17.(a), it seems that the magnetic helicity growth rate converges then to a constant close to 0.5 – 0.6 for all runs but the M01s4 one. A more precise investigation reveals that the curves are convex, see subfigure (b), where only the curves corresponding to the M7s and M8c runs are shown, with a tangent for each of these curves (dotted black line). This is expected since magnetic helicity is transferred to ever larger scales where dissipation is expected to be smaller, leading to a growth of the slope. The time axis for the M7s and M8c curves plotted in subfigure (b) is in code units (and the y-axis has been adapted accordingly). This shows that the faster growth of $\mathcal{I}_{\mathcal{H}^M}$ is not due to increased magnetic helicity dissipation in highly compressible flows: the M7s and M8c runs have the same parameters regarding the magnetic energy injection (table A.1) and hence the same $\epsilon_{inj}^{\mathcal{H}^M}$ rate so that a higher M8c curve as compared to the M7s one at later times means indeed a faster inverse transfer to larger scales, where magnetic helicity is better conserved.

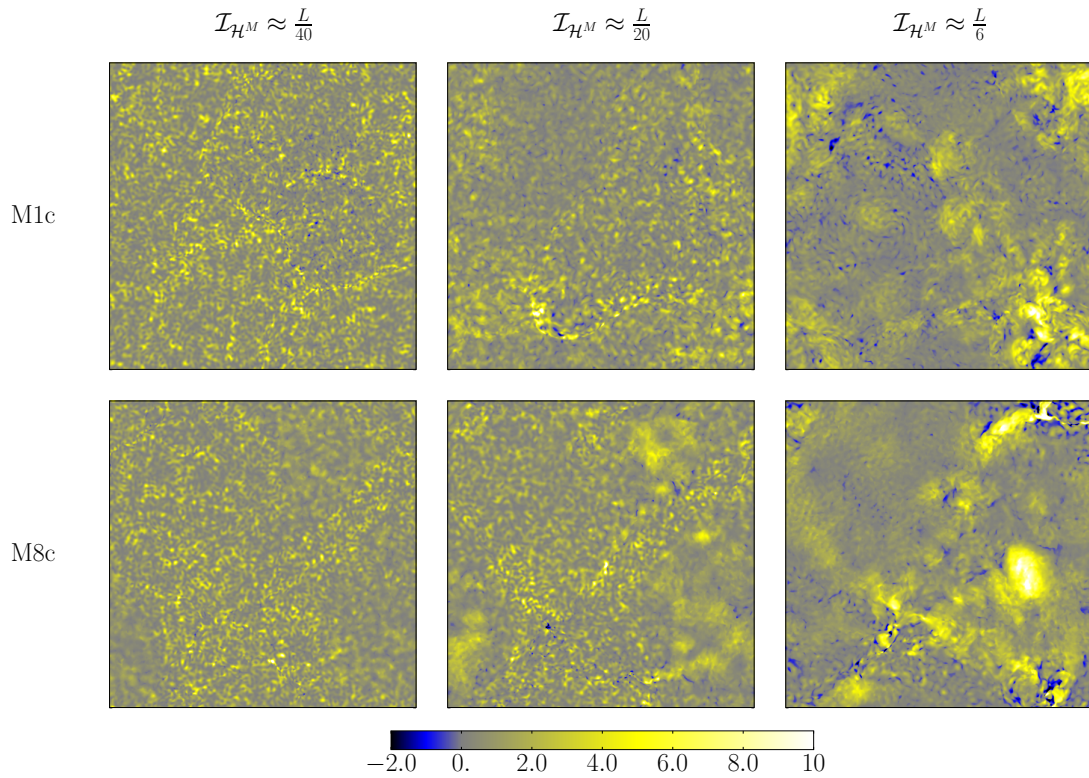


Figure 4.16: Time evolution of magnetic helicity density slices for the M1c and M8c runs, normalised by the mean magnetic helicity density in the system. The instants are chosen so that $\mathcal{I}_{\mathcal{H}^M} \approx \frac{L}{40}$, $\mathcal{I}_{\mathcal{H}^M} \approx \frac{L}{20}$ and $\mathcal{I}_{\mathcal{H}^M} \approx \frac{L}{6}$ (from left to right).

The above interpretation, done by comparing the magnetic helicity present in the system to an estimate of its injection rate, is possible in the present case since magnetic helicity of one sign dominates by far the system at all scales in the inverse transfer region. Since magnetic helicity is not a sign-definite quantity, in situations when both positive and negative magnetic helicity are present in comparable proportions, such a simple approach would not be feasible.

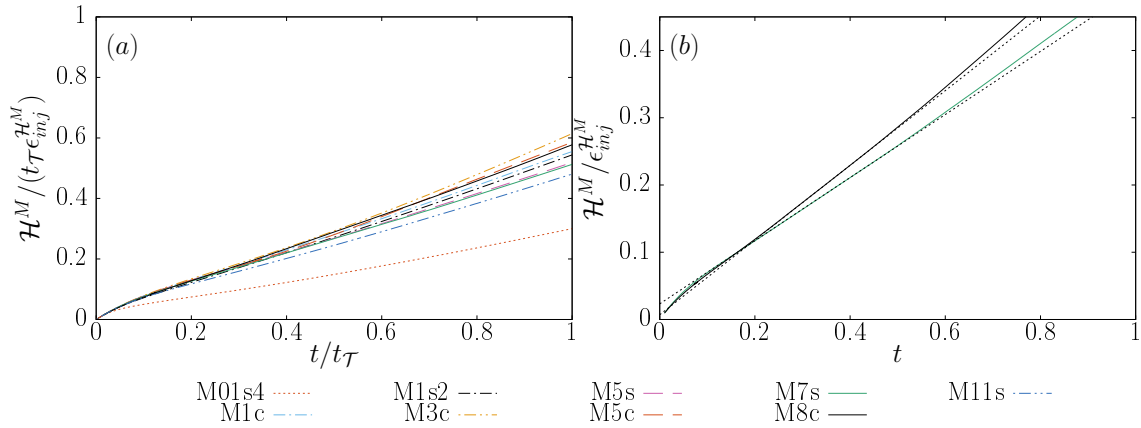


Figure 4.17: Total magnetic helicity in the system, normalised by its injection rate. (a) For all the main runs considered in this work. (b) Comparison between the M7s and M8c runs, which have the same magnetic energy injection rate. The time is here in code units and the black dotted lines are the tangents at $t = 0.40$.

4.2.2 Effects on the hydrodynamic variables

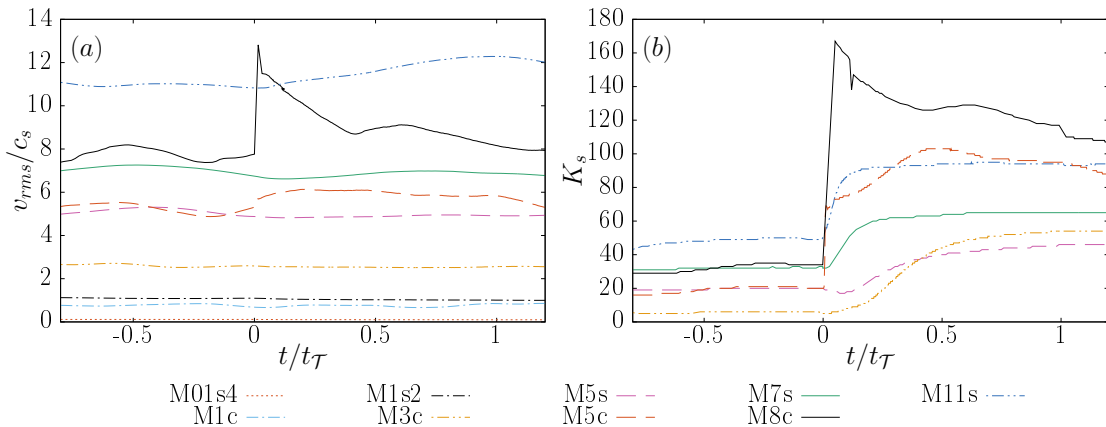


Figure 4.18: RMS Mach number (a) and sonic wavenumber shell (b), as a function of time. The time origin corresponds to the instant when magnetic helicity injection starts, so that a negative value of t means the hydrodynamic steady-state at resolution 512^3 .

Through the action of the Lorentz force, the plasma is accelerated very strongly in the least dense regions for highly compressible flows, leading to an abrupt increase of the RMS Mach number for the M5c and M8c runs (figure 4.18.(a)). This effect is not visible for other runs with a lower density contrast. The plasma acceleration leads to a hump in the velocity power spectra (figure C.1), which is reflected on the sonic wavenumber (figure 4.18.(b)): for the supersonic runs, essentially all the scales in the inverse transfer region are indeed at later times in the supersonic regime.

Figures 4.19 and 4.20 show density and Mach number slices of the M8c and M11s runs respectively. For the M8c run, very high velocities of the order of hundred times the sound speed appear at very early times, predominantly in the regions of very low density. Since the lowest densities are about two orders of magnitude higher for the M11s run (table 4.1), this effect is less visible there, even though small scale velocity structures appear in low density regions as well.

These changes in the velocity field imply important changes in the mass density. The

formation of numerous, relatively small density filaments can be observed in the slices of figures 4.19 and 4.20. A more detailed study of these density filaments is out of the scope of the present work, but they may be attributed to mixing by Alfvén modes perpendicular to the local magnetic field [105].

The injection of magnetic fluctuations tends indeed to reduce the compressive ratio (figure 4.21): when it was about $1/3$ for the supersonic solenoidally-driven runs and $1/2$ for the supersonic compressively-driven run in a significant region before the magnetic helicity injection started (figure 4.5), it is close to 0.2 for $10 \lesssim K \lesssim 40$ for the supersonic runs at an instant when $\mathcal{I}_{HM} \approx \frac{1}{6}L$. This is due to the fact that magnetic energy is preferentially converted in kinetic energy associated with the positive helical part of the velocity field (as shown in section 6.2.3). For the M1c run, the compressive ratio does not drop as much, probably because it does not contain very low density regions. This drop of the $\nabla \cdot \mathbf{v}$ component of the flow leads in turn both to a reduction of the density spread (figure 4.22) and a smoothing of the logarithm mass density PDF for the compressively-driven runs. As shown in this figure, the initially irregular shape of the M8c run’s density PDF bears at later times more resemblance with the PDF snapshots of solenoidally-driven runs.

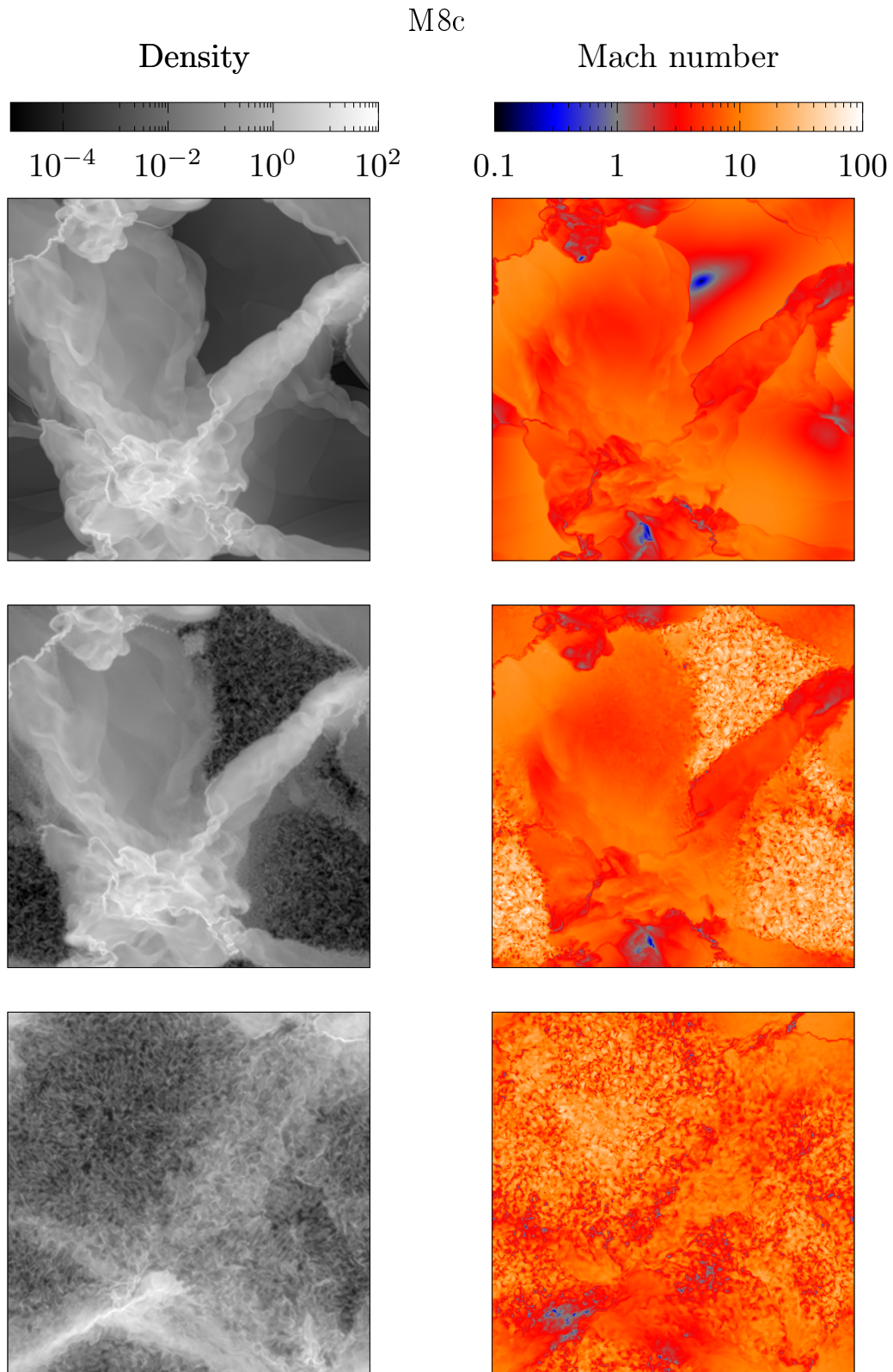


Figure 4.19: Density and Mach number slices for the M8c run. The top figures correspond to the starting hydrodynamic frame, the middle ones at an early time $t = 0.0504t_{\mathcal{T}}$, when $\mathcal{I}_{\mathcal{H}M} = 0.0250L$ and the bottom ones at a later instant $t = 0.637t_{\mathcal{T}}$, when $\mathcal{I}_{\mathcal{H}M} = 0.172L \approx \frac{1}{6}L$.

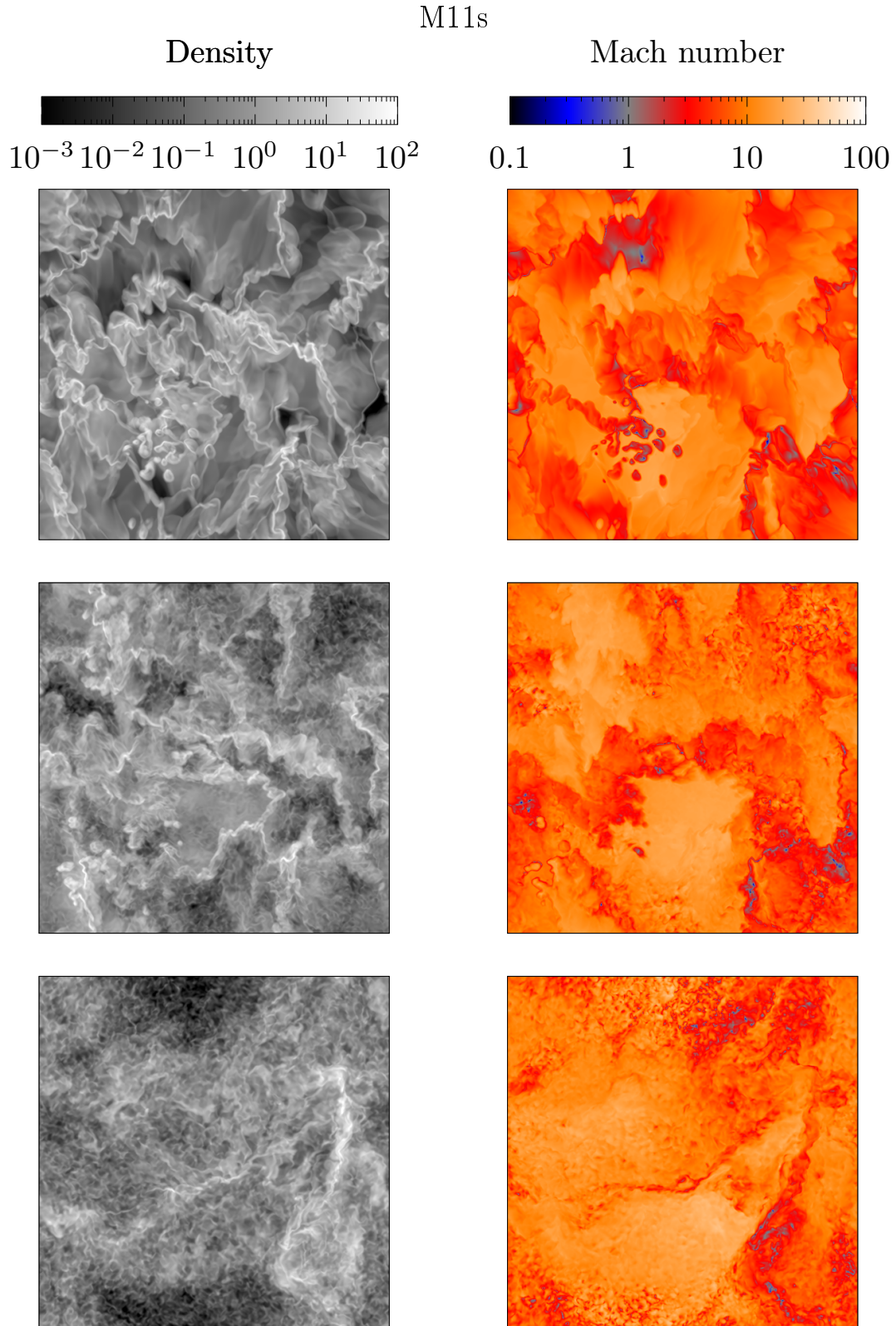


Figure 4.20: Density and Mach number slices for the M11s run. The top figures correspond to the starting hydrodynamic frame, the middle ones at an early time $t = 0.220t_{\mathcal{T}}$, when $\mathcal{I}_{\mathcal{H}M} = 0.0350L$ and the bottom ones at a later instant $t = 1.40t_{\mathcal{T}}$, when $\mathcal{I}_{\mathcal{H}M} = 0.168L \approx \frac{1}{6}L$.

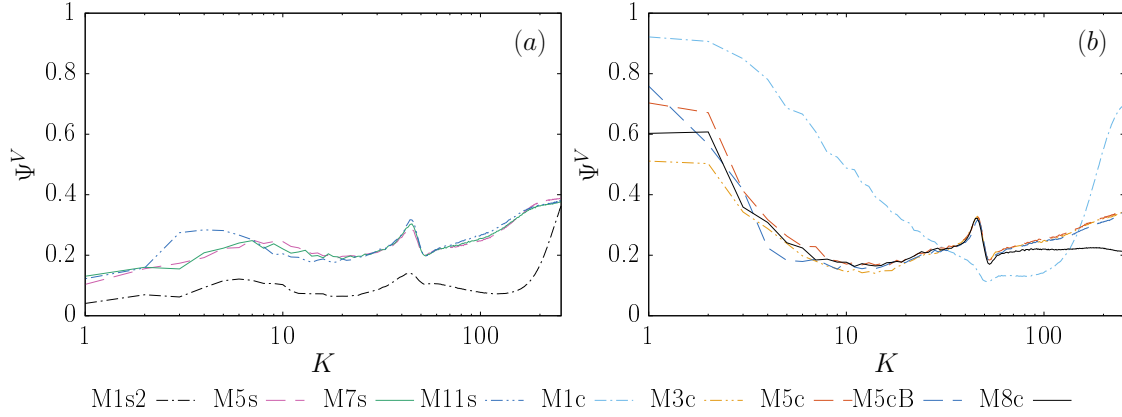


Figure 4.21: Velocity spectra compressive ratio for (a) the transonic and supersonic solenoidally-driven and (b) the compressively-driven runs, at an instant when $\mathcal{I}_{HM} \approx \frac{1}{6}L$.

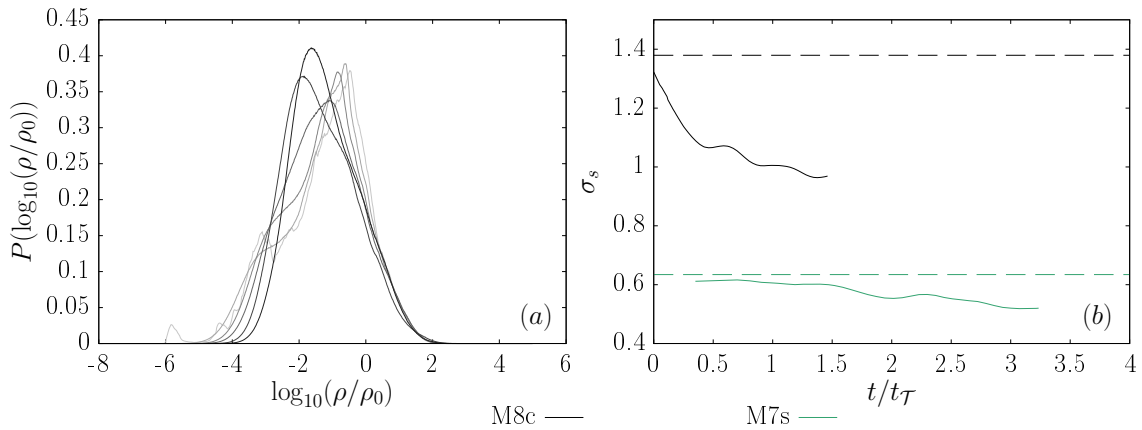


Figure 4.22: (a) Time evolution of the logarithm density PDF for the M8c run, the darker the curve, the later it is. The chosen instants are $t \in \{0., 0.0818, 0.161, 0.239, 0.639, 1.02\}t_{\mathcal{T}}$, (b) Time evolution of the logarithm mass density standard deviation σ_s , for the M7s and M8c runs. The dashed horizontal lines correspond to the value measured for the time-averaged PDFs.

4.3 Importance of the large scale velocity field

In order to relate the present work with previous research [74, 82], a run labelled Mf without large-scale mechanical driving is considered. For this run, only the electromotive forcing is switched on, with a constant magnetic energy injection rate equal to the M1s run's kinetic energy injection rate. This leads to a subsonic flow with a Mach number of the order of 0.2, where the density stays approximately in the range [0.5, 1.5]. The time evolution of the magnetic helicity spectra is displayed in figure 4.23 and compared with the M1s2 run. While for the latter, the convergence to a clear scaling range with a -3.3 exponent is observed very fast, it is not the case for the Mf run: the magnetic helicity inverse transfer proceeds towards larger scales without a clear power-law behaviour, until large scales are reached. Nevertheless, at the latest considered point in time, an exponent close to the incompressible -3.3 one is observed in the small range $10 \lesssim K \lesssim 20$ (figure 4.23.(b)). This observation has to be taken with caution, since boundary effects could be greater at this point in time, where the peak of magnetic helicity is located at $K \approx 3$.

This suggests that the presence of a large scale velocity field is beneficial in order to observe power-law behaviours in spectral space. For the Mf run, this large scale field is generated through magnetic \leftrightarrow kinetic energy exchanges and appears hence only at a later point in time.

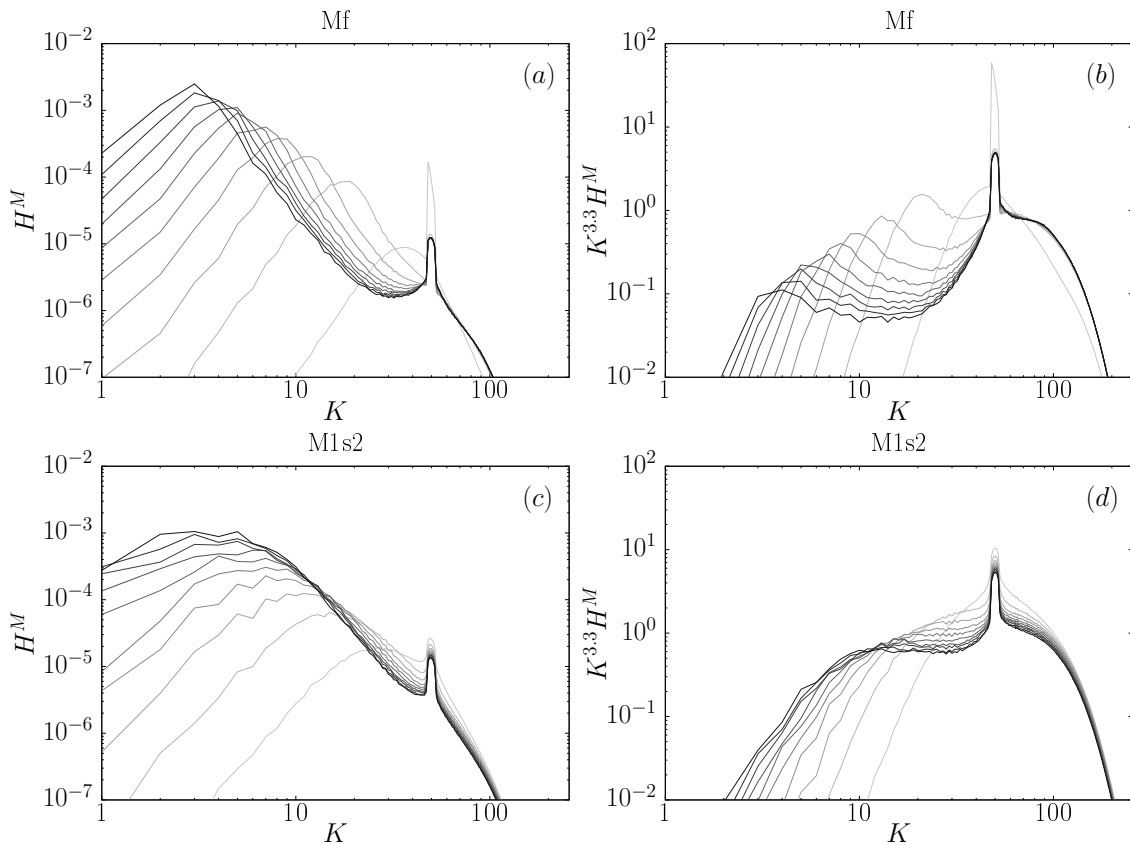


Figure 4.23: Left: time evolution of the magnetic helicity spectra for the Mf (top) and M1s2 (bottom) runs, right: the same spectra compensated by $K^{3.3}$. The darker the curve, the later in time it is.

4.4 Summary

The direct numerical simulations confirm the presence of a magnetic helicity inverse transfer in highly compressible isothermal flows. This inverse transfer occurs faster with increasing compressibility, owing to the velocity field's backreaction on the magnetic field time evolution, which is better accelerated in low density regions. The magnetic helicity exhibits a power-law behaviour in the inverse transfer spectral range. For solenoidally-driven runs, deviations from the incompressible -3.3 exponent [82] are quite weak even for a flow with a RMS Mach number of about $\mathcal{M} \approx 11$, whereas for compressively-driven runs, a flow with $\mathcal{M} \approx 3$ already shows significant deviations from this scaling.

Since the snapshot-to-snapshot variations of the hydrodynamic steady-state density statistics are very important for the supersonic compressively-driven runs however (compare the M5c and M5cB runs), the inverse transfer speed and power-law exponents measured can vary a lot depending on the frame chosen as initial conditions for these runs. This suggests that, for compressively-driven runs, even though the magnetic helicity power-law exponents are certainly flatter at supersonic speeds, a quantitative measure of the power-law exponent as a function of the Mach number from a single inverse transfer realisation is not very significant and that statistics over many realisations would have to be done for this purpose.

Because of numerical issues however (underresolution of high Mach number flows and bottleneck effect), the exponents measured are to be taken with appropriate caution. This point is discussed further in section 7.2.

Chapter 5

Power-law scaling and Alfvénic balance

In 3D incompressible hydrodynamic turbulence, the kinetic energy cascades locally from the largest to ever smaller scales through a local self-similar process, namely the breaking up of large eddies into smaller ones, which are also subject to this phenomenon (see section 2.2.1). As a consequence, in the inertial range, there is no characteristic scale with a particular meaning. This is expressed by the fact that the kinetic energy spectrum exhibits a power-law scaling in Fourier space (with an exponent of $-5/3$).

When a characteristic scale is present however, which is usually the case for non-local processes, a self-similar behaviour is not expected. During the inverse transfer of magnetic helicity, its integral scale is for example characteristic of the scale which destabilises larger scales through the helicity effect, while encouraging equipartition at smaller scales through the Alfvén effect (section 2.2.4). *A priori*, one would hence not expect to see a power-law behaviour, which is also what is observed for the Mf run, driven only magnetically (section 4.3).

Nevertheless, the presence of a large scale velocity field leads to a period of self-similar dynamics regarding the magnetic helicity inverse transfer (section 4.3). Scaling laws are observed after a short transient phase and should then persist until boundary effects lead to condensation of magnetic helicity at the largest available scales.

In the incompressible case, scaling laws have been observed for several quantities, including the magnetic and kinetic energies and helicities [74]. Furthermore, a balance in spectral space between the ratio of kinetic-to-magnetic energy on the one hand and the ratio of kinetic-to-current helicity on the other hand is observed [74, 82, 79, 53], which is referred to in section 2.2.4 as the “Alfvénic balance”.

In the compressible case, the magnetic field time evolution is [27]:

$$\partial_t \mathbf{b} = -(\mathbf{v} \cdot \nabla) \mathbf{b} + (\mathbf{b} \cdot \nabla) \mathbf{v} - \mathbf{b}(\nabla \cdot \mathbf{v}). \quad (5.1)$$

For flows where the compressive part of the velocity field \mathbf{v}^C is low (section 2.4.4), such as low Mach number flows with a solenoidal mechanical driving, the dynamics are expected to be close to the incompressible case ones. However, for a large \mathbf{v}^C field, the right-hand side of relation (5.1) presents important differences, as compared to the incompressible case:

- there is a new compression term $-\mathbf{b}(\nabla \cdot \mathbf{v})$, which explicitly contains the velocity field divergence (in the incompressible case, $\nabla \cdot \mathbf{v} = 0$),

- the advective $-(\mathbf{v} \cdot \nabla)\mathbf{b}$ and stretching $(\mathbf{b} \cdot \nabla)\mathbf{b}$ terms, even though present in the incompressible case as well, are expected to behave differently, since they contain now contributions from the compressive part of the velocity field.

This chapter aims hence at assessing similarities and differences between the compressible and the incompressible cases. Section 5.1 explores the presence of scaling laws in the inverse transfer region and shows that some exponents found in the incompressible case can be retrieved with an appropriate choice of variables. The ‘‘Alfvénic balance’’ observed in the incompressible case is reviewed in section 5.2 and an extension of the same is proposed, which seems to be valid in highly compressible flows. Section 5.3 summarises the results and gives some concluding remarks.

All the Fourier spectra shown in the present chapter are normalised in the way described in section 3.4.

5.1 Power-law scaling

Table 5.1: Spectral domain where the LSF are performed for the figures in sections 4.2.1, 5.1 and appendix C.1 as well as tables 5.2 and 5.3.

$[K_{min}, K_{max}]$	M01s4, M1s2, M5s, M7s, M11s	M1c	M3c, M5c, M5cB, M8c
[8-15]	-	$E^V, E^{V,sol.}$	$E^A, E^V, E^{V,sol.}$
[10-25]	-	H^A	H^A
[15-25]	$E^A, H^V, E^K,$ $E^V, E^{V,sol.}, E^U$	$H^M, E^M, E^A,$ H^V, E^K, E^U	$H^M, E^M, H^V,$ E^K, E^U
[15-30]	H^A	-	-
[20-30]	H^M, E^M	-	-

In this section, power-law behaviours are reported and compared to those observed in the incompressible case. The quantities considered correspond to the ones involved in the Alfvénic balance: $E^V, E^M, H^J = K^2 H^M$ and H^V , with some variable changes relevant in the compressible case. The tables 5.2 and 5.3 at the end of this section summarise the measured values.

The results are gained by considering the solenoidally-driven M01s4, M1s2, M5s, M7s, M11s runs and the compressively-driven M1c, M3c, M5c, M5cB and M8c ones, all at resolution 512^3 . The spectra are shown, as in section 4.2.1, at an instant where the integral scale of the magnetic helicity is $\mathcal{I}_{\mathcal{H}^M} \approx \frac{1}{6}L$ so that a sufficient distance in wavenumber space both from the largest and the magnetically-forced scales is present.

In order to assess the presence of a time-independent power-law exponent, the exponents’ time evolution is also shown. Since the domain where a power-law is observed may differ for each quantity X and run R , a different spectral domain $[K_{min,X,R}, K_{max,X,R}]$ is chosen for each quantity and run. Table 5.1 displays the considered domains. On these domains, the power-law exponent is measured through a linear least squares fit (LSF) of $\log(X)$ as a function of $\log(K)$. Even though the region where a power-law behaviour also changes with the progress of the magnetic helicity inverse transfer, the chosen domains do not depend on the considered instant in time for reasons of simplicity. The domains are indeed chosen so that, after a transient phase, the quantities exhibit a power-law behaviour on them over a long period of time. This means however that for too early times,

when the inverse transfer has not reached a large enough scale, the computed exponents are not relevant. On the other hand, an exponent that stays close to a certain constant at later times is a good indication for a time-independent power-law.

5.1.1 Magnetic energy and helicity

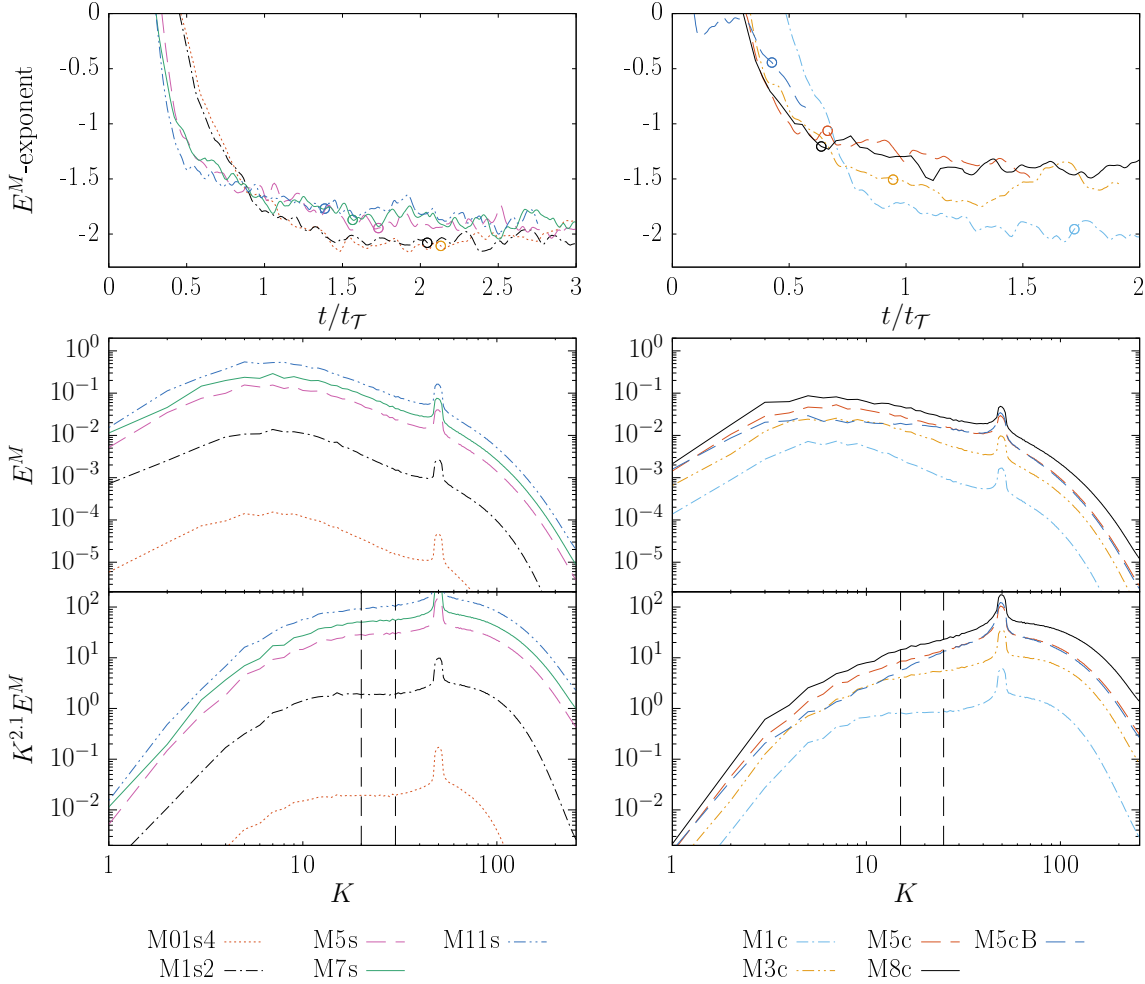


Figure 5.1: Top: time evolution of the E^M -exponent, obtained through a LSF in the domain marked with dashed vertical lines at the bottom subfigures and repeated in table 5.1. Bottom: snapshots of the E^M -spectra at an instant when $\mathcal{I}_{\mathcal{H}^M} \approx \frac{1}{6}L$ (marked with a circle in the top subfigures), compensated as well with the observed exponent in the incompressible case. The measured exponents are given in tables 5.2 and 5.3.

Both in the incompressible and in the compressible cases, the magnetic helicity and magnetic energy exhibit a power-law behaviour in Fourier space, when a large scale velocity field is present. As already shown in section 4.2.1, the magnetic helicity inverse transfer takes place more rapidly with increasing compressibility, leading to significantly flatter H^M spectra for highly compressible runs. For solenoidally-driven runs, the deviations from the -3.3 incompressible exponent are not that big (for the M11s run, the measured exponent is -3.03 when $\mathcal{I}_{\mathcal{H}^M} \approx \frac{1}{6}L$). However, for compressively-driven runs, the deviations are already significant at relatively low RMS Mach numbers, since the M3c run presents an exponent of -2.64 at the same magnetic helicity integral scale.

This effect is also reflected on the magnetic energy spectra (figure 5.1). The -2.1 exponent found in the incompressible case [74] is also observed for the M01s4, M1s2 and

M1c runs. For the high Mach number solenoidally-driven runs, the exponents are similar to the incompressible one, even though slightly flatter.

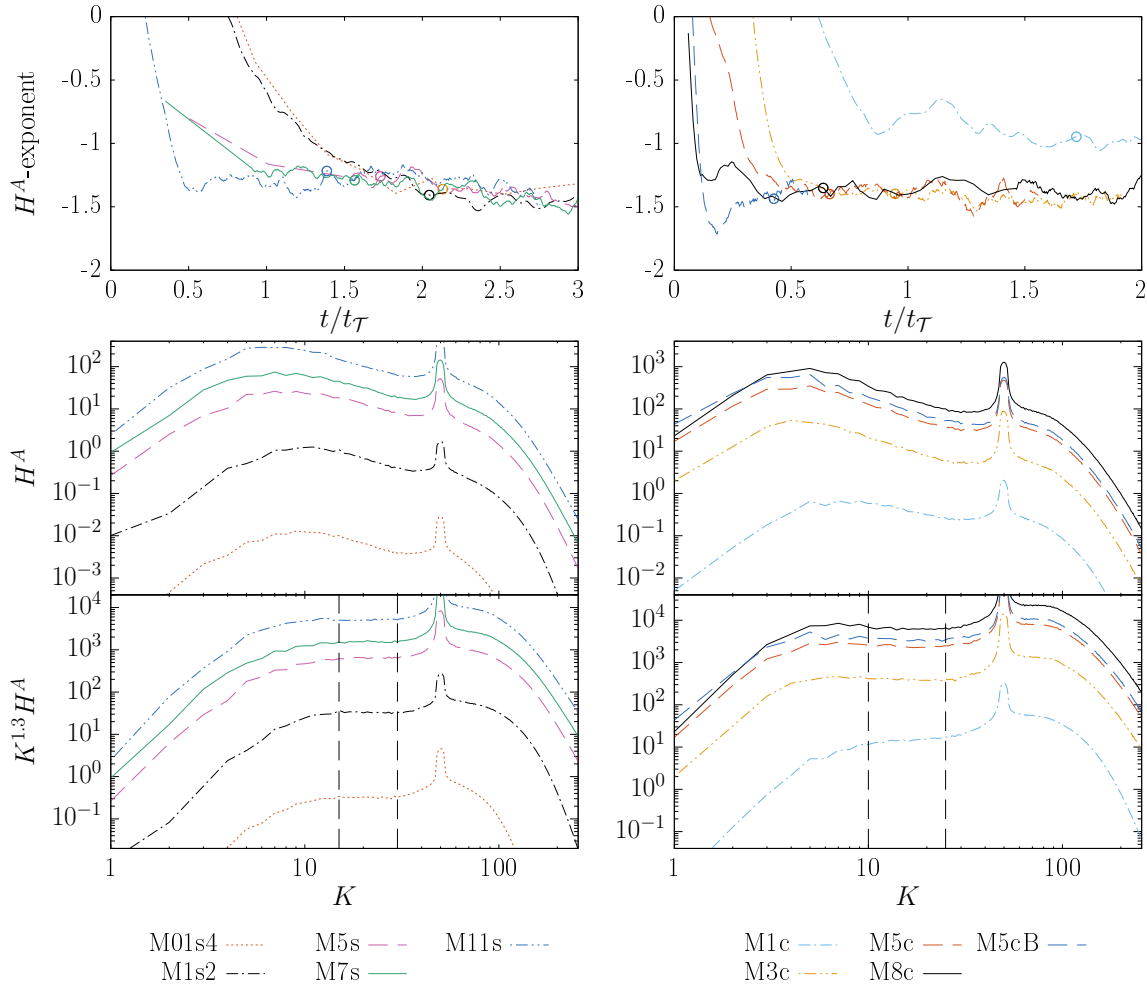


Figure 5.2: Same as figure 5.1, but for H^A .

For the compressively-driven runs however, significant deviations are already visible for the M3c run. More than the averaged RMS Mach number in the hydrodynamic steady-state however, the repartition of the mass density plays a determinant role in the inverse transfer dynamics. Both the M5c and M5cB runs start with a hydrodynamic state with a RMS Mach number of roughly 5. However, the M5cB run (see section 4.2), for which the peak in the logarithmic density PDF is located at a smaller number, exhibits a significantly flatter magnetic energy spectrum. For this reason, when the variations due to the initial frame choice may not be too high for solenoidally-driven runs, these are very important for high Mach number compressively-driven runs, so that drawing a conclusion about the exponent as a function of the Mach number is not feasible from only one particular realisation.

5.1.2 Alfvén velocity and helicity

The inverse transfer of magnetic helicity occurs faster in very low density regions, due to the enhanced effect of the Lorentz force on the velocity field, which backreacts on the magnetic field (section 4.2.1). In the incompressible case, since the density is constant,

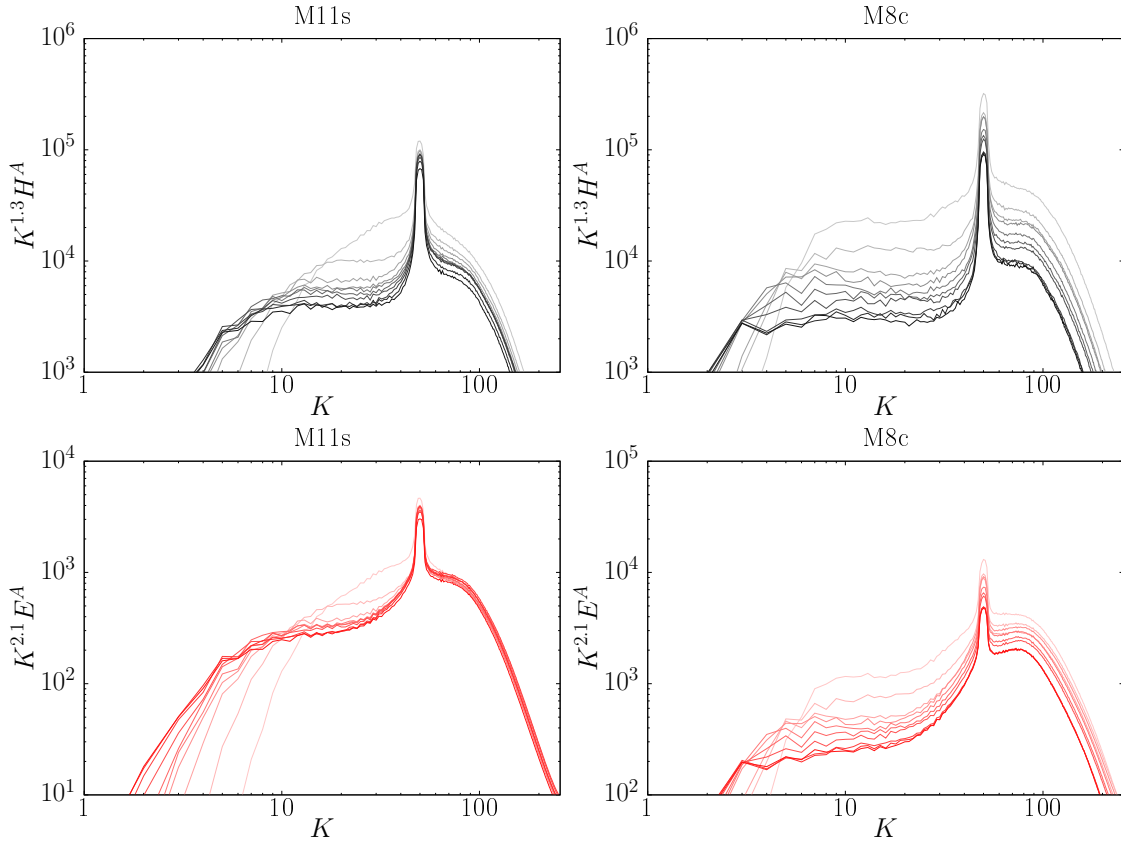


Figure 5.3: Time evolution of the compensated Alfvénic helicity (black) and Alfvén velocity power spectra (red) for the M11s and M8c runs. The spectra are equally spaced in time, from $t = t_f/10$ until $t_f = 2.2t_\tau$ and $t_f = 1.6t_\tau$ for the M11s and M8c runs respectively. The darker the curve, the further in time it is.

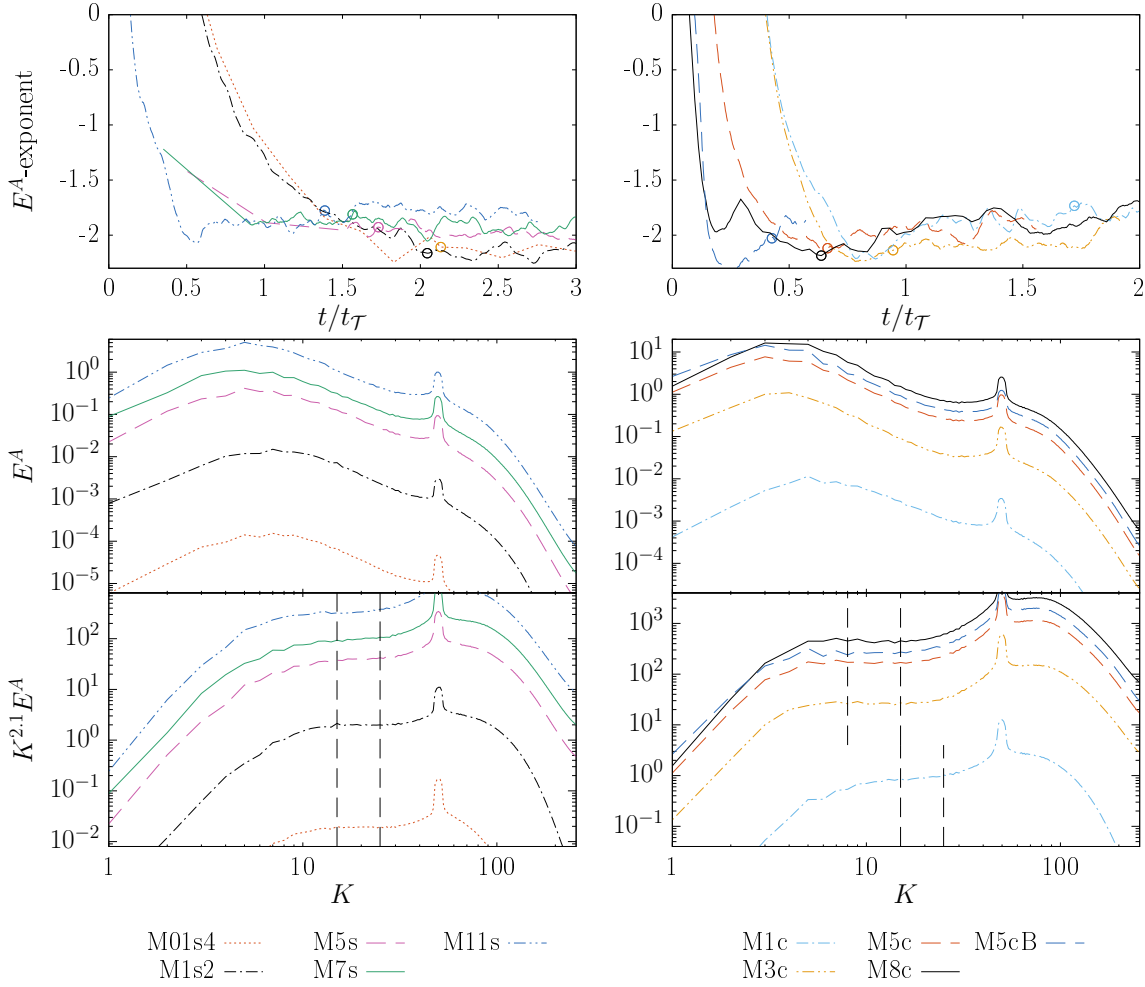
the magnetic field and the Alfvén velocity $\mathbf{v}_A = \mathbf{b}/\sqrt{\rho}$ have the same spectra (up to a constant multiplicative factor). In the compressible case however, the low density regions are associated with higher Alfvén speeds, which means that the dynamical timescales are faster there.

This motivates the consideration of the Alfvén velocity power and helicity spectra. The helicity of the Alfvén velocity is defined by:

$$\mathcal{H}^A = \int \mathbf{v}_A \cdot (\nabla \times \mathbf{v}_A) dV, \quad (5.2)$$

and is called hereafter the “Alfvénic helicity”. Its spectrum is $H^A = \mathcal{Q}(\mathbf{v}_A, \nabla \times \mathbf{v}_A)$ (see section 2.1.2 for the definition of \mathcal{Q}). The power spectrum of the Alfvén velocity is noted $E^A = \mathcal{P}(\mathbf{v}_A)$.

Even though the magnetic helicity spectra are flatter with higher compressibility, the incompressible behaviour is recovered when considering “Alfvénic helicity” spectra. In the incompressible case, an exponent close to -3.3 is observed for the magnetic helicity. Since the magnetic field is solenoidal, this is equivalent to an exponent close to -1.3 for the current helicity H^J , which is equivalent to the Alfvénic helicity in the incompressible case. An exponent close to -1.3 is indeed observed for H^A for all the runs, both solenoidally- and compressively-driven, but the M1c one, as shown in figure 5.2. This is not only the case at the particular instant when $\mathcal{I}_{\mathcal{H}M} \approx \frac{1}{6}L$ but in a consequent time window (figures 5.2

Figure 5.4: Same as figure 5.1, but for E^A .

(top) and 5.3). Moreover, even the M5cB run, which presents clearly flatter H^M (figure 4.15) and E^M (figure 5.1) spectra, also shows this scaling close to -1.3 .

The different exponent for the M1c run is probably linked to its significantly higher velocity spectrum compressive ratio (figure 4.21). For this run, the velocity spectrum is less affected by magnetic energy injection, because of the absence of very low density regions, as compared to compressively-driven runs at higher RMS Mach numbers. This affects in turn the magnetic transfer dynamics.

The power spectra of the Alfvén velocity E^A present as well a more universal behaviour for the compressively-driven runs, as compared to the magnetic energy spectra E^M . The exponent is closer to the -2.1 incompressible exponent [74] for the M3c, M5c, M5cB and M8c runs as well. The scaling appears however to become flatter at later times, with values becoming closer to the ones in the solenoidally-driven cases (figures 5.4 (top) and 5.3). The reason for this behaviour would require further investigations.

Since contrary to the magnetic field \mathbf{b} , the Alfvén velocity field \mathbf{v}_A is not solenoidal, it is meaningful to consider the solenoidal part of the E^A field as well, since this is the energy associated with the Alfvénic helicity. These curves (not shown in this dissertation) present only minor deviations from those in figure 5.4 since $\Psi^A = \mathcal{P}^{comp}(\mathbf{v}_A)/\mathcal{P}(\mathbf{v}_A)$, the Alfvén velocity compressive ratio, is quite small, less than 0.15 over a wide range in the inverse transfer region (figure 5.5).

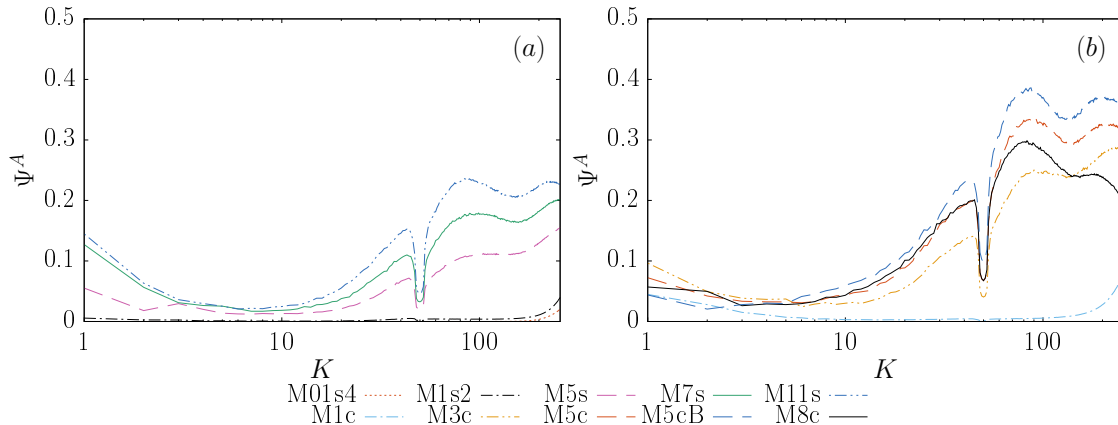


Figure 5.5: Compressive ratio of the Alfvén velocity power spectrum for the main runs at an instant when $\mathcal{L}_{\mathcal{H}^M} = \frac{1}{6}L$.

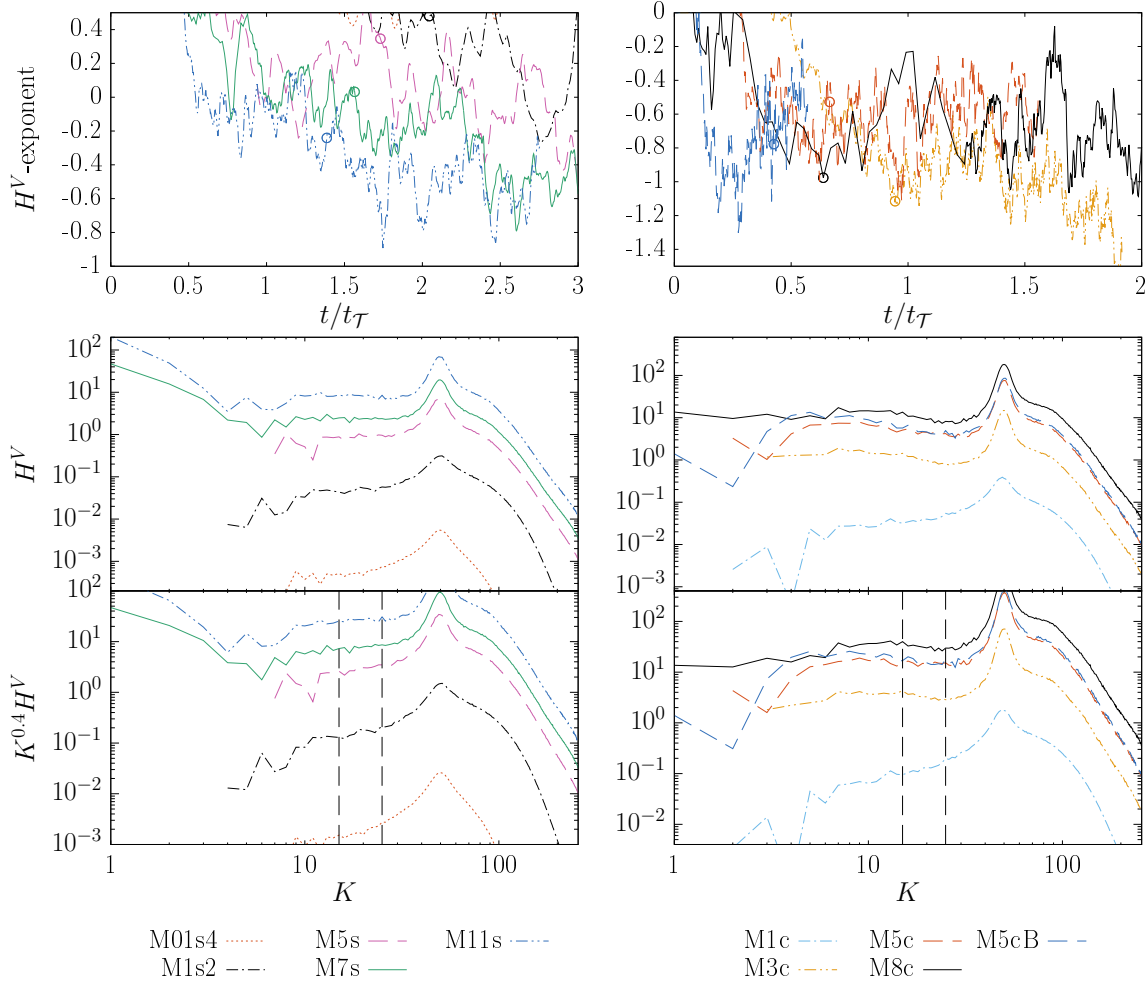
The observations made in the present subsection pinpoint to a systematic scale-dependent correlation between the density and the magnetic fields which would need to be investigated in greater detail in future research. They suggest as well the use of the Alfvén velocity instead of the magnetic field in the Alfvénic balance for compressible flows (see section 5.2).

5.1.3 Kinetic energy and helicity

In the incompressible case, the kinetic helicity H^V exhibits a scaling law with an exponent close to -0.4 [74]. For the runs presented here, this exponent *could* be compatible with the most compressible runs, but the low Mach number runs present way flatter spectra, or even spectra with a positive exponent (figure 5.6). This is probably linked with the presence of a relatively strong direct cascade of energy from the largest scales, in contrast to the numerical experiments in reference [74]. The time evolution of the kinetic helicity spectrum for the Mf run (figure 5.7), with no velocity field at the largest scales, presents indeed a power-law with an exponent compatible with the -0.4 value. In the hydrodynamic case, it has been shown that the energy cascade tends to “restore reflection invariance at small scales” [33], or, with other words, leads to an equipartition of energy among the positive and negative helical parts of the velocity field at large wavenumbers. As a consequence, for the mechanically-forced runs, scales larger than the magnetically-forced scale, but small with respect to the large scale mechanical driving, would tend to lose kinetic helicity. This effect is less pronounced for the highly compressible runs, since they present a significantly faster inverse transfer timescale, as compared to the hydrodynamic direct cascade timescale.

For the runs with a large-scale mechanical driving, the kinetic helicity power-law exponents present a very high temporal variation. These are mostly due to the more irregular shape of the spectra (as compared for example with the magnetic helicity spectra), giving fluctuations in the LSF computation.

Apart from the magnetic energy E^M , the current helicity $H^J = K^2 H^M$ and the kinetic helicity H^V , the fourth and last quantity considered in the Alfvénic balance found in the incompressible case (see section 2.2.4) is the kinetic energy. However, the kinetic energy in the incompressible case could correspond to several quantities in the compressible case. Among others, it could correspond to the specific kinetic energy $E^V = \mathcal{P}(\mathbf{v})$, or the power spectrum of the velocity, weighted by some power of the density, such as $E^K = \mathcal{P}(\mathbf{w})$

Figure 5.6: Same as figure 5.1, but for H^V .

or $E^U = \mathcal{P}(\mathbf{u})$ with $\mathbf{w} = \sqrt{\rho}\mathbf{v}$ and $\mathbf{u} = \rho^{1/3}\mathbf{v}$. The power spectrum of \mathbf{w} is directly linked with the kinetic energy, whereas \mathbf{u} is the quantity which is expected to recover the Kolmogorov power spectrum in high Mach number low $\nabla \cdot \mathbf{v}$ flows (see section 2.2.1).

The spectra associated with the kinetic energy E^K and the solenoidal part of the specific kinetic energy $E^{V,sol.}$ are shown in figures 5.8 and 5.9 respectively. For the solenoidally-driven runs, both variables exhibit exponents close to the -1.2 one observed in the incompressible case [74]. For the compressively-driven runs however, the agreement with the incompressible exponent is better for $E^{V,sol.}$. Even though the exponent is slightly flatter than -1.2 for the least compressive M01s4 and M1s2 runs when $\mathcal{I}_{\mathcal{HM}} = \frac{L}{6}$, it gets closer to this value at later times (see the top subfigures).

The reason why the solenoidal part of E^V is shown here is because it contains only the energy associated with the kinetic helicity. The velocity power spectra E^V are shown in the appendix (figure C.1) and present only noticeable differences where the compressive ratio is high (see figure 4.21): at low wavenumbers for the supersonic compressively-driven runs and over a larger domain for the M1c one. The curves for E^U are also shown in the appendix (figure C.2) and present a behaviour intermediate between the $E^{V,sol.}$ and E^K ones.

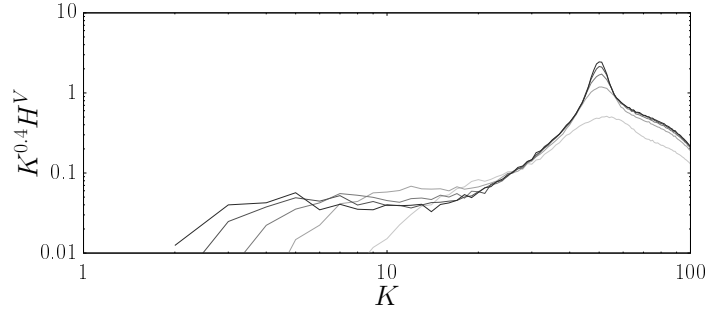


Figure 5.7: Time evolution of the kinetic helicity spectrum (compensated by $K^{-0.4}$) for the Mf run. The darker the curve, the later in time it is. The curves are equally spaced in time, from an instant when $\mathcal{I}_{\mathcal{H}^M} \approx \frac{L}{19}$ till $\mathcal{I}_{\mathcal{H}^M} \approx \frac{L}{3}$.

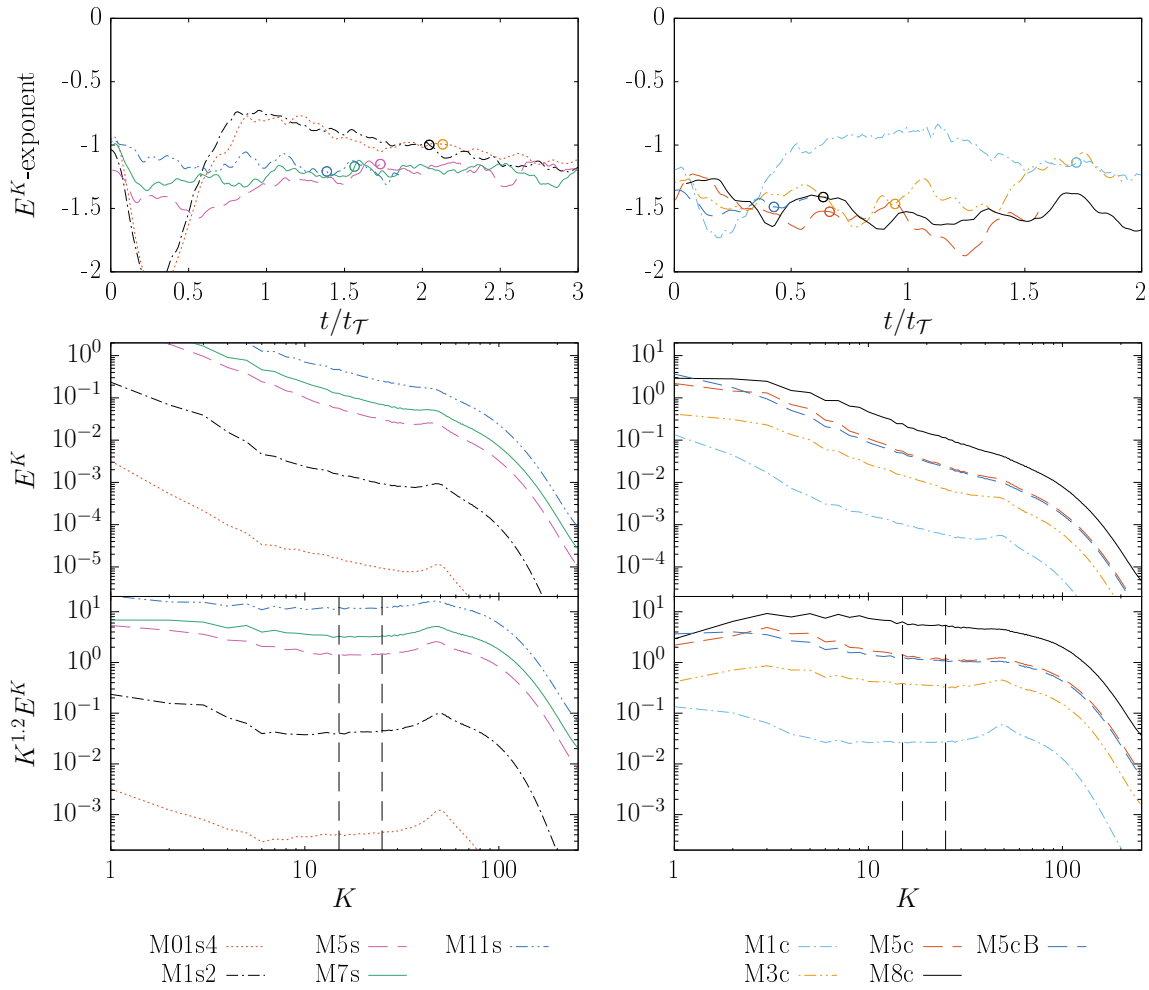
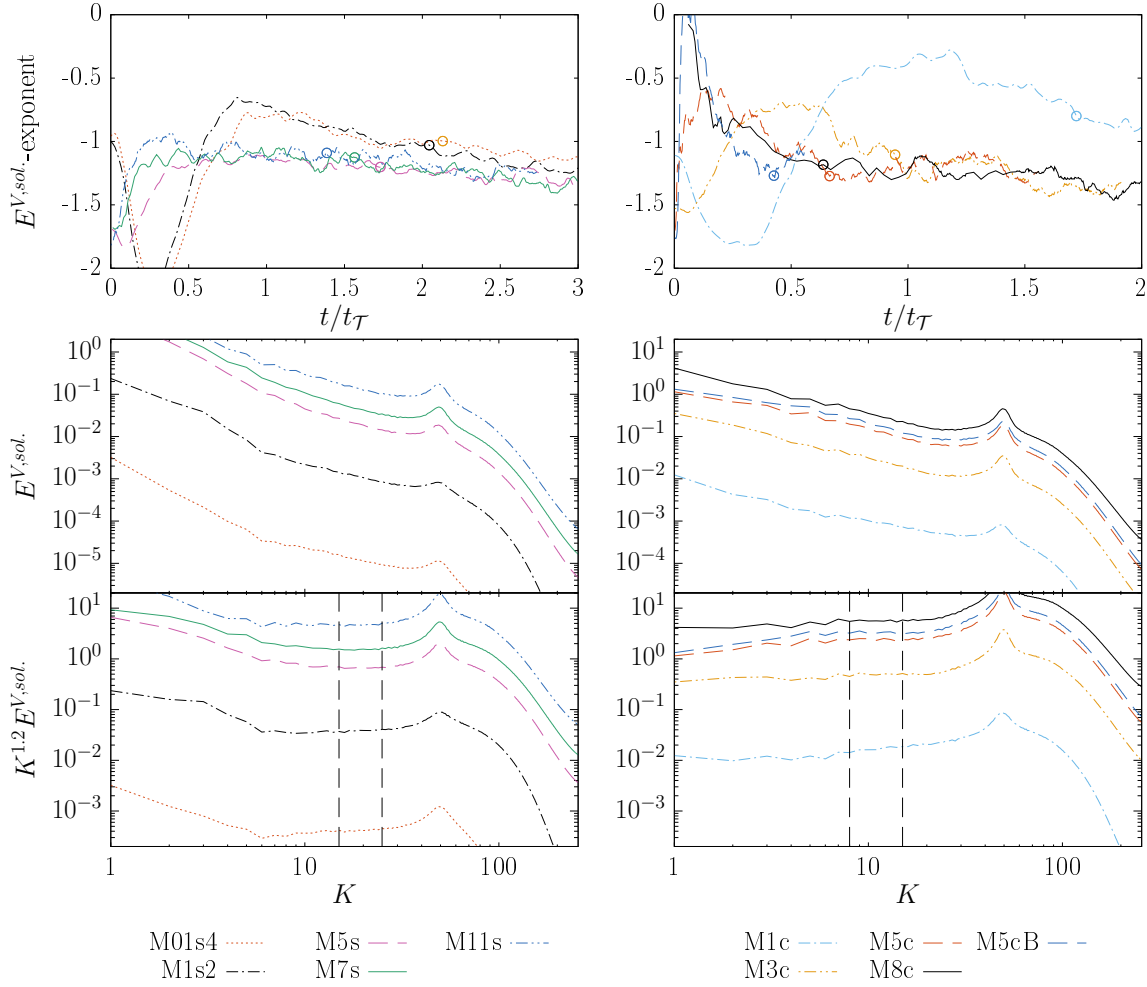


Figure 5.8: Same as figure 5.1, but for E^K .

This good agreement even at high compressibility of $E^{V,sol.}$ with the -1.2 incompressible exponent suggests that the incompressible Alfvénic balance could be extended to the compressible case when using $E^{V,sol.}$ (see section 5.2).

Figure 5.9: Same as figure 5.1, but for $E^{V, sol.}$.

5.1.4 Summary of the scaling behaviours

The time-averaged measured exponents for the solenoidally- and compressively-driven runs are summarised in tables 5.2 and 5.3 respectively and compared to those of the incompressible case [74]. These time-averaged exponents are measured by averaging the exponents obtained through a LSF (top subfigures in the previous subsections) over a certain time window. The time window for each run starts at an instant close to the one when $\mathcal{I}_{\mathcal{H}^M} \approx \frac{1}{6}L$ (marked by circles in the previous subsections' top curves), so that the quantities present indeed a power-law behaviour in the domain where the LSF takes place (see table 5.1). For the M01s4 and M1s2 runs, the time window is $[2t_{\mathcal{T}}, 3t_{\mathcal{T}}]$, for the M5s, M7s and M11s runs, it is $[1.5t_{\mathcal{T}}, 3t_{\mathcal{T}}]$, for the M1c run $[1.5t_{\mathcal{T}}, 2t_{\mathcal{T}}]$ and for the M3c, M5c and M8c runs $[1t_{\mathcal{T}}, 2t_{\mathcal{T}}]$. The error estimates are such that the measured exponents are more than 95% of the time in the written interval.

Because of the high temporal variations, the kinetic helicity exponents are not measured. For the compressively-driven runs, the H^M and E^M exponents are not shown either, since they could be highly dependent on the starting hydrodynamic frame.

Table 5.2: Power-law scalings found for the solenoidally-driven runs. The measure is done through a LSF in the spectral domains mentioned in table 5.1 and by averaging in the temporal domain $t \in [2t_{\mathcal{T}}, 3t_{\mathcal{T}}]$ for the M01s4 and M1s2 runs and $t \in [1.5t_{\mathcal{T}}, 3t_{\mathcal{T}}]$ for the hypersonic runs. The error estimates are such that the measured exponents are more than 95% of the time in the written interval. The second column labelled “Inc.” repeats the results found in the incompressible case [74]. The values with a star * for the M01s4 and M1s2 runs are more uncertain, since they do not present a steady value but decrease in the considered time window.

	Inc.	M01s4	M1s2	M5s	M7s	M11s
H^M	-3.3 ± 0.2	-3.25 ± 0.14	-3.35 ± 0.15	-3.21 ± 0.19	-3.19 ± 0.21	-3.13 ± 0.22
H^A	-1.3 ± 0.2	-1.36 ± 0.08	-1.45 ± 0.07	-1.35 ± 0.14	-1.38 ± 0.14	-1.29 ± 0.12
E^M	-2.1 ± 0.3	-2.03 ± 0.14	-2.05 ± 0.10	-1.92 ± 0.11	-1.87 ± 0.14	-1.82 ± 0.16
E^A	-2.1 ± 0.3	-2.12 ± 0.11	-2.16 ± 0.09	-1.97 ± 0.09	-1.91 ± 0.14	-1.78 ± 0.09
E^K	-1.2 ± 0.2	$-1.07 \pm 0.08^*$	$-1.12 \pm 0.13^*$	-1.20 ± 0.12	-1.21 ± 0.10	-1.20 ± 0.10
E^V	-1.2 ± 0.2	$-1.07 \pm 0.08^*$	$-1.14 \pm 0.10^*$	-1.27 ± 0.07	-1.24 ± 0.13	-1.16 ± 0.10
$E^{V,sol.}$	-1.2 ± 0.2	$-1.08 \pm 0.08^*$	$-1.16 \pm 0.13^*$	-1.26 ± 0.09	-1.25 ± 0.15	-1.20 ± 0.11
E^U	-1.2 ± 0.2	$-1.07 \pm 0.08^*$	$-1.13 \pm 0.12^*$	-1.26 ± 0.10	-1.28 ± 0.10	-1.25 ± 0.09

Table 5.3: Power-law scalings found for the compressively-driven runs. The measure is done through a LSF in the spectral domains mentioned in table 5.1 and by averaging in the temporal domain $t \in [1.5t_{\mathcal{T}}, 2t_{\mathcal{T}}]$ for the M1c run and $t \in [1t_{\mathcal{T}}, 2t_{\mathcal{T}}]$ for the others. The error estimates are such that the measured exponents are more than 95% of the time in the written interval. The second column labelled “Inc.” repeats the results found in the incompressible case [74].

	Inc.	M1c	M3c	M5c	M8c
H^A	-1.3 ± 0.2	-0.99 ± 0.06	-1.44 ± 0.07	-1.40 ± 0.14	-1.36 ± 0.10
E^A	-2.1 ± 0.3	-1.82 ± 0.11	-2.06 ± 0.21	-1.92 ± 0.14	-1.86 ± 0.11
E^K	-1.2 ± 0.2	-1.18 ± 0.09	-1.30 ± 0.23	-1.68 ± 0.18	-1.55 ± 0.17
E^V	-1.2 ± 0.2	-1.38 ± 0.13	-1.28 ± 0.13	-1.24 ± 0.12	-1.31 ± 0.11
$E^{V,sol.}$	-1.2 ± 0.2	-0.77 ± 0.22	-1.28 ± 0.15	-1.19 ± 0.13	-1.28 ± 0.16
E^U	-1.2 ± 0.2	-1.19 ± 0.08	-1.18 ± 0.08	-1.41 ± 0.16	-1.45 ± 0.12

Through these tables and the figures presented in the previous subsections, the following conclusions can be drawn:

- Even though the magnetic helicity inverse transfer is non-local, several power-law behaviours are observed. In the presence of a large-scale velocity field, this is among others the case for the magnetic, kinetic and Alfvénic helicities, as well as the associated energies.
- For solenoidally-driven runs, the time-averaged exponents for H^M , E^M , E^K , E^V , $E^{V,sol.}$ and E^U remain relatively close to the ones in the incompressible case even for a RMS Mach number up to about 11.
- For compressively-driven runs, strong deviations are measured for the H^M , E^M , E^K and E^U exponents even at relatively low RMS Mach numbers (of the order of 3). As mentioned in sections 4.2.1 and 5.1.1, the hydrodynamic starting frame plays an important role in the measured H^M and E^M exponents, which is why they are not

shown in table 5.3. However, the E^V and $E^{V,sol.}$ spectra show scaling laws that are very close to the incompressible case, even for the M8c run.

- When considering the Alfvénic helicity spectra, an exponent very close to the incompressible -1.3 exponent is measured, for all the runs but the M1c one. This includes the M5c and M5cB runs which exhibit very big differences for the H^M and E^M spectra. The power spectra of the Alfvén velocity are however flatter than the -2.1 exponent for highly compressible runs, even though the behaviour is more universal for this quantity as well, as compared to the magnetic energy. This more universal behaviour seems to be valid as soon as the velocity power spectrum compressive part becomes low in the inverse transfer region, which is the case for the solenoidally-driven runs and the compressively-driven ones with a high enough Mach number.

Some scaling laws found in the incompressible case remain hence valid in the highly compressible case (in particular E^V , $E^{V,sol.}$ and H^A). Thus, based on these observations, the Alfvénic balance found in the incompressible case is extended to the compressible case in the next section.

5.2 Alfvénic balance

As mentioned in section 2.2.4, it has been found in the framework of incompressible MHD that the relation

$$\left(\frac{E^V}{E^M}\right)^\gamma \propto \frac{H^V}{H^J}. \quad (5.3)$$

is approximately verified in an adequate range with $\gamma = 1$ [74, 79, 53]. However, for the numerical setup closest to the one presented in this work (with an electromotive forcing at large wavenumbers [74]), it has been found in a later work that an exponent of $\gamma = 2$ would fit the numerical data better [82]. Whether relation (5.3) still holds in the compressible case is investigated in the following.

5.2.1 Considered ratios

In order to seek for an Alfvénic balance valid in the compressible case, the ratio

$$\Lambda(E^V, E^M, \gamma) = \left(\frac{E^V}{E^M}\right)^\gamma \frac{H^J}{H^V} \quad (5.4)$$

is plotted for $\gamma \in \{1, 2\}$ and a certain range where it would be constant is looked for. As explained through section 5.1, some quantities in the incompressible case can however correspond to several ones in compressible MHD (for example the Alfvén velocity \mathbf{v}_A and the magnetic field \mathbf{b} are the same up to a multiplicative constant usually set to 1 in the incompressible case, whereas they may differ greatly in the compressible case). This is why some other ratios similar to the one in relation (5.4) are considered as well. Namely $\Lambda(E^K, E^M, \gamma)$, where the specific kinetic energy spectrum E^V is replaced by $E^K = \mathcal{P}(\mathbf{w})$ and $\Lambda(E^{V,sol.}, E^M, \gamma)$, where only the solenoidal part of the E^V spectrum is considered. The latter choice stems from the fact that in the incompressible case, no energy can be stored in the modes parallel to \mathbf{k} in Fourier space, that is $E^V = E^{V,sol.}$, and that $E^{V,sol.}$ corresponds to the energy associated with the kinetic helicity.

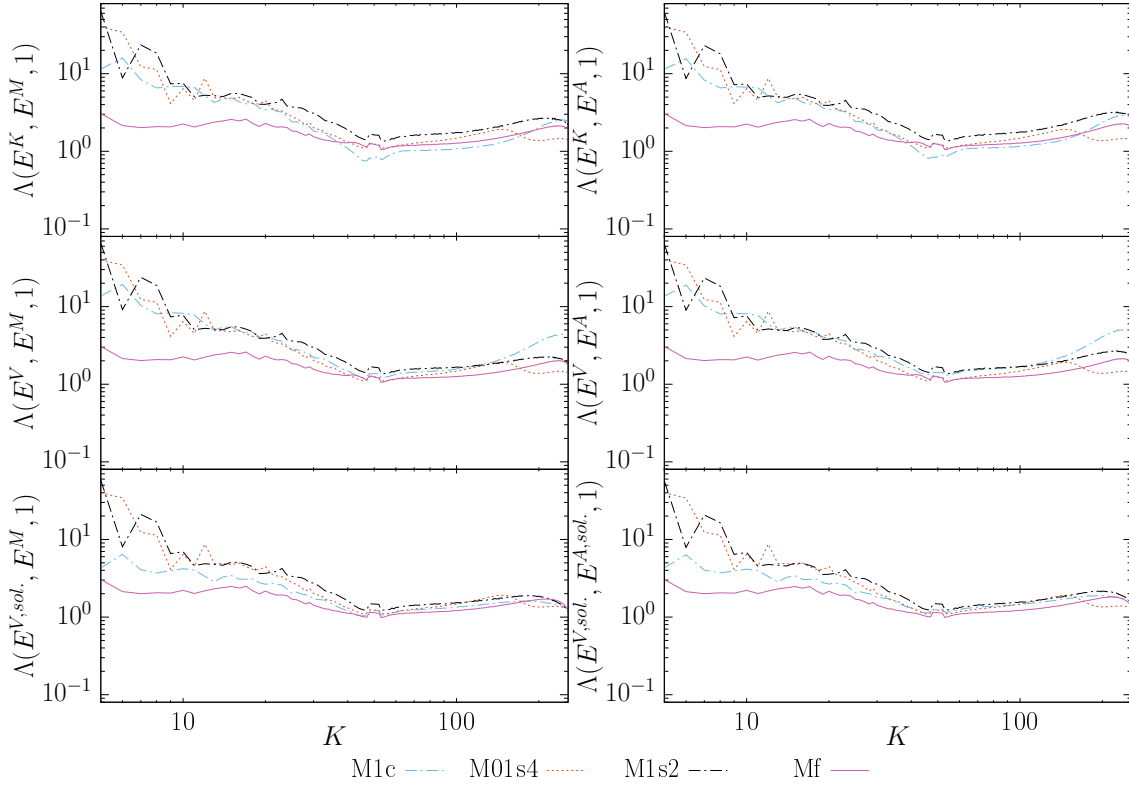


Figure 5.10: Test of relations of the type (5.4) for the subsonic and transonic runs with $\gamma = 1$, at an instant when $\mathcal{I}_{\mathcal{H}^M} \approx \frac{1}{6}L$.

Furthermore, as shown in section 5.1.2, the Alfvénic helicity exhibits in a wide range of compressibility the scaling law $H^A \sim K^m$ with $m \approx -1.3$. This exponent being the same than the current helicity one in the incompressible case, this motivates the consideration of the ratio (5.4), but replacing (E^M, H^J) with (E^A, H^A) . This is done as well when replacing E^V by E^K or $E^{V,sol.}$. In the latter case however, E^M is not replaced with E^A but with its solenoidal part $E^{A,sol.}$. For example:

$$\Lambda(E^K, E^A, \gamma) = \left(\frac{E^K}{E^A} \right)^\gamma \frac{H^A}{H^V}, \quad (5.5)$$

$$\Lambda(E^{V,sol.}, E^{A,sol.}, \gamma) = \left(\frac{E^{V,sol.}}{E^{A,sol.}} \right)^\gamma \frac{H^A}{H^V}. \quad (5.6)$$

In total, twelve possibilities are hence investigated for $\Lambda(E^1, E^2, \gamma)$, namely $(E^1, E^2) \in \{(E^K, E^M), (E^K, E^A), (E^V, E^M), (E^V, E^A), (E^{V,sol.}, E^M), (E^{V,sol.}, E^{A,sol.})\}$ and $\gamma \in \{1, 2\}$. They are plotted for all the considered runs at a comparable instant (when $\mathcal{I}_{\mathcal{H}^M} \approx \frac{1}{6}L$) on three decades in a double-logarithmic plot. A horizontal line in the region where the inverse transfer of magnetic helicity takes place is sought for, so as to verify relation (5.3).

For the sake of completeness, another possibility is presented in appendix C.1, with $E^1 = E^U = \mathcal{P}(\rho^{1/3}\mathbf{v})$. These figures are not shown in the main text since they exhibit in general a worse horizontal feature, as compared to the twelve above-mentioned ones.

5.2.2 Subsonic and transonic runs

Figures 5.10 and 5.11 show the twelve relations mentioned in section 5.2.1 for the subsonic and transonic runs M01s4, M1s2 and M1c, as well as for the Mf run. For these runs,

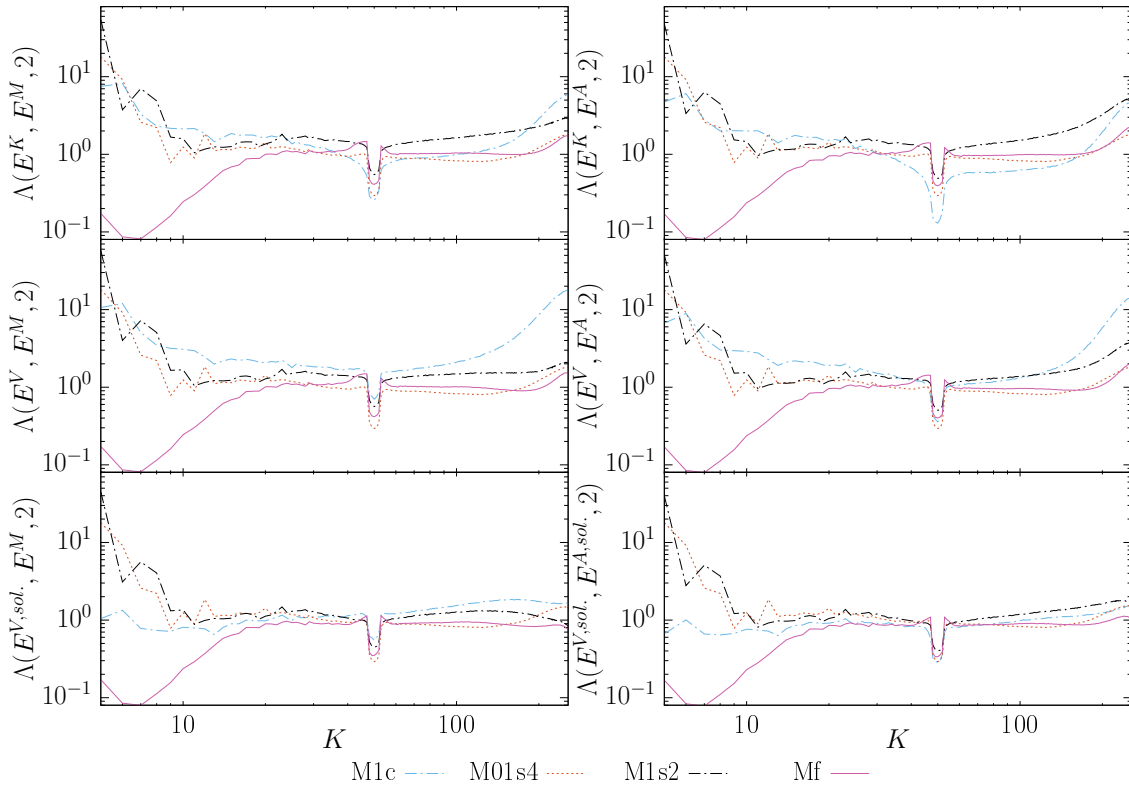


Figure 5.11: Test of relations of the type (5.4) for the subsonic and transonic runs with $\gamma = 2$, at an instant when $\mathcal{I}_{\mathcal{H}M} \approx \frac{1}{6}L$.

consistently with the findings in the incompressible case [82], the exponent $\gamma = 2$ gives in general a better horizontal line in the region $20 \leq K \leq 44$. Which of the (E^1, E^2) combination suits the relation best is not evident. The spread in the curves is smallest for $\Lambda(E^{V,sol}, E^M, 2)$ and $\Lambda(E^{V,sol}, E^{A,sol}, 2)$, and the M1c run exhibits a more horizontal curve for the choice $\Lambda(E^{V,sol}, E^{A,sol}, 2)$. For this last choice, $\Lambda \approx 1.1 \pm 0.3$ in the region $20 \leq K \leq 44$ for all these four runs. It is worth noticing that even though the Mf run does not present a power-law behaviour for the magnetic helicity and the magnetic energy (section 4.3), the Alfvénic balance found in the incompressible case [82] is still well verified.

5.2.3 Highly compressive runs

For the supersonic compressively-driven runs (figures 5.12 and 5.13), the exponent $\gamma = 1$ is more appropriate, even though for some runs and some variants of relation (5.4), a horizontal line is also found for $\gamma = 2$. Among the $\gamma = 1$ curves, it is similarly to the sub- and transonic curves not evident to tell which one of the variants is the most suitable. For example, the $\Lambda(E^K, E^M, 1)$ and $\Lambda(E^K, E^A, 1)$ ratios (see figure 5.12) are constant in a range $10 \lesssim K \lesssim 30$ for all the runs. As shown in section 7.2.3 however, these variants do not exhibit such a good horizontal at a higher resolution. On the other hand, when looking at the spread in the curves, it is clearly smallest for $\Lambda(E^V, E^A, 1)$ and $\Lambda(E^{V,sol}, E^{A,sol}, 1)$ with the ratio being approximately constant $\Lambda \approx 3 \pm 0.5$ and $\Lambda \approx 2.7 \pm 0.5$ respectively for $13 \leq K \leq 33$. Both choices (E^V, E^A) and $(E^{V,sol}, E^{A,sol})$ give similar results in the considered range, since the compressive parts of the \mathbf{v} and \mathbf{v}_A fields are quite small (see figures 4.21 and 5.5).

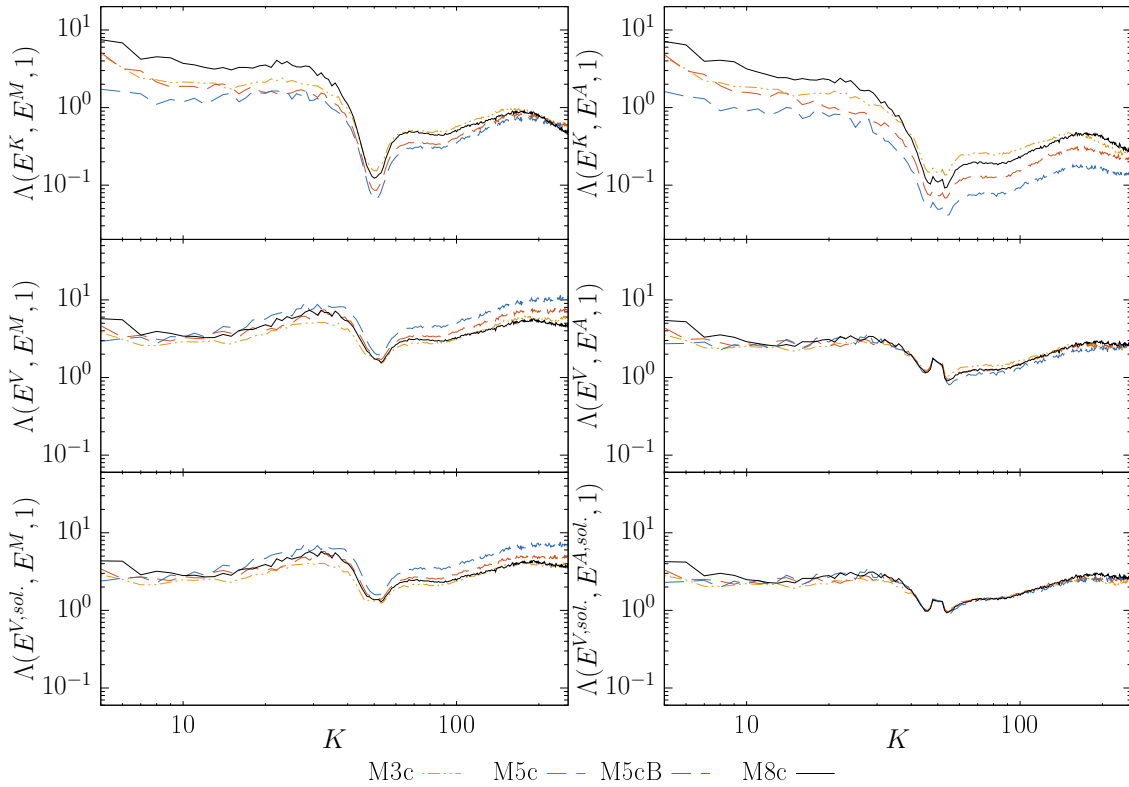


Figure 5.12: Test of relations of the type (5.4) for the supersonic compressively driven runs with $\gamma = 1$, at an instant when $\mathcal{I}_{\mathcal{M}} \approx \frac{1}{6}L$.

5.2.4 Supersonic solenoidally-driven runs

Lastly, the supersonic solenoidally-driven runs (figures 5.14 and 5.15) exhibit aspects that are intermediate between the sub- and transonic and the compressively-driven supersonic cases. For $\gamma = 2$ (figure 5.15), the M5s curves exhibit a good horizontal feature, comparable to the curves in the subsonic and transonic runs (figure 5.11). It would be included in the $\Lambda(E^{V,sol}, E^{A,sol}, 2) \approx 1.1 \pm 0.3$ relation found for the M01s4, M1s2, M1c and Mf runs in the range $12 \leq K \leq 40$. With increasing RMS Mach numbers, the horizontal gets worse with this $\gamma = 2$ exponent. On the other hand, the curves with $\gamma = 1$ (figure 5.14) exhibit the higher the RMS Mach number, the better a horizontal feature. The $\Lambda(E^{V,sol}, E^{A,sol}, 1)$ and $\Lambda(E^V, E^A, 1)$ relations, that exhibit a good horizontal and the least spread for the hypersonic compressively-driven runs (figure 5.12) would also include the M11s run: for this run, these two curves exhibit $\Lambda(E^{V,sol}, E^{A,sol}, 1) \approx 2.7 \pm 0.3$ and $\Lambda(E^V, E^A, 1) \approx 3.1 \pm 0.3$, in the $16 \leq K \leq 31$ range, which is very close to the values for the compressively-driven supersonic runs.

These results need however to be taken with appropriate caution. For the highly supersonic solenoidally-driven runs, some other variants exhibit good horizontals and very little spread as well. This is most notably the case for the $\Lambda(E^K, E^A, 2)$ and $\Lambda(E^K, E^M, 1)$ curves.

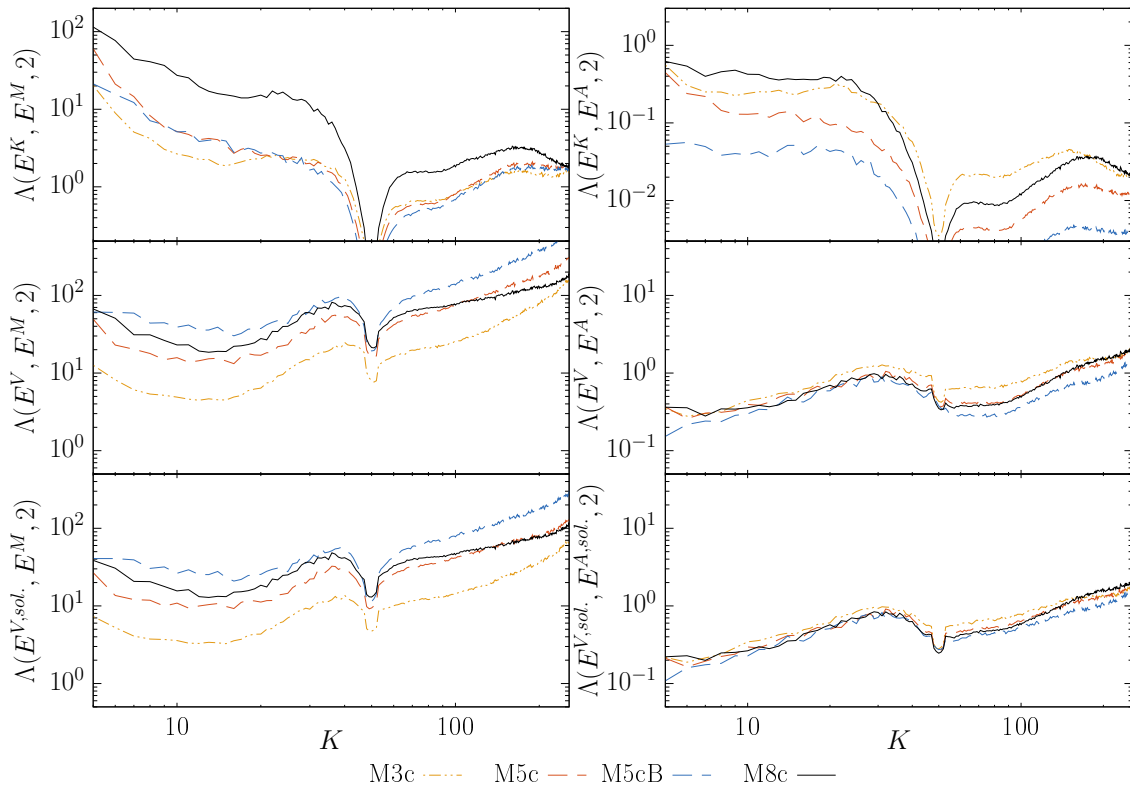


Figure 5.13: Test of relations of the type (5.4) for the supersonic compressively driven runs with $\gamma = 2$, at an instant when $\mathcal{I}_{\mathcal{H}M} \approx \frac{1}{6}L$.

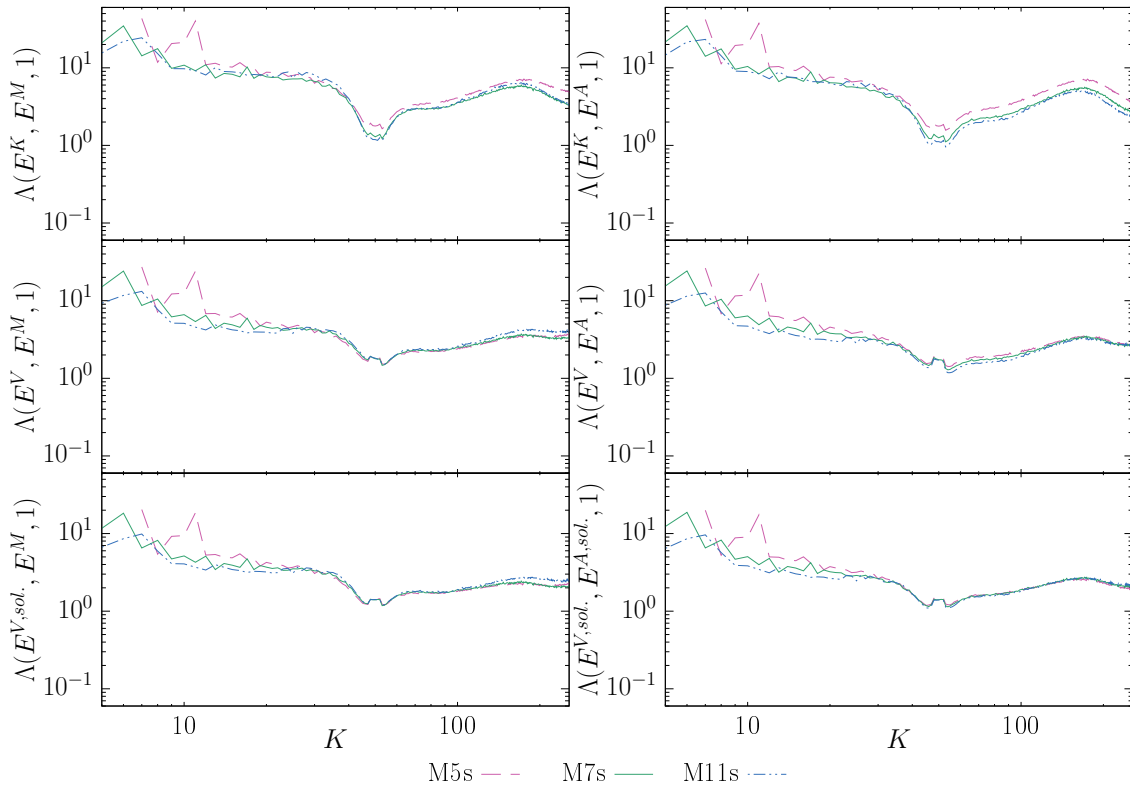


Figure 5.14: Test of relations of the type (5.4) for the supersonic solenoidally driven runs with $\gamma = 1$, at an instant when $\mathcal{I}_{\mathcal{H}M} \approx \frac{1}{6}L$.

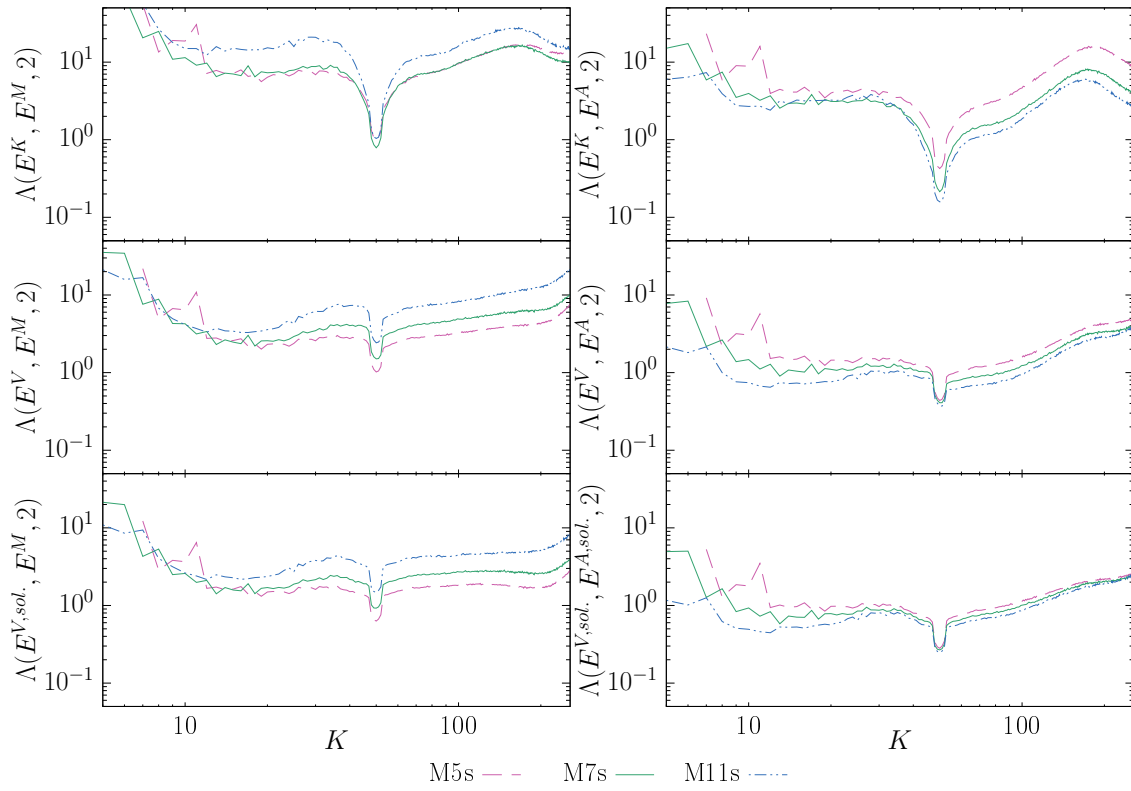


Figure 5.15: Test of relations of the type (5.4) for the supersonic solenoidally driven runs with $\gamma = 2$, at an instant when $\mathcal{I}_{\mathcal{H}^M} \approx \frac{1}{6}L$.

5.3 Conclusion

The magnetic helicity and energy spectra are flatter with increasing compressibility. While the deviations are relatively small for solenoidally-driven runs even at high Mach numbers of the order of 10, they are considerable for compressively-driven runs already at RMS Mach numbers of the order of 3. Remarkably however, the incompressible exponent of -1.3 for the current helicity is retrieved when considering the Alfvénic helicity spectra, even at high Mach number compressively-driven runs, with an RMS Mach number of the order of 8. Furthermore, even though the power spectra of $\mathbf{w} = \sqrt{\rho}\mathbf{v}$ and $\mathbf{u} = \rho^{1/3}\mathbf{v}$ present strong deviations at high compressibility, the velocity power spectra and their solenoidal part present a more universal behaviour, with an exponent close to the -1.2 one found in the incompressible case. This more universal behaviour seems valid as soon as the velocity spectrum compressive ratio is low enough in the inverse transfer region, which is the case for the solenoidally-driven runs and the compressively-driven ones with a high enough RMS Mach number.

This suggests that the quantities that matter for the Alfvénic balance are the kinetic and Alfvénic helicities, with the energy associated with them, that is $E^{V,sol.}$ and $E^{A,sol.}$ respectively. In all the runs analysed here, a balance consistent with the relation

$$\left(\frac{E^{V,sol.}}{E^{A,sol.}}\right)^\gamma \propto \frac{H^V}{H^A} \quad (5.7)$$

is indeed found in a certain range where the inverse transfer of magnetic helicity takes place. As observed in the incompressible case [82], the exponent $\gamma = 2$ is better suited for relatively low levels of compression, and tends to $\gamma = 1$ at higher compressibility. The proportionality constant seems quite stable even though the runs are very different: for low levels of compression it is around 1.1, and for high levels at around 2.7.

This last result is however to be taken with appropriate caution. A lot of variants of relation (5.7) exhibit indeed domains where a horizontal line is visible. The fact that many relations seem to work could partially be caused by a lack of numerical resolution, as discussed in section 7.2.3, so that studies at higher resolutions should be performed in order to confirm the validity of relation (5.7), and possibly discard some of its variants. The relation (5.7) is preferred because of: (i) the lesser spread of the curves at the two extreme cases (sub- and transonic runs and compressively-driven supersonic runs) and (ii) the natural extension of the incompressible case when considering the power spectra associated with the kinetic and Alfvénic helicities. However, (i) the Alfvénic balance already observed in the incompressible case (relation (5.3)) does not require a universal constant of proportionality, so that a small spread could maybe not be such a relevant feature, and (ii) the parallelism with the incompressible case is not a necessity, even though it appears plausible because of the incompressible scaling laws for H^A and $E^{V,sol.}$ are still observed even at high compressibility.

Nevertheless, the collapse of the curves with a certain proportionality constant over a wide range of compressibility is worth to be documented and could help to understand better the dynamics of magnetic helicity transfers in strongly compressible turbulence in the future.

Chapter 6

Spectral transfer analysis

The shell-to-shell transfer functions (section 2.4) and the helical decomposition (section 2.3) are jointly used in this chapter in order to disentangle aspects of the magnetic helicity's inverse transfer dynamics. First, the most compressive M8c run is studied in greater detail in sections 6.1 to 6.3. One particular instant in time, namely $t \approx 0.131t_\tau$ is chosen, when the magnetic helicity integral scale is $\mathcal{I}_{\mathcal{H}^M} \approx \frac{1}{10}L$. This instant is preferred over the one when $\mathcal{I}_{\mathcal{H}^M} \approx \frac{1}{6}L$ (the instant chosen for most of the figures in this work) since some aspects are more easily visible when the integral scale is somewhat closer to the magnetically-driven scales. As described in section 2.4.1, the magnetic helicity transfer function $\mathcal{T}^{\mathcal{H}^M}(Q, P, K) = 2 \int \mathbf{b}_K \cdot (\mathbf{v}_P \times \mathbf{b}_Q) dV$ represents the transfer rate of magnetic helicity from magnetic shell Q to magnetic shell K mediated by the velocity field at shell P . This function can also be decomposed in helical components, as described in section 2.4.4. In sections 6.1 to 6.3 these functions are analysed in three steps:

- In section 6.1, the magnetic helicity transfer spectra are considered. This is equivalent to summing the $\mathcal{T}^{\mathcal{H}^M}$ transfer function over $P, Q \in [1, K_{max}]$. In this section, the helical contributions which play the biggest roles are determined.
- Section 6.2 considers sums of transfer functions along one dimension, for example summing $\mathcal{T}^{\mathcal{H}^M}$ over $P \in [1, K_{max}]$ in order to see the shell-to-shell transfer rates. Further analysis through helical decomposition, the exploration of the role of the mediating velocity field as well as the study of energy exchanges both between magnetic shells and between the magnetic and the velocity fields allow to identify which terms are responsible for which features in the shell-to-shell transfers as well as a phenomenology of the underlying physical mechanisms.
- Lastly, section 6.3 deals with the helical geometric factor regulating the triadic interactions governing the magnetic field evolution and puts it in parallel with the 3D transfer function $\mathcal{T}^{\mathcal{H}^M}(Q, P, K)$. This analysis sheds some light on the observations made in section 6.2.

The conclusions drawn are then confronted to other turbulent states. In section 6.4.1, the extreme cases considered in this work, namely the most compressible solenoidally-driven run M11s, the least compressible compressively-driven run M1c as well as the subsonic M01s4 run are considered, at an instant when $\mathcal{I}_{\mathcal{H}^M} \approx \frac{1}{10}L$. The analysis is not performed in great detail, as only the most striking similitudes and differences with respect to the M8c run are underlined. Some results are also compared with previous research in section 6.4.2.

Lastly, section 6.5 gives a summary of the results gained in this chapter and proposes some possibilities for future work.

The shell-to-shell transfer functions are computed as described in section 3.4. The functions linked with energy transfers, such as $\mathcal{U}^{\mathcal{E}^M}(Q, P, K)$ and all its various decompositions (helical decomposition, or in terms of magnetic \leftrightarrow magnetic exchanges and magnetic \leftrightarrow kinetic exchanges, etc.), are normalised by the magnetic energy injection rate ϵ_{inj}^M . Similarly, the transfer functions linked with magnetic helicity transfers, that is $\mathcal{T}^{\mathcal{H}^M}(Q, P, K)$ and its various decompositions, are normalised by the magnetic helicity injection rate estimated through relation (4.5) with $h_f = +1$, $K_{inj}^{\mathcal{H}^M} = 50$. Hence, even if it is not written explicitly in the different figures, the transfer rates are expressed in units of the corresponding injection rate, unless specified otherwise.

6.1 Fourier transfer spectra

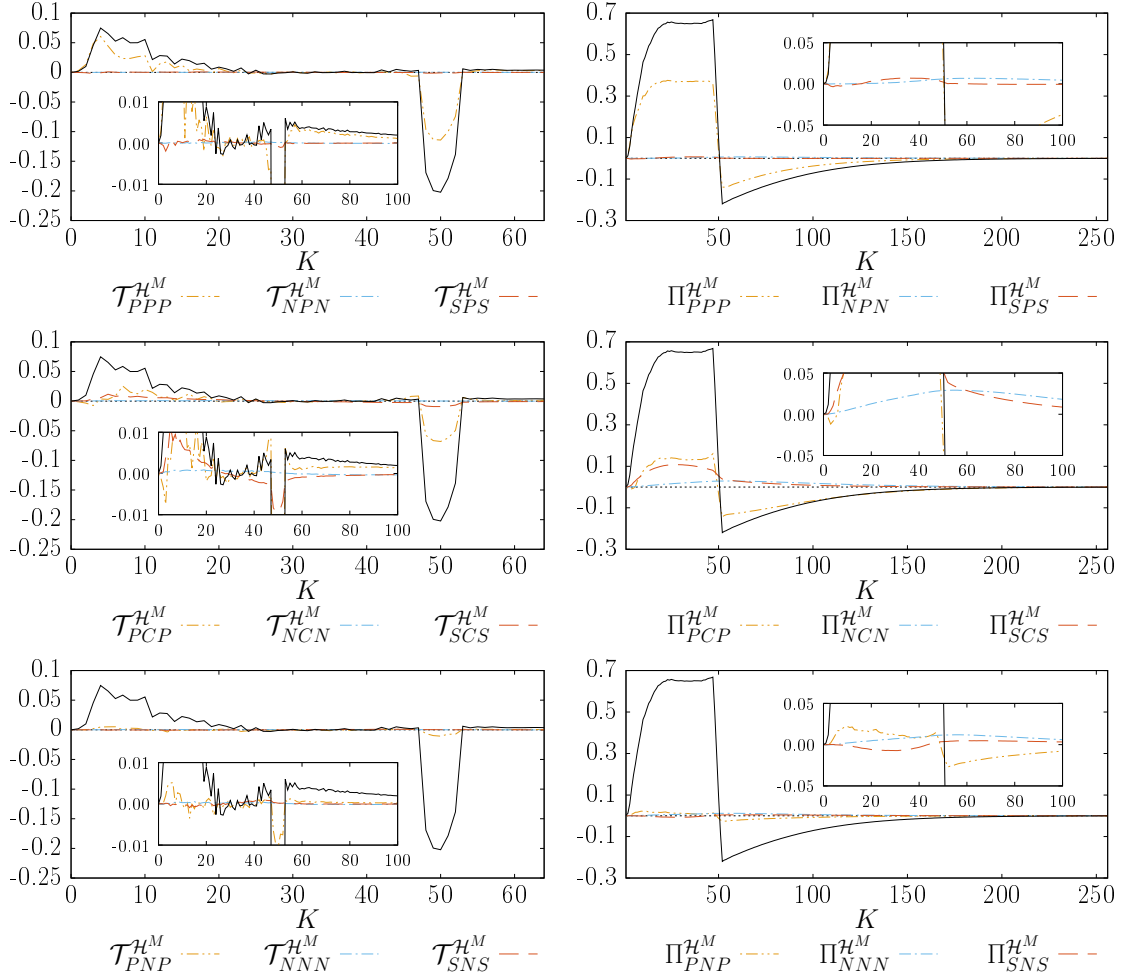


Figure 6.1: Magnetic helicity transfer spectra (left) and fluxes (right), for the M8c run at an instant when $\mathcal{I}_{\mathcal{H}^M} \approx \frac{1}{10}L$, split in nine different helical contributions (top, mediated by the positively helical field, middle, bottom: by the negatively helical velocity field). The solid black curve in each plot corresponds to the total curve (transfer spectrum or flux), sum of the nine contributions. The dotted black line corresponds to $y = 0$ and the insets present a zoom on the region close to $y = 0$.

In order to estimate which helical contributions play the biggest roles, the nine conservative helically-decomposed transfer spectra $\mathcal{T}_{s_K s_P s_Q}^{\mathcal{H}^M}(K) = \sum_Q \sum_P \mathcal{T}_{s_K s_P s_Q}^{\mathcal{H}^M}(Q, P, K)$ (section 2.4.4) are compared to each other and to the total transfer spectrum $\mathcal{T}^{\mathcal{H}^M}(K) = 2\mathcal{Q}(\mathbf{b}, \mathbf{v} \times \mathbf{b})$ (section 2.1.2). The corresponding spectral fluxes:

$$\Pi_{s_K s_P s_Q}^{\mathcal{H}^M}(K) = \sum_{K_0=1}^K \mathcal{T}_{s_K s_P s_Q}^{\mathcal{H}^M}(K_0) \quad (6.1)$$

are also considered. They express the transfer rate of magnetic helicity coming into the ball of radius K from all shells $K_0 > K$ outside the ball. The magnetic helicity transfer and flux spectra are shown in figure 6.1 for the M8c run at an instant when $\mathcal{I}_{\mathcal{H}^M} \approx \frac{1}{10}L$.

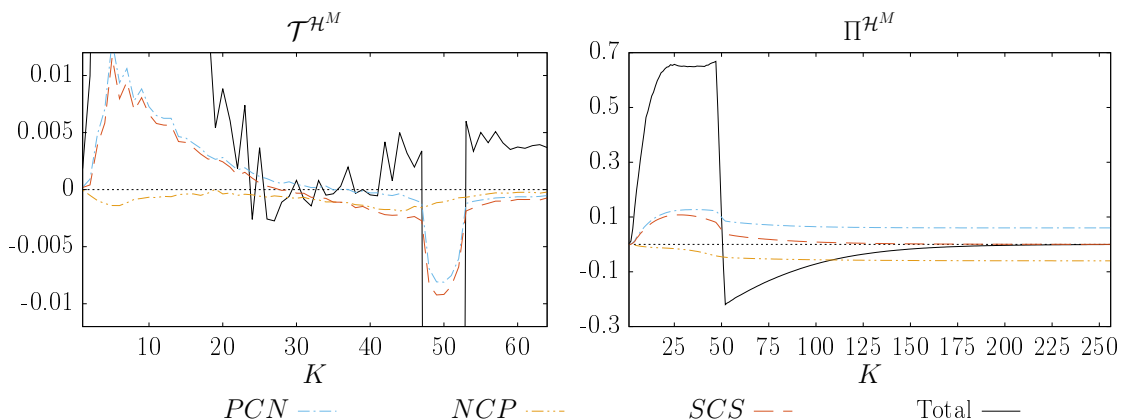


Figure 6.2: Illustration of the fact that the heterochiral terms are not conservative when not considered in pairs by considering the two terms in the $SCS = PCN + NCP$ term of figure 6.1 individually.

As expected, all the fluxes are conservative, that is $\Pi_{s_K s_P s_Q}^{\mathcal{H}^M}(K) \xrightarrow{K \rightarrow K_{max}} 0$ for the $\{PPP, PCP, PNP, NPN, NCN, NNN, SPS, SCS, SNS\}$ combinations. Figure 6.2 illustrates the fact that the heterochiral terms are not conservative on their own but need to be taken in pairs (see section 2.4.4) by showing as an example the transfer spectra and fluxes associated with PCN , NCP and their sum.

The dominant transfer term for the M8c run at this instant when $\mathcal{I}_{\mathcal{H}^M} \approx \frac{1}{10}L$ is the PPP one, which accounts for most of the transfers, especially at the largest scales, and about half of the (negative) transfers at the electromotive forcing scales. Then comes the PCP term, which is responsible for roughly a third of the negative transfer at the electromotive forcing scale and plays a significant role at large scales, albeit smaller than the one of the PPP term. The two other terms that play a visible role in the $\mathcal{T}^{\mathcal{H}^M}$ curves are the SCS and PNP terms, while the others are barely visible. Figure 6.3 shows the sum of the four dominant PPP , PCP , SCS and PNP terms. Even though their sum represents quite well the total transfer, some differences are still noticeable, especially when considering the flux $\Pi^{\mathcal{H}^M}(K)$. The $\Pi^{\mathcal{H}^M}$ plots show that among the smallest terms, the NCN one plays a bigger role.

The spectral flux $\Pi^{\mathcal{H}^M}(K)$ being normalised by an estimate of the magnetic helicity injection rate, it provides some information about the numerical scheme's dissipation. Indeed, about two thirds of the injected magnetic helicity is transferred to scales larger than the electromotive forcing scale (because $\Pi^{\mathcal{H}^M}(K = 47) \approx 0.67$). This is consistent with figure 4.17.(b), which shows that the total magnetic helicity present in the system grows at a rate of about 60 percent of the magnetic helicity injection for the M8c run.

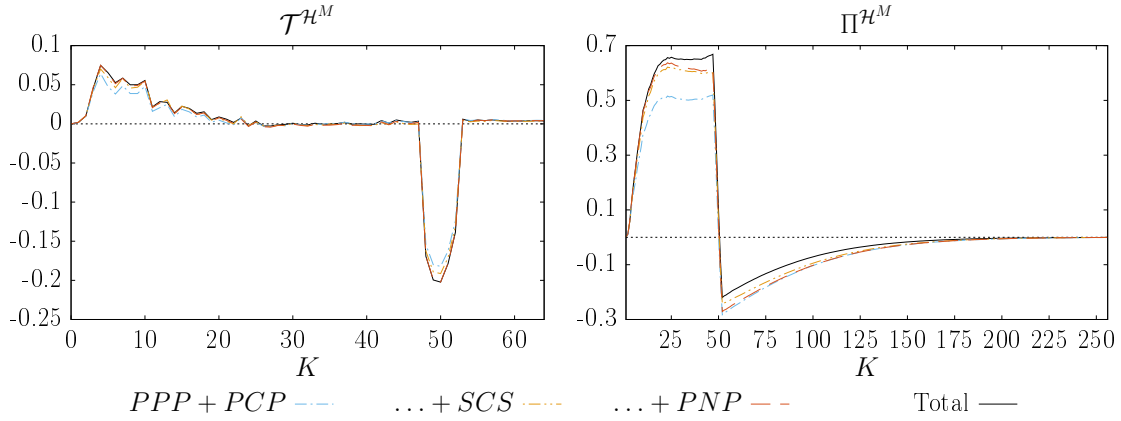


Figure 6.3: Comparison of the sum of two, three or four dominant terms of figure 6.1 to the total transfer spectrum and flux.

This growth rate is smaller than two thirds because of numerical dissipative effects. The rest of the injected magnetic helicity is either transferred to smaller scales ($\Pi^{\mathcal{H}^M}(K = 52) \approx -0.22$, so that a direct transfer concerns about one fifth of the injected magnetic helicity), where it is predominantly dissipated. The remaining ten percent of injected magnetic helicity are dissipated at the magnetically-forced scales.

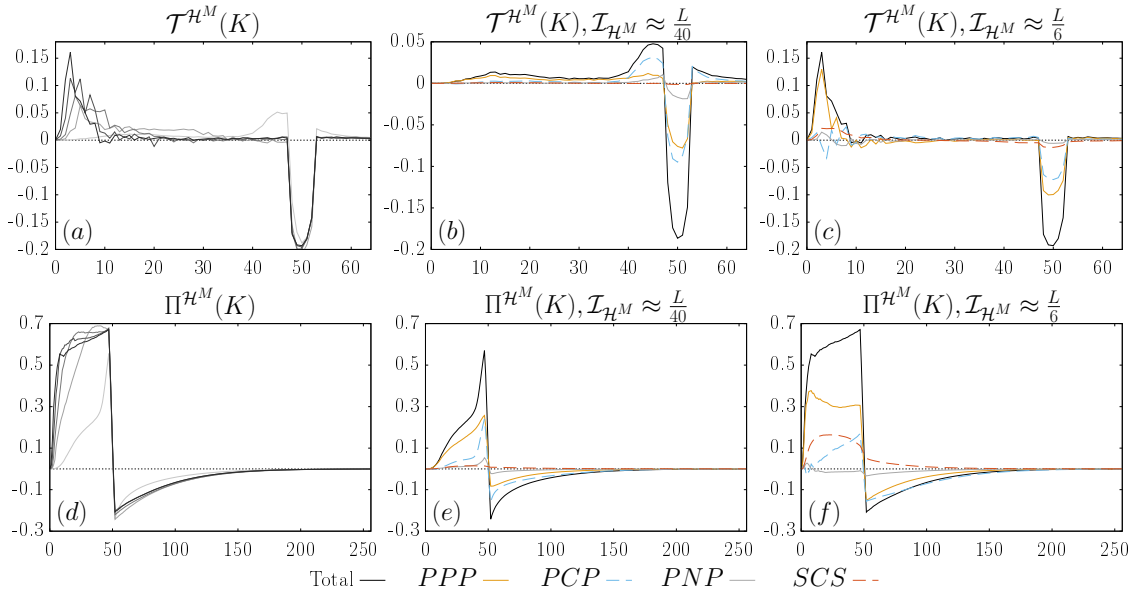


Figure 6.4: (a) Time evolution of the magnetic helicity transfer Fourier spectra for the M8c run, 5 snapshots equally spaced in time from $t \approx 0.020t_{\mathcal{T}}$ to $t \approx 0.25t_{\mathcal{T}}$. (b, c) Magnetic helicity transfer spectra at the extreme instants of subfigure (a), when $\mathcal{I}_{\mathcal{H}^M} \approx \frac{1}{40}L$ and $\mathcal{I}_{\mathcal{H}^M} \approx \frac{1}{6}L$ respectively and some important helical contributions. (d-f) Same as (a-c) but with the magnetic helicity fluxes.

In hydrodynamic turbulence, since the nonlinear direct energy flux is constant in the inertial range, one expects to see a plateau in that region. A perfect plateau behaviour is however hard to observe in practice, even at relatively high resolutions, due to non-ideal numerical effects (see for example reference [1]). For the inverse transfer of magnetic helicity, since power-law scalings are observed (section 5.1), one could as well expect a plateau behaviour. This is indeed the case in the range $25 \lesssim K \lesssim 45$ (figure 6.1), where the total flux is roughly constant. This plateau is however strongly affected by adverse

effects due both to non-ideal numerical effects and possibly boundary-effects at later times. Figures 6.4.(a, d) show the time evolution of magnetic helicity transfer spectra and fluxes. At other instants in time, even though the plateau behaviour does not look as good, the flux is still roughly constant: at the latest considered instant (the darkest curve when $\mathcal{I}_{\mathcal{H}^M} \approx \frac{1}{6}L$), the flux is roughly $0.6 \pm 10\%$. When using lower-order numerics or a lower resolution, the plateau behaviour may be significantly affected, see section 7.2.

Which helical contributions play which role depends also on the considered instant in time: at early times the *PCP* term is responsible for strong local inverse transfers (close to the magnetically-forced scales, see figure 6.4.(b)), whereas at later times its role is more non-local. The *PNP* term plays as well a greater role at early instants, as compared to later times, whereas the *SCS* term, which is very small at the inverse transfer's beginning, plays a greater role at later times.

6.2 Transfer functions: 2D plots

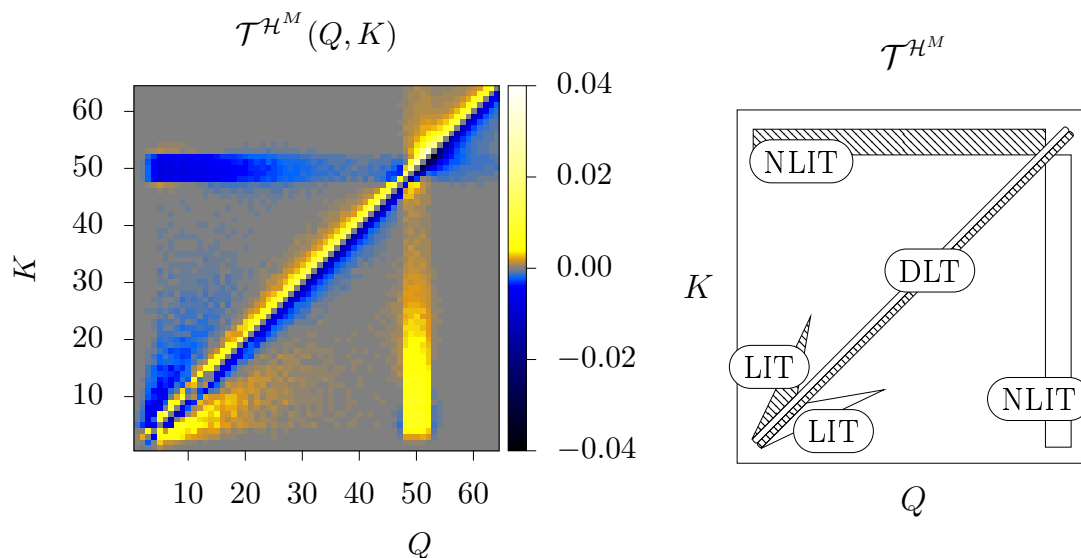


Figure 6.5: Magnetic helicity transfer rates from shell Q to shell K for the M8c run, at an instant when $\mathcal{I}_{\mathcal{H}^M} \approx \frac{1}{10}L$.

A shell-to-shell approach reveals that within the general picture of an inverse transfer of magnetic helicity, three different features, corresponding to three different physical mechanisms are occurring. Figure 6.5, which shows $\mathcal{T}^{\mathcal{H}^M}(Q, K)$ of the M8c run at an instant when $\mathcal{I}_{\mathcal{H}^M} \approx \frac{1}{10}L$, reveals the existence of:

1. A (d)irect (l)ocal (t)ransfer of magnetic helicity (along the diagonal, labelled “DLT” on the sketch and named so henceforth). This direct magnetic helicity cascade would remain “hidden” if one would only consider 1D Fourier transfer spectra.
2. A mostly (l)ocal (i)nverse (t)ransfer (wing-shaped, labelled “LIT” on the sketch and named so hereafter), close to the magnetic helicity integral scale.
3. A mostly (n)on-(l)ocal (i)nverse (t)ransfer (vertical and horizontal bars, labelled “NLIT” on the sketch and named so in the following), from the electromotive forcing

scale, up to scales even larger than the integral scale.

This kind of figures allow indeed to determine the transfer's direction and locality. They can be interpreted as written below:

- A local transfer between shells Q and K means that $Q \approx K$, that is, the term is close to the diagonal. Since a linear binning is used here for the shells however, one should be careful when considering transfers that are not close to the diagonal: a linear binning tends indeed to overestimate the non-locality of the transfers, as compared to a logarithmic binning (see section 2.4). Furthermore, locality of the *magnetic helicity transfer* between shells Q and K does not necessarily mean that the *interactions* themselves are local, since mediating P shells could be far from $Q \approx K$. Some aspects about the locality of the *interactions* are reviewed in section 6.3.
- The transfer's direction is given by the sign of $\mathcal{T}^{\mathcal{H}^M}(Q, K)$. For example, above the main diagonal, that is, for $K > Q$, when $\mathcal{T}^{\mathcal{H}^M}(Q, K) > 0$ (orange/bright color), then shell Q gives magnetic helicity to shell $K > Q$, which means a direct transfer, whereas when $\mathcal{T}^{\mathcal{H}^M}(Q, K) < 0$ (blue/dark color), the shell Q receives magnetic helicity from shell $K > Q$ and the transfer is inverse. Under the main diagonal, the situation is opposite: a positive value means an inverse transfer whereas a negative one a direct transfer.

In the following subsections, the aim is to shed some light on the causes behind these three DLT, LIT and NLIT features through several approaches. Section 6.2.1 considers a helical decomposition of the magnetic helicity transfer function, section 6.2.2 explores the role of the mediating velocity field and section 6.2.3 splits the transfer function in terms of energy exchanges: magnetic \leftrightarrow magnetic exchanges as well as kinetic \leftrightarrow magnetic exchanges. Several observations made in these subsections are justified by the geometric factor analysis of section 6.3.

For visualisation purposes, the extremes of the 2D plots' colour bars in this chapter are *not* the extremes of the plotted functions, but typically smaller. Otherwise, relatively isolated extrema would make some features less visible on the graphs. These plots aim rather at displaying the qualitative behaviour: between which and which shells do direct/inverse transfer occur. The differences in colour are there to provide only an approximate idea of their relative strength. When more precise quantitative aspects need to be underlined, cuts of the 2D plots are presented.

6.2.1 Helical decomposition

As already observed in section 6.1, the two terms contributing the most to the magnetic helicity inverse transfer are the *PPP* and *PCP* ones. Their role differ: when both terms contribute to the NLIT in comparable proportions, the *PPP* term is mostly responsible for the LIT whereas the *PCP* term plays the major role for the DLT (figure 6.6).

Cuts along $K_0 \in \{10, 30, 50\}$, displayed in figure 6.7, give a more quantitative picture. These cuts correspond to the magnetic helicity integral scale, the magnetically-forced scale, and a region in between. A positive (negative) value at a certain Q shell means that the K_0 shell receives (gives) magnetic helicity from (to) shell Q . In addition to another visualisation of the LIT (visible through the *PPP* term in subfigures (a) and (b)), these cuts reveal that the contribution of the *PCP* term to the DLT is about an order of magnitude larger than the *PPP* term's contribution (subfigure (b)) and that the NLIT

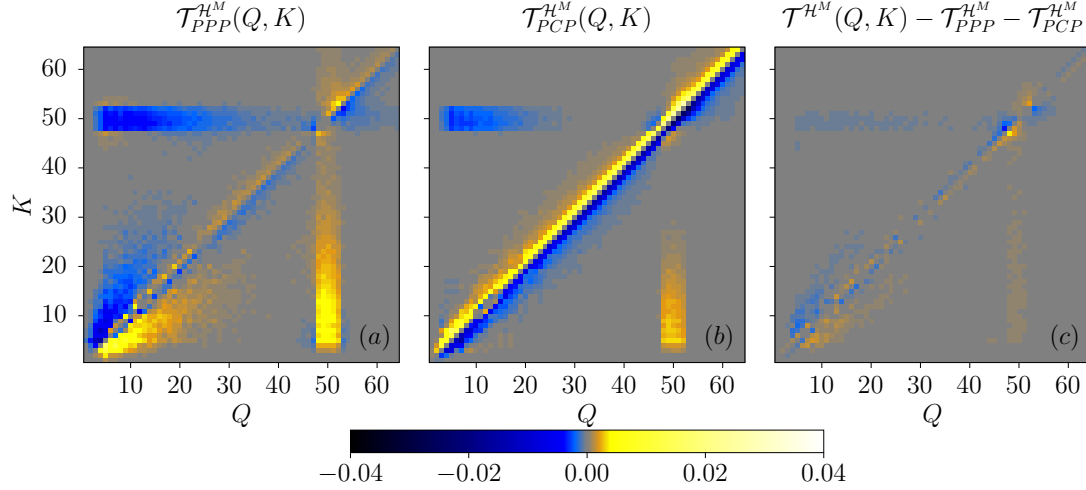


Figure 6.6: Contributions from the *PPP* and *PCP* terms to the magnetic helicity transfer rates for the M8c run, at an instant when $\mathcal{I}_{\mathcal{H}^M} \approx \frac{1}{10}L$. Their sum is close to the total transfer function from figure 6.5 and the remaining contributions come mostly from the terms shown in figure 6.8.

is stronger and spreading over more shells for the *PPP* term as compared to the *PCP* one (subfigure (c)): at $K_0 = 50$, $\mathcal{T}_{PPP}^{\mathcal{H}^M}(Q, 50) < 0$ for all the shells $Q < K_0$ whereas $\mathcal{T}_{PCP}^{\mathcal{H}^M}(Q, 50) < 0$ in a visible way only starting $Q \gtrsim 30$.

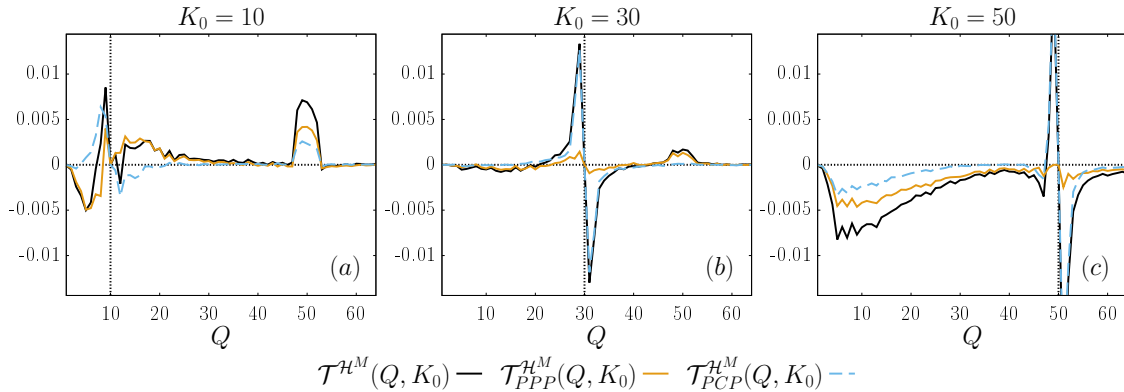


Figure 6.7: Cuts from the 2D plots of figure 6.6 for $K_0 \in \{10, 30, 50\}$. The horizontal dotted line corresponds to $y = 0$ and the vertical one to $Q = K_0$.

The remaining smaller helical contributions are responsible for an *inverse* (small) transfer along the diagonal, and some additional (small) contributions to the LIT and NLIT (figure 6.6.(c)). These features are essentially due to the *PNP*, *NCN* and *SCS* terms, which transfer functions are shown in figure 6.8 (note that the colour bar extremes are smaller by a factor of 10 as compared to figure 6.6). The *PNP* term exhibits a shape similar to the *PPP* one, with a DLT, a LIT and a small NLIT. Both the LIT and the NLIT due to the *PNP* term are more local, as compared to the ones due to the *PPP* term: the LIT “wings” are closer to the diagonal and the NLIT “rectangular bars” are closer to the magnetically-forced scales. The *NCN* term corresponds to a direct cascade of negative magnetic helicity (since the Fourier transformed $\mathbf{v}^C \times \mathbf{b}^N$ term is projected on the negatively helical magnetic field), which results in a contribution equivalent to an inverse cascade of (positive) magnetic helicity along the diagonal. The *SCS* term has a more exotic shape: while it contributes to an inverse transfer in a wide range of scales, including the LIT, its biggest contribution is associated with a kidney-like shape for the

non-local inverse transfer from the magnetically-forced scales. A short discussion about this *SCS* term can be found in appendix C.2.

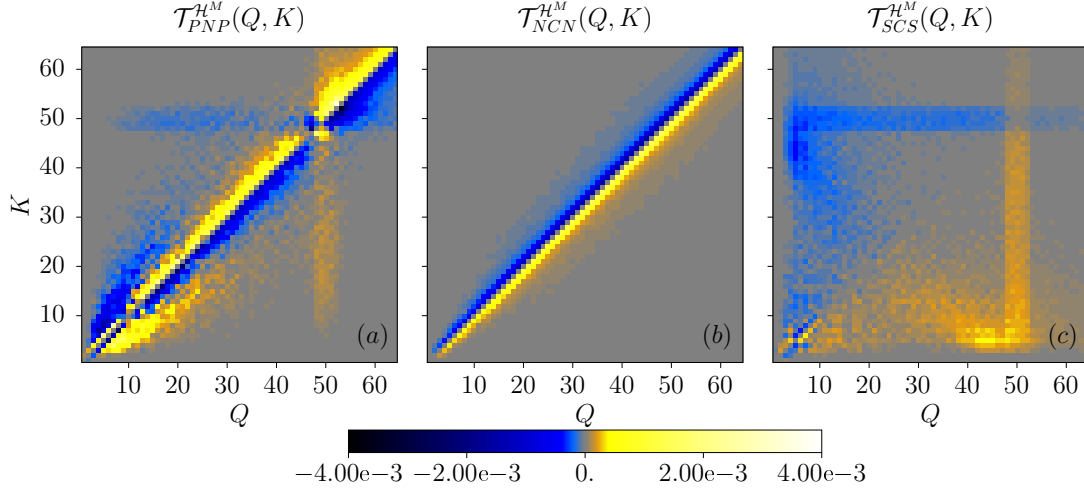


Figure 6.8: Contributions from the *PNP*, *NCN* and *SCS* terms to the magnetic helicity transfer rates for the M8c run, at an instant when $\mathcal{L}_{\mathcal{H}^M} \approx \frac{1}{10}L$.

The cuts displayed in figure 6.9 give another angle of view of the last paragraph’s observations.

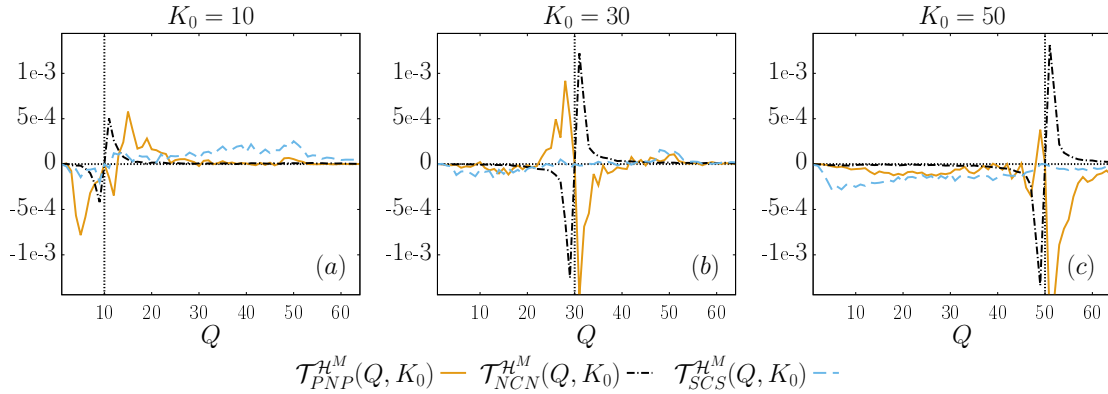


Figure 6.9: Cuts from the 2D plots of figure 6.8 for $K_0 \in \{10, 30, 50\}$. The horizontal dotted line corresponds to $y = 0$ and the vertical one to $Q = K_0$.

As for the four remaining smallest helical contributions, *NPN*, *NNN*, *SPS* and *SNS*, even though they present amplitudes smaller by about two orders of magnitude as compared to the total term (see figure 6.10 and its colour bar), it is still instructive to consider their shape in the (Q, K) plane. These terms could indeed play more dominant roles in different numerical setups (see for example section 7.1). The *NPN* and *NNN* terms consist of a weak direct local transfer of negative magnetic helicity along the diagonal, which results in a (very small) contribution as an inverse local transfer of magnetic helicity. A small local inverse transfer of negative magnetic helicity also occurs at the largest scales for the *NNN* term, which is the pendant of the LIT “wings” of the *PPP* term. Small hints for such an inverse transfer are also present for the *NPN* term (orange dots above the main diagonal and blue dots under it). The heterochiral *SPS* and *SNS* terms have more exotic shapes: more about them can be found in appendix C.2.

To summarise, even though each helical contribution plays different roles of varying relative importance, the dynamics are mostly governed by the *PPP* and *PCP* terms.

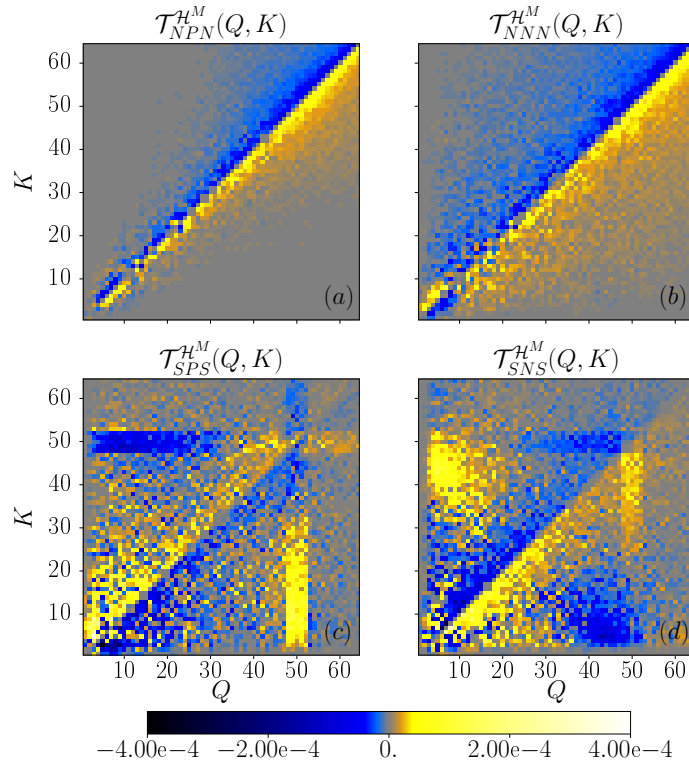


Figure 6.10: Contributions from the NPN , NNN , SPS and SNS terms to the magnetic helicity transfer rates for the M8c run, at an instant when $\mathcal{I}_{\mathcal{H}^M} \approx \frac{1}{10}L$.

This is expected since the electromotive forcing injects fully positive helical fluctuations so that positive magnetic helicity dominates the system at all scales. The leading role in the magnetic helicity inverse transfer is taken by the PPP term, which contributes most to the LIT and the NLIT. The compressive part of the velocity field participates significantly in the inverse transfer through non-local transfers, but takes as well the leading role in the DLT of magnetic helicity to smaller scales. These aspects can be well explained by comparing the geometric factors in the triadic interactions (see section 6.3).

6.2.2 Role of the mediator

As mentioned in section 2.2.3, the velocity field cannot generate magnetic helicity and simply acts as a mediator. Each of the DLT, LIT and NLIT features can be associated with different velocity scales, as shown in figure 6.11. This figure displays $\mathcal{M}^{\mathcal{H}^M}(P, K)_{\Sigma_Q} = \sum_Q \mathcal{T}^{\mathcal{H}^M}(Q, P, K)$, which quantifies the importance of the mediating velocity field at shell P with respect to transfers of magnetic helicity to shell K . Three clear regions can be delimited along the P -axis, each of them corresponding to one of the three features:

1. At small scales ($P \in [30, K_{max}]$), magnetic helicity is taken from the shells $K \approx 50$ and given essentially to the shells $K \lesssim 30$. This corresponds to the NLIT.
2. The intermediate scales ($P \in [4, 30]$), are responsible for the LIT since magnetic helicity is taken from shells $K \lesssim 30$ and given to shells at larger scales which are relatively close.

3. At large scales ($P \in [1, 4]$), $\mathcal{M}^{\mathcal{H}^M}(P, K)_{\Sigma_Q}$ alternates signs for $10 \lesssim K \lesssim 45$. This corresponds to the DLT.

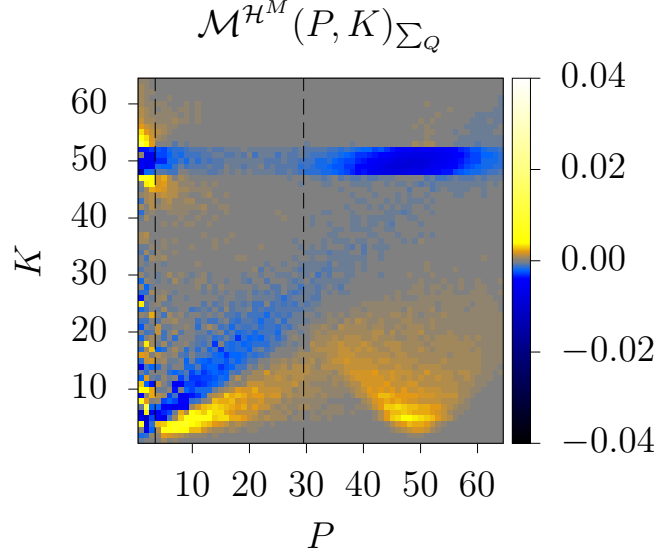


Figure 6.11: Magnetic helicity transfer function summed over the Q index, showing the influence of the mediating velocity field at shell P on the magnetic field at shell K for the transfers from all the magnetic field Q shells, for the M8c run at an instant when $\mathcal{I}_{\mathcal{H}^M} \approx \frac{1}{10}L$. The two dashed vertical lines delimit the domains labelled “small scales”, “intermediate scales” and “large scales” as described in the text.

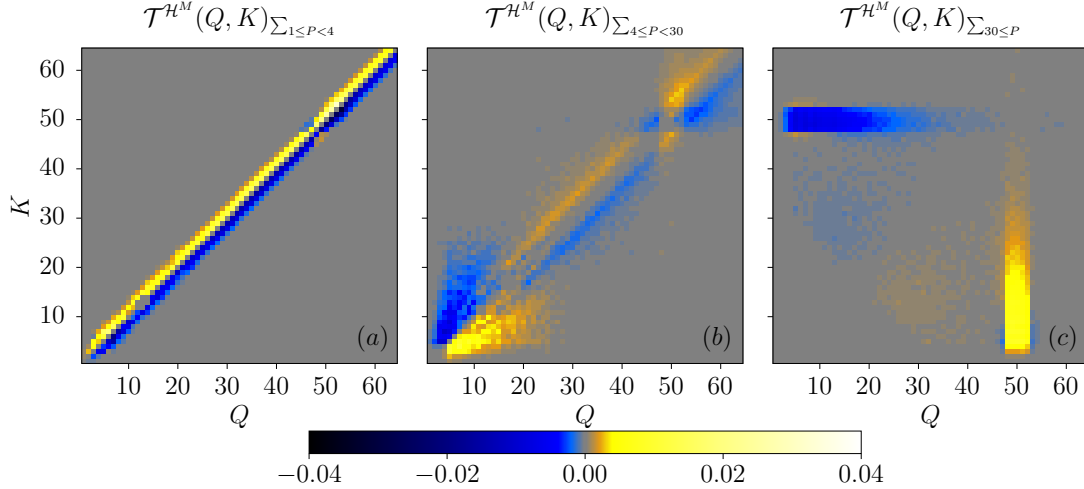


Figure 6.12: Magnetic helicity transfer rates from shell Q to shell K , but taking into consideration only the large ($P \in [1, 4]$), intermediate ($P \in [4, 30]$), and small ($P \in [30, K_{max}]$) scales of the mediating velocity field (M8c run, at an instant when $\mathcal{I}_{\mathcal{H}^M} \approx \frac{1}{10}L$).

This interpretation is confirmed through figure 6.12, which shows the transfer function mediated only by the velocity at the above-defined scales: $\mathcal{T}^{\mathcal{H}^M}(Q, K)_{\Sigma_{p_1 \leq P < p_2}} = \sum_{p_1 \leq P < p_2} \mathcal{T}^{\mathcal{H}^M}(Q, P, K)$, with $P \in [30, K_{max}], [4, 30], [1, 4]$. Two other visualisations of this fact are given in figure 6.13, which displays cuts of figure 6.12 across $K_0 = 10$ as well as the influence of each velocity scale on the total transfer spectrum (by showing $\mathcal{T}^{\mathcal{H}^M}(K)_{\Sigma_{P \in \Phi_{\mathbf{v}}}} = \sum_{P \in \Phi_{\mathbf{v}}} \sum_{Q \in [1, K_{max}]}$ $\mathcal{T}^{\mathcal{H}^M}(Q, P, K)$ for $\Phi_{\mathbf{v}} = [30, K_{max}], [4, 30], [1, 4]$).

The fact that the DLT is mediated by the large scale velocity field shows that even though the magnetic helicity transfer is local, the triadic interactions which result in this direct local transfer are not (see section 6.3).

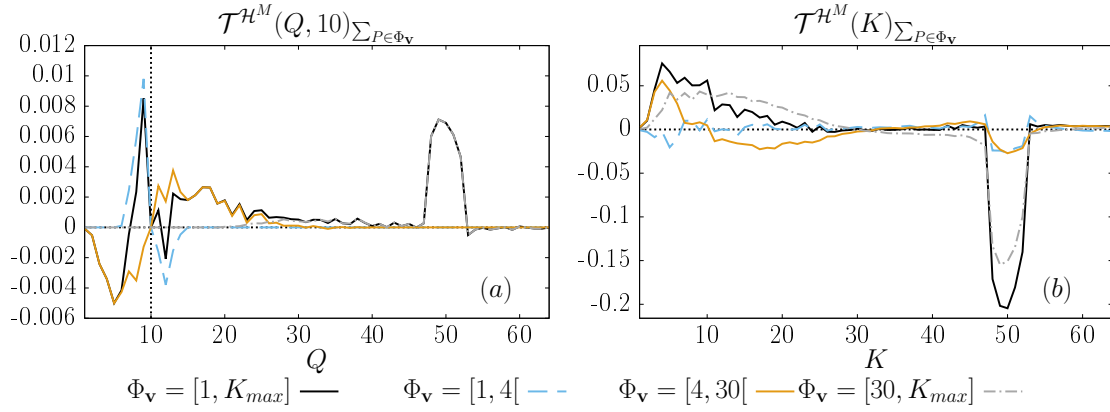


Figure 6.13: (a) Cuts from figure 6.12 at $K = 10$, the total curve where $\Phi_{\mathbf{v}} = [1, K_{max}]$ corresponds to the one in figure 6.7.(a). (b) Total transfer spectra corresponding to the different velocity field contributions. The total one ($\Phi_{\mathbf{v}} = [1, K_{max}]$) corresponds to the transfer spectra of section 6.1.

6.2.3 Energy exchanges

Decomposition in kinetic \leftrightarrow magnetic and magnetic \leftrightarrow magnetic exchanges

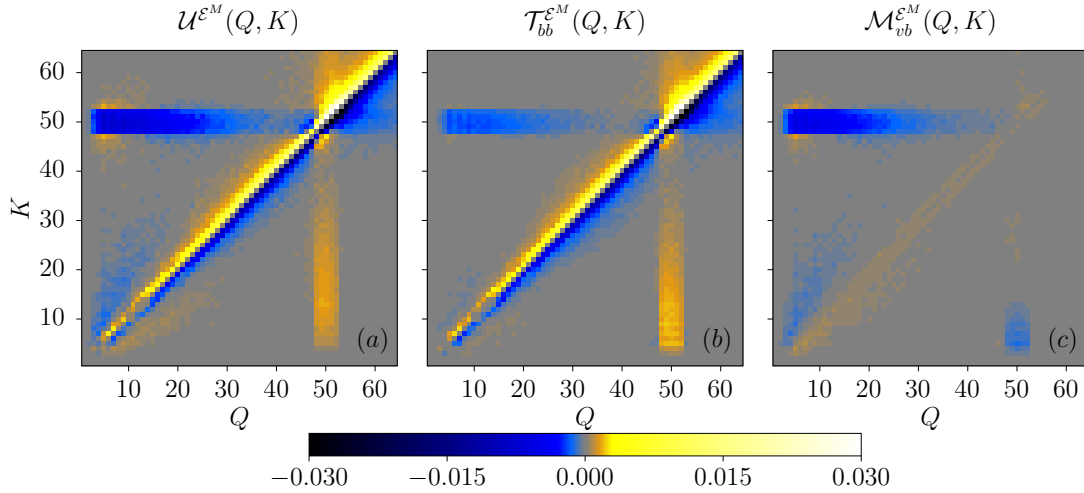


Figure 6.14: (a) Magnetic energy changes in shell K under the influence of the whole velocity field and the magnetic shell Q , M8c run at an instant when $\mathcal{I}_{\mathcal{H}^M} \approx \frac{1}{10} L$. (b) Shell-to-shell magnetic energy transfer rates. (c) Magnetic energy changes in shell K due to exchanges with the velocity field and mediated by magnetic shell Q .

Two types of energy exchanges are susceptible to play a role in the magnetic helicity transfers: exchanges between scales among the magnetic energy reservoir (hereafter called “ $B \leftrightarrow B$ ” exchanges) and exchanges between the kinetic and the magnetic fields (henceforth “ $V \leftrightarrow B$ ” exchanges). Figure 6.14.(a) shows the function:

$$\mathcal{U}^{\mathcal{E}^M}(Q, K) = \int \mathbf{b}_K \cdot \nabla \times (\mathbf{v} \times \mathbf{b}_Q) dV. \quad (6.2)$$

As mentioned in section 2.4.3, this function cannot be interpreted as the transfer of magnetic energy in shell Q to magnetic energy in shell K , since it is not antisymmetric: $\mathcal{U}^{\mathcal{E}^M}(Q, K) \neq -\mathcal{U}^{\mathcal{E}^M}(K, Q)$. This is why, in order to prevent confusion, the letter \mathcal{T} , which stands for “transfer” is not used, but the letter \mathcal{U} is used instead. This function $\mathcal{U}^{\mathcal{E}^M}(Q, K)$ shows how the magnetic energy in shell K changes under the influence of the

whole velocity field and the magnetic field at shell Q , whether this energy comes indeed from the magnetic energy at shell Q or from the kinetic field. In order to distinguish between the transfers of magnetic energy between scales and those with the kinetic energy field, one can write $\mathcal{U}^{\mathcal{E}^M}(Q, K) = \mathcal{T}_{bb}^{\mathcal{E}^M}(Q, K) + \mathcal{M}_{vb}^{\mathcal{E}^M}(Q, K)$ with (section 2.4.3):

$$\mathcal{T}_{bb}^{\mathcal{E}^M}(Q, K) = \int (-\mathbf{b}_K \cdot (\mathbf{v} \cdot \nabla) \mathbf{b}_Q - \frac{1}{2} (\mathbf{b}_K \cdot \mathbf{b}_Q) \nabla \cdot \mathbf{v}) dV, \quad (6.3)$$

$$\mathcal{M}_{vb}^{\mathcal{E}^M}(Q, K) = \int \left(-\frac{1}{2} (\mathbf{b}_K \cdot \mathbf{b}_Q) \nabla \cdot \mathbf{v} + \mathbf{b}_K \cdot (\mathbf{b}_Q \cdot \nabla) \mathbf{v} \right) dV. \quad (6.4)$$

The $\mathcal{T}_{bb}^{\mathcal{E}^M}(Q, K)$ term corresponds indeed to a pure magnetic energy exchange between shells Q and K , as shown in section 2.4.2, and is as such antisymmetric, as illustrated in figure 6.14.(b). The $\mathcal{M}_{vb}^{\mathcal{E}^M}(Q, K)$ term, in figure 6.14.(c), corresponds to energy exchanges with the kinetic field. It is hence not an energy transfer term between the shells Q and K , since the Q and K shells are associated with the magnetic field, but rather the rate of change of magnetic energy in shell K coming from exchanges with the whole velocity field and *mediated* by the Q magnetic shell.

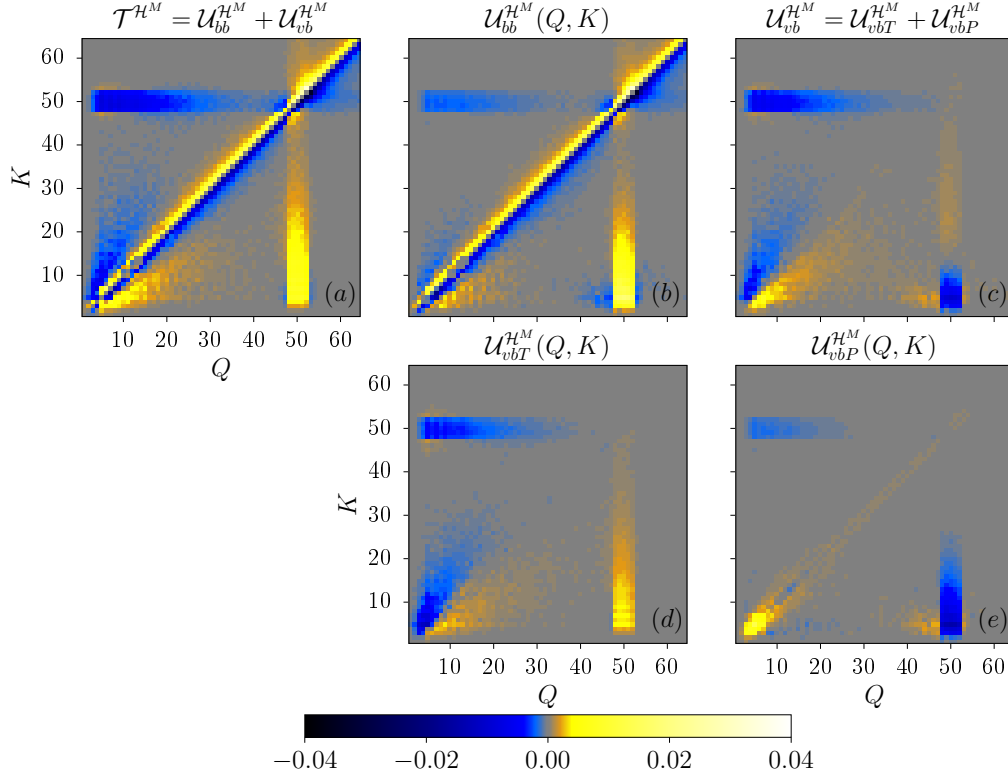


Figure 6.15: Decomposition of the magnetic helicity transfer rate from shell Q to shell K (subfigure (a), which is the same as figure 6.5) in different contributions: (b) associated with $B \leftrightarrow B$ exchanges, (c) associated with $V \leftrightarrow B$ exchanges, the latter being the sum of: (d) contributions from the magnetic tension and (e) from the magnetic pressure.

This decomposition shows that when the NLIT is associated both with $B \leftrightarrow B$ and $V \leftrightarrow B$ exchanges, the DLT of magnetic helicity, associated with a direct cascade of magnetic energy, consists essentially of purely $B \leftrightarrow B$ exchanges (figure 6.14). Regarding the LIT, this figure could be misleading: one could conclude that it is essentially associated with $V \leftrightarrow B$ exchanges. However, a direct look at the $\mathcal{T}_{bb}^{\mathcal{E}^M}(Q, K)$ and $\mathcal{M}_{vb}^{\mathcal{E}^M}(Q, K)$ terms

translated in terms of magnetic helicity transfers (figure 6.15) shows that both $B \leftrightarrow B$ and $V \leftrightarrow B$ exchanges are involved in comparable proportions. On that figure, the functions:

$$\mathcal{U}_{bb}^{\mathcal{H}^M}(Q, K) = \int \mathbf{b}_K \cdot \mathbf{rot}^{-1}((-\mathbf{v} \cdot \nabla)\mathbf{b}_Q - \frac{1}{2}\mathbf{b}_Q \nabla \cdot \mathbf{v})dV, \quad (6.5)$$

$$\mathcal{U}_{vb}^{\mathcal{H}^M}(Q, K) = \int \mathbf{b}_K \cdot \mathbf{rot}^{-1}(-\frac{1}{2}\mathbf{b}_Q \nabla \cdot \mathbf{v} + (\mathbf{b}_Q \cdot \nabla)\mathbf{v})dV, \quad (6.6)$$

are considered. The operator $\mathbf{rot}^{-1}(\mathbf{f})$ returns the solenoidal field \mathbf{g} whose curl is the *solenoidal* part of \mathbf{f} (see section 2.2.3).

While the sum $\mathcal{T}^{\mathcal{H}^M}(Q, K) = \mathcal{U}_{bb}^{\mathcal{H}^M}(Q, K) + \mathcal{U}_{vb}^{\mathcal{H}^M}(Q, K)$ can indeed be interpreted as the magnetic helicity transfer rates from shell Q to shell K (in the same way that the $\mathcal{T}_{bb}^{\mathcal{E}^M}(Q, K)$ term represents the magnetic energy transfer rates from shell Q to shell K), these two $\mathcal{U}_{bb}^{\mathcal{H}^M}(Q, K)$ and $\mathcal{U}_{vb}^{\mathcal{H}^M}(Q, K)$ terms cannot be interpreted as magnetic helicity transfers from shell Q to K . They quantify only variations of magnetic helicity in shell K due to the magnetic field in shell Q and the total velocity field, since they are not antisymmetric. Nevertheless, these terms confirm that the DLT is mostly associated with $B \leftrightarrow B$ exchanges and that the LIT and the NLIT are associated with both $B \leftrightarrow B$ and $V \leftrightarrow B$ exchanges.

The $\mathcal{U}_{vb}^{\mathcal{H}^M}(Q, K)$ function can further be decomposed into contributions from the magnetic tension $\mathcal{U}_{vbT}^{\mathcal{H}^M}(Q, K)$ and from the magnetic pressure, $\mathcal{U}_{vbP}^{\mathcal{H}^M}(Q, K)$:

$$\mathcal{U}_{vbT}^{\mathcal{H}^M}(Q, K) = \int \mathbf{b}_K \cdot \mathbf{rot}^{-1}((\mathbf{b}_Q \cdot \nabla)\mathbf{v})dV, \quad (6.7)$$

$$\mathcal{U}_{vbP}^{\mathcal{H}^M}(Q, K) = \int \mathbf{b}_K \cdot \mathbf{rot}^{-1}(-\frac{1}{2}\mathbf{b}_Q \nabla \cdot \mathbf{v})dV. \quad (6.8)$$

These two functions are plotted in figures 6.15.(d-e) and show that the LIT is predominantly caused by the magnetic tension term. This is expected from the analysis of section 6.2.1, since the LIT are mostly associated with the *PPP* term (and to a lesser degree to the *PNP* one), but not with the *PCP* term. The *PPP* and *PNP* terms do not contribute to the magnetic pressure term, since the latter is only associated with the compressive part of the velocity field.

In appendix A.4.1, a way in order to estimate the relative importance of the $B \leftrightarrow B$ and $V \leftrightarrow B$ exchanges on the LIT is presented. For the M8c run at an instant when $\mathcal{I}_{\mathcal{H}^M} \approx \frac{1}{10}L$, it can be estimated that about 40 percent of the LIT strength is associated with purely $B \leftrightarrow B$ exchanges and the rest with $V \leftrightarrow B$ exchanges.

Kinetic \leftrightarrow magnetic energy exchanges

As mentioned in section 2.4.2, energy exchanges between the magnetic and kinetic field shells can be expressed as:

$$\mathcal{T}_{vb}^{\mathcal{E}^M}(P, K) = \int (-\frac{1}{2}(\mathbf{b}_K \cdot \mathbf{b})\nabla \cdot \mathbf{v}_P + \mathbf{b}_K \cdot (\mathbf{b} \cdot \nabla)\mathbf{v}_P)dV. \quad (6.9)$$

This function cannot however be interpreted in terms of kinetic energy transfers from shell P to magnetic energy in shell K , but only as $V \leftrightarrow B$ energy transfers to the magnetic field at shell K linked with variations in the power spectrum of the velocity field at shell P . As underlined in section 2.4.2, another formulation of the $\mathcal{T}_{vb}^{\mathcal{E}^M}(P, K)$ using the variable

$\mathbf{w} = \sqrt{\rho}\mathbf{v}$ should indeed be used for this purpose, as done for example in reference [55]. The choice of considering the velocity field in the present work, instead of \mathbf{w} , is motivated by the use of a helical decomposition of the velocity field. The kinetic helicity is indeed defined as the helicity of \mathbf{v} , not of \mathbf{w} .

Figure 6.16 shows several relevant functions for this purpose. Following the previous notations, the functions associated with the letter \mathcal{T} correspond to energy transfers between the kinetic and the magnetic fields, and are split into contributions coming from the magnetic pressure $\mathcal{T}_{vbP}^{\mathcal{E}^M}(P, K)$ (subfigure (i)) and the magnetic stretching $\mathcal{T}_{vbT}^{\mathcal{E}^M}(P, K)$ terms (subfigure (b)), so that $\mathcal{U}^{\mathcal{E}^M}(P, K)_{\Sigma_Q} = \mathcal{T}_{vbP}^{\mathcal{E}^M}(P, K) + \mathcal{T}_{vbT}^{\mathcal{E}^M}(P, K)$ (subfigure (f)). The magnetic stretching term is separated into contributions from only a certain helical part of the velocity field $\mathcal{T}_{vbT}^{\mathcal{E}^M}(P, K)_{v^P}$, $\mathcal{T}_{vbT}^{\mathcal{E}^M}(P, K)_{v^C}$ and $\mathcal{T}_{vbT}^{\mathcal{E}^M}(P, K)_{v^N}$, where the corresponding helical part is written as a subscript (subfigures (e), (h) and (k)). In these subfigures, transfer rates of energy from the kinetic to the magnetic field are plotted, so that a negative value means that magnetic energy from shell K is converted into kinetic energy associated with the velocity field at shell P , and a positive value that kinetic energy associated with the velocity field at shell P is converted into magnetic energy at shell K . The functions associated with the letter \mathcal{M} correspond to the importance of the mediation of the velocity field for the $B \leftrightarrow B$ transfers, and are as well decomposed in helical contributions following the same notations (subfigures (a), (d), (g) and (j)). Lastly, the \mathcal{U} function (subfigure (c)) is a hybrid function, sum along Q of the total $\mathcal{U}^{\mathcal{E}^M}(Q, P, K)$ function, that is $\mathcal{U}^{\mathcal{E}^M}(P, K)_{\Sigma_Q} = \mathcal{T}_{vb}^{\mathcal{E}^M}(P, K) + \mathcal{M}_{bb}^{\mathcal{E}^M}(P, K)_{\Sigma_Q}$. It neither corresponds to $V \leftrightarrow B$ transfers, nor to the mediating role of the velocity field in $B \leftrightarrow B$ transfers, but allows to see the general importance of the velocity field at shell P for the transfers to the magnetic shell K .

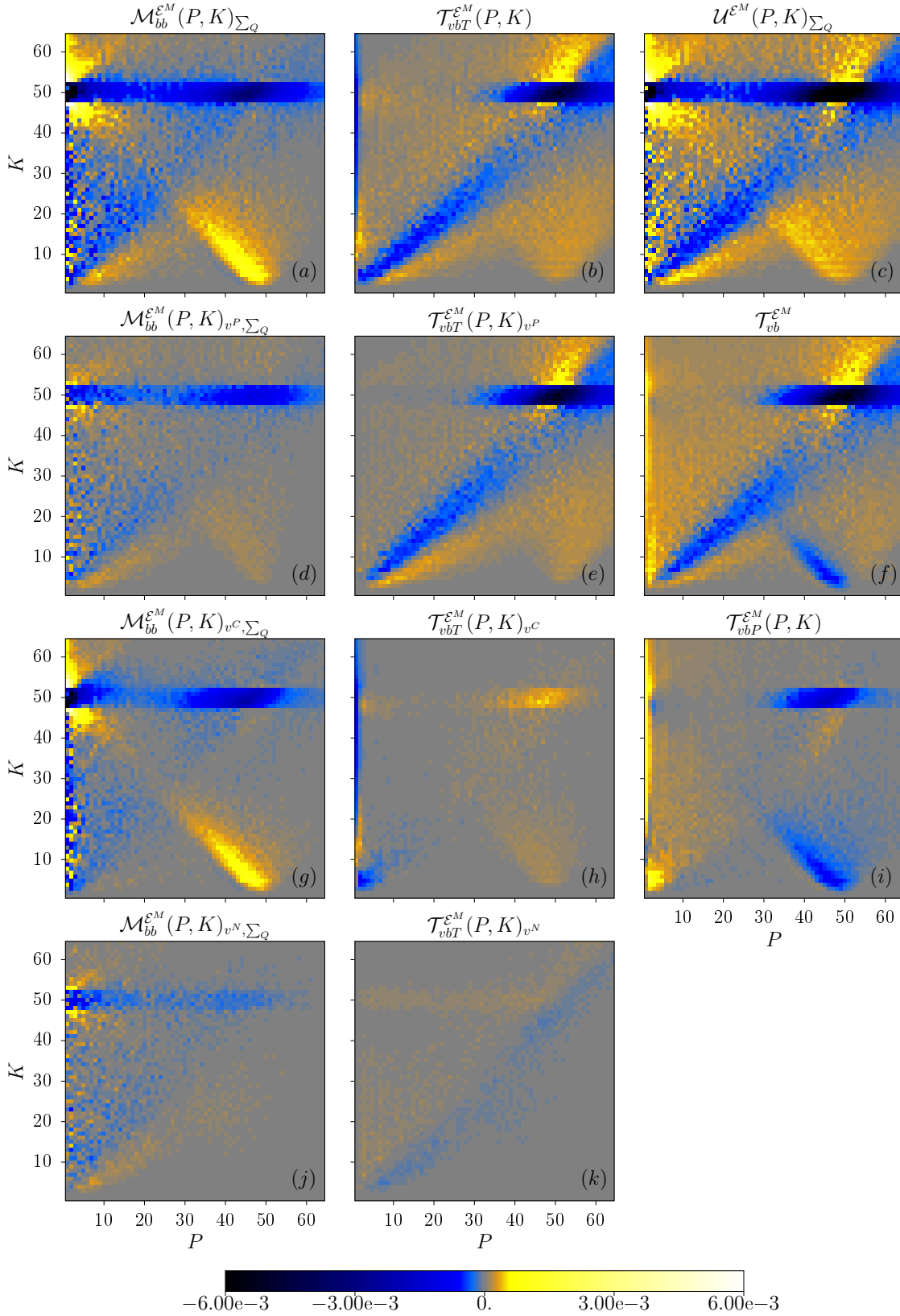


Figure 6.16: Several functions showing energy exchanges between magnetic and velocity fields as well as the mediating role of the velocity field, M8c run at an instant when $\mathcal{I}_{\mathcal{H}^M} \approx \frac{1}{10}L$. A more detailed explanation is to be found in the text. The following relations between these subfigures hold: $\mathcal{M}_{bb}^{\varepsilon^M}(P, K)_{\Sigma_Q} = \mathcal{M}_{bb, v^P}^{\varepsilon^M} + \mathcal{M}_{bb, v^C}^{\varepsilon^M} + \mathcal{M}_{bb, v^N}^{\varepsilon^M}$, $\mathcal{T}_{vbT}^{\varepsilon^M} = \mathcal{T}_{vbT, v^P}^{\varepsilon^M} + \mathcal{T}_{vbT, v^C}^{\varepsilon^M} + \mathcal{T}_{vbT, v^N}^{\varepsilon^M}$ (helical decomposition of the velocity field), $\mathcal{T}_{vb}^{\varepsilon^M} = \mathcal{T}_{vbT}^{\varepsilon^M} + \mathcal{T}_{vbP}^{\varepsilon^M}$ (sum of magnetic stretching and magnetic pressure terms), $\mathcal{U}^{\varepsilon^M}(P, K)_{\Sigma_Q} = \mathcal{T}_{bb}^{\varepsilon^M} + \mathcal{T}_{vbT}^{\varepsilon^M} + \mathcal{T}_{vbP}^{\varepsilon^M} = \mathcal{T}_{bb}^{\varepsilon^M} + \mathcal{T}_{vb}^{\varepsilon^M}$ (sum of the $B \leftrightarrow B$ velocity-field mediation and $V \leftrightarrow B$ transfers).

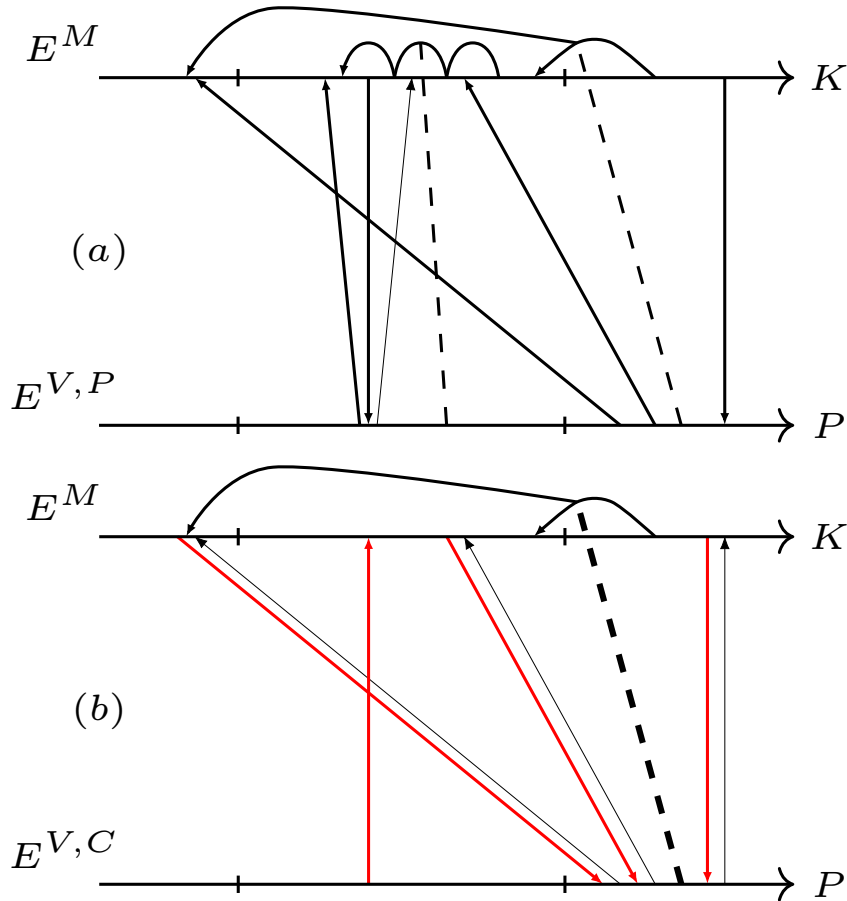


Figure 6.17: Sketch of the $V \leftrightarrow B$ energy exchanges, as well as the mediating role of the velocity field for the $B \leftrightarrow B$ exchanges, done from the plots of figure 6.16. (a) Energy exchanges involving the velocity field's positive helical part. (b) Energy exchanges involving the velocity field's compressive part. The black arrows between the K - and P -axis correspond to magnetic stretching and the red arrows to magnetic pressure. The dashed lines correspond to $B \leftrightarrow B$ exchanges, where the velocity field acts as a mediator. The thicker the lines, the more important the energy transfers. The ticks along the P - and K -axis delimit the large, intermediate and small scales. These limits are different for the magnetic and the velocity fields: “small” means here $K, P \gtrsim 40$, “large” means $K \lesssim 10, P \lesssim 3$, and “intermediate” is in between. The LIT, associated with the positive helical velocity field and with both $V \leftrightarrow B$ and $B \leftrightarrow B$ exchanges also occurs at small K but is not drawn in order not to overload the sketch.

The main energy exchanges that take place concerning the LIT and the NLIT are represented schematically in figure 6.17. The positive helical part \mathbf{v}^P and the compressive part \mathbf{v}^C of the velocity field play clearly distinct roles:

- Through magnetic stretching, a small-scale \mathbf{v}^P field is generated, which plays an important role in both the LIT and NLIT: it is indeed converted into magnetic energy at intermediate and large scales and mediates both the local and non-local magnetic energy inverse transfers. The LIT is also associated with $V \leftrightarrow B$ exchanges at intermediate scales between relatively close magnetic and \mathbf{v}^P shells. This can be seen as a consequence of the realisability condition (section 2.2.3). Indeed, assuming that a certain quantity of magnetic helicity $\tilde{H}_{K_A}^M$ at shell K_A is transferred to a shell $K_B < K_A$, and assuming furthermore for the sake of simplicity that the field is fully helical at all scales, this would mean that $\tilde{E}^M = \frac{1}{2}K_A\tilde{H}_{K_A}^M$ units of magnetic energy would leave shell K_A . However, only $\frac{1}{2}K_B\tilde{H}_{K_A}^M < \tilde{E}^M$ can be transferred to shell K_B without breaking the realisability condition. As a consequence, the remaining energy has to be transferred to the kinetic field.
- Contrary to \mathbf{v}^P , the $V \leftrightarrow B$ energy exchanges with \mathbf{v}^C tend to act against the inverse transfer. Indeed, although the magnetic stretching term converts small scale kinetic energy associated with \mathbf{v}^C to magnetic energy at larger scales, the energy transfers due to the magnetic pressure term are in the opposite direction (from larger scale magnetic field to smaller scale \mathbf{v}^C field), and are stronger¹. However, the small scale \mathbf{v}^C plays an important role in the mediation of $B \leftrightarrow B$ transfers to larger scales, which overruns the direct transfer of magnetic energy to smaller scales. This results in a net magnetic energy transfer to larger scales, through the NLIT.

These energetic transfers explain the repartition of the specific kinetic energy in helical components (figure 6.18) and the low compressive ratio at intermediate scales during the magnetic helicity inverse transfer (figure 4.21). Magnetic stretching and magnetic pressure induce respectively a positive helical and a compressive velocity field at small scales (peaks in figure 6.18), whereas the compressive part of the velocity field tends to be converted into magnetic energy at intermediate scales through the magnetic pressure (figure 6.16.(i)), lowering the compressive ratio.

About the DLT, mediated by the large scale velocity field, even though most of the energy exchanges occur through $B \leftrightarrow B$ transfers (figure 6.14), it is also associated with $V \leftrightarrow B$ energy exchanges. The global energy flux is from the kinetic field to the magnetic field (subfigure (f)). However, the direction of these energy exchanges depend on the helical component of the velocity field: for the solenoidal part of the velocity field, the exchange is from kinetic to magnetic energy through the magnetic stretching term, whereas for the compressive part of the velocity field, the magnetic stretching and magnetic pressure term have opposite directions: exchanges through the magnetic stretching term are globally from the magnetic field to the compressive kinetic field and exchanges through the magnetic pressure term from the kinetic field to the magnetic field.

Lastly, concerning the terms associated with the negative helical part of the velocity field (subfigures (j) and (k)), even though the energetic exchanges are relatively weak, its mediating role in the LIT seems to be of the same order of magnitude as the velocity field's positive helical part.

¹The energy removed from the larger scale magnetic field is essentially due to the *PCP* term, not to the *NCN* or *SCS* terms – figure not shown. This means that this energy transfer indeed plays against the magnetic helicity inverse transfer. If energy associated with the negative helical part of the magnetic field would be removed, it would result in a positive role regarding the inverse transfer of magnetic helicity.

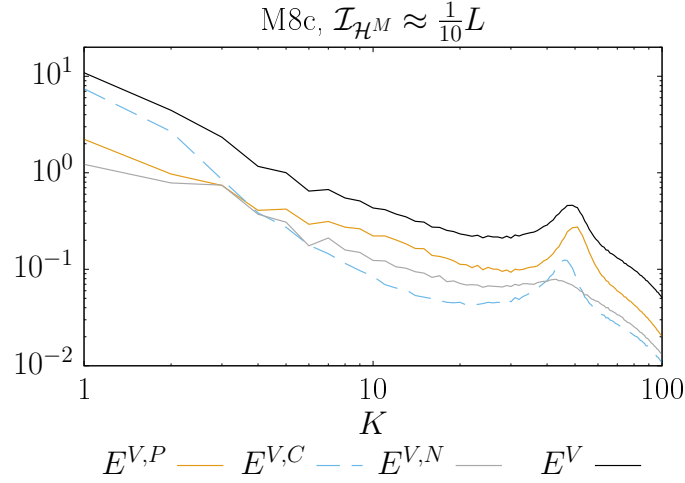


Figure 6.18: Specific kinetic energy stored in each helical component of the velocity field, M8c run at an instant when $\mathcal{I}_{HM} \approx \frac{1}{10}L$.

Summary: energy transfers

When the DLT is mostly associated with purely $B \leftrightarrow B$ exchanges, the LIT and NLIT are associated with both $V \leftrightarrow B$ and $B \leftrightarrow B$ exchanges. The velocity field's positive helical part acts in favour of the inverse transfer, both energetically and through its mediating roles. As for its compressive part, from the perspective of energy exchanges, a competition between the weaker magnetic stretching (in favour of the inverse transfer) and the stronger magnetic pressure (against the inverse transfer) takes place, which tends to act generally against the inverse transfer. However, the mediating role of the compressive velocity field counteracts this effect, leading to a net positive participation in the NLIT.

6.3 Geometric triadic factors

As explained in section 2.3.1, the magnetic field's evolution equation, decomposed in helical components, can be expressed as triadic interactions, even in the compressible case, namely:

$$\partial_t b_{\mathbf{k}}^{s_k} = s_k k \sum_{\mathbf{k}+\mathbf{p}+\mathbf{q}=0} \sum_{s_p, s_q} v_{\mathbf{p}}^{s_p*} b_{\mathbf{q}}^{s_q*} g_{k,p,q}^{s_k, s_p, s_q}, \quad (6.10)$$

where $s_k, s_q \in \{+, -\}$ and correspond to the positive and negative helical parts of the magnetic field and $s_p \in \{+, 0, -\}$ corresponds to the velocity field's helical parts (and to its compressive part for $s_p = 0$). The factor $g_{k,p,q}^{s_k, s_p, s_q} \in \mathbb{C}$ is defined by:

$$g_{k,p,q}^{s_k, s_p, s_q} = (\hat{\mathbf{h}}_{\mathbf{p}}^{s_p*} \times \hat{\mathbf{h}}_{\mathbf{q}}^{s_q*}) \cdot \hat{\mathbf{h}}_{\mathbf{k}}^{s_k*} \quad (6.11)$$

with $\hat{\mathbf{h}}_{\mathbf{k}}^{s_k}, \hat{\mathbf{h}}_{\mathbf{p}}^{s_p}$ and $\hat{\mathbf{h}}_{\mathbf{q}}^{s_q}$ the helical eigenvectors. It can be viewed as a geometric factor whose module $G = |g|$ weights the triadic interactions' strength. In the incompressible case (where $s_p \in \{+, -\}$), it yields [102]:

$$G_{s_p \in \{+, -\}} = \frac{|s_k k + s_p p + s_q q| \sqrt{2k^2 p^2 + 2p^2 q^2 + 2q^2 k^2 - k^4 - p^4 - q^4}}{2k p q} \quad (6.12)$$

The derivations performed in reference [102] can be extended to the compressible case. As derived in section 2.3.2, the geometric factor's module is, for $s_p = 0$, $s_k = S \in \{+, -\}$ and $s_q = \pm S$:

$$G_{s_k=S, s_p=0, s_q=\pm S} = \frac{|(k \mp q)(p^2 - k^2 - q^2 \mp 2qk)|}{2kpq} \quad (6.13)$$

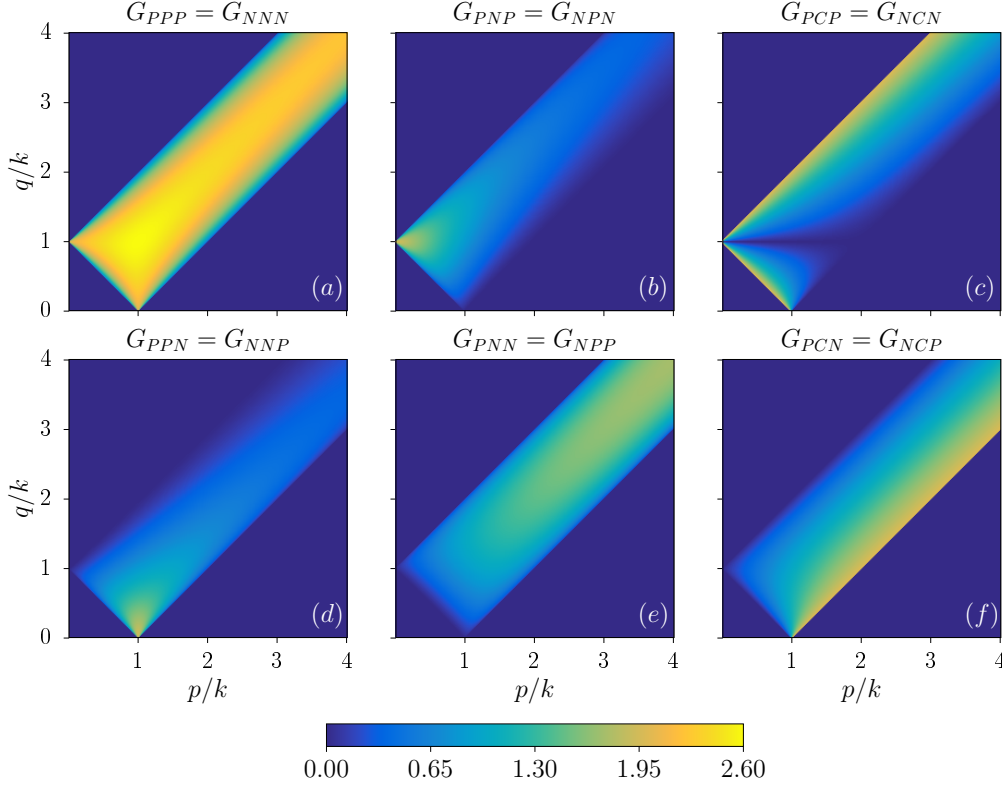


Figure 6.19: Magnitude of the geometric factor of the triadic interactions G for the different helical components corresponding to equations (6.12) and (6.13). The interactions happen between the wavevector \mathbf{k} and \mathbf{q} of the magnetic field and \mathbf{p} of the mediating velocity field, which helical components are given in the three letters of the subscript in this order: \mathbf{k} , then \mathbf{p} , then \mathbf{q} .

The geometric factor's module is shown in the (p, q) -plane in figure 6.19 for all the helical combinations. Only the regions compatible with triads, that is, satisfying $k+p \leq q$, $p+q \leq k$ and $q+k \leq p$ may have a non-zero value. Only six plots for the twelve (s_k, s_p, s_q) possibilities are present since G_{s_k, s_p, s_q} is symmetric with respect to a change of all the (s_k, s_p, s_q) signs. Furthermore, the (b), (d) and (e) subfigures actually represent the same term but with a permutation in (k, p, q) .

As shown in section 2.4.4, the geometric factors can be used to a certain extent for shell-to-shell transfers, even though they are strictly speaking valid only for triadic interactions. Hence, in order to harmonise the notations with that section, a contribution from the positive helical part of a field can be noted by either $+$ or P , one from the negative helical part of a field by either $-$ or N and one from the compressive part of the velocity field by 0 or C . With other words, $G_{PPP} = |g_{+,+,+}|$, $G_{PCP} = |g_{+,0,+}|$, $G_{PCN} = |g_{+,0,-}|$ etc.

Although G is not the only factor to consider in the magnetic field evolution (equation (6.10)), it allows on its own to explain all the observations made in sections 6.2.1 and 6.2.2 regarding the locality and relative strength of the homochiral (non-heterochiral) terms, as shown below. Indeed, since the three DLT, LIT and NLIT features are associated with distinct velocity shells acting as mediators (see section 6.2.2), each of these features can

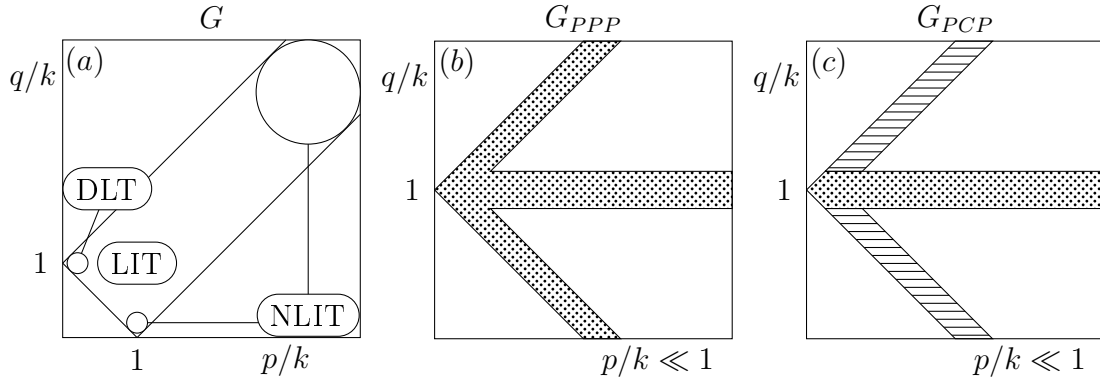


Figure 6.20: (a) Sketch of the general appearance of the plots displayed in figure 6.19, showing the regions corresponding to the three DLT, LIT and NLIT features. (b-c) Zoom on the $p \ll k$ region, corresponding to the DLT, for the *PPP* and *PCP* terms respectively. The dotted regions correspond either to a vanishing geometric factor or to the $k = q$ line, which plays no role in magnetic helicity shell-to-shell transfers. On the contrary, the regions with a horizontal lines pattern in the *PCP* term correspond to a geometric factor of high magnitude, as described in the text.

be associated with a different region in the (p, q) plane for the G plots, as sketched in figure 6.20.(a). The DLT is mostly mediated by the large scale velocity field, so that it corresponds to the region $p \ll k \approx q$. The NLIT on the other hand is mediated by the small scale velocity field, so that it corresponds to the regions $k \ll p \approx q$ and $q \ll p \approx k$. As for the LIT, it is mediated by the velocity field at intermediate scales so that it corresponds to $k \approx p \approx q$.

The LIT corresponds indeed not only to a mostly local inverse *transfer*, but as well to mostly local *interactions*². The geometric factor strength in the region $k \approx p \approx q$ explains the relative importance of the *PPP*, *PNP* and *PCP* terms with respect to the LIT. Indeed, G_{PPP} presents a global maximum for $k = p = q$, equal to $\frac{3\sqrt{3}}{2} \approx 2.6$, whereas $G_{PNP} < G_{PPP}$ by a factor of roughly three and G_{PCP} vanishes for local interactions (figures 6.19.(a-c)). Hence, the LIT is favoured geometrically for the *PPP* and, to a lesser extent, the *PNP* terms, but is disfavoured for the *PCP* term, consistently with the observations in figures 6.6.(a-b) and 6.8.(a), which show that the LIT is mostly carried out by the *PPP* term, visible but smaller for the *PNP* term and not distinguishable for the *PCP* term. The NLIT corresponds to non-local interactions $k \ll p \approx q$ and $q \ll p \approx k$ and is mostly carried out by the *PPP* and *PCP* terms (section 6.2.1). This is consistent with the geometric factor: even if $G_{PPP} = 0$ as soon as \mathbf{k} , \mathbf{p} and \mathbf{q} are strictly colinear, when $k \ll p = q$, $G_{PPP} \xrightarrow[k \ll p = q]{} 2$ (and symmetrically for all permutations of (k, p, q)), even for vectors that are “almost colinear”. For the *PCP* term, when $q = p + k$ (the upper line limiting the domain where triangles can be formed) and $q = -p + k$ (the bottom-left limiting line), $G_{PCP} = 2$, even for $k \ll p \approx q$ and $q \ll p \approx k$. As a consequence, the relative importance of the *PPP* and *PCP* terms are comparable for the NLIT. However, as G_{PCP} vanishes for $k \approx p \approx q$, the NLIT is less local for the *PCP* term as compared to

²In this section, it is important to make a distinction between local *interactions* and local magnetic helicity *transfers*. As already mentioned in section 6.2, a local magnetic helicity transfer from shell Q to shell $K \approx Q$ does not require the mediating velocity shells P to be close to $K \approx Q$. If P is far from K and Q , the magnetic helicity transfer is local, but the *interaction* is not, since a local interaction means that $K \approx P \approx Q$. For example, for the DLT, $P \ll K \approx Q$, which means that magnetic structures of similar size interact and exchange magnetic helicity. From the point of view of the magnetic field, this means a local transfer, even though the velocity field acts as a mediator on a significantly larger scale.

the *PPP* term, as visible in figures 6.6 and 6.7.c, where the rectangular bars at $K \approx 50$ and $Q \approx 50$ present a lesser extension for the *PCP* term. The *PNP* term does not contribute much to the NLIT, since its geometric factor vanishes for $k \ll p \approx q$ and $q \ll p \approx k$.

The prediction of more local *PNP* transfers (local in the sense $K \approx Q$), as compared to the *PPP* ones, has already been mentioned in an analysis in the incompressible case [69].

Finally, the DLT mediated by the large-scale velocity field corresponds to non-local $p \ll k \approx q$ interactions. In this region, the three G_{PPP} , G_{PNP} and G_{PCP} geometric factors are relatively big. Why it is strongest for the *PCP* term (figure 6.7.(b)) cannot be explained alone through the fact that the compressive part of the velocity contains more energy than the positive helical part at large scales (see figure 6.18). As shown in section 6.4.1 below, for the M1s at an equivalent instant in time, a direct cascade with similar amplitudes for both the *PPP* and *PCP* terms is obtained even though significantly more energy is contained in the positive helical velocity power spectrum (figure 6.23.(b)). This means that the *PCP* term is favoured geometrically for the DLT, as compared to the *PPP* one. This fact is not obvious when comparing figures 6.19.(a) and 6.19.(c) directly, since both G_{PPP} and G_{PCP} geometric factors are relatively high in the $p \ll k \approx q$ region. However, when considering magnetic helicity transfers between shells Q and K , they are necessarily 0 when $K = Q$. That is, even though the geometric factor is non-zero on the $q = k$ horizontal line for the *PPP* term, it is not relevant for shell-to-shell magnetic helicity transfers. As a consequence, the geometric factor is greater in the $p \ll k \approx q$ region for the *PCP* term, as compared to the *PPP* one, since it is big on the $q = p + k$ and $q = -p + k$ lines, a region where G_{PPP} vanishes, as shown schematically in figures 6.20.(b-c). Nevertheless, as shown in section 6.4, a different energy distribution among the helical velocity modes could lead to a stronger DLT due to the *PPP* term in other situations, even though it is less favoured geometrically.

Because of symmetry reasons, the *NNN*, *NCN* and *NPN* terms present the same G geometric factors as the *PPP*, *PCP* and *PNP* terms respectively. This explains why the three of them exhibit a direct cascade of negative magnetic helicity, as displayed in figures 6.10 and 6.8.(b) and the terms *NNN* and *NPN* exhibit small LIT of negative magnetic helicity at the largest scales. None of them present a NLIT since the injected magnetic fluctuations are fully positive helical, which means that there is almost no negative helicity that could be transferred to larger scales.

Concerning the heterochiral terms, their analysis is more complex since they are sums of two terms with different geometric factors. As they do not play dominant roles in the inverse transfer dynamics for the systems considered here, their detailed study is not within the scope of the present work. In other situations however, they could play a greater role and their study would become more relevant (see section 7.1). This is why a short discussion based on the geometric factors can still be found in appendix C.2.

The discussion above assumed that the shapes of the helically-decomposed transfer rates $\mathcal{T}_{SKSPSQ}^{\mathcal{H}^M}(Q, P, K)$ are similar to the geometric factors' ones. This is of course not guaranteed. Written in helical components, the magnetic helicity at a wavevector \mathbf{k} is $H_{\mathbf{k}}^M = \frac{1}{k}(|\hat{b}_{\mathbf{k}}^+|^2 - |\hat{b}_{\mathbf{k}}^-|^2)$ and its time evolution therefore:

$$\partial_t H_{\mathbf{k}}^M = \frac{1}{k}(2\Re(\hat{b}_{\mathbf{k}}^{+*} \partial_t \hat{b}_{\mathbf{k}}^+ + \hat{b}_{\mathbf{k}}^{-*} \partial_t \hat{b}_{\mathbf{k}}^-)), \quad (6.14)$$

with $\Re(z)$ the real part of the complex number z . As a consequence, $\partial_t H_{\mathbf{k}}^M$ depends, apart from the phase information and the geometric factor, on the modules of $\hat{b}_{\mathbf{k}}^{sk}$, $\hat{v}_{\mathbf{p}}^{sp}$ and $\hat{b}_{\mathbf{q}}^{sq}$ (see equation (6.10)). One can however plot tentatively slices at a particular K_0 of

the different helical components $\mathcal{T}_{s_K s_P s_Q}^{\mathcal{H}^M}(Q, P, K_0)$ normalised by the typical interacting fields' modules. For example, the typical interacting module for the s_Q magnetic field helical component in the Q shell is $\sqrt{2E_Q^{M,s_Q}}$ with E_Q^{M,s_Q} the power spectrum of the s_Q -helical part of the magnetic field, and similarly for the other two interacting shells. Figure 6.21 shows hence the (n)ormalised helically-decomposed magnetic helicity transfer rates:

$$\mathcal{N}_{s_K s_P s_Q}^{\mathcal{H}^M}(Q, P, K_0) = \frac{\mathcal{T}_{s_K s_P s_Q}^{\mathcal{H}^M}(Q, P, K_0)}{2\sqrt{2E_{K_0}^{M,s_K} E_P^{V,s_P} E_Q^{M,s_Q}}}, \quad (6.15)$$

for the M8c run at an instant when $\mathcal{I}_{\mathcal{H}^M} \approx \frac{1}{10}L$ at $K_0 = 10$. The $\mathcal{N}_{s_K s_P s_Q}^{\mathcal{H}^M}(Q, P, K_0)$ functions are normalised in these plots by $\max_{Q,P}(|\mathcal{N}_{s_K s_P s_Q}^{\mathcal{H}^M}(Q, P, K_0)|)$ for visualisation purposes. Indeed, the main aim is here to compare these normalised transfer rates with the geometric factor, and not the helical contributions with one another.

In figure 6.21, the NLIT corresponds to the positive horizontal band for $P, Q \approx 50$ and the negative values at the $P \approx K$ angle in the PPP and PCP terms, the LIT to the mostly positive values for $Q > K_0$ and negative for $Q < K_0$ for intermediate values of P , visible in the PPP and PNP terms and the DLT to the negative value for $Q > K_0$ and positive value for $Q < K_0$ at small P . The geometric factors' shapes are well reflected in most of the subfigures, the most notable exceptions being the heterochiral PNN and NPP terms, where the contributions are quite big even for $P, Q \ll K$ and the heterochiral PCN and NCP terms, where the regions close to the lines $Q = \pm P + K$ have higher contributions than one would expect from the geometric factor.

The geometric factors' shapes are even more clearly reflected when considering the average of all the K_0 slices of $\mathcal{N}_{s_K s_P s_Q}^{\mathcal{H}^M}(Q, P, K_0)$ in one plot, see figure 6.22. This figure is obtained by resizing and merging all the slices of $\mathcal{N}_{s_K s_P s_Q}^{\mathcal{H}^M}(Q, P, K)$ for $K \in [5, 50]$, through the procedure described in appendix A.4.2.

Since the geometric factor alone does not contain all the information about the transfers, the fact that the normalised interactions agree so well with their shape is worth to be emphasised. This good agreement allows indeed to explain the relative importance of the different helical contributions to the three features (DLT, LIT and NLIT) visible in the shell-to-shell magnetic helicity transfers.

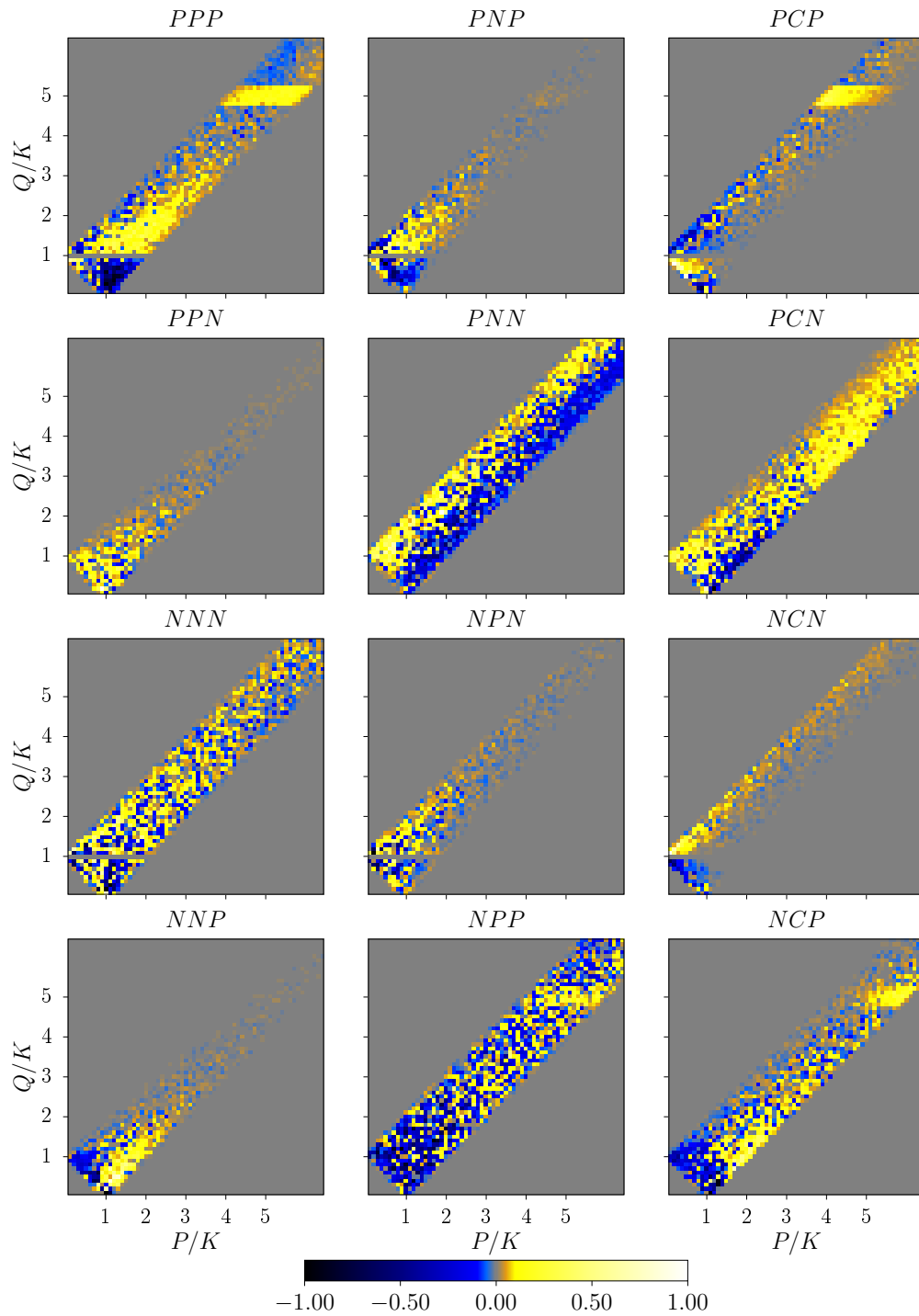


Figure 6.21: Slices of the different helical components of $\mathcal{N}_{s_K s_P s_Q}^{\mathcal{H}^M}(Q, P, K_0)$ at $K_0 = 10$ for the M8c run at an instant when $\mathcal{I}_{\mathcal{H}^M} \approx \frac{1}{10}L$. The slices have been normalised by the maximum absolute value they contain, so as to allow a better comparison with the geometric factors in figure 6.19.

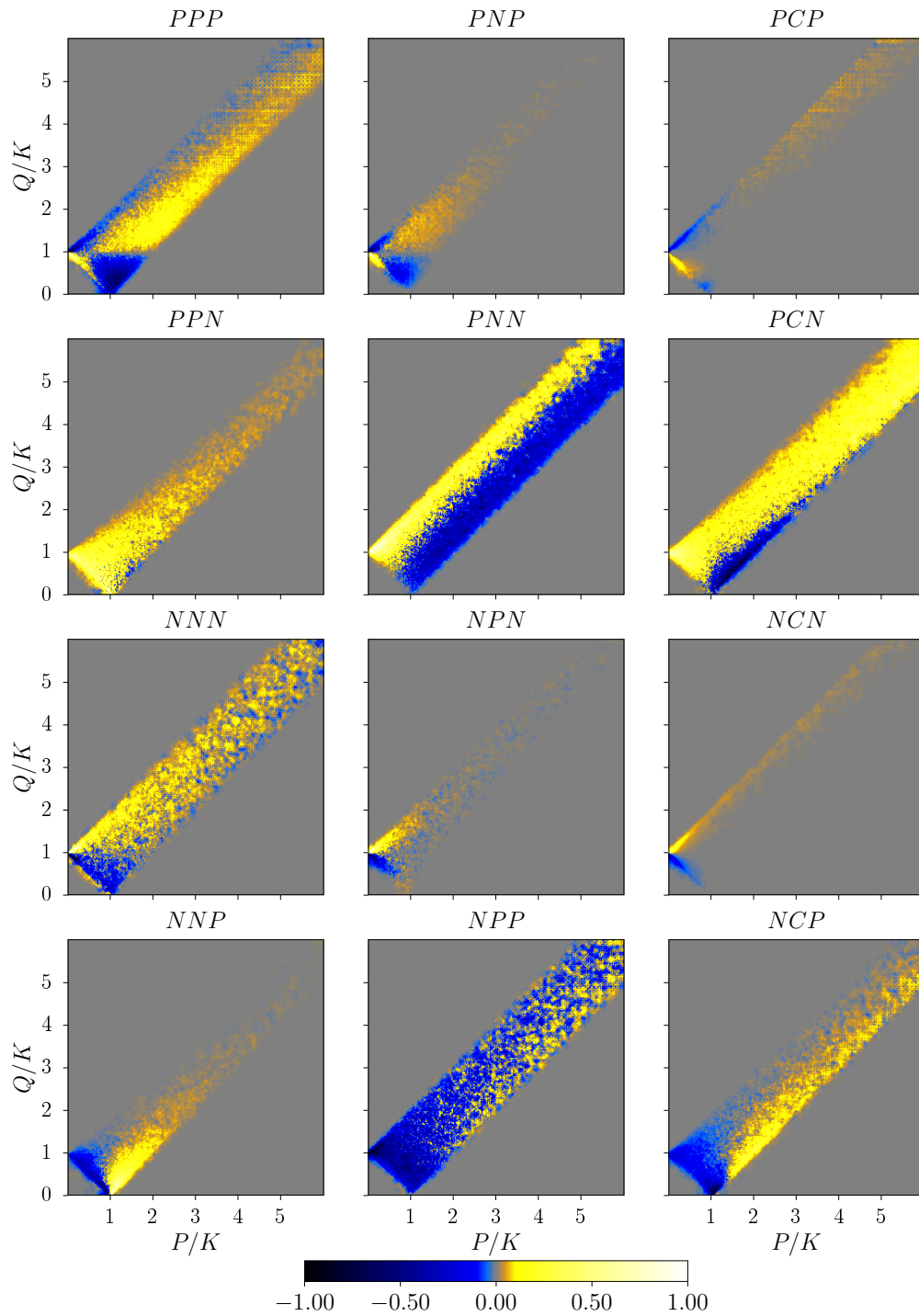


Figure 6.22: Average of the $\mathcal{N}_{s_K s_P s_Q}^{\mathcal{H}^M}(Q, P, K)$ slices for $K \in [5, 50]$, generated in the way presented in appendix A.4.2. The square structures are artifacts coming from the resizing step of the procedure.

6.4 Additional measurements

6.4.1 Comparison with other runs

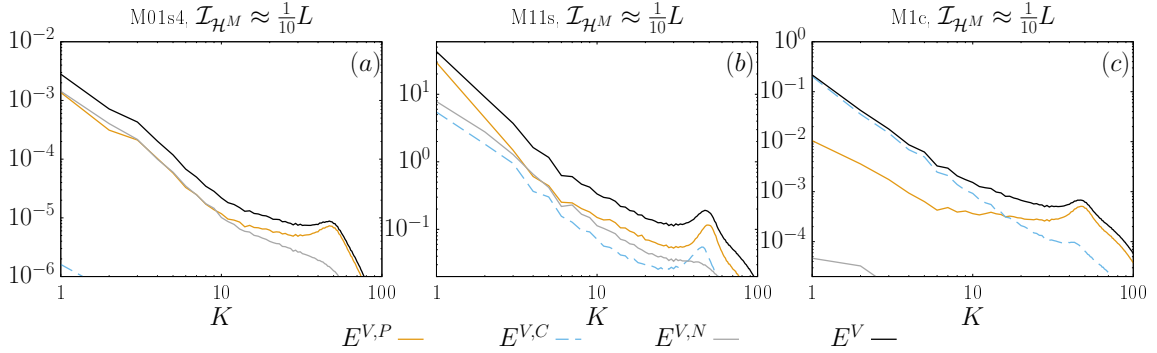


Figure 6.23: Velocity power spectra (black) as well as their decomposition in helical components (P, C and N) for the M01s4, M11s and M1c runs at an instant when $\mathcal{I}_{\mathcal{H}^M} \approx \frac{1}{10}L$.

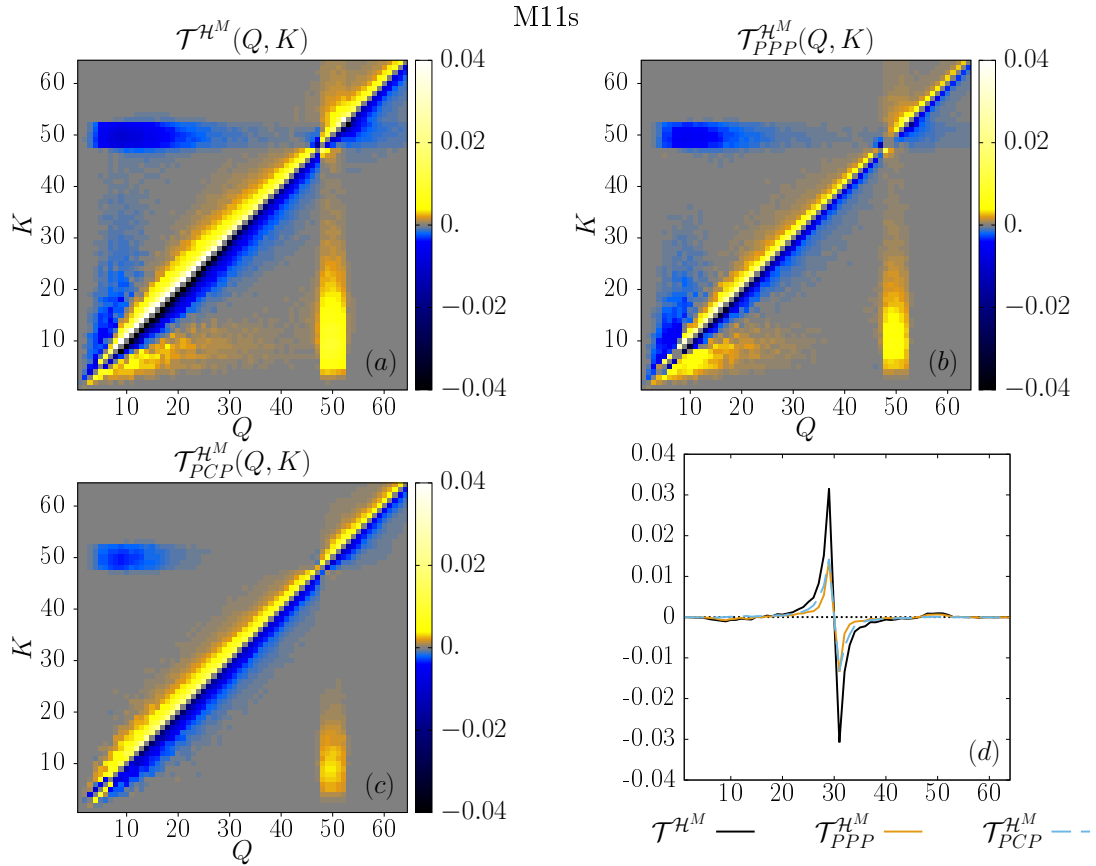


Figure 6.24: (a-c) Magnetic helicity transfer rates between the shells Q and K and their greatest helical contributions for the M11s run at an instant when $\mathcal{I}_{\mathcal{H}^M} \approx \frac{1}{10}L$. (d) Cut of subfigures (a-c) at $K_0 = 30$.

In the following, the three other runs corresponding to the extreme cases M01s4, M11s and M1c are considered and compared to each other and the M8c run. Each of them is taken at an instant when $\mathcal{I}_{\mathcal{H}^M} \approx \frac{1}{10}L$.

The most striking observation is that, even though the studied turbulent states span over a wide range of compressibility, the magnetic helicity transfers in these different settings present a lot of common points: the shell-to-shell magnetic helicity transfer rates

always present the same three features (DLT, LIT and NLIT) observed in figure 6.5, which are mediated by the velocity field at the same scales (see section 6.2.2). The DLT is furthermore always mostly associated with $B \leftrightarrow B$ exchanges whereas the LIT and NLIT with both $B \leftrightarrow B$ and $V \leftrightarrow B$ exchanges through magnetic stretching (section 6.2.3).

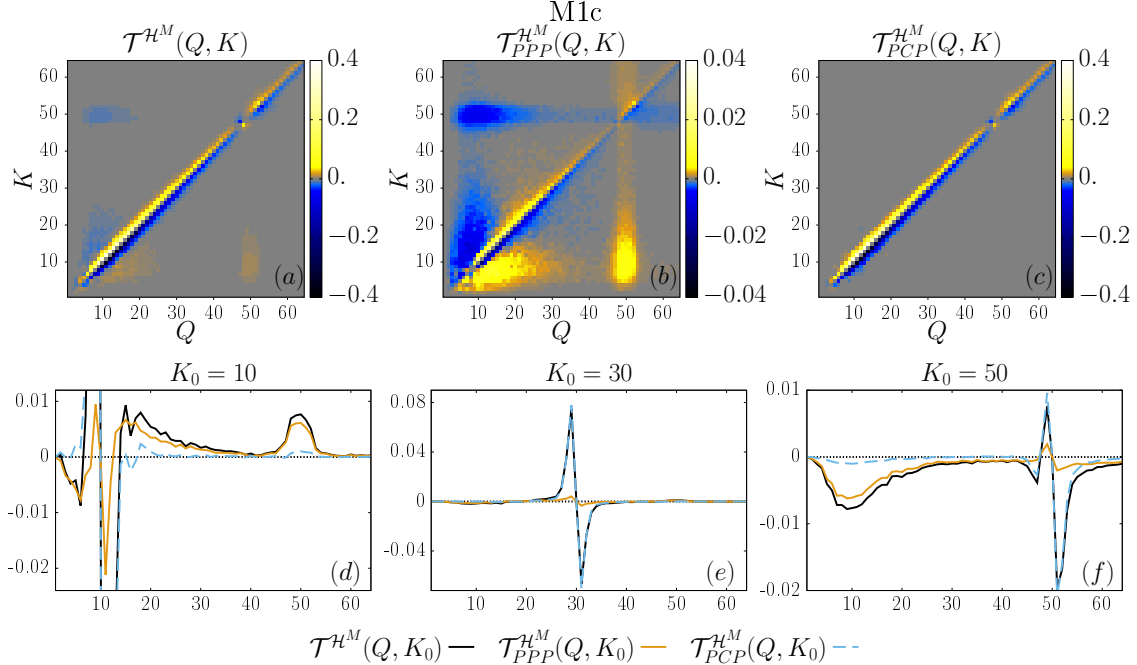


Figure 6.25: (a-c) Magnetic helicity transfer rates between the shells Q and K and their greatest helical contributions for the M1c run at an instant when $\mathcal{I}_{\mathcal{H}^M} \approx \frac{1}{10}L$. Please note that the extremes of the colour bar of subfigure (b) are an order of magnitude lower as compared to subfigures (a) and (c). (d-f) Cuts of the subfigures (a-c) at $K_0 = 10$, $K_0 = 30$ and $K_0 = 50$ respectively.

This section underlines hence the most striking differences between these runs. These are essentially quantitative and can be explained by the energy repartition in the velocity helical components, shown in figure 6.23.

For the M11s run, the PPP and PCP terms contribute almost equally to the DLT (see figure 6.24). This strong contrast with the M8c run, where the PPP contribution to the direct cascade is clearly smaller (see figure 6.7.(b)), can be attributed to the fact that at large scales, the positive helical velocity field contains considerably more energy than the compressive part (figure 6.23.(b)). As a consequence, even though interactions with $P \ll K \approx Q$ are more favoured by the PCP geometric factor than the PPP one (see section 6.3), they play here similar roles.

The opposite extreme happens for the M1c run, see figure 6.25. For this run, the $E^{V,P}/E^{V,C}$ ratio is much lower at large scales, and much bigger at scales around the magnetically-forced scales (figure 6.23.(c)). This has two consequences: (i) a very strong direct cascade mediated by the compressive part of the velocity field and (ii) a quite small contribution of the PCP term to the NLIT from the magnetically-forced scales (figure 6.25.(f)). For this run, due to the strong DLT, the transfer and flux spectra shown in figure 6.26 are quite different than those from the M8c run.

Finally, for the subsonic M01s4 run, since there is essentially no energy in the velocity field's compressive part, the DLT is mediated by both positive and negative helical parts in equal proportions, whereas the LIT and the NLIT are essentially due to the PPP term, as shown in figure 6.27. The fact that the direct cascade is equally carried out by the PPP

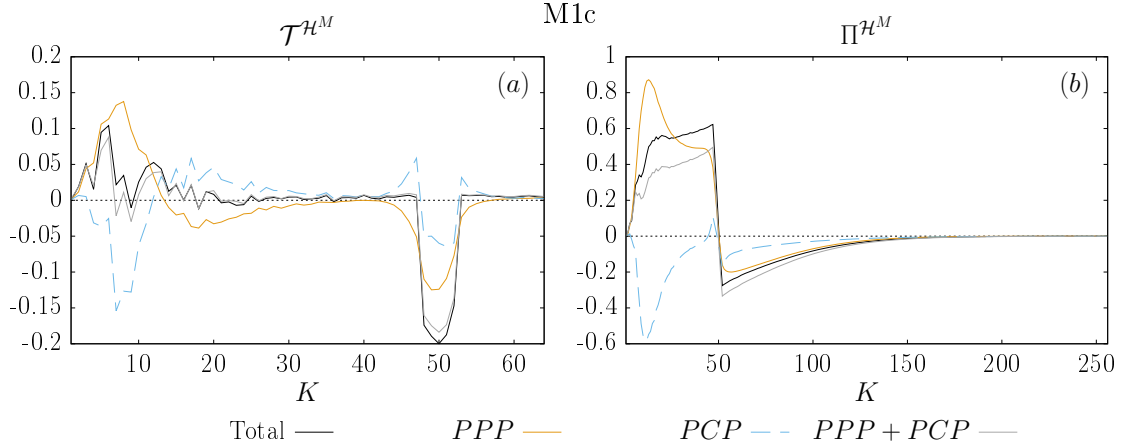


Figure 6.26: Magnetic helicity transfer spectra and flux for the M1c run at an instant when $\mathcal{I}_{\mathcal{H}^M} \approx \frac{1}{10}L$, as well as their biggest helical contributions.

and PNP terms is due both to the facts that, at large scales, the positive and negative helical contributions contain the same amount of energy (figure 6.23.(a)) and that the geometric factors G_{PPP} and G_{PNP} have very close values for $p \ll k \approx q$. This is not only true for low compressibility: for the M8c run, the DLT is indeed carried in similar proportions by the PPP and PNP terms (compare figure 6.9.(b) to figure 6.7.(b), where both PPP and PNP cuts have an amplitude of the order of 0.001).

Concerning the relative importance of the $B \leftrightarrow B$ and the $V \leftrightarrow B$ exchanges on the LIT, the approach described in appendix A.4.1 gives the estimate that about 25-50 percent of the LIT “wings” strength is associated with purely $B \leftrightarrow B$ exchanges and the rest with $V \leftrightarrow B$ exchanges. This confirms the fact that the LIT “wings” are associated with both $V \leftrightarrow B$ and $B \leftrightarrow B$ exchanges playing quantitatively a similar role, even though the $V \leftrightarrow B$ transfers seem to play a greater role, at least for these runs and at this chosen instant in time.

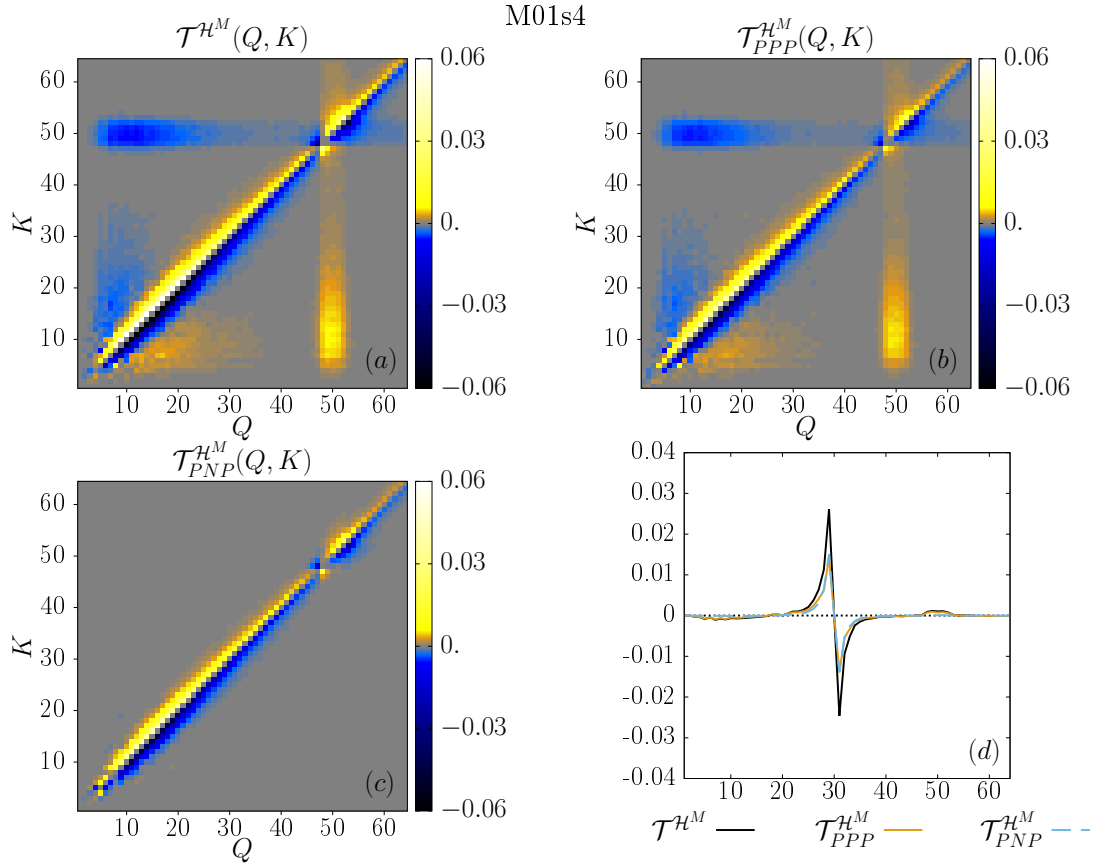


Figure 6.27: (a-c) Magnetic helicity transfer rates from shell Q to shell K for the M01s4 run at an instant when $\mathcal{L}_{\mathcal{H}^M} \approx \frac{1}{10}L$, as well as the biggest helical contributions. (d) Cut of subfigures (a-c) at $K_0 = 30$.

6.4.2 Comparison with previous research

In reference [3], a numerical experiment is carried out in a setting very similar to the present work's Mf run (see section 3.5.2): magnetic helicity fluctuations are injected to a fluid initially at rest, at small enough scales in order to observe an inverse transfer. This inverse transfer takes place in the absence of a large-scale mechanical driving.

In that work, the following observations are reported [3]:

1. At early times, a local inverse transfer of magnetic helicity for $K < K_{inj}^{\mathcal{H}^M*}$, where $K_{inj}^{\mathcal{H}^M*} = 8$ corresponds to the scales where the electromotive forcing takes place (in that reference).
2. At early times, a magnetic helicity direct transfer towards smaller $K > K_{inj}^{\mathcal{H}^M*}$ scales.
3. At later times, when the magnetic helicity reaches the largest scales of the system, the transfer is mostly non-local: from the forced scales directly to the largest ones.
4. At later times, a direct transfer also occurs at intermediate scales $1 < K < K_{inj}^{\mathcal{H}^M*}$.

The observation (1) of a local inverse transfer at early times can be put in parallel with figure 6.28, where magnetic helicity transfer spectra at an instant when its integral scale $\mathcal{L}_{\mathcal{H}^M} \approx \frac{1}{40}L$ are shown for the Mf, M01s4, M11s, M1c and M8c runs. At this early

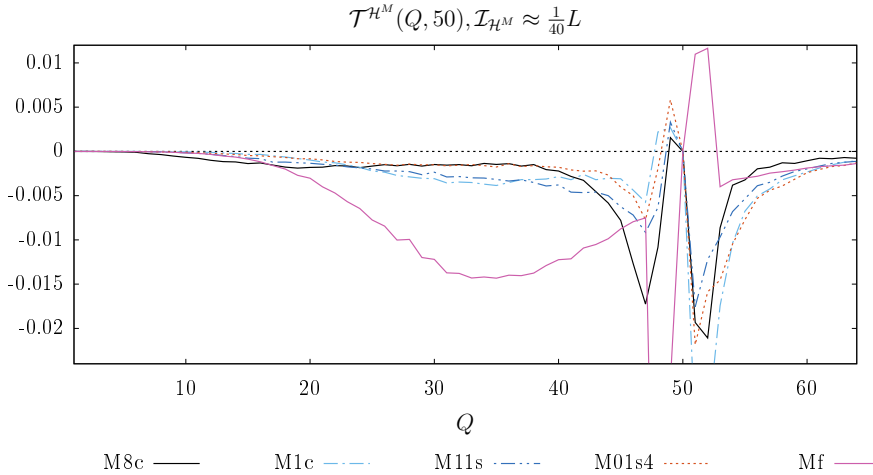


Figure 6.28: Cuts at $K_0 = 50$ of the magnetic helicity transfer rates $\mathcal{T}^{\mathcal{H}^M}(Q, K)$ for the Mf, M01s4, M11s, M1c and M8c runs, at the early instant when $\mathcal{I}_{\mathcal{H}^M} \approx \frac{1}{40}L$.

instant, significant inverse transfers already occur up to scales larger than the integral scale by a factor of two to four, depending on the run. This instant, when the magnetic helicity spectrum peaks at around $K \approx 40 = \frac{4}{5}K_{inj}^{\mathcal{H}^M}$, with $K_{inj}^{\mathcal{H}^M} = 50$ the shell around which the electromotive forcing is done *in the present work* (not to be confused with $K_{inj}^{\mathcal{H}^M*} = 8$ for reference [3]), corresponds to an even earlier instant than the t_1 one considered in reference [3]. Indeed, for $t = t_1$ in that work, the magnetic helicity peaks close to $K = 5 < \frac{4}{5} \times 8 = \frac{4}{5}K_{inj}^{\mathcal{H}^M*}$. In reference [3], the transfers from shell $K = K_{inj}^{\mathcal{H}^M*} = 8$ to larger scales are indeed relatively high, up to shell 3, which is about a factor two to three larger than the magnetic helicity integral scale in that run³. Whether these transfers can truly be qualified as “local” or not is here somewhat ambiguous, since a linear binning has been taken for the shells (see section 2.4). What is clear however, is that at later times, similarly to observation (3), the transfers are less local (compare figure 6.28 with 6.7.(c)): at early times, the transfers from the magnetically-forced scales are strongest for shells between the integral and the forced scales, whereas at later times, they are strongest to scales larger than the integral scale.

Concerning the direct cascades both at early and later times (observations (2) and (4)): as shown in this chapter, the DLT is mostly caused by the large scale velocity field. When forcing only magnetically, magnetic energy is at early times rapidly converted in kinetic energy close to the electromotive forcing scale. Hence, relative to the magnetic field at scales smaller than the forced scales, a “large scale” velocity field emerges, which causes a direct cascade in the wavenumber region above the forcing scale. At later times, when magnetic helicity reaches larger scales, kinetic energy is also transported to these scales (see figure 6.30), which means that a direct cascade is expected to happen at the intermediate scales as well. As shown in figure 6.29.(a), for the Mf run, the direct cascade is not as close to the diagonal as compared to the M8c, M11s, M1c and M01s4 runs. This is because the “large scale” velocity field corresponds to shells around 10, and not to $P \in [1, 4[$. A similar feature is visible in figure 6.12.(b), where a smaller part of the direct cascade for the M8c run at an instant when $\mathcal{I}_{\mathcal{H}^M} \approx \frac{1}{10}L$ is indeed carried out by the velocity field at shells $P \in [4, 30[$. For the Mf run, it is thus not possible to clearly

³Please note that in reference [3], the inverse convention is taken, namely the transfer from shell Q to shell K is noted $T(K, Q)$, and not $T(Q, K)$.

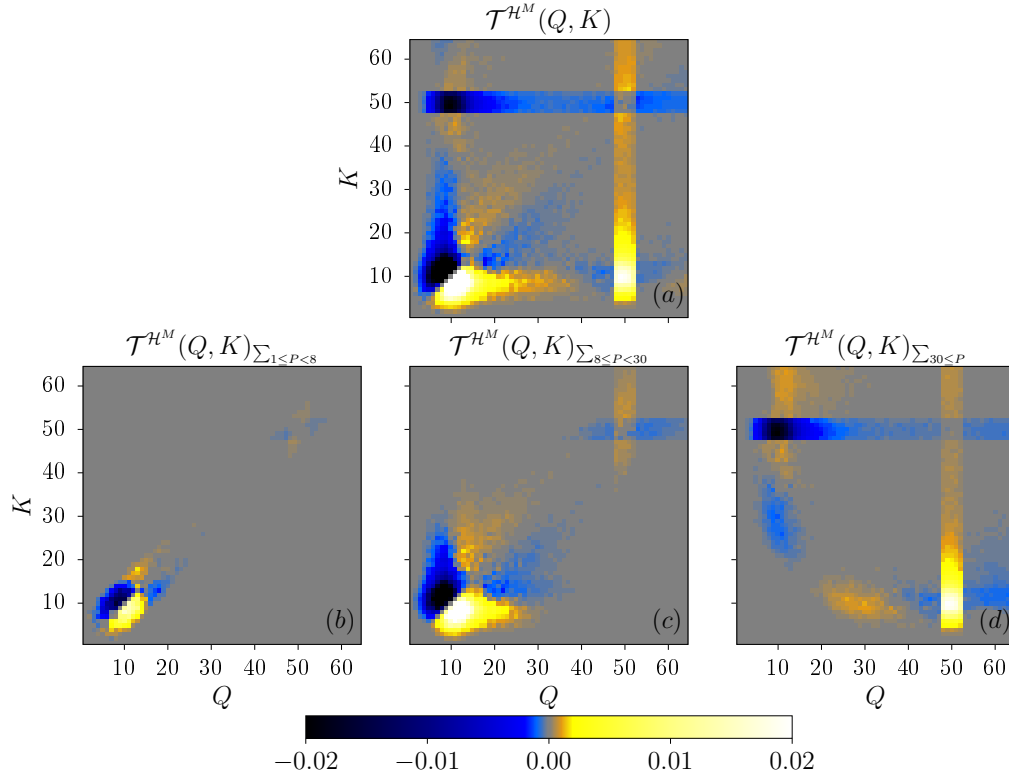


Figure 6.29: (a) Magnetic helicity transfer rates from shell Q to shell K for the Mf run at an instant when $\mathcal{I}_{\mathcal{H}^M} \approx \frac{1}{10}L$. (b-d), the same, but filtered for different velocity field shells.

split the LIT from the DLT by filtering the velocity field: the velocity field at a certain scale is responsible for both the LIT close to this scale and the DLT occurring at smaller scales (figure 6.29.(b-c), to be compared with figure 6.12 – please note that the limits of the shell-filter are different in both cases).

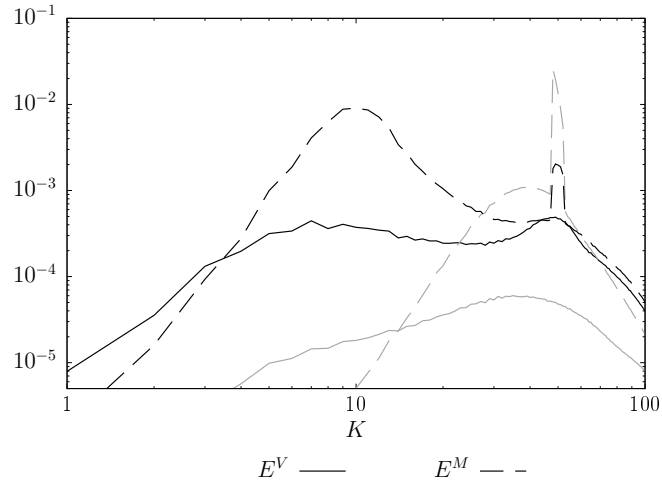


Figure 6.30: Velocity power spectrum and magnetic energy for the Mf run at an early instant (gray curves – $\mathcal{I}_{\mathcal{H}^M} \approx \frac{1}{40}L$) and later in time (black curves – $\mathcal{I}_{\mathcal{H}^M} \approx \frac{1}{10}L$).

6.5 Summary

The analysis performed on the most compressible run, namely the M8c run at an instant when $\mathcal{I}_{HM} \approx \frac{1}{10}L$, allows to draw a more complete picture of the magnetic helicity inverse transfer in highly compressible turbulence. The results are consistent with previous research in the incompressible case regarding the locality and direction of the transfers [3] and the locality and relative strength of the interactions involving the like-signed and opposite-signed helical part of the velocity field [69]. Comparisons done with the three other extreme cases: the M01s4, M11s and M1c runs, show that the general behaviour is very similar over this region of the parameter-space, despite the wide range of compressibility. The main differences seem to be quantitative and to resort to the question of which helical term play an important role for which phenomena, which can be well explained through the triadic geometric factors and the helical energy content of the mediating velocity field. In short:

- Three distinct phenomena are associated with the general picture of an inverse transfer of magnetic helicity: a mostly local inverse transfer (LIT), a non-local inverse transfer (NLIT) from the magnetically-forced scales and a “hidden” direct local transfer (DLT) of magnetic helicity (figure 6.5).
- These three phenomena can be clearly associated with different scales of the velocity field, which acts as a mediator: the NLIT is due to the small scale velocity field, the DLT is mediated by the large scale velocity field and the LIT is associated to the velocity field at intermediate scales (section 6.2.2).
- The direct cascade of magnetic helicity is associated with a direct cascade of magnetic energy. It is mostly due to a redistribution of magnetic energy across scales and involves relatively little magnetic \leftrightarrow kinetic energy exchanges, as compared to the strength of the magnetic transfers (figure 6.14).
- The inverse transfers, both the LIT and the NLIT, are associated with both magnetic \leftrightarrow magnetic energy exchanges and magnetic \leftrightarrow kinetic energy exchanges. The LIT is predominantly associated with the magnetic stretching term, whereas the NLIT is associated with both magnetic stretching and magnetic pressure (figures 6.14 and 6.16).
- The helical terms playing the biggest roles are the ones of the form PXP , with $X \in \{P, C, N\}$. Which X plays the dominant role for which feature depends both on the helical repartition of energy of the mediating velocity field and on the geometric triadic factors (section 6.4.1).
- In general, the PPP and PNP terms have a tendency to carry the leading role in the LIT, the PPP and PCP in the NLIT and the PCP term is favoured for the DLT, as compared to the PNP and PCP terms, at least for highly compressible flows (sections 6.3 and 6.4.1).
- The helical triadic geometric factors can explain surprisingly well the role and relative importance of the different helical contributions to the shell-to-shell magnetic helicity transfer rates, including the aspects mentioned in the previous point (section 6.3).
- Depending on the helical energy content of the mediating velocity field however, some terms which are less favoured geometrically can take a leading role if the helical velocity part is big enough (section 6.4.1).

Some observed aspects could benefit from more detailed studies, which are not within the scope of the present work:

- The injected magnetic fluctuations considered here are fully (positive) helical. As a consequence, the dynamics are mostly governed by the *PPP* and *PCP* terms (and the *PNP* term for low compressibility). In other situations however, for example if the electromotive forcing would contain very small helicity, or in settings allowing dynamo studies (for example, using a helical mechanical forcing, not necessarily at the largest scales, and add a small non-helical magnetic seed when the steady-state is reached, as in the second numerical experiment of reference [3]), one could expect a greater influence of the *NXN* terms and of the heterochiral terms. An example of such a situation where the heterochiral terms are more important is shown in section 7.1. These heterochiral terms are however quite complex to interpret, as sketched in appendix C.2. Even though the *SPS* and *SNS* terms play here a very small role, the *SCS* term, even though not dominant, has a non-negligible role which would benefit from further investigation.
- Since the dynamics of the magnetic helicity inverse transfer largely depends on the energy distribution among the helical and compressive parts of the velocity field, it may be beneficial to study helically decomposed shell-to-shell kinetic and/or specific kinetic energy transfers as well. Studying such transfers could reveal some unsuspected mechanisms. For example, the study of helically-decomposed fluxes in 3D incompressible hydrodynamic turbulence has led to the discovery of an inverse transfer of *kinetic* energy caused by helical terms where the three interacting velocity shells have the same helicity sign [1]. This inverse transfer is sub-dominant in the direct cascade of energy for 3D hydrodynamical turbulence. In order to extend this approach to the compressible case, some thoughts would have first to be given about which formalism to use, since the kinetic energy entails a non-constant density whereas the kinetic helicity does not.

Chapter 7

Discussion and conclusion

Before recapitulating the present work’s main findings, this chapter assesses their robustness by varying the electromotive forcing (section 7.1) and the numerical scheme and resolution (section 7.2). These verifications are necessary since the magnetic-to-kinetic energy injection rate, equal to 1 for most of the runs, has been chosen arbitrarily. Some effects of a non-fully helical forcing are also of interest. Furthermore, as noted in section 4.1.2, the main runs suffer from bottleneck pollution, in addition to being underresolved for high Mach number flows. Hence, even though the dynamics are expected to be dominated by the magnetic helicity inverse transfer, it is important to check for convergence of the measured exponents with respect to the numerical resolution. Furthermore, the fact that many cells are reconstructed at lower order for high Mach number flows (appendix A.3) could as well impact the results’ quality, so that a comparison with a lower-order scheme is pertinent.

Section 7.3 then summarises the main results and underlines limitations with respect to their applicability to real astrophysical systems.

7.1 Electromotive forcing variations

Starting with the same hydrodynamic steady-state as the one for the M1s2 run, this section considers other runs, changing both the forcing helical fraction h_f and the energy injection ratio $R_{inj} = \epsilon_{inj}^M / \epsilon_{inj}^K$. Namely, eight runs are considered in addition to the M1s2 run for which $h_f = +1$ and $R_{inj} = 2$. Four runs with $R_{inj} = 2$ and $h_f \in \{0.2, 0.4, 0.6, 0.8\}$ in order to see the influence of the forcing helical fraction and four runs with $h_f = +1$ and $R_{inj} \in \{1, 1.5, 5, 10\}$, in order to test the influence of the energy injection ratios. These runs are done with the same fallback strategy as the one used for the M1s2 run. This parameter study is done for the sake of estimating the robustness of the results with respect to the magnetic helicity injection rate.

Consistently with the observations of section 4.2.1, the higher the magnetic helicity injection rate (higher R_{inj} or higher h_f), the better it is conserved. This is displayed in figure 7.1.(a-b), which shows the total magnetic helicity in the system as a function of time, normalised by its estimated injection rate according to relation (4.5). Indeed, more magnetic helicity injection means a faster inverse transfer (as seen in subfigures (c-d), where the integral scale grows faster when the injection is greater). Since at larger scales, dissipation effects are smaller, a faster transfer means a better conservation. This interpretation is supported by the fact that at early times, when dissipation is still relatively low since magnetic helicity did not cascade to the lowest scales yet, all curves of subfigures (a-b) are overlapping.

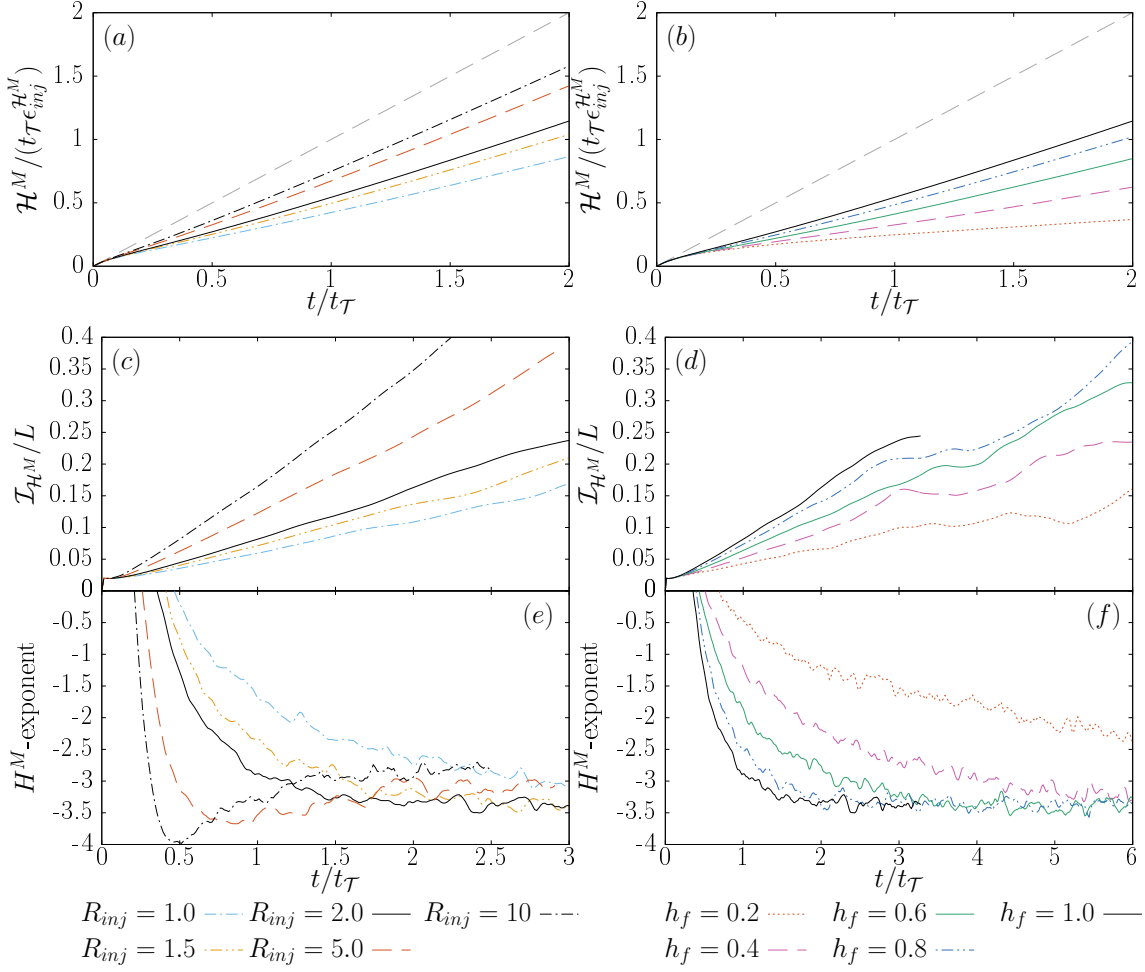


Figure 7.1: Influence of the energy injection ratio R_{inj} and the electromotive forcing helical fraction h_f on several dynamic aspects of the inverse transfer. All runs are done at resolution 512^3 starting from the hydrodynamic frame used for the main M1s2 run (which corresponds to $R_{inj} = 2, h_f = 1$). (a-b) Total magnetic helicity present in the system normalised by its injection rate. (c-d) Magnetic helicity integral scale as a function of time. (e-f) Magnetic helicity exponent as a function of time from a LSF in the region $20 \leq K \leq 30$. Why it becomes flatter at later instants for $R_{inj} = 5$ and $R_{inj} = 10$ is explained in the text.

Regarding the exponent in the magnetic helicity Fourier spectra, figures 7.1.(e-f) show that a lower energy injection ratio or a lower magnetic helicity fraction means a later convergence towards the same value, close to -3.3 , which is the same exponent observed in section 4.2.1 and in the incompressible case [74]. For a too high magnetic energy injection however ($R_{inj} \geq 5$), the -3.3 scaling is lost at later times, as shown in subfigure (e). This is consistent with the findings of section 4.3, where for the Mf run (where an electromotive forcing is applied in the absence of a mechanical driving, corresponding hence to the limit case $R_{inj} \rightarrow \infty$), no scaling law is found with respect to the magnetic helicity spectra before the largest scales are reached. Figure 7.2.(a) shows with this respect the magnetic helicity spectra for the runs with $R_{inj} \in \{2, 5, 10\}$ and the Mf run at an instant when $\mathcal{I}_{\mathcal{H}^M} \approx \frac{1}{6}L$. A clear scaling law cannot be found for $R_{inj} \in \{10, \infty\}$, since there is no range with a clear plateau in the exponents computed through a LSF in a moving window. Figure 7.2.(b) shows to this end the exponent computed from a LSF in

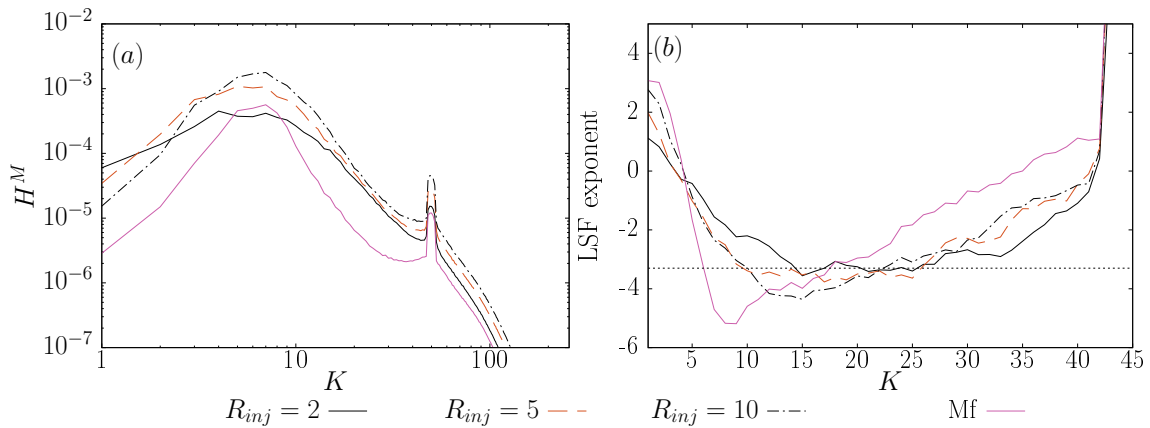


Figure 7.2: (a) Magnetic helicity spectra at an instant when $\mathcal{I}_{\mathcal{H}M} = \frac{1}{6}L$ for runs with varying R_{inj} . (b) Exponent computed through a LSF in a window of size 5 starting at the shell indicated in the abscissa. The horizontal dotted line corresponds to the incompressible -3.3 exponent.

a window of size 5 starting at the shell in the abscissa.

These observations deliver arguments in favour of the robustness of the observed scaling laws. They indeed indicate that there is a certain range of magnetic helicity injection rate, which depends on both the helical fraction and the magnetic energy injection rate, where the exponents converge to the same value. Hence, when injecting less magnetic helicity in the system, the scaling exponents should be recovered but at later times. However, injecting too much magnetic energy as compared to the kinetic one could lead to the absence of a clear power-law behaviour.

As mentioned in section 6.5, the shell-to-shell helically-decomposed heterochiral terms could play a more important role in situations where the total magnetic helicity in the system is smaller, when for example helical components of both signs are present in comparable proportions. This is confirmed through the transfer functions of the run with $R_{inj} = 2$, $h_f = 0.2$, displayed in figure 7.3 at an instant when $\mathcal{I}_{\mathcal{H}M} \approx \frac{1}{10}L$. For this run, most of the inverse transfer occurs through the non-local inverse transfer from the magnetically-forced scales, since the inverse transfer local “wings” are less intense (see chapter 6 for the terminology and comparisons with the main runs). The *SPS* and *SNS* heterochiral terms play a greater role: when for the main runs in chapter 6, their intensity is about two orders of magnitude lower than the *PPP* term, they have here a similar order of magnitude (the colour bar extremes are the same for all the helically-decomposed terms). The *SNS* term in particular presents the interesting feature of transferring magnetic helicity to the magnetically-forced scales, acting against the inverse transfer. As mentioned in appendix C.2, interpreting these heterochiral terms is not trivial when one considers the energy transfer directions. A more detailed analysis of these terms is however not in the scope of the present work, since they play a relatively small role in situations with a fully helical forcing $h_f = +1$.

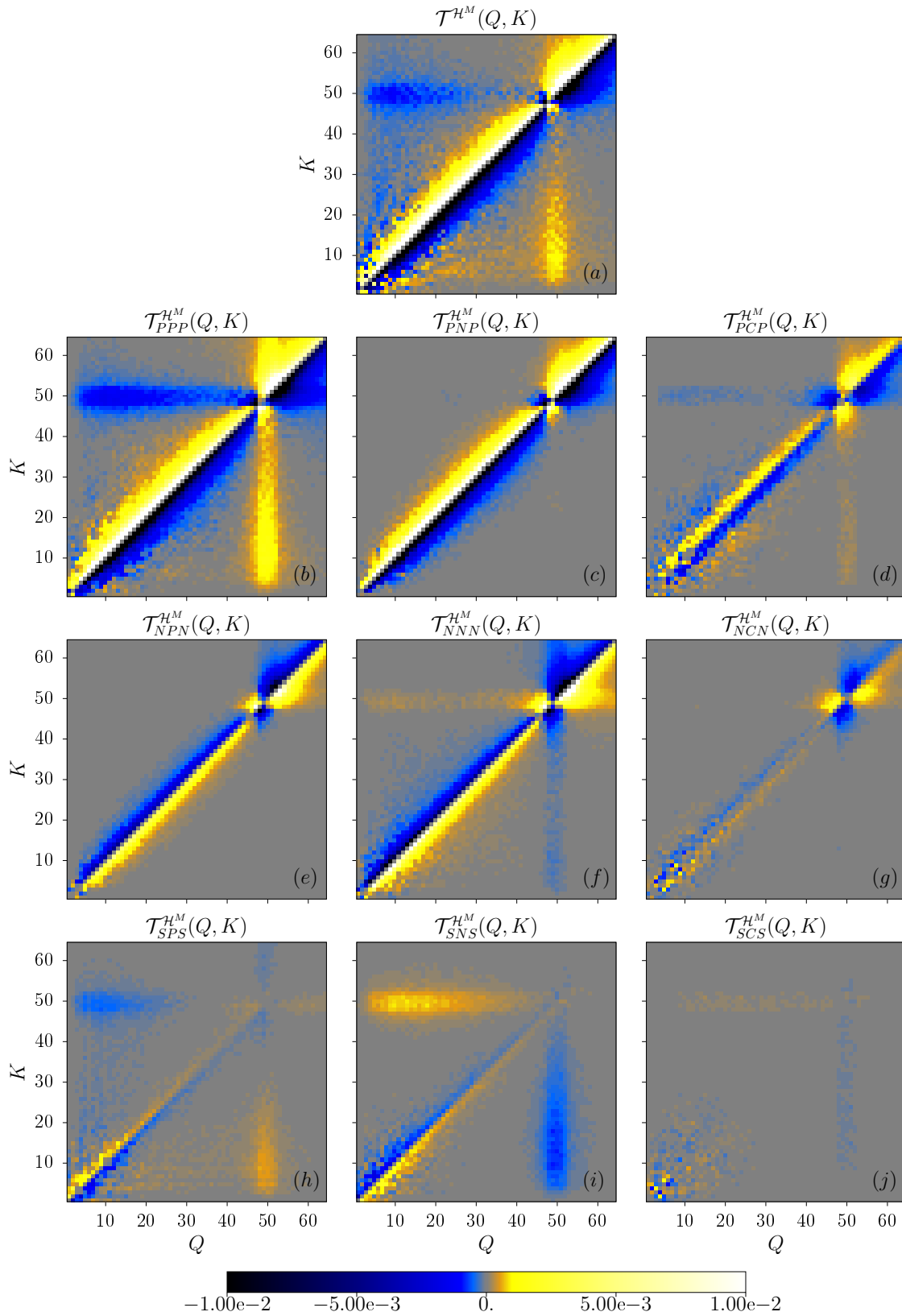


Figure 7.3: Helically-decomposed shell-to-shell magnetic helicity transfer rates for the run with $R_{inj} = 2$ and $h_f = 0.2$ starting with the same hydrodynamic frame as the M1s2 main run. These transfer rates are computed at an instant when $\mathcal{I}_{\mathcal{H}^M} \approx \frac{1}{10}L$.

7.2 Scheme's order and resolution

Since the main runs suffer from bottleneck pollution and are underresolved for high Mach number flows, two runs at the higher 1024^3 resolution are considered in order to confirm the main results. These runs are performed by upscaling the M1s and M8c hydrodynamic frames as described in appendix A.1. Magnetic helicity injection is switched on after the system's adaptation to its new resolution. These two runs are labelled “M1s2HR” and “M8cHR” (where the “HR” letters stand for “(h)igher (r)esolution”). Similarly, runs at the 256^3 (l)ower (r)esolution are considered, which are labelled “M1s2LR” and “M8cLR” accordingly.

At resolution 1024^3 , some very low density regions in the plasma lead to very high local magneto-sonic speeds, which lead in turn to a strong limitation of the timestep. As a consequence, only an early instant in time is considered for the M8cHR run, namely $t \approx 0.14t_\tau$, at which $\mathcal{I}_{\mathcal{H}M} \approx 0.045L$.

Furthermore, since a relatively high amount of reconstructions occur at lower-order for high Mach numbers (see appendix A.3), the M1s2 and M8c runs at resolution 512^3 are relaunched but using a second-order scheme, setting the reconstruction order map (see section 3.2) to 2 everywhere, so as to assess the effects of lower-order numerics on the turbulent flows. These runs are labelled “M1s2LO” and “M8cLO” respectively, where “LO” stands for “(l)ower (o)rder”. The effects of lower-order numerics on a standard test problem, the 3D MHD vortex, are discussed in appendix B, even though their transposition to turbulent flows is limited.

The fallback strategy used for the “M1s2 family”, consisting of the M1s2, M1s2LR, M1s2LO and the M1s2HR runs, is the same as the one used for the M1s2 run (see appendix A.2), apart for the M1s2LO for which no fallback approach is needed. The proportion of reconstructions performed at an order lower than four peaks at around 1/10000 for the M1s2LR and M1s2HR runs, so that almost all cells are reconstructed at high order at all times.

Regarding the “M8c family”, the fallback strategies used for the M8cLR, M8cLO and M8cHR runs are shown in table 7.1. For the 1024^3 M8cHR run the proportion of reconstructions done at fourth-order is about 90% in the hydrodynamic steady-state, and decreases down to 60% at the last considered instant in time. For the 256^3 M8cLR run, these proportions are about 70% in the hydrodynamic steady-state and about one third at later instant in times (when $\mathcal{I}_{\mathcal{H}M} \approx \frac{1}{6}L$). As for the M8cLO run, it presents about 1-2% of first-order reconstructions.

Table 7.1: Fallback strategies used for the “M8c family” (see section 3.2). The “Upc.” column stands for “upcoming shocks”: when the value is (y)es, it means that the refinement described in relation (3.11) is used.

Run	$(\tau_{4,p}^+, \tau_{3,p}^-, \tau_{3,p}^+, \tau_{2,p}^-, \tau_{2,p}^+, \tau_{1,p}^-)$	$(\tau_{4,\Delta t}^+, \tau_{3,\Delta t}^-, \tau_{3,\Delta t}^+, \tau_{2,\Delta t}^-, \tau_{2,\Delta t}^+, \tau_{1,\Delta t}^-)$	Upc.
M8cHR	(0.35, 0.45, 1.2, 1.8, 3, 3.5)	(0.35, 0.35, 0.35, 0.35, 0.45, 0.5)	y
M8cLR	(0.35, 0.45, 1.2, 1.8, 3, 3.5)	not used	y
M8cLO	(0, 0, 0, 0, 3, 3.5)	not used	y

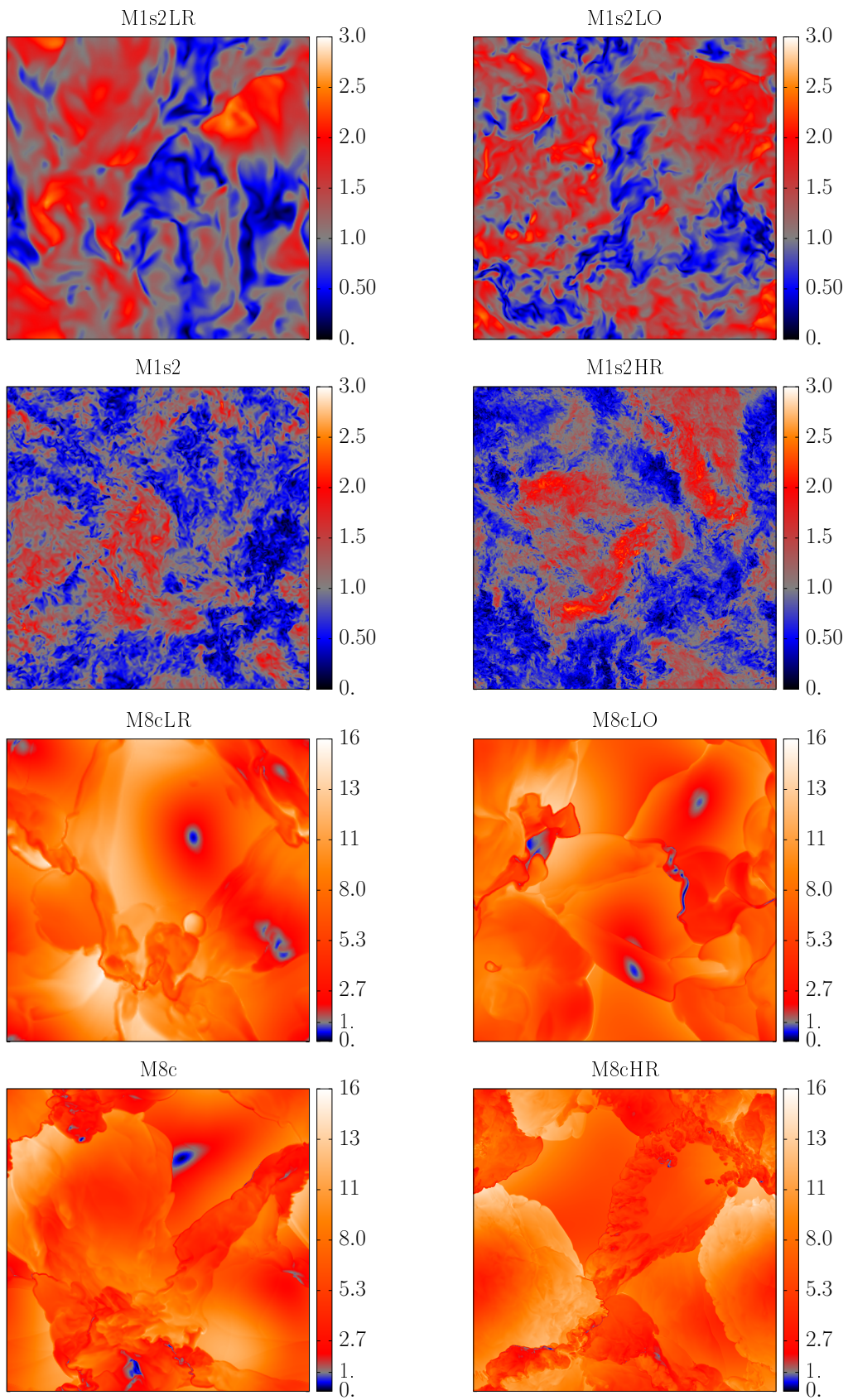


Figure 7.4: Mach number slices during the hydrodynamic steady-state for different resolutions and schemes with varying order.

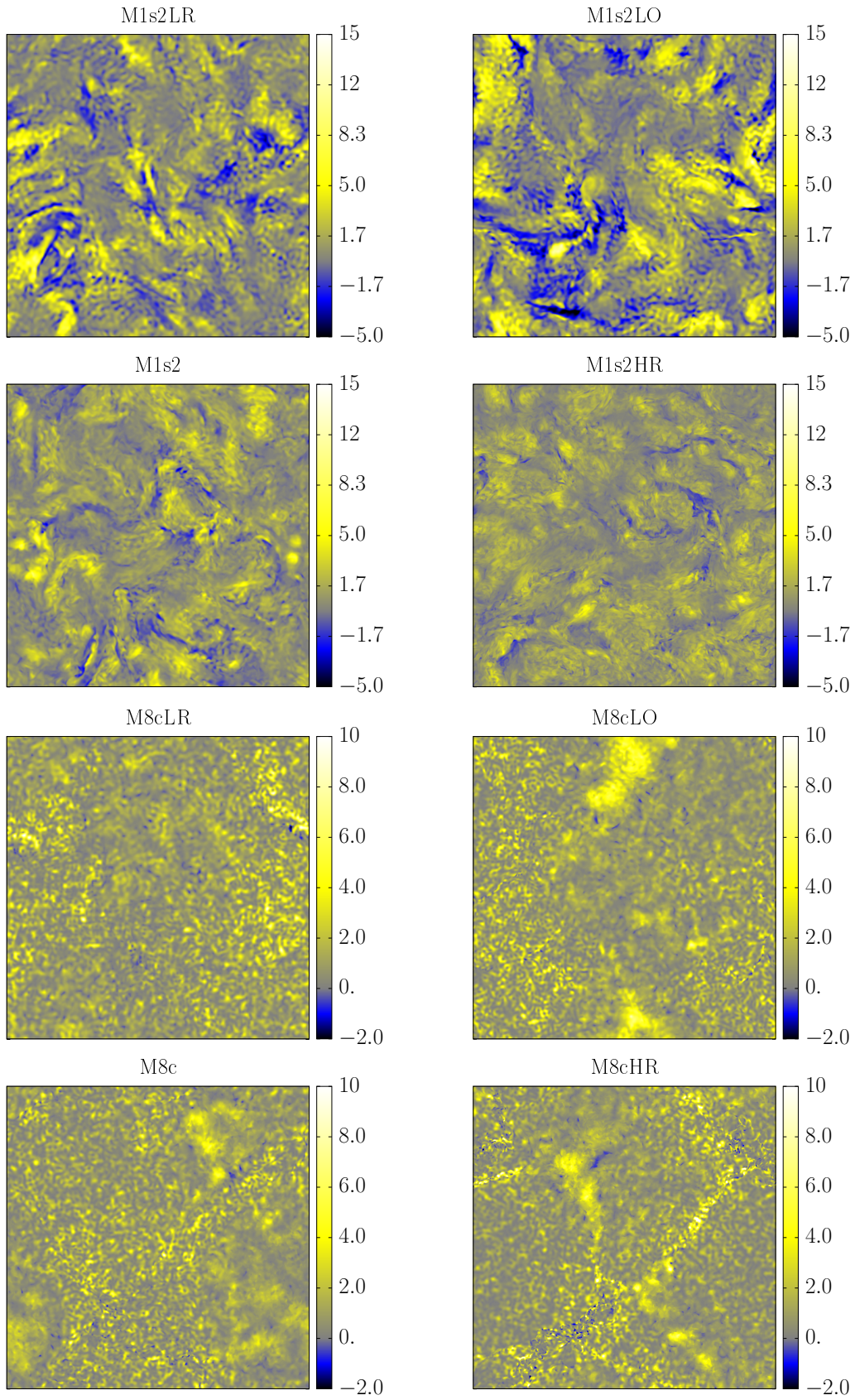


Figure 7.5: Magnetic helicity density slices. For the M1s2 family, at an instant when $\mathcal{I}_{\mathcal{H}M} \approx \frac{1}{6}L$, for the M8c family, at an instant when $\mathcal{I}_{\mathcal{H}M} \approx 0.045L \approx \frac{1}{20}L$. The slices are normalised by the mean magnetic helicity density in the system.

7.2.1 Level of details

Both higher resolution and higher-order numerics allow to see finer structures in the turbulent flows. This is illustrated in figure 7.4 in the hydrodynamic M1s and M8c steady states and in figure 7.5 after the electromotive forcing is switched on, through magnetic helicity density slices. At low Mach numbers, the slices from the 512^3 runs with the second-order scheme look qualitatively very similar to the ones at resolution 256^3 using higher-order numerics. This illustrates the potential significant increase in quality when using higher-order numerics and the subsequent savings with respect to computing resources. Higher-order numerics require indeed a coarser grid to reach a certain result's quality, as compared to lower-order numerics. For the highly shocked M8c family, even though finer structures are visible for the M8c run as compared to the M8cLO one for the hydrodynamic slices, the difference is not as big for the magnetic helicity density slices. This is because a lot of cells are not reconstructed at fourth-order as soon as the electromotive forcing is switched on, see figure A.2.

7.2.2 Magnetic helicity conservation

When increasing the resolution and/or the scheme's order, the magnetic helicity is, as expected, better conserved. For the M1s2 run, about 60% of the injected magnetic helicity is conserved (because at $t = 3t_{\mathcal{T}}$, $\mathcal{H}^M / (\epsilon_{inj}^{\mathcal{H}^M} t_{\mathcal{T}}) \approx 1.8$), whereas this rate rises to 85% for the M1s2HR one (figure 7.6.(a)). For the M1s2LO and the M1s2LR runs, magnetic helicity is considerably less well conserved, about 13% and 10% respectively (measured at $t = 6t_{\mathcal{T}}$). This is as well visible through the plateau behaviours in the magnetic helicity flux in figure 7.6.(b): when a good plateau is observed for the M1s2 and M1s2HR runs, suggesting the presence of an inertial range, no horizontal line is visible for the lower-order scheme, or the lower 256^3 resolution run, suggesting a high numerical dissipation in the inverse transfer range. This better conservation of magnetic helicity leads to a faster inverse transfer to larger scales (see subfigure (c)).

For the M8c family, as already observed from the magnetic helicity density slices, the differences at resolution 512^3 between the second-order and the high-order scheme are not as big (figures 7.7.(a-b)), due to the fact that many cells are reconstructed at lower order through the fallback approach. Increasing the resolution up to 1024^3 yields however a clearly better magnetic helicity conservation, see subfigure (a).

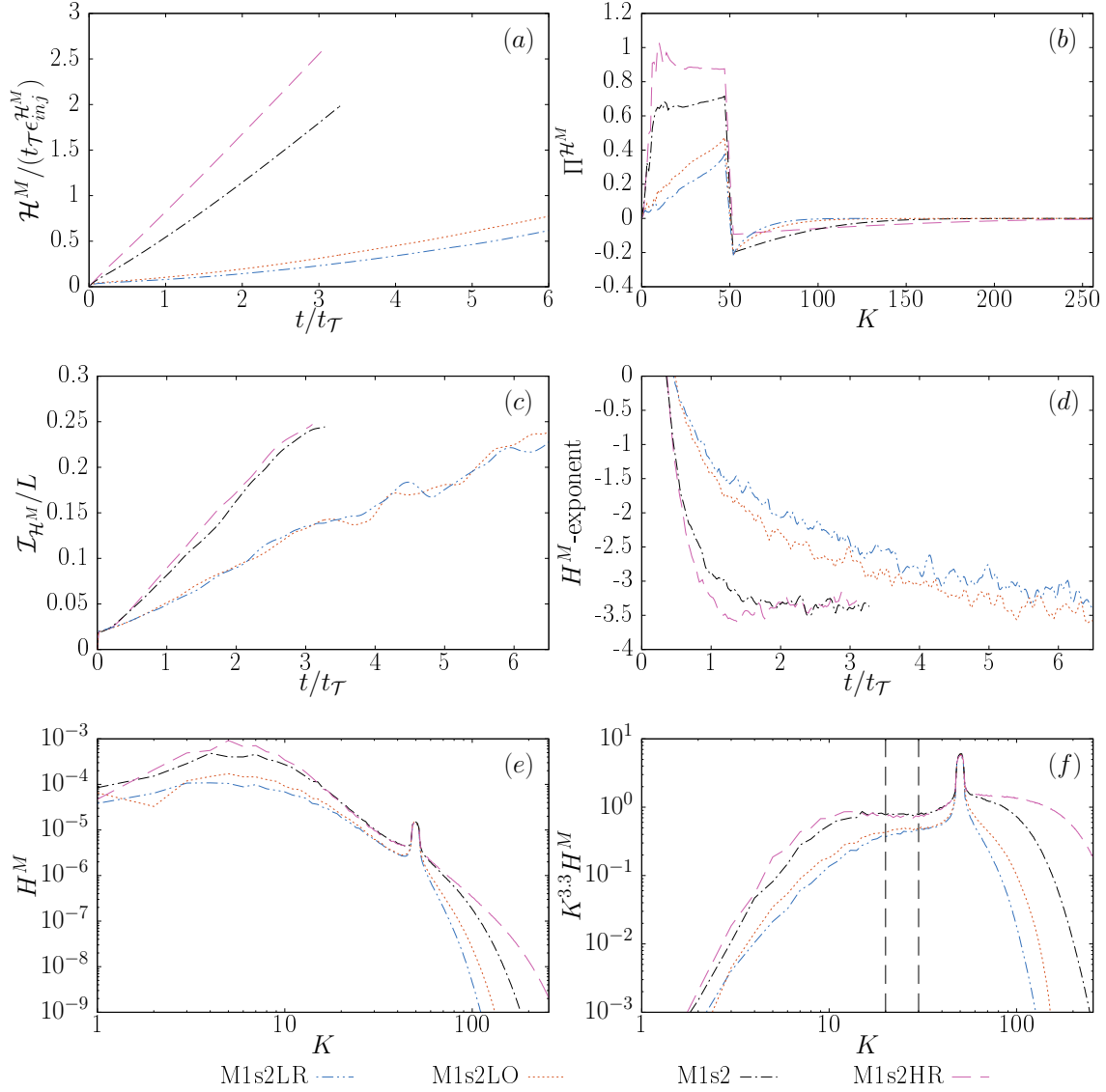


Figure 7.6: Magnetic helicity inverse transfer for the M1s2 family. (a) Time evolution of the total magnetic helicity in the system, normalised by its injection rate. (b) Magnetic helicity spectral flux at an instant when $\mathcal{I}_{\mathcal{H}^M} \approx \frac{1}{6}L$. (c) Magnetic helicity integral scale as a function of time. (d) Time evolution of the magnetic helicity spectral scaling index, measured through a least squares fit (LSF) in the region $20 \leq K \leq 30$. (e) Magnetic helicity spectra at an instant when $\mathcal{I}_{\mathcal{H}^M} \approx \frac{1}{6}L$. (f) Same as (e) but compensated by $K^{3.3}$. The vertical lines correspond to the domain where a LSF is performed for the measure of its power-law exponent.

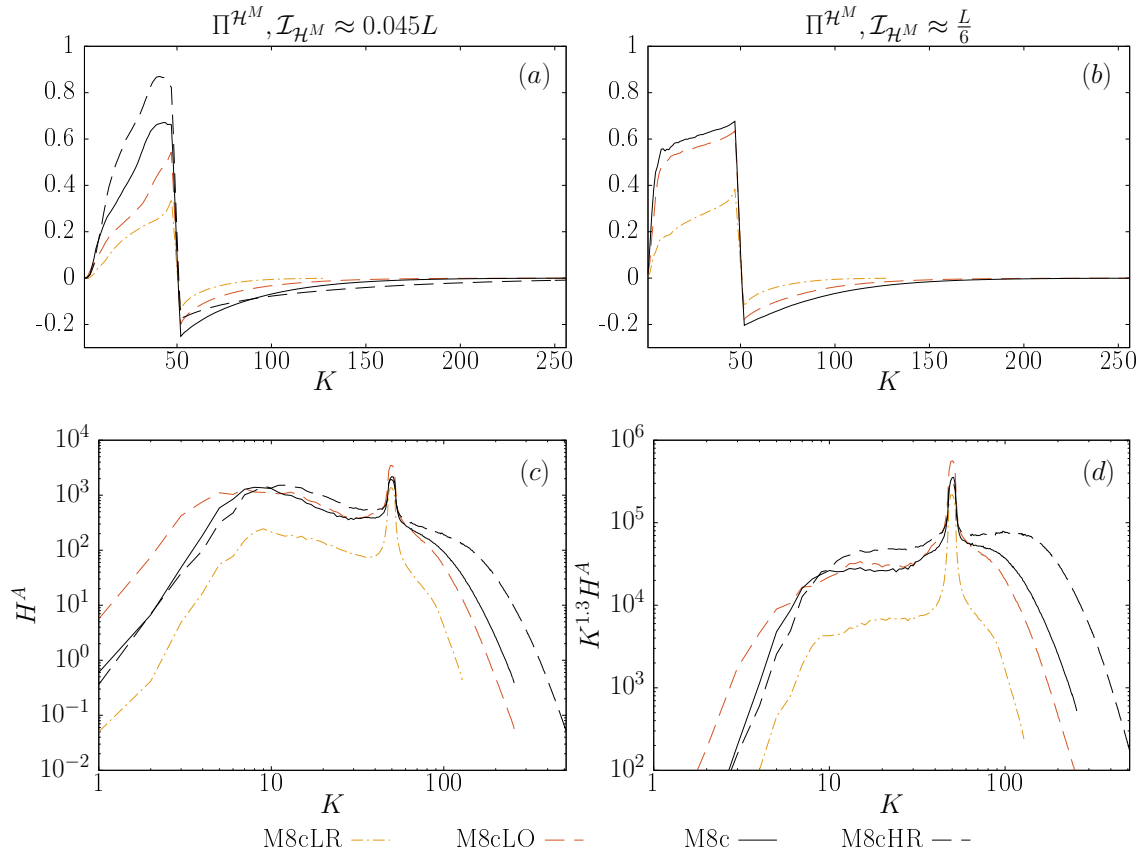
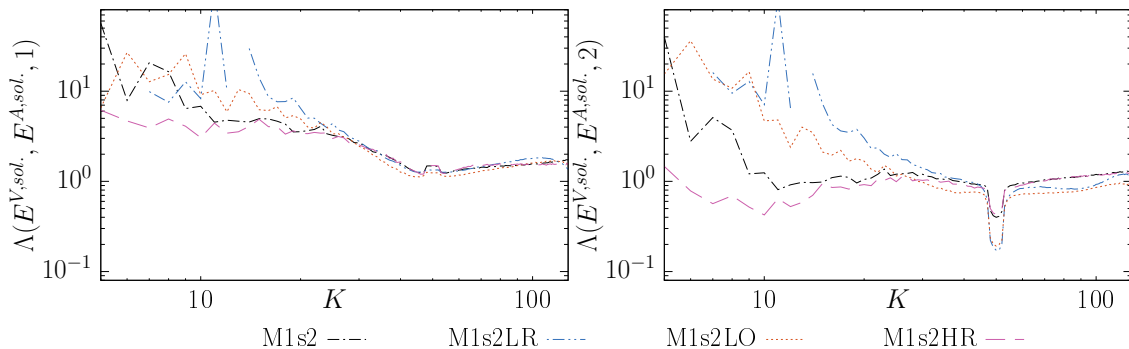
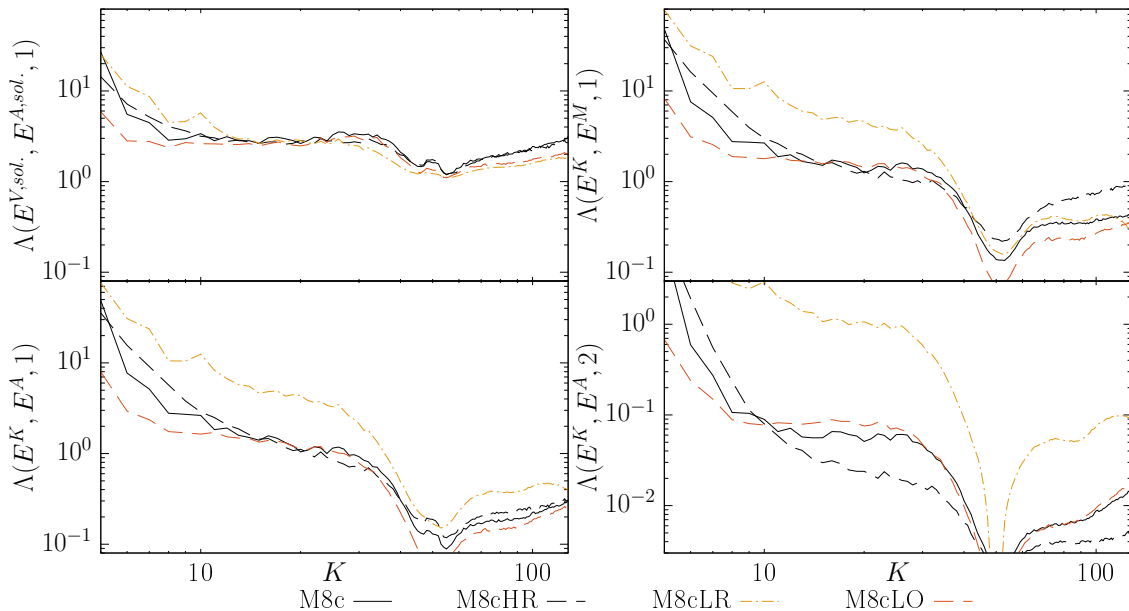


Figure 7.7: (a) Magnetic helicity spectral flux at an early instant when $\mathcal{I}_{\mathcal{H}^M} \approx 0.045L$, (b) Same as (a) but when $\mathcal{I}_{\mathcal{H}^M} \approx \frac{L}{6}$, (c) Alfvénic helicity spectra, at the same early instant when $\mathcal{I}_{\mathcal{H}^M} \approx 0.045L$, (d) Same as (c), but compensated by $K^{1.3}$.

7.2.3 Power-law scaling and Alfvénic balance

Figure 7.8: Some variants of the Alfvénic balance for the M1s2 family, at an instant when $\mathcal{I}_{\mathcal{H}^M} \approx \frac{1}{6}L$.Figure 7.9: Some variants of the Alfvénic balance for the M8c family, at an instant when $\mathcal{I}_{\mathcal{H}^M} \approx 0.045L$.

The Alfvénic helicity spectra have been found to exhibit a scaling law with an exponent close to -1.3 , over a wide range of flow compressibility (section 5.1.2). This is confirmed by the higher resolution M8cHR run, as shown in figure 7.7.(d). Even though the resolution is probably still too low to resolve properly small scale structures, the direct cascade region $K > 50$ seems as well to exhibit a scaling law with an exponent close to the same -1.3 value for the M8cHR run. The convergence to a \mathcal{H}^M -exponent close to -3.3 seems as well verified for the M1s2 family: the lower resolution M1s2LR and lower order M1s2LO runs give a spectral scaling close to -3.3 at later times, while the 512^3 and 1024^3 present this exponent already starting $t \gtrsim 2t_\tau$ (figures 7.6.(d-f)).

Hence, high-order numerics allow in the M1s2 case to observe a clear scaling behaviour at an earlier instant in time. Lower-order numerics at the same 512^3 resolution require longer simulation times and exhibit a less clear scaling, the result's quality being similar to the one at resolution 256^3 with the fourth-order scheme. For highly compressible turbulence, it seems that higher-order numerics is beneficial but less essential, consistently with the fact that discontinuities are difficult to represent at higher-order.

Furthermore, the Alfvénic balance found in chapter 5:

$$\left(\frac{E^{V,sol.}}{E^{A,sol.}}\right)^\gamma \propto \frac{H^V}{H^A}, \quad (7.1)$$

with $\gamma = 2$ for the subsonic and transonic runs and $\gamma = 1$ for the highly compressible ones is confirmed by the higher resolution runs (figures 7.8.(b) and 7.9.(a) – see section 5.2.1 for the definition of Λ). This Alfvénic balance appears hence to be quite robust: at this early instant in time for the M8c family (where $t \approx 0.14t_\tau$), even though the Alfvénic helicity H^A already presents a scaling close to -1.3 , some other spectra involved in the Alfvénic balance present indeed strong spectral slope differences with respect to their value at later times. For example, the solenoidal part of the specific kinetic energy spectra $E^{V,sol.}$ are significantly flatter than the later time exponents close to the incompressible -1.2 value (see figure 5.9 for the 512^3 M8c run).

The higher resolution M8cHR run allows furthermore to discard some variants of relation (7.1), which exhibit a good horizontal in section 5.2. For the highly compressive runs, this is for example the case for the $\Lambda(E^K, E^M, 1)$, $\Lambda(E^K, E^A, 1)$ and $\Lambda(E^K, E^A, 2)$ variants (see figures 5.12 and 5.13). At this earlier instant in time as compared to the one chosen in section 5.2, the horizontal is relatively well observed for the M8c and M8cLO 512^3 run, but gets worse for the M8cHR 1024^3 run, indicating that relation (7.1) is indeed more appropriate.

These results suggest that, even though a study at higher resolutions and/or using even higher order numerics in order to resolve properly a greater range of scales would certainly be beneficial and permit more precise power-law estimates, the general scaling law behaviours, both qualitatively and quantitatively, are quite robust. Nevertheless, the numerical values measured for the power-law exponents still need to be considered with appropriate caution, since the inverse transfer region is quite small so that adverse effects from bottleneck contamination, underresolved structures and/or boundary effects can not be fully excluded.

7.3 Conclusion

Direct numerical simulations of the magnetic helicity inverse transfer have so far been done in the incompressible [3, 74, 82, 69] and in the subsonic and transonic cases [8, 34, 25]. The present work investigates the magnetic helicity inverse transfer in high Mach number compressible isothermal MHD turbulence, which is a more realistic setting for many astrophysical systems. The protocol of the numerical experiments is the following: a turbulent steady state is generated by a large scale mechanical driving using either a purely solenoidal or purely compressive forcing up to a desired RMS Mach number \mathcal{M} , to which fully helical magnetic small-scale fluctuations are injected (see section 3.5.1). The considered Mach numbers in the hydrodynamic steady-state range up to about 10, which corresponds to typical values observed in the interstellar medium. The use of a fourth-order numerical method allows to obtain results of convincing accuracy even at the relatively low 512^3 resolution, since the spectral scaling laws don't change significantly at the higher 1024^3 resolution. Some developments have been proposed in order to enhance the robustness of the numerical method at high Mach numbers. The results are gained mostly from Fourier spectra analysis, as well as helically-decomposed shell-to-shell transfer functions (sections 2.3 and 2.4). The main results are summarised below:

1. Even in highly compressible turbulence, magnetic helicity exhibits an inverse transfer

in Fourier space (section 4.2). The higher the compressibility, the faster magnetic structures are formed.

2. Several quantities present a power-law scaling in Fourier space (sections 4.2 and 5.1). For solenoidally-driven turbulence up to $\mathcal{M} \approx 11$, the deviations from the incompressible power-law exponents are relatively small, whereas for compressively-driven runs, strong deviations are already observed for $\mathcal{M} \approx 3$. An exception is the specific kinetic energy spectra and their solenoidal part, which exhibit a scaling close to the incompressible one even for highly compressible flows.
3. When considering the ‘‘Alfvénic helicity’’ spectra (the helicity spectra of the Alfvén velocity $\mathbf{v}_{\mathbf{A}} = \mathbf{b}/\sqrt{\rho}$) however, exponents close to the one found in the incompressible case are observed over a wide range of compressibility (section 5.1.2).
4. An extension of the Alfvénic balance, valid for highly compressible flows, is proposed (section 5.3).
5. Shell-to-shell transfers reveal that three phenomena take place in the general picture of a magnetic helicity inverse transfer (section 6.2): a mostly local inverse transfer relatively close to the magnetic helicity integral scale, a non-local inverse transfer from the magnetically-forced scales and a direct local transfer from the largest energy containing scales down to the smallest scales, associated with the magnetic energy direct cascade.
6. The geometric helical triadic factors have been derived for the compressible MHD equations (section 2.3.2) and allow to explain the locality and relative strength of the different helical homochiral contributions (section 6.3).
7. When injecting positive helical magnetic fluctuations, the positive helical part of the velocity field plays the major role in the inverse transfer through both local and non-local transfers (section 6.2.1).
8. The compressive part of the velocity field participates in the inverse transfer essentially through non-local effects (section 6.2.1). In highly compressible flows, mediation by the velocity field’s compressive part is geometrically favoured for the direct cascade of magnetic energy/helicity, as compared to mediation by the velocity field’s positive helical part (section 6.3).

Several effects of compressibility on the magnetic helicity dynamics are hence assessed in the present work, justified phenomenologically through an extension of the Alfvénic balance and the helical triadic geometric factors’ analysis. They indicate that in astrophysical systems of interest, important changes as compared to the incompressible case are expected as soon as the velocity field’s compressive part is important, and this, already at relatively low RMS Mach number flows. However, some of the results found in the incompressible case remain valid even at high compressibility with appropriate changes of variable (when considering for example the Alfvén velocity instead of the magnetic field). This universality could be associated with the lowering of the velocity compressive ratio in the inverse transfer range, which happens both for solenoidally-driven turbulence and for compressively-driven turbulence with a high enough Mach number.

Nevertheless, several simplifying assumptions have been made which could limit the applicability of the results to real astrophysical systems and ought to be underlined:

- The electromotive forcing chosen, which injects fully helical fluctuations of one sign at small scales is not physically motivated, but chosen so that one sign of magnetic helicity dominates the system. In astrophysical dynamos for example, kinetic helicity generates magnetic helicity of both signs (so that it cancels out in total), each of which is transferred towards opposite directions in Fourier space.
- The isothermal equation of state describes well the interstellar medium with low enough density to be optically thin to radiative cooling. The dynamics may differ in situations when the isothermality assumption does not hold [7].
- Both purely solenoidal and purely compressive forcing are very unlikely to occur in nature [45]. The study of both extreme cases allows thus to visualise differences at once, but is lacking in realism. Furthermore, driving solely at large scales is also an approximation. In the interstellar medium, the driving is thought to occur, among others, through rotation at large scales, self-gravity at intermediate scales and stellar feedback on intermediate to small scales, for example in the form of stellar winds or supernovae explosions ([37], sections 3 and 5.5). Some regions of the interstellar medium may also be better described by decaying turbulence [45].
- Self-gravity has not been considered. Since the density spreads over several orders of magnitude, it could however play an important role.
- The runs are performed under periodic boundary conditions. Even though the spectra are considered in the present work at instants in time when the magnetic helicity integral scale is still relatively far from the largest scales, such boundary conditions may lead to finite-size effects. Furthermore, periodic boundary conditions do not take into account boundary effects that are expected to happen at the borders of real systems.

Finally, even though the main results are confirmed through the higher resolution runs in section 7.2, the inverse transfer range is relatively small, so that the numerical value of the measured exponents should be considered with appropriate caution. Indeed, numerical non-ideal effects due to bottleneck contamination, underresolution and/or boundary effects which could influence the measured scalings can not be entirely excluded.

Appendix A

Technical details

Technical details regarding the performed numerical experiments are presented in this chapter. Section A.1 describes the hydrodynamic steady-state's generation, to which magnetic helical fluctuations are injected, while section A.2 details the parameters used for each run, regarding both the mechanical and electromotive driving and the fallback approach. Section A.3 shows how many reconstructions are indeed performed at lower order. Finally, section A.4 presents technical details regarding some tools used in chapter 6.

A.1 Generation of the initial hydrodynamic frames

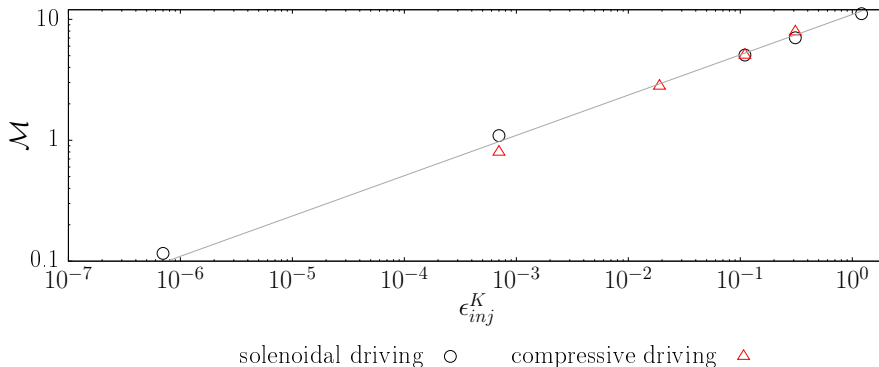


Figure A.1: Steady-state RMS Mach number as a function of the kinetic energy injection rate for the runs with solenoidal driving M01s, M1s, M5s, M7s and M11s as well as the runs with compressive driving M1c, M3c, M5c and M8c, resolution 256^3 (see table A.1). The gray line corresponds to a slope of $\frac{1}{3}$.

The main runs inject magnetic helical fluctuations, choosing a particular hydrodynamic initial frame of quasi-stationary turbulence. This initial frame is generated starting with a fluid at rest ($\mathbf{v} = 0$) with constant density ($\rho = \rho_0 = 1$). An Ornstein-Uhlenbeck mechanical driving with a constant kinetic energy injection rate ϵ_{inj}^K drives the turbulence (see section 3.5.1). The presence of numerical viscosity leads then to a statistical steady-state. A simple relation between ϵ_{inj}^K and \mathcal{M} was found in reference [73]. It is argued there on dimensional grounds that $\epsilon_{inj}^K \sim v^3/l$ with v a characteristic velocity and l a characteristic length scale of the turbulence. The numerical experiments performed there in the isothermal hydrodynamic compressible case, with RMS Mach numbers ranging up to 15, show that this relation is well observed for the choice $v = v_{rms} = c_s \mathcal{M}$ [73]. This

leads to the scaling:

$$\mathcal{M} \sim \epsilon_{inj}^K \frac{1}{3} \quad (\text{A.1})$$

provided that the forcing wavenumber is the same for all the numerical experiments, as is the case for the main runs. This scaling is reasonably well observed in the present work, both with purely solenoidal and purely compressive drivings (figure A.1), which allows to control ϵ_{inj}^K in order to reach a desired \mathcal{M} . The initial turbulent density and velocity fields are thus generated through the following procedure, starting with an isothermal fluid at rest:

1. Generate a fiducial turbulent state at a target Mach number \mathcal{M} using a fully solenoidal driving ($\zeta = 1$) by adjusting ϵ_{inj}^K .
2. Set the forcing autocorrelation time t_{auto} to the turbulent turnover time $t_{\mathcal{T}} = L/(2c_s\mathcal{M})$, as in reference [43], and restart the numerical experiment from the beginning ($\mathbf{v} = 0$, $\rho = \rho_0$), which leads to a convergence to a slightly different \mathcal{M} . At this point, all free parameters (ζ , ϵ_{inj}^K , t_{auto}) of the forcing are defined.
3. Further numerical experiments with different ϵ_{inj}^K and/or different spectral weight ζ are done directly by applying the scaling relation (A.1) to obtain an expected steady-state RMS Mach number \mathcal{M}^* and the autocorrelation time is set through $t_{auto} = t_{\mathcal{T}}^* = L/(2c_s\mathcal{M}^*)$.

The steady-state RMS Mach number \mathcal{M} is computed for each run by taking the time average:

$$\mathcal{M} = \frac{1}{t_2 - t_1} \int_{t_1}^{t_2} \frac{v_{rms}(t)}{c_s} dt, \quad (\text{A.2})$$

with the time window $[t_1, t_2]$ different for solenoidal and compressive driving. For solenoidal driving, $t_1 = 2.5t_{\mathcal{T}}^*$ and $t_2 = 6t_{\mathcal{T}}^*$ since a steady-state is obtained after about $2t_{\mathcal{T}}^*$, whereas for compressive driving $t_1 = 6t_{\mathcal{T}}^*$ and $t_2 = 12t_{\mathcal{T}}^*$ in order to avoid the RMS Mach number peak for the hypersonic runs (see figure 4.1). From the measured \mathcal{M} , the turbulent turnover time $t_{\mathcal{T}}$ is deduced, which serves as a time unit in the results presented here. The influence of the window bounds t_1 and t_2 has been tested by taking $t_1 \in [2t_{\mathcal{T}}^*, 5t_{\mathcal{T}}^*]$ and $t_1 \in [5.5t_{\mathcal{T}}^*, 11t_{\mathcal{T}}^*]$ for the solenoidally and compressively driven runs respectively, and t_2 such that $t_2 - t_1 \geq t_{\mathcal{T}}^*$. This makes the resulting \mathcal{M} vary by a few percent (ranging from 2 to about 8 percent, depending on the run).

In order to spare computer time, the runs are done at resolution 256^3 at least during $6t_{\mathcal{T}}^*$ and then upscaled to resolution 512^3 , through the following procedure: the hydrodynamic volume averages (ρ , $\rho\mathbf{v}$) of each cell of the lower resolution frame are copied to the corresponding cells of the finer 512^3 resolution. For example, a cell indexed by (i, j, k) in the 256^3 frame corresponds to the eight cells $(2i - \Delta_i, 2j - \Delta_j, 2k - \Delta_k)$ with $\Delta_i, \Delta_j, \Delta_k \in \{0, 1\}$ at resolution 512^3 . Then, the simulations are run at the higher resolution for at least one $t_{\mathcal{T}}^*$, which has been found to be sufficient for the turbulent system to adapt to the new resolution (see as well reference [43]). Indeed, an eddy of size l and velocity v_l should adapt to the new resolution on the timescale of an eddy-turnover time $\frac{v_l}{l}$. As a consequence, the new available small scales are very rapidly in a steady-state. Regarding the largest eddies, an estimate of their size is $L/2$ and their characteristic velocity is of the order of v_{rms} , that is, their turnover time is of the order of $t_{\mathcal{T}}^*$.

Analogously, for the numerical experiments using 1024^3 grid points, the steady-states obtained at resolution 512^3 are upscaled through the same procedure and run for one more $t_{\mathcal{T}}^*$.

A.2 Runs' parameters

Five solenoidally-driven runs (labelled with an “s”) and five compressively-driven runs (labelled with a “c”) at resolution 512^3 are considered in the present work. The numbers in their label correspond to their approximate RMS Mach number. The M5c and the M5cB runs both use as initial conditions different hydrodynamic frames at a RMS Mach number of about 5, so as to assess the influence of the starting hydrodynamic state. The Mf run is only (m)agnetically (f)orced. The parameters for these runs are displayed in table A.1, and the parameters corresponding to the fallback strategy used in table A.2.

Table A.1: Forcing parameters, fallback strategy used and resulting time-averaged steady-state RMS Mach number \mathcal{M} .

Name	ϵ_{inj}^K	ζ	t_{auto}	ϵ_{inj}^M	Fallback strategy	\mathcal{M}
M01s4	7×10^{-7}	1	50	$4 \times (7 \times 10^{-7})$	None	0.116
M1s2	7×10^{-4}	1	5	$2 \times (7 \times 10^{-4})$	I	1.09
M5s	0.11	1	1	0.11	II	5.06
M7s	0.31	1	$\frac{5}{7}$	0.31	II	7.03
M11s	1.21	1	$\frac{5}{12}$	1.21	IV	11.1
M1c	7×10^{-4}	0	5	7×10^{-4}	I	0.797
M3c	1.9×10^{-2}	0	$\frac{5}{3}$	1.9×10^{-2}	II	2.80
M5c, M5cB	0.11	0	1	0.11	II	5.05
M8c	0.31	0	$\frac{5}{7}$	0.31	III	7.87
Mf	0.	–	–	7×10^{-4}	None	–

Table A.2: Fallback strategies used (see section 3.2). The “Upc.” column stands for “upcoming shocks”: when the value is (y)es, it means that the refinement described in relation (3.11) is used, otherwise not.

Name	$(\tau_{4,p}^+, \tau_{3,p}^-, \tau_{3,p}^+, \tau_{2,p}^-, \tau_{2,p}^+, \tau_{1,p}^-)$	$(\tau_{4,\Delta t}^+, \tau_{3,\Delta t}^-, \tau_{3,\Delta t}^+, \tau_{2,\Delta t}^-, \tau_{2,\Delta t}^+, \tau_{1,\Delta t}^-)$	Upc.
I	(1, 2, 3.6, 3.6, ∞ , ∞)	not used	n
II	(0.4, 0.8, 1.8, 2.5, 3, 3.5)	(0.4, 0.4, 0.4, 0.4, 0.45, 0.5)	y
III	(0.38, 0.8, 1.5, 2, 3, 3.5)	(0.38, 0.38, 0.38, 0.38, 0.45, 0.5)	y
IV	(0.35, 0.5, 1.5, 2, 3, 3.5)	(0.35, 0.35, 0.35, 0.35, 0.45, 0.5)	y

A.3 Fallback statistics

In highly supersonic flows, strong shocks develop which cause stability issues for the fourth-order numerical method (see section 3.1). As a consequence, the reconstruction order is adapted locally according to a “reconstruction order map” (or ROM), as described in section 3.2. The criteria deciding which cells are reconstructed at lower order aim at allowing a stable numerical solution, while restricting as much as possible lower order reconstruc-

tions. The latter imply indeed a lesser result's quality, due to enhanced dissipation which smooths out small scale structures, as shown in section 7.2 and appendix B.

However, at high Mach numbers, a non-negligible proportion of the cells is reconstructed at lower order. Figure A.2 shows the time evolution of the proportion of cells with ROM in a certain range for the main supersonic runs. The time axis starts with the initial fluid at rest, accelerated until a hydrodynamic steady-state at resolution 256^3 is reached. The system is then upscaled to resolution 512^3 and allowed to adapt to this new resolution for at least $1t_{\tau}^*$ before magnetic helicity injection is switched on. The discontinuity occurring around $t = 6t_{\tau}$ in each plot corresponds to the change of resolution, whereas the abrupt change (discontinuity of the derivative) corresponds to the start of the electromotive forcing. The reason why the amount of lower-order reconstructions ($ROM < 4$) is changed by a factor of about two through the upscaling is principally due to the definition of the shock indicator for spatial gradients (relation (3.6)), since it is halved when the resolution is doubled. When magnetic helicity is injected, density filaments are formed (section 4.2.2), leading to small scale density gradients and hence more lower-order reconstructions. In the end, a relatively high proportion of reconstructions occurs at lower order. For the M11s and M8c runs, even the majority of the cells present $3 \leq ROM < 4$.

These plots show that there is room for improvement regarding the ROM computation. In order to improve the results' quality at a given resolution, it could indeed be very beneficial to find more selective criteria in order to detect better the situations that could lead to unphysical reconstructed values. Such a study is not in the scope of the present work.

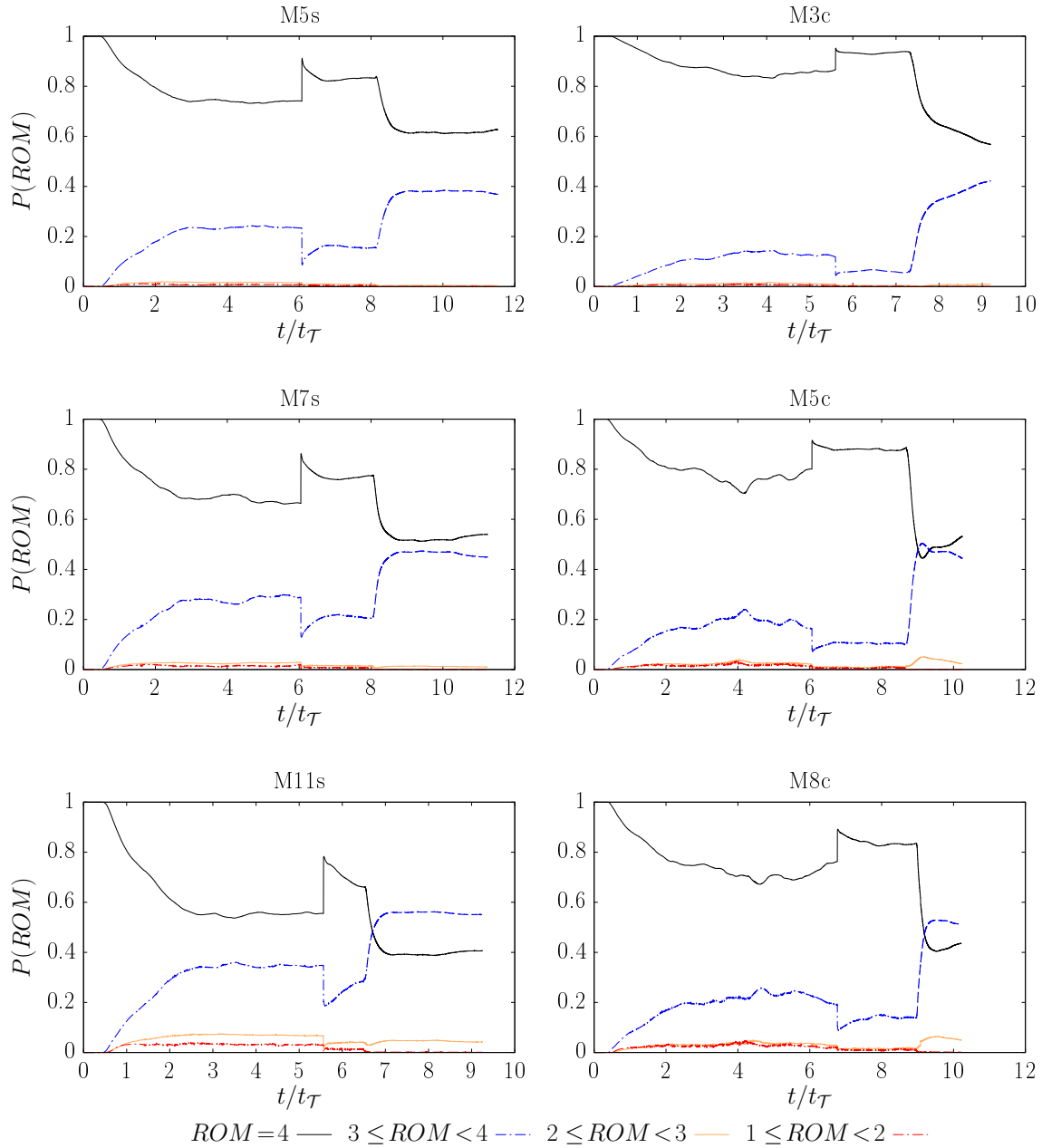


Figure A.2: Lower-order reconstructions as a function of time. The discontinuity corresponds to the change of resolution ($256^3 \rightarrow 512^3$) and the subsequent abrupt change to the switching on of the electro-motive forcing. For the M1s and M1c runs, only a very small proportion of cells (less than 1 per 10000) is reconstructed at lower order.

A.4 Additional shell-to-shell analysis tools

This section describes technical details regarding more specific tools used for the helically-decomposed shell-to-shell analysis (chapter 6). Descriptions and technical aspects at a more general level can be found in sections 2.3, 2.4 and 3.4.

A.4.1 Relative importance of energy exchanges in the “wings”

As observed in section 6.2, the mostly local inverse transfer “wings” are associated with both magnetic \leftrightarrow magnetic energy exchanges ($B \leftrightarrow B$ exchanges) and kinetic \leftrightarrow magnetic energy exchanges ($V \leftrightarrow B$ exchanges). In order to quantify their relative importance, one can build the following ratio:

$$\zeta_{wings} = \frac{\sum_{Q=1}^{40} \sum_{P \in [4, 30[} \sum_{K=1}^{40} \lambda_{\mathcal{U}_{bb}^{\mathcal{H}^M}} |\mathcal{U}_{bb}^{\mathcal{H}^M}(Q, P, K)|}{\sum_{Q=1}^{40} \sum_{P \in [4, 30[} \sum_{K=1}^{40} (\lambda_{\mathcal{U}_{bb}^{\mathcal{H}^M}} |\mathcal{U}_{bb}^{\mathcal{H}^M}(Q, P, K)| + |\lambda_{\mathcal{U}_{vb}^{\mathcal{H}^M}} \mathcal{U}_{vb}^{\mathcal{H}^M}(Q, P, K)|)}, \quad (\text{A.3})$$

with $\lambda_{\mathcal{U}_{bb}^{\mathcal{H}^M}}/\lambda_{\mathcal{U}_{vb}^{\mathcal{H}^M}}$ factors equal to zero or one depending on a criterion defined later in this paragraph. The domain $(K, Q) \in [1, 40]^2$ is chosen as a reasonable region containing the “wings” at the chosen instant when $\mathcal{I}_{\mathcal{H}^M} \approx \frac{1}{10}L$ and excluding the non-local transfer from the magnetically-forced scales. In addition, the velocity field shell P is filtered in the intermediate scales $[4, 30[$, since the “wings” are essentially caused by them, as reported in section 6.2.2. If the filter over P would not be applied, the “wings” in the $\mathcal{U}_{bb}^{\mathcal{H}^M}$ term would be superimposed on the direct cascade along the diagonal, underestimating hence its role. As for the $\lambda_{\mathcal{U}_{bb}^{\mathcal{H}^M}}/\lambda_{\mathcal{U}_{vb}^{\mathcal{H}^M}}$ factors, they are equal to one when the corresponding term ($\mathcal{U}_{bb}^{\mathcal{H}^M}$ or $\mathcal{U}_{vb}^{\mathcal{H}^M}$) is associated to an inverse transfer (negative strictly above the main diagonal and positive strictly underneath) and zero otherwise, so as to remove the remaining contributions of the velocity field at intermediate scales to the direct local transfer, which are visible in figure 6.12.(b).

For the runs presented in chapter 6, at an instant when $\mathcal{I}_{\mathcal{H}^M} \approx \frac{1}{10}L$, the ratio is found to be $\zeta_{wings} \approx 0.379$ for the M8c run, $\zeta_{wings} \approx 0.256$ for the M11s run, $\zeta_{wings} \approx 0.492$ for the M1c run and $\zeta_{wings} \approx 0.408$ for the M01s4 run, which means that both the $B \leftrightarrow B$ and $V \leftrightarrow B$ exchanges have a similar importance, even though the $V \leftrightarrow B$ exchanges are favoured, for these runs and at this instant of time.

A.4.2 Normalised geometric factor shape

Figure 6.22, which shows that the geometric helical triadic factors are well reflected in the shell-to-shell interactions (see section 6.3), is obtained by merging all the slices of $\mathcal{N}_{s_K s_P s_Q}^{\mathcal{H}^M}(Q, P, K)$ for $K \in [5, 50]$ through the following procedure, illustrated in figure A.3:

1. all forty six slices can be considered as “pictures” and are resized so that the angles $P = K$ and $Q = K$ arrive at the same location. They are as well normalised by the maximum of their respective absolute value so that all 46 slices have the same weight in the average.
2. the 46 resized “pictures” are superposed in order to obtain a new “picture” S by taking for each (P, Q) coordinate the sum of these slices,

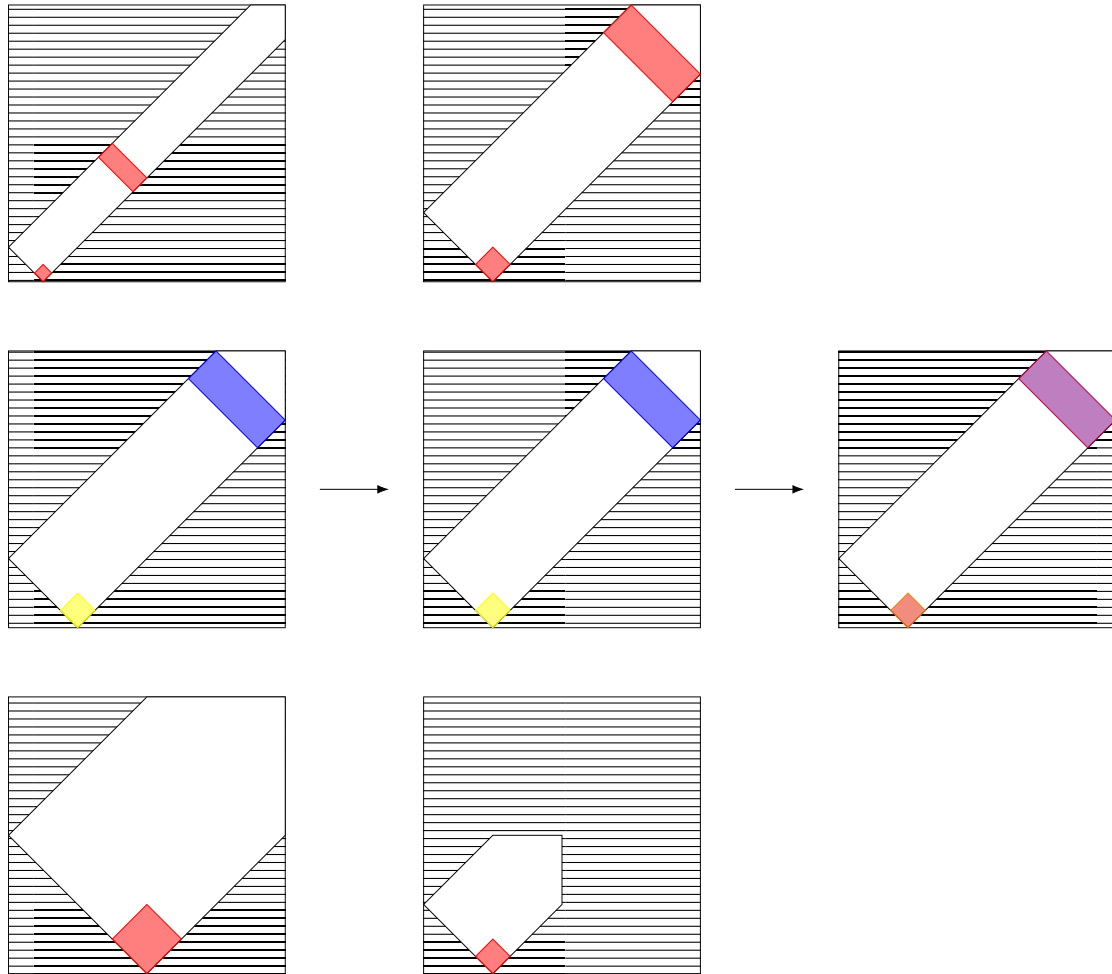


Figure A.3: Illustration of the algorithm generating figure 6.22, considering three pictures that are being merged (left). In the middle, the three pictures after being resized so that their angles coincide. Right: the final merged picture. The larger purple band comes from the sum of the red and blue bands from the top and middle pictures and is hence normalised by a factor 2, since only two of the three picture contributed to it. On the contrary, the smaller orange square comes from all the three pictures, so that it is normalised by a factor 3.

3. since the 46 resized pictures each occupy a different domain (for example, the slice at $K = 50$ does not contain values $P, Q \gg K$ whereas the slice at $K = 5$ contains many of them), each (P, Q) coordinate in the S picture is normalised by the amount of pictures that contributed to it,
4. this averaged S picture is then normalised by its maximum absolute value and shown in figure 6.22.

The reason why only the slices starting $K = 5$ are considered is that the low K slices are more imprecisely resized, causing square-like artifacts visible in that figure.

Appendix B

Discretisation order and dissipation

In this appendix, some effects related with the discretisation error are shown through the MHD vortex problem, studied with schemes of varying order of accuracy. Even though a direct quantitative transposition of the results obtained here to a turbulent system simulated using several reconstruction methods with different discretisation errors is not straightforward, some orders of magnitude can still be underlined.

The MHD vortex is a classical setting consisting of a smooth magnetised vortex structure in force equilibrium, advected by a velocity field. As a smooth nonlinear solution of the MHD equations, it is a good accuracy test for any numerical method. It was first introduced in 2D in reference [9] and extended in 3D in reference [77], from which the initial conditions are taken:

$$\mathbf{U} = \begin{pmatrix} \rho \\ v_x \\ v_y \\ v_z \\ p \\ b_x \\ b_y \\ b_z \end{pmatrix} = \begin{pmatrix} 1 \\ 1 - y\kappa \exp[q(1 - r^2)] \\ 1 + x\kappa \exp[q(1 - r^2)] \\ 2 \\ 1 + \frac{1}{4q} [\mu^2(1 - 2q(r^2 - z^2)) - \kappa^2\rho] \exp[2q(1 - r^2)] \\ -y\mu \exp[q(1 - r^2)] \\ x\mu \exp[q(1 - r^2)] \\ 0 \end{pmatrix}, \quad (\text{B.1})$$

with $r = \sqrt{x^2 + y^2 + z^2}$ and the parameters $\kappa = \mu = 1/(2\pi)$ and $q = 1$. The *adiabatic* equation of state is considered here, with a specific heat ratio of $\gamma_{adia} = 5/3$. As in the other 3D simulations presented in this work, the Courant number is set to $C_{CFL} = 1.5$. The computational domain $[-5, 5] \times [-5, 5] \times [-5, 5]$ with periodic boundary conditions is taken and the vortex is advected for one period of motion, until $t = 10$, after which it is compared to the initial conditions using the mean of the L_1 discrete error in all variables [100]:

$$\delta U = \frac{1}{8} \sum_{m=1}^8 \sum_{i,j,k} \frac{|U_{m,i,j,k}(t = 10) - U_{m,i,j,k}(t = 0)|}{N^3}, \quad (\text{B.2})$$

with N the linear resolution so that $N_x = N_y = N_z = N$ and (U_m) the \mathbf{U} components from relation (B.1). The experimental order of convergence *EOC* is then obtained by repeating the numerical experiment for several resolutions N_j through:

$$EOC_j = \frac{|\log(\delta U(N = N_j)) - \log(\delta U(N = N_{j-1}))|}{|\log(N_j) - \log(N_{j-1})|}. \quad (\text{B.3})$$

Table B.1: Convergence of errors and energy dissipation for the 3D MHD vortex problem for different scheme's order.

	Resolution	64^3	128^3	256^3	512^3
1 st order	δU	1.09×10^{-3}	1.05×10^{-3}	8.96×10^{-4}	6.61×10^{-4}
	EOC	-	0.0467	0.234	0.438
	E_{loss}	0.996	0.981	0.932	0.817
2 nd order	δU	4.33×10^{-4}	1.35×10^{-4}	3.92×10^{-5}	1.02×10^{-5}
	EOC	-	1.68	1.79	1.94
	E_{loss}	0.585	0.152	2.02×10^{-2}	2.39×10^{-3}
3 rd order	δU	1.88×10^{-4}	2.96×10^{-5}	3.87×10^{-6}	4.87×10^{-7}
	EOC	-	2.67	2.94	2.99
	E_{loss}	0.223	3.83×10^{-2}	5.07×10^{-3}	6.39×10^{-4}
4 th order	δU	4.35×10^{-5}	2.12×10^{-6}	8.86×10^{-8}	4.40×10^{-9}
	EOC	-	4.36	4.58	4.33
	E_{loss}	6.36×10^{-2}	2.29×10^{-3}	7.00×10^{-5}	2.04×10^{-6}

Table B.1 shows the convergence of errors for schemes of convergence order ranging from 1 to 4 as well as the dissipation of energy associated with them. The obtained EOC is consistent with the scheme's order (for the first order scheme, the asymptotic region where the order of convergence is observed is not reached yet, so that $EOC < 1$). The fourth-order scheme corresponds to the one presented in chapter 3 without fallback approach. The lower-order schemes are the ones that would be obtained when setting the reconstruction order map ROM (see section 3.2) to three, two or one in the whole computational domain. This means that not all the steps are lower-order for these schemes: the time integration is still the ten-stage fourth-order SSPRK one and the computation of the magnetic field volume averages from the face averages is done through a fourth-order interpolation. The changes concern the reconstruction method (limO3 for the 3rd order scheme, TVD limiter of Van-Leer for the 2nd and Godunov's scheme for the 1st order, see section 3.2.1) and the point value transformations: they are only kept for the 3rd order scheme and disabled for the 2nd and 1st order ones (see section 3.2.3).

The energy dissipation E_{loss} is computed through:

$$E_{loss} = 1 - \frac{E(t = 10)}{E(t = 0)}, \quad (\text{B.4})$$

with $E = \sum_{i,j,k} \frac{1}{2} \rho (\mathbf{v} - \mathbf{v}_{mean})^2 + \frac{1}{2} \mathbf{b}^2$ the sum of magnetic and kinetic energies, removing the mean velocity field (there is no mean magnetic field). The dissipation level achieved with the second-order scheme at a resolution of 512^3 is very close to the one with the fourth-order scheme at the much lower 128^3 resolution (table B.1). This illustrates why higher-order schemes, even though computationally more expensive at a given resolution, allow to spare computer time in the end since a coarser resolution is needed to obtain a similar result's quality. Even though the computational cost depends highly on the implementation, the compiler optimisation level etc., table B.2 presents a comparison of the average computational time for one iteration of the different schemes (on the

Table B.2: Computational cost comparison for schemes of different accuracy. The iteration duration has been measured by averaging over all the iterations of one period of motion for the 512^3 run and is normalised by the one required for the second-order scheme. Please note that the time integration method is the same fourth-order SSPRK one for all the schemes presented here.

Scheme's order	Average iteration duration
1	0.67
2	1
3	1.62
4	2.45

same computing cluster, with the same compiler and optimisation options). Although the fourth-order scheme requires a more than two times longer duration for each iteration, this factor is small as compared to the factor 16, consisting of a factor 8 for the number of cells and a factor 2 for the smaller required timestep according to the CFL criterion, that would be needed in order to double the numerical resolution.

Figure B.1 illustrates this further by showing 2D slices of the magnetic energy at $z \approx L/2$ after one period of motion. At resolution 64^3 , when for lower-order schemes, the energy diffuses more, making the vortex appear bigger (this effect is still slightly visible for the third-order scheme) and with less energy, the fourth-order scheme preserves the size very well and the amplitude quite well already at this low resolution. At resolution 512^3 , the energy amplitude is very well preserved for all schemes with order greater than one, even though some small deviations in the vortex' shape are visible for the second-order scheme.

The transition from a certain reconstruction method to another lower-order one (in the fallback approach) occurs gradually through the use of a weight (see section 3.2). Figure B.2 shows the energy lost during one period of motion for 256^3 runs when setting the ROM to a constant from 1 to 4 with 0.2 increments. One can see two abrupt transitions, corresponding to the passages from $ROM = 1.8$ to $ROM = 2$ and $ROM = 3.8$ to $ROM = 4$, where about an order of magnitude is gained regarding energy conservation. The transition between second and third order is not so sudden, even though between $ROM = 2$ and $ROM = 3.8$, about one order of magnitude of difference is also observed. This shows that, even though using a weighted average between two reconstruction methods allows indeed to limit the occurring dissipation due to lower-order reconstruction, the effect on the dissipation is clearly visible as soon as one departs even slightly from a purely fourth-order reconstruction method.

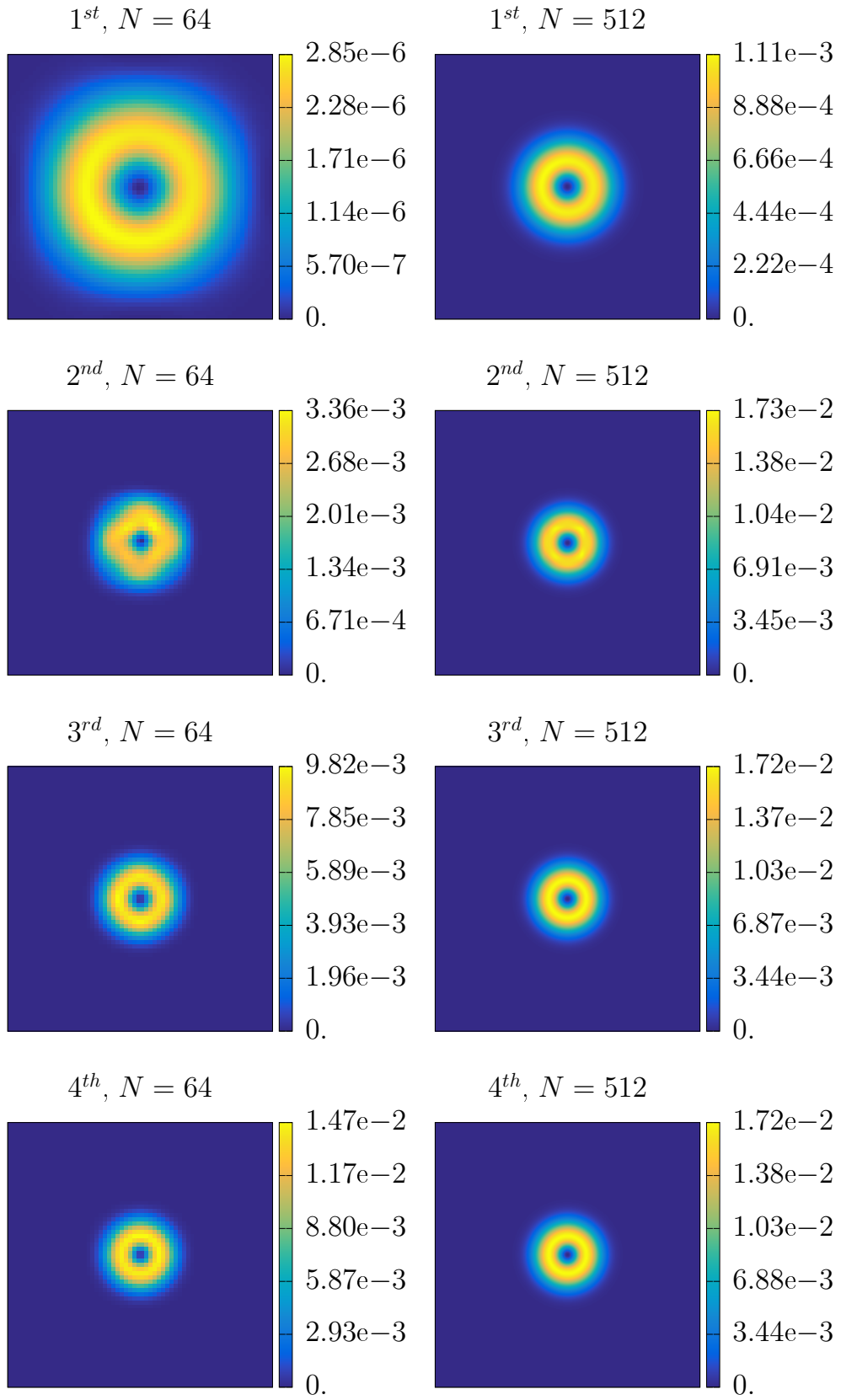


Figure B.1: 3D MHD vortex problem: slices at $z \approx L/2$ of the magnetic energy after one period of motion at different resolutions and for schemes of different orders.

The results presented in this appendix illustrate that, more than increasing the resolution, increasing the scheme's order can lead to significant improvements of the results' quality. For the turbulent states studied here however, structures with size varying in a wide range of scales are present and interact with each other. This means that even though the study of the MHD vortex problem gives some intuition of the role of high-order numerics, a direct transposition from this simple problem to turbulent flows is not applicable. Furthermore, the reconstruction order map is not constant in the numerical runs, but is adapted locally and dynamically, so that the proportion of lower-order reconstructions varies over time (see appendix A.3). One hence need to assess these effects on the turbulent systems directly. This issue is discussed in section 7.2, where some effects linked to both the discretisation order and the numerical resolution are considered for the M1s2 and M8c runs.

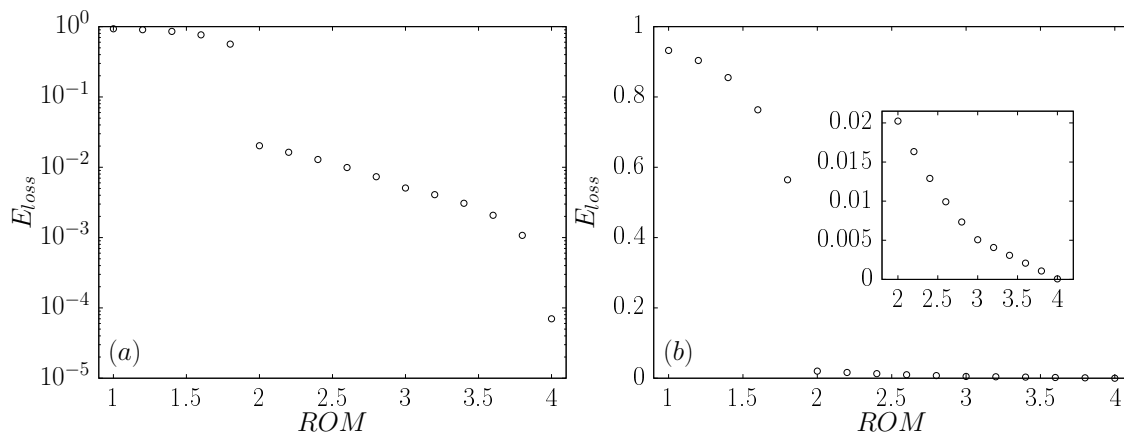


Figure B.2: Energy lost (measured in proportion to the initial energy) in one period of motion for the 3D MHD vortex as a function of the constant value of the reconstruction order map, resolution 256^3 . (a) Linear-logarithmic scale, (b) Linear-linear scale. The inset is a zoom in the region $ROM > 2$.

Appendix C

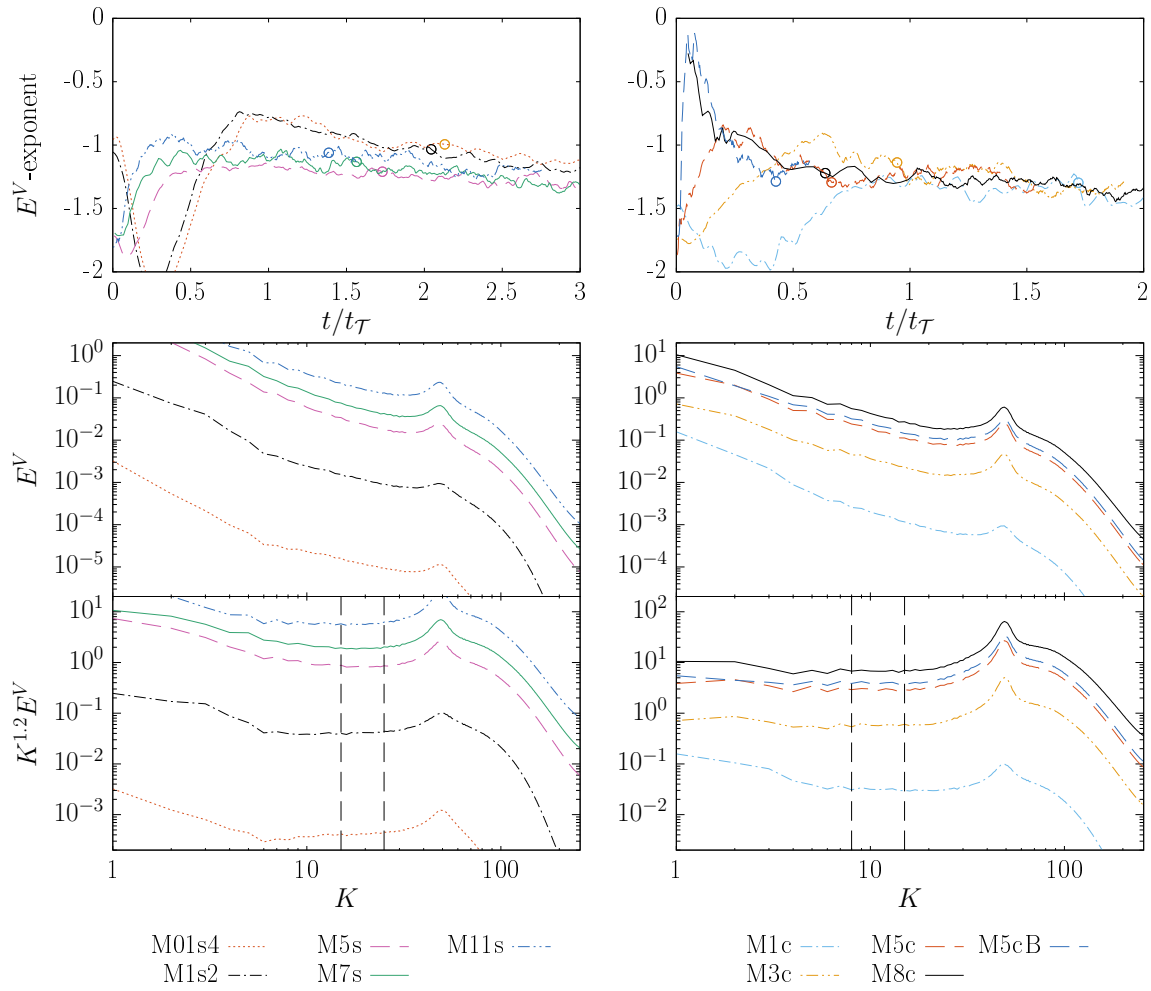
Supplementary material

Additional measurements are presented in this appendix, linked with the observed scaling laws and Alfvénic balance from chapter 5 (section C.1) and the heterochiral terms from the helically-decomposed shell-to-shell transfer analysis of chapter 6 (section C.2).

C.1 Power-law scaling and Alfvénic balance

The specific kinetic energy spectra as well as the power spectra of $\mathbf{u} = \rho^{1/3}\mathbf{v}$ both exhibit a power-law scaling in the inverse transfer region. These are shown in figures C.1 and C.2 respectively. The spectra (middle and bottom subfigures) are shown at an instant when $\mathcal{I}_{HM} \approx \frac{1}{6}L$ whereas the top subfigures show the time evolution computed through a least squares fit in the domain delimited by the vertical dashed lines. As mentioned in section 5.1.3, the specific kinetic energy exhibits an exponent close to the incompressible -1.2 one [74] even at high compressibility, whereas deviations are observed for the E^U spectra for the high Mach number compressively-driven runs.

The Alfvénic balance is tested as well with E^U . Even though some variants of relation (5.4) exhibit good horizontal lines, the Alfvénic balance is generally not as well verified with this quantity (figures C.3, C.4 and C.5), as compared to $E^{V,sol.}$ (see section 5.2).

Figure C.1: Same as figure 5.1, but for E^V .

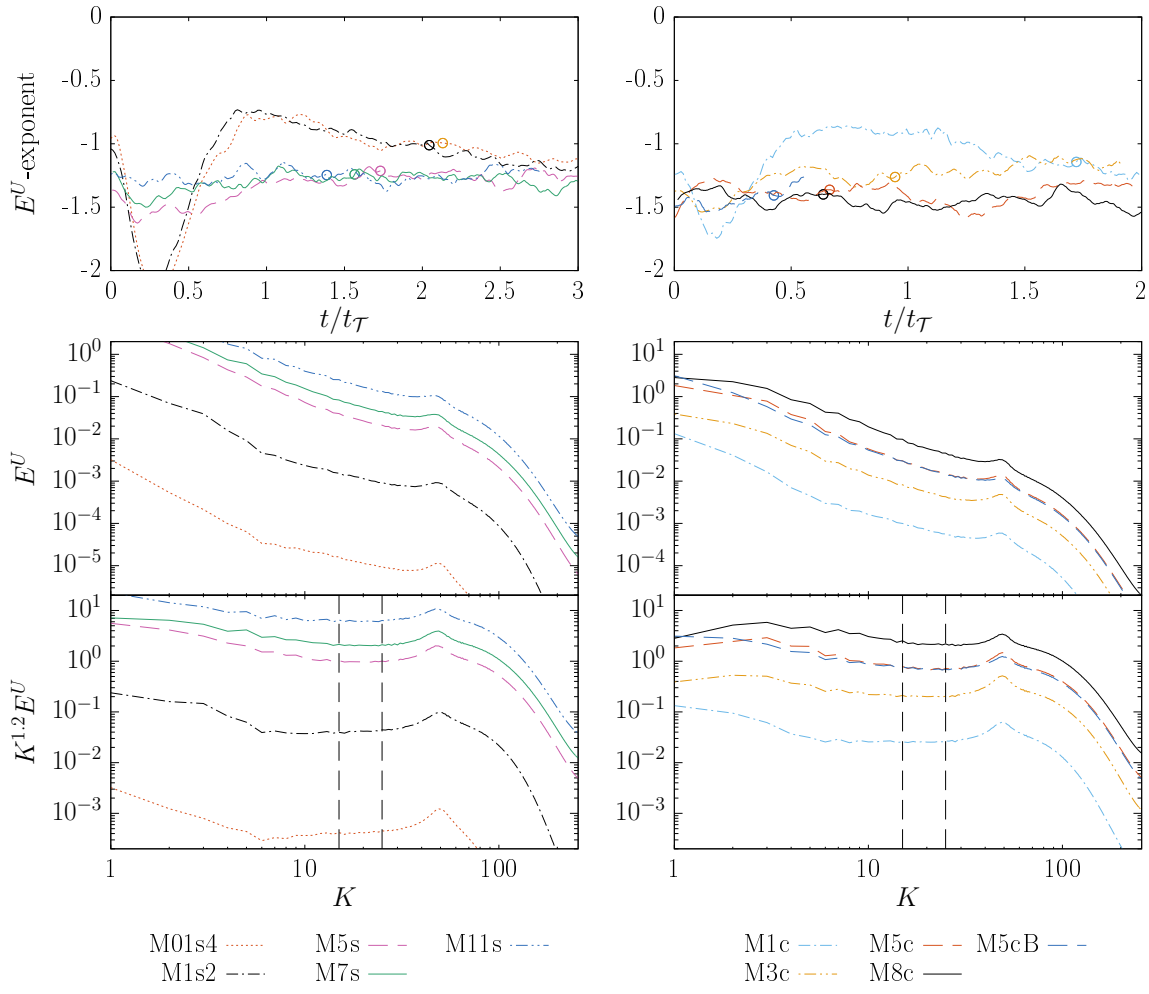


Figure C.2: Same as figure 5.1, but for E^U .

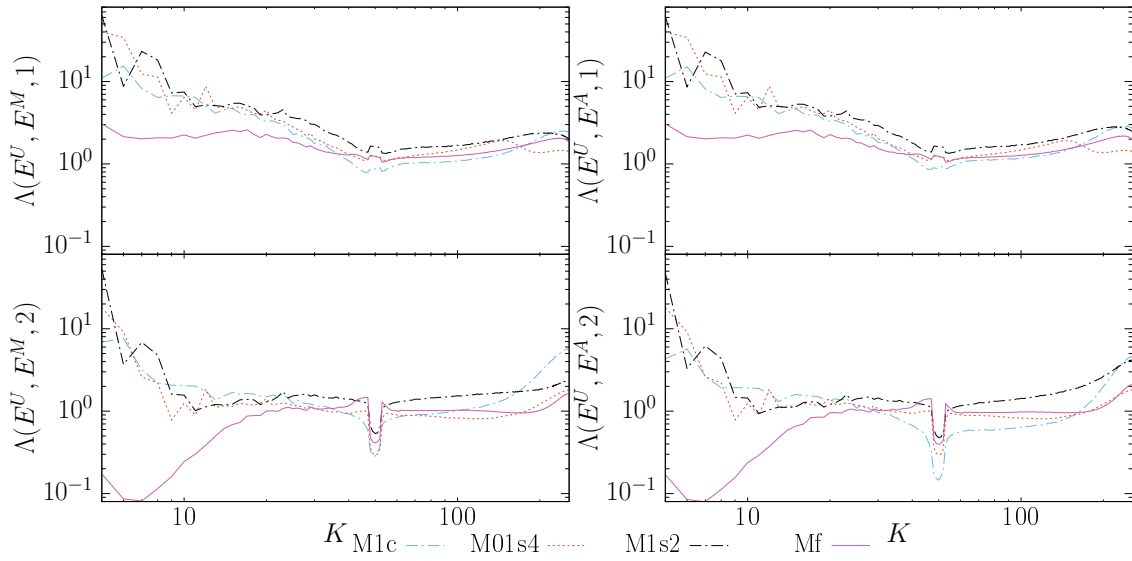


Figure C.3: Test of relations of the type (5.4) for the subsonic and transonic runs, at an instant when $\mathcal{I}_{\mathcal{H}^M} \approx \frac{1}{6}L$.

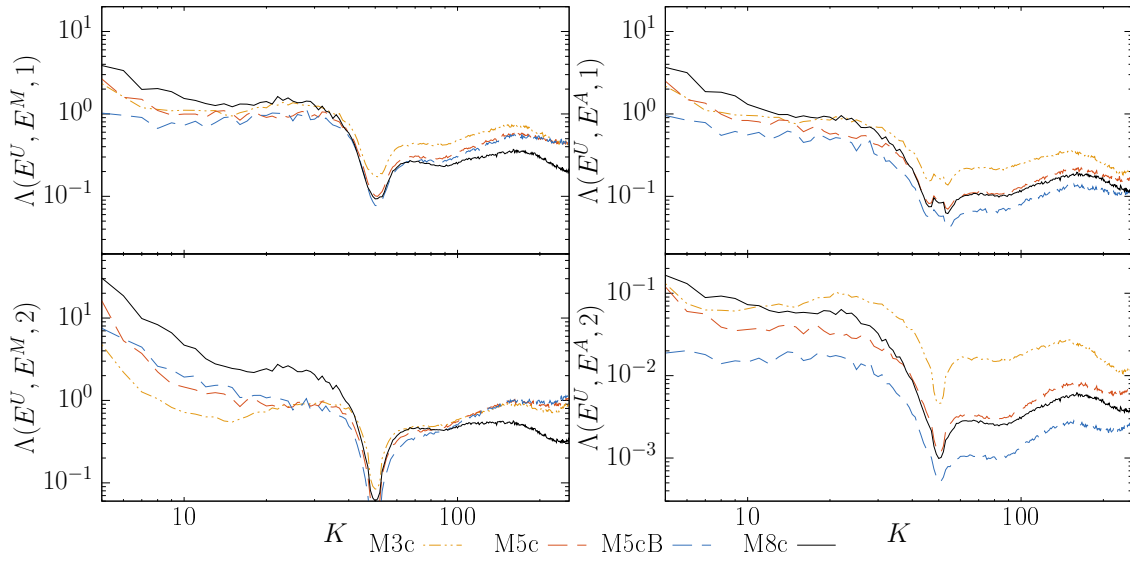


Figure C.4: Test of relations of the type (5.4) for the supersonic compressively-driven runs, at an instant when $\mathcal{I}_{\mathcal{M}} \approx \frac{1}{6}L$.

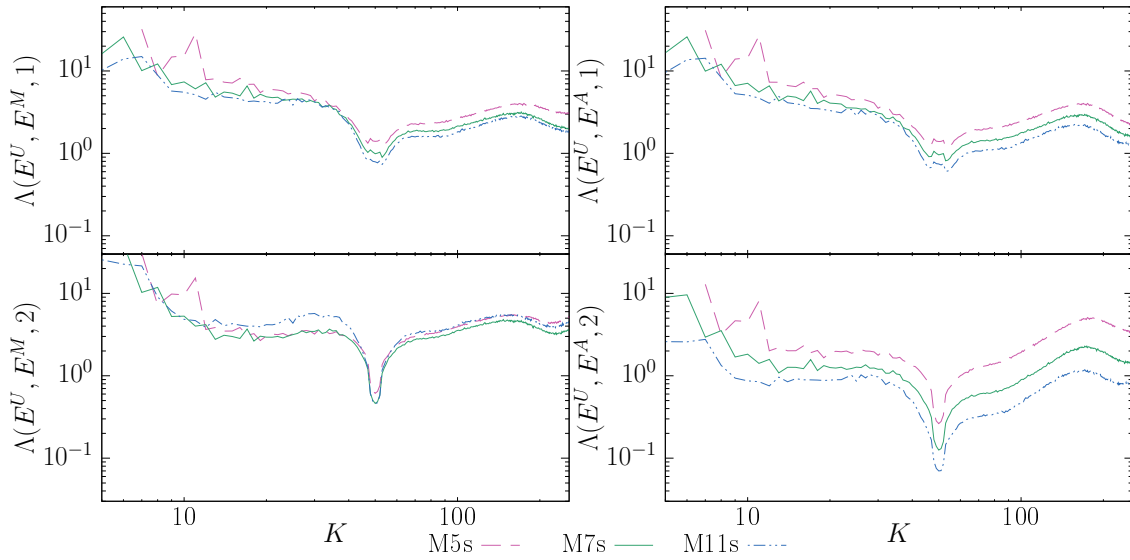


Figure C.5: Test of relations of the type (5.4) for the supersonic solenoidally-driven runs, at an instant when $\mathcal{I}_{\mathcal{M}} \approx \frac{1}{6}L$.

C.2 Heterochiral terms

As observed in section 6.2, the heterochiral magnetic helicity transfer terms present a more exotic shape, as compared to the PPP , PCP , PNP , NPN , NCN and NNN ones. This section gives some first elements about the origin of the observed shapes, focusing on the NLIT. Since the heterochiral terms are relatively small in the runs considered here, a more detailed study is not in the scope of this dissertation. Situations where they may play a greater role could be systems with low total magnetic helicity, such as the amplification of a small non-helical seed magnetic field through dynamo action.

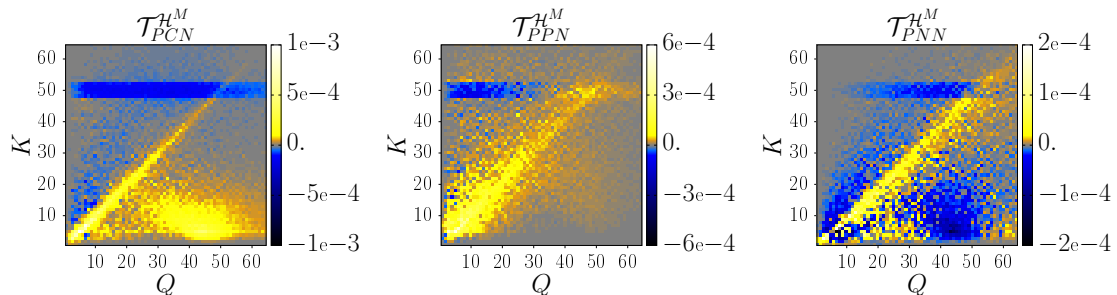


Figure C.6: One part of the magnetic helicity heterochiral transfer terms, for the M8c run at an instant when $\mathcal{I}_{\mathcal{H}^M} \approx \frac{1}{10}L$.

The heterochiral flux terms are the sum of two terms (for example, $SCS = PCN + NCP$, so as to make the flux conservative). It is hence instructive to consider the non-symmetrised terms PCN , PPN and PNN , which are displayed in figure C.6 for the M8c run at an instant when $\mathcal{I}_{\mathcal{H}^M} \approx \frac{1}{10}L$. The NCP , NPP and NNP terms can be deduced from the PCN , PPN and PNN terms respectively by taking the opposite of their transposition, since $\mathcal{T}_{PCN}^{HM}(Q, K) = -\mathcal{T}_{NCP}^{HM}(K, Q)$ and analogously for the other terms.

On these figures, two shapes correspond to the NLIT: (i) horizontal negative bars at $K \approx 50$ which extend over different Q domains depending on the considered term and (ii) an ellipse-shaped transfer for K relatively small and Q between 40 and 50 for the PCN and PNN terms. The domain on which the horizontal rectangles extend and the presence of the ellipse-like shape can both be justified from the helical geometric factors (figure 6.19). The horizontal rectangle extends over a wide range for the PCN term since G_{PCN} has high values on the $q = p - k$ line, even for $k \ll p, q$ and does not vanish for local $k \approx p \approx q$ interactions. For the same reason, it is not surprising to see the ellipse-like shape. Regarding the PPN term, the geometric factor G_{PPN} is largest for $q \ll k \approx p$, hence the regions with lower Q are preferred for the horizontal rectangle, whereas the ellipse at high Q is not favoured geometrically. On the contrary, for the PNN term, the geometric factor G_{PNN} is largest for $k \ll p \approx q$, hence only the largest Q shells are preferred for the horizontal rectangle, and these largest Q shells also include the ellipse.

However, the interpretation in terms of magnetic helicity transfers is relatively complex. As an example, for the PNN term, since the cross-product of the negative helical parts of the velocity and magnetic field, $\mathbf{v}^N \times \mathbf{b}^N$, is projected on the positive helical magnetic field (see section 2.4.4), the negative horizontal rectangle means that the $\hat{\mathbf{b}}^P$ component in Fourier space loses energy around $K \approx 50$ and the negative ellipse means that the $\hat{\mathbf{b}}^P$ component loses energy at these scales. Conversely, if one would consider the NNP term, which is the opposite of the transposed PNN plot, one would see a vertical positive rectangle around $Q \approx 50$ and a positive ellipse around $5 \lesssim Q \lesssim 15$ (see figure C.7). Yet,

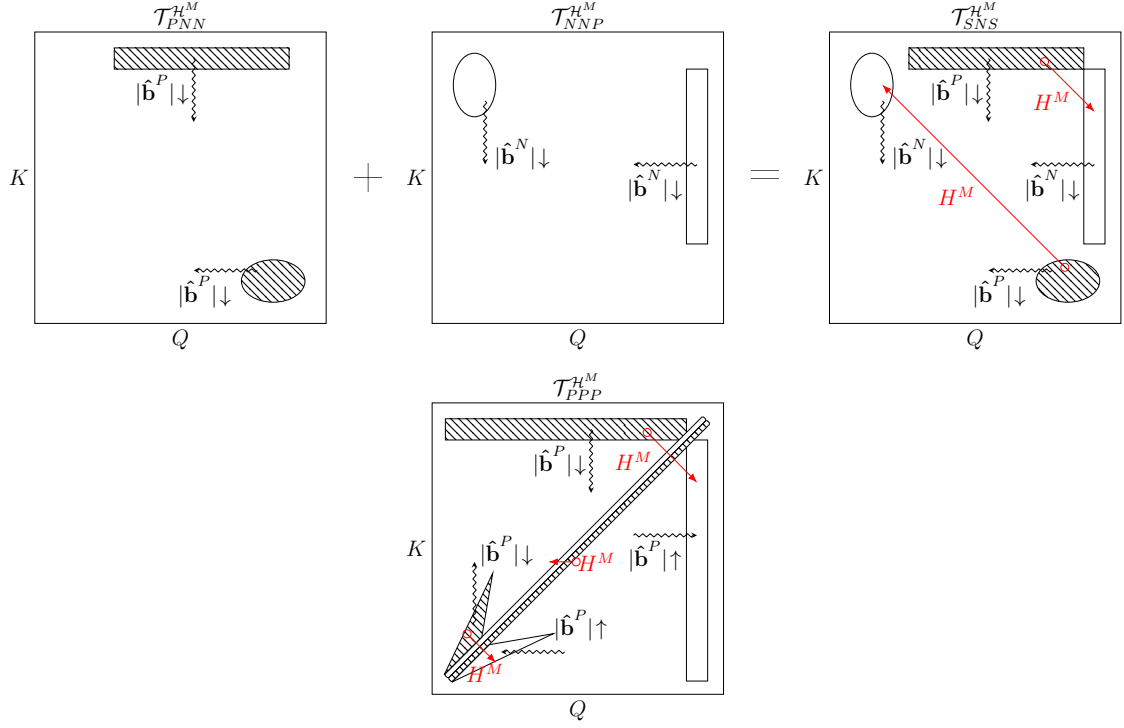


Figure C.7: Illustration of the magnetic energy changes associated with the magnetic helicity transfers for the $SNS = PNN + NNP$ and PPP terms. A \downarrow arrow (\uparrow arrow) means that energy is lost (gained) for either the positive helical part $\hat{\mathbf{b}}^P$ of the magnetic field or its negative helical part $\hat{\mathbf{b}}^N$ (similar arrows along the diagonal of the \mathcal{T}_{PPP}^{HM} term should be present but are not drawn in order not to overload the sketch). The red arrows show the direction of the magnetic helicity transfers.

the NNP term considers the $\mathbf{v}^N \times \mathbf{b}^P$ term projected on the negative helical magnetic field. This means that these shapes are also associated with energy *losses*. In order to gain magnetic helicity through sole changes in the $\hat{\mathbf{b}}^N$ component, one indeed has to make this component along the negative helical eigenvector lose energy (see relation (2.54)). These losses of the $\hat{\mathbf{b}}^N$ components would compensate the loss of energy of the $\hat{\mathbf{b}}^P$ components of the PNN term in such a way that, effectively, the magnetic helicity leaving the concerned shells through the rectangle and the ellipse of the PNN term would be transferred to other shells through the mirrored shapes of the NNP term, resulting in a magnetic helicity transfer between scales for the total SNS heterochiral term (this situation is depicted in figure C.7). This behaviour where magnetic helicity is effectively transferred between scales through losses of energy, is in contrast to the situation happening through the PPP term (figure C.7, bottom). In this case, a transfer of magnetic helicity from a certain shell is associated to energy losses at that shell but with an energy gain in the shell receiving it. One can as well draw similar conclusions when considering the PCN and PPN terms. Nevertheless, as mentioned before, since these terms do not play a dominant role in the present dissertation, a more detailed analysis would be out of scope.

Bibliography

- [1] A. Alexakis. Helically decomposed turbulence. *Journal of Fluid Mechanics* 812, pages 752–770, 2017.
- [2] A. Alexakis, P. D. Mininni, and A. Pouquet. Shell-to-shell energy transfer in magnetohydrodynamics. I. Steady state turbulence. *Physical Review E* 72, 046301, 2005.
- [3] A. Alexakis, P. D. Mininni, and A. Pouquet. On the inverse cascade of magnetic helicity. *The Astrophysical Journal* 640, pages 335–343, 2006.
- [4] H. Aluie. Compressible turbulence: the cascade and its locality. *Physical Review Letters* 106, 174502, 2011.
- [5] H. Aluie. Scale decomposition in compressible turbulence. *Physica D* 247, pages 54–65, 2013.
- [6] H. Aluie and G. L. Eyink. Scale locality of magnetohydrodynamic turbulence. *Physical Review Letters* 104, 081101, 2010.
- [7] E. Audit and P. Hennebelle. On the structure of the turbulent interstellar clouds – influence of the equation of state on the dynamics of 3D compressible flows. *Astronomy and Astrophysics* 511, A76, 2010.
- [8] D. Balsara and A. Pouquet. The formation of large-scale structures in supersonic magnetohydrodynamic flows. *Physics of Plasmas Vol. 6 No. 1*, pages 89–99, 1999.
- [9] D. S. Balsara. Second-order-accurate schemes for magnetohydrodynamics with divergence-free reconstruction. *The Astrophysical Journal Supplement Series* 151, pages 149–184, 2004.
- [10] D. S. Balsara. Multidimensional HLLE Riemann solver: Application to Euler and magnetohydrodynamic flows. *Journal of Computational Physics* 229, pages 1970–1993, 2010.
- [11] D. S. Balsara. Self-adjusting, positivity preserving high order schemes for hydrodynamics and magnetohydrodynamics. *Journal of Computational Physics* 231, pages 7504–7517, 2012.
- [12] D. S. Balsara, S. Garain, and C.-W. Shu. An efficient class of WENO schemes with adaptive order. *Journal of Computational Physics* 326, pages 780–804, 2016.
- [13] W. Baumjohann and R. A. Treumann. *Basic Space Plasma Physics*. Imperial College Press, 1997.
- [14] M. A. Berger. Rigorous new limits on magnetic helicity dissipation in the solar corona. *Geophysical and Astrophysical Fluid Dynamics* 30, pages 79–104, 1984.

- [15] M. A. Berger. Magnetic helicity in a periodic domain. *Journal of Geophysical Research* 102 No. A2, pages 2637–2644, 1997.
- [16] M. A. Berger. Introduction to magnetic helicity. *Plasma Physics and Controlled Fusion* 41, pages B167–B175, 1999.
- [17] M. A. Berger and G. B. Field. The topological properties of magnetic helicity. *Journal of Fluid Mechanics* 147, pages 133–148, 1984.
- [18] J. W. Bieber, P. A. Evenson, and W. H. Matthaeus. Magnetic helicity of the Parker field. *The Astrophysical Journal*, 315, pages 700–705, 1987.
- [19] D. Biskamp. *Magnetohydrodynamic Turbulence*. Cambridge University Press, 2003.
- [20] D. Biskamp and W.-C. Müller. Scaling properties of three-dimensional isotropic magnetohydrodynamic turbulence. *Physics of Plasmas* 7, pages 4889–4900, 2000.
- [21] E. G. Blackman. Magnetic helicity and large scale magnetic fields: A primer. *Space Science Reviews* 188, pages 59–91, 2015.
- [22] R. N. Bracewell. *The Fourier Transform and its Applications, third edition*. McGraw-Hill, 2000.
- [23] J. Brackbill. Fluid modeling of magnetized plasmas. *Space Science Reviews* 42, pages 153–167, 1985.
- [24] J. U. Brackbill and D. C. Barnes. The effect of nonzero $\nabla \cdot b$ on the numerical solution of the magnetohydrodynamic equations. *Journal of Computational Physics* 35, pages 426–430, 1980.
- [25] A. Brandenburg. The inverse cascade and nonlinear alpha-effect in simulations of isotropic helical hydromagnetic turbulence. *The Astrophysical Journal* 550, pages 824–840, 2001.
- [26] A. Brandenburg and A. Lazarian. Astrophysical hydromagnetic turbulence. *Space Science Reviews* 178, pages 163–200, 2013.
- [27] A. Brandenburg and K. Subramanian. Astrophysical magnetic fields and nonlinear dynamo theory. *Physics Reports* 417, pages 1–209, 2005.
- [28] P. Buchmüller and C. Helzel. Improved accuracy of high-order WENO finite volume methods on cartesian grids. *Journal of Scientific Computing* 61, pages 343–368, 2014.
- [29] J. M. Burgers. A mathematical model illustrating the theory of turbulence. *Advances in Applied Mechanics* 1, pages 171–199, 1948.
- [30] M. Čada and M. Torrilhon. Compact third-order limiter functions for finite volume methods. *Journal of Computational Physics* 228, pages 4118–4145, 2009.
- [31] B. W. Carroll and D. A. Ostlie. *An Introduction to Modern Astrophysics, second edition*. Pearson Education, 2007.
- [32] S. Chandrasekhar and P. C. Kendall. On force-free magnetic fields. *Astrophysical Journal* 126, pages 457–460, 1957.

- [33] Q. Chen, S. Chen, and G. L. Eyink. The joint cascade of energy and helicity in three-dimensional turbulence. *Physics of Fluids* 15, pages 361–374, 2003.
- [34] M. Christensson and M. Hindmarsh. Inverse cascade in decaying three-dimensional magnetohydrodynamic turbulence. *Physical Review E* 64, 056405, 2001.
- [35] P. Colella and P. R. Woodward. The piecewise parabolic method (PPM) for gas-dynamical simulations. *Journal of Computational Physics* 54, pages 174–201, 1984.
- [36] W. Dobler, N. E. L. Haugen, T. A. Yousef, and A. Brandenburg. Bottleneck effect in three-dimensional turbulence simulations. *Physical Review E* 68, 026304, 2003.
- [37] B. G. Elmegreen and J. Scalo. Interstellar turbulence I: Observations. *Annual Review of Astronomy and Astrophysics* 42, pages 211–273, 2004.
- [38] W. M. Elsässer. Hydromagnetic dynamo theory. *Reviews of Modern Physics* 28, No. 2, pages 135–163, 1956.
- [39] D. F. Escande, P. Martin, S. Ortolani, A. Buffa, P. Franz, L. Marrelli, E. Martines, G. Spizzo, S. Cappello, A. Murari, R. Pasqualotto, and P. Zanca. Quasi-single-helicity reversed-field-pinch plasmas. *Physical Review Letters* 85, No. 8, pages 1662–1665, 2000.
- [40] V. Eswaran and S. B. Pope. An examination of forcing in direct numerical simulations of turbulence. *Computers and Fluids* 16, No. 3, pages 257–278, 1988.
- [41] C. R. Evans and J. F. Hawley. Simulation of magnetohydrodynamic flows: a constrained transport method. *The Astrophysical Journal* 332, pages 659–677, 1988.
- [42] G. Falkovich. Bottleneck phenomenon in developed turbulence. *Physics of Fluids* 6, pages 1411–1414, 1994.
- [43] C. Federrath. On the universality of supersonic turbulence. *Monthly Notices of the Royal Astronomical Society* 436, pages 1245–1257, 2013.
- [44] C. Federrath, R. S. Klessen, L. Iapinicho, and N. J. Hammer. The world’s largest turbulence simulations. *arXiv:1607.00630*, 2016.
- [45] C. Federrath, J. Roman-Duval, R. S. Klessen, W. Schmidt, and M.-M. Mac Low. Comparing the statistics of interstellar turbulence in simulations and observations, solenoidal versus compressive turbulence forcing. *Astronomy and Astrophysics* 512, A81, 2010.
- [46] R. C. Fleck, Jr. Scaling relations for the turbulent, non-self-gravitating, neutral component of the interstellar medium. *The Astrophysical Journal* 458, pages 739–741, 1996.
- [47] U. Frisch. *Turbulence: the legacy of A. N. Kolmogorov*. Cambridge University Press, 1995.
- [48] U. Frisch, A. Pouquet, J. Léorat, and A. Mazure. Possibility of an inverse cascade of magnetic helicity in magnetohydrodynamic turbulence. *Journal of Fluid Mechanics* 68 Part 4, pages 769–778, 1975.

- [49] S. Galtier and S. Banerjee. Exact relation for correlation functions in compressible isothermal turbulence. *Physical Review Letters* 107, 134501, 2011.
- [50] S. K. Godunov. A difference scheme for numerical solution of discontinuous solution of hydrodynamic equations. *Matematicheskii Sbornik* 47, pages 271–306, 1959. English: US Joint Publications Research Service 7226, 1969.
- [51] S. Gottlieb and C.-W. Shu. Total variation diminishing Runge-Kutta schemes. *Mathematics of Computation Vol. 67, No. 221*, pages 73–85, 1998.
- [52] S. Gottlieb, C.-W. Shu, and E. Tadmor. Strong stability-preserving high-order time discretization methods. *Society for Industrial and Applied Mathematics Review Vol. 51, No. 1*, pages 89–112, 2001.
- [53] J. Graham, P. D. Mininni, and A. Pouquet. High Reynolds number magnetohydrodynamic turbulence using a Lagrangian model. *Physical Review E* 84, 016314, 2011.
- [54] J. P. Graham, R. Cameron, and M. Schüssler. Turbulent small-scale dynamo action in solar surface simulations. *The Astrophysical Journal* 714, pages 1606–1616, 2010.
- [55] P. Grete, B. W. O’Shea, K. Beckwith, W. Schmidt, and A. Christlieb. Energy transfer in compressible magnetohydrodynamic turbulence. *Physics of Plasmas* 24, 092311, 2017.
- [56] A. Harten, B. Engquist, S. Osher, and S. R. Chakravarthy. Uniformly high order accurate essentially non-oscillatory schemes, III. *Journal of Computational Physics* 71, pages 231–303, 1987.
- [57] N. E. L. Haugen and A. Brandenburg. Inertial range scaling in numerical turbulence with hyperviscosity. *Physical Review E* 70, 026405, 2004.
- [58] G.-S. Jiang and C.-W. Shu. Efficient implementation of weighted ENO schemes. *Journal of Computational Physics* 126, pages 202–228, 1996.
- [59] D. I. Ketcheson. Highly efficient strong stability-preserving Runge-Kutta methods with low-storage implementations. *Society for Industrial and Applied Mathematics Journal on Scientific Computing* 30, No. 4, pages 2113–2136, 2008.
- [60] M. G. Kivelson. Physics of space plasmas. In M. G. Kivelson and C. T. Russell, editors, *Introduction to Space Physics*, chapter 2. Cambridge University Press, 1995.
- [61] A. N. Kolmogorov. Dissipation of energy in locally isotropic turbulence. *Doklady Akademii Nauk SSSR* 32, pages 16–18, 1941. Reprinted: Proceedings of the Royal Society of London A 434, 15–17, 1991.
- [62] A. G. Kritsuk, M. L. Norman, P. Padoan, and R. Wagner. The statistics of supersonic isothermal turbulence. *The Astrophysical Journal* 665, pages 416–431, 2007.
- [63] A. G. Kritsuk, R. Wagner, and M. L. Norman. Energy cascade and scaling in supersonic isothermal turbulence. *Journal of Fluid Mechanics Vol. 729, R1*, 2013.
- [64] A. Kumar and D. M. Rust. Interplanetary magnetic clouds, helicity conservation, and current-core flux-ropes. *Journal of Geophysical Research* 101, pages 667–684, 1996.

- [65] T. Lessinnes, F. Plunian, and D. Carati. Helical shell models for MHD. *Theoretical and Computational Fluid Dynamics 23*, pages 439–450, 2009.
- [66] D. Levy, G. Puppo, and G. Russo. Central WENO schemes for hyperbolic systems of conservation laws. *Mathematical Modelling and Numerical Analysis 33*, No. 3, pages 547–571, 1999.
- [67] M. J. Lighthill. The effect of compressibility on turbulence. In *Gas Dynamics of Cosmic Clouds, International Astronomical Union Symposium 2*, pages 121–130. North Holland Publishing Company, Amsterdam, 1955.
- [68] M. Linkmann, A. Berera, M. McKay, and J. Jäger. Helical mode interactions and spectral transfer processes in magnetohydrodynamic turbulence. *Journal of Fluid Mechanics 791*, pages 61–96, 2016.
- [69] M. Linkmann, G. Sahoo, M. McKay, A. Berera, and L. Biferale. Effects of magnetic and kinetic helicities on the growth of magnetic fields in laminar and turbulent flows by helical fourier decomposition. *The Astrophysical Journal 836:26*, 2017.
- [70] X.-D. Liu, S. Osher, and T. Chan. Weighted essentially non-oscillatory schemes. *Journal of Computational Physics 115*, pages 200–212, 1994.
- [71] P. Londrillo and L. Del Zanna. High-order upwind schemes for multidimensional magnetohydrodynamics. *The Astrophysical Journal 530*, pages 508–524, 2000.
- [72] B. C. Low. Magnetohydrodynamic processes in the solar corona: Flares, coronal mass ejections, and magnetic helicity. *Physics of Plasmas 1*, pages 1684–1690, 1994.
- [73] M.-M. Mac Low. The energy dissipation rate of supersonic, MHD turbulence in molecular clouds. *The Astrophysical Journal 524*, pages 169–178, 1999.
- [74] S. K. Malapaka. *A Study of Magnetic Helicity in Decaying and Forced 3D-MHD Turbulence*. PhD thesis, Universität Bayreuth, 2009.
- [75] P. McCorquodale and P. Colella. A high-order finite-volume method for conservation laws on locally refined grids. *Communications in Applied Mathematics and Computational Science 6*, No. 1, pages 1–25, 2011.
- [76] M. Meneguzzi, U. Frisch, and A. Pouquet. Helical and nonhelical turbulent dynamos. *Physical Review Letters 47*, No. 15, pages 1060–1064, 1981.
- [77] A. Mignone, P. Tzeferacos, and G. Bodo. High-order conservative finite difference GLM-MHD schemes for cell-centered MHD. *Journal of Computational Physics 229*, pages 5896–5920, 2010.
- [78] P. D. Mininni, A. Alexakis, and A. Pouquet. Large-scale flow effects, energy transfer, and self-similarity on turbulence. *Physical Review E 74*, 016303, 2006.
- [79] P. D. Mininni and A. Pouquet. Finite dissipation and intermittency in magnetohydrodynamics. *Physical Review E 80*, 025401, 2009.
- [80] H. K. Moffatt. The degree of knottedness of tangled vortex lines. *Journal of Fluid Mechanics 35*, pages 117–129, 1969.

- [81] H. K. Moffatt. Note on the triad interactions of homogeneous turbulence. *Journal of Fluid Mechanics* 741, R3, 2014.
- [82] W.-C. Müller, S. K. Malapaka, and A. Busse. Inverse cascade of magnetic helicity in magnetohydrodynamic turbulence. *Physical Review E* 85, 015302, 2012.
- [83] J. Núñez-de la Rosa and C.-D. Munz. XTROEM-FV: A new code for computational astrophysics based on very high-order finite volume methods- I. Magnetohydrodynamics. *Monthly Notices of the Royal Astronomical Society* 455, pages 3458–3479, 2016.
- [84] S. A. Orszag. Analytical theories of turbulence. *Journal of Fluid Mechanics* 41, pages 363–386, 1970.
- [85] S. B. Pope. *Turbulent flows*. Cambridge University Press, 2000.
- [86] A. Pouquet, U. Frisch, and J. Léorat. Strong MHD helical turbulence and the nonlinear dynamo effect. *Journal of Fluid Mechanics* 77, part 2, pages 321–354, 1976.
- [87] A. Pouquet and G. S. Patterson. Numerical simulation of helical magnetohydrodynamic turbulence. *Journal of Fluid Mechanics* 85, part 2, pages 305–323, 1978.
- [88] R. E. Pudritz and N. K.-R. Kevlahan. Shock interactions, turbulence and the origin of the stellar mass spectrum. *Philosophical Transactions of the Royal Society A* 371:20120248, 2013.
- [89] L. F. Richardson. *Weather Prediction by Numerical Process*. Cambridge University Press, 1922.
- [90] V. V. Rusanov. The calculation of the interaction of non-stationary shock waves with barriers. *Zhurnal Vychislitel'noi Matematiki i Matematicheskoi Fiziki*, 1:2, pages 267–279, 1961. English: USSR Computational Mathematics and Mathematical Physics, 1:2, 304-320, 1962.
- [91] W. Schmidt, C. Federrath, M. Hupp, S. Kern, and J. C. Niemeyer. Numerical simulations of compressively driven interstellar turbulence, I. Isothermal gas. *Astronomy and Astrophysics* 494, pages 127–145, 2009.
- [92] W. Schmidt, W. Hillebrandt, and J. C. Niemeyer. Numerical dissipation and the bottleneck effect in simulations of compressible isotropic turbulence. *Computer and Fluids* 35, pages 353–371, 2006.
- [93] C.-W. Shu. Essentially non-oscillatory and weighted essentially non-oscillatory schemes for hyperbolic conservation laws. *ICASE Report No. 97-65*, 1997.
- [94] C.-W. Shu. High order weighted essentially nonoscillatory schemes for convection dominated problems. *Society for Industrial and Applied Mathematics Review Vol. 51, No. 1*, pages 82–126, 2009.
- [95] J. B. Taylor. Relaxation of toroidal plasma and generation of reverse magnetic fields. *Physical Review Letters Vol. 33, No. 19*, pages 1139–1141, 1974.
- [96] J. B. Taylor. Relaxation and magnetic reconnection in plasmas. *Review of Modern Physics Vol. 58, No. 3*, pages 741–763, 1986.

- [97] J.-M. Teissier and W.-C. Müller. Higher-order magnetohydrodynamic numerics. In *Space Plasma Simulation: Approaches, codes and applications*. 2019. submitted.
- [98] E. F. Toro. *Riemann Solvers and Numerical Methods for Fluid Dynamics, Third Edition*. Springer, Heidelberg, 2009.
- [99] B. van Leer. Towards the ultimate conservative difference scheme. IV. A new approach to numerical convection. *Journal of Computational Physics* 23, pages 276–299, 1977.
- [100] P. S. Verma, J.-M. Teissier, O. Henze, and W.-C. Müller. Fourth order accurate finite volume CWENO scheme for astrophysical MHD problems. *Monthly Notices of the Royal Astronomical Society* 482, pages 416–437, 2019.
- [101] C. F. von Weizsäcker. The evolution of galaxies and stars. *The Astrophysical Journal* 114, pages 165–186, 1951.
- [102] F. Waleffe. The nature of triad interactions in homogeneous turbulence. *Physics of Fluids A: Fluid Dynamics* 4, pages 350–363, 1992.
- [103] L. Woltjer. On hydromagnetic equilibrium. *Proceedings of the National Academy of Sciences* 44, No. 9, pages 833–841, 1958.
- [104] L. Woltjer. A theorem on force-free magnetic fields. *Proceedings of the National Academy of Sciences* 44, No. 6, pages 489–491, 1958.
- [105] S. Xu, S. Ji, and A. Lazarian. On the formation of density filaments in the turbulent interstellar medium. *The Astrophysical Journal* 878:157, 2019.
- [106] U. Ziegler. A central-constrained transport scheme for ideal magnetohydrodynamics. *Journal of Computational Physics* 196, pages 393–416, 2004.